University of Manchester

Functionalised graphene for biomedical applications

A thesis submitted to the University of Manchester for the degree Doctor of Philosophy in the Faculty of Science and Engineering.

2017

Philippa M. Shellard

School of Chemistry

TABLE OF CONTENTS

Word count: 58,332

LIST OF FIGURES

Chapter 1

Chapter 2

Chapter 3

Chapter 4

Chapter 5

Chapter 6

Appendix

LIST OF TABLES

Chapter 1

Chapter 2

Chapter 3

Chapter 4

Chapter 5

LIST OF ABBREVIATIONS

Abbreviation	Meaning
2D	2 Dimensional
3T3-SA	3T3-Swiss Albino cells
AFM	atomic force microscopy
AKT/PKB	protein-kinase B
ALCAM	activated leukocyte cell adhesion molecule
Allyl-DO3A	cyclen-1-allyl-4,7,10-triacetic acid
Allyl-DO3A	cyclen-1-allyl-4,7,10-triacetic acid
Allyl-DO3A-tBu	cyclen-1-allyl-4,7,10-tri-tertbutyl ester
AMP	antimicrobial peptides
Arg-Gly-Asp	arginylglycylaspartic acid
ATP	adenosine triphosphate
AuNPs	gold nanoparticles
BALP	bone alkaline phosphatase
BET	Brunauer-Emmet-Teller
BLG	bilayer graphene
BMP-2	bone morphogenetic protein 2
BSA	bovine serum albumin
BSP	bone sialoprotein
C/EBPs	CCAAT-enhancer binding proteins
CHNS	Carbon Hydrogen Nitrogen Sulphur
CNTs	carbon nanotubes
conA	Concanavalin A
CS	chitosan
CT	campothecin
CVD	chemical vapour deposition
Da	Dalton
DAPI	4',6-diamidino-2-phenylindole
DCM	dichloromethane
DLS	dynamic light scattering
DMEM	Dulbecco's modified eagle's medium
DMF	dimethyl formamide
DMSO	dimethyl sulfoxide
DNA	deoxyribonucleic acid
DO3A	cyclen-4,7,10-triacetic acid
DO3A-tBu	cyclen-4,7,10-tri-tertbutylester
DOTA	cyclen-1,4,7,10-tetraacetic acid
dsDNA	double-stranded DNA
DXR	doxorubicin
ECM	extracellular matrix

EDC	1-ethyl-3(3-dimethylaminopropyl)-carbodiimide
EDX	energy dispersive X-ray spectroscopy
FACS	fluorescence activated cell sorting
FAKs	focal adhesion kinases
FAM	fluorophore carboxyfluorescein
Fas	focal adhesions
FBS	foetal bovine serum
FET	field effect transistor
FHL2	four and a half LIM domains protein 2
FITC-conA	fluorescein isothiocyanate-labelled conA
FLG	few-layer graphene
Fn	fibronectin
FOXA2	forkhead box protein A2
FOXO1	forkhead box protein O1
FRET	fluorescence resonance energy transfer
FTIR	fourier-transform infrared
FWHM	full width at half maximum
GFAP	glial fibrillary acid protein
GFN	graphene-family nanomaterial
GHA	gelatin-hydroxyapatite
G-NH_2	aminographene
G-NO_2	nitrographene
GnPs	graphene nanoplatelets
GO	graphene oxide
GO-ns	graphene oxide nanosheets
GO-SO_3	graphene oxide sulfonate
GOx	glucose oxidase
GQD	graphene quantum dots
G-SH	graphene thiol
G-SO_3	graphene sulfonate
HDAC1	histone deacytelase-1
hMSCs	human mesenchymal stem cells
hNSCs	human neural stem cells
HOPG	highly ordered pyrolytic graphite
H-rGO	hydrazine reduced GO
HSC	hematopoietic stem cells
I_{590}	fluorescence Intensity at 590 nm
$I_D/I_{D'}$	intensity of Raman D peak/ intensity of the Raman D' peak
I_D/I_G	intensity of Raman D peak/ intensity of the Raman G peak
IGF1	insulin growth-factor-1
IR	infrared

IRS	insulin receptor substrate
LbL	layer-by-layer
LDH	lactate dehydrogenase
MAP-2	microtubule associated protein 2
MAPK	mitogen activated protein kinase
MEFs	mouse embryonic fibroblasts
mL	millilitres
M-rGO	microbially reduced GO
MRI	magnetic resonance imaging
MSC	mesenchymal stem cells/ mesenchymal stromal cells
MWNT	multiwalled carbon nanotube
NADH	nicotinamide adenine dinucleotide
NGS	nanographene sheets
NHS	*N*-hydroxyl succinimide
NIH-3T3s	National Institute of Health mouse embryonic fibroblast cells
NIR	near-infrared
NMP	*N*-methyl pyrrolidone
NMR	nuclear magnetic resonance
NOTCH	neurogenic locus notch homolog
OCN	osteocalcin
ORR	oxygen reduction reaction
OTf	triflate
PAA	poly(acrylic acid)
PAH	poly(allylamine hydrochloride)
PAM	poly(acryl amide)
PANI	polyaniline
PDDA	poly(diallyl dimethylammonium chloride)
PDI	3,4,9,10-perylenetetracarboxylic diimidebisbenzenesulfonic acid
PDMS	polydimethylsiloxane
PEDOT	poly (3,4-ethylenedioxythiophene)
PEG	polyethylene glycol
PEI	polyethyleneimine
PEI/GO	polyethyleneimine/ graphene oxide
PEI/GO-SO_3	polyethyleneimine/ graphene oxide sulfonate
PEI/G-SO_3	polyethyleneimine/ graphene sulfonate
PEI/PSS(-)	polyethyleneimine/ polystyrene sulfonate (polystyrene sulfonate terminated)
PEI/PSS(+)	polyethyleneimine/ polystyrene sulfonate (polyethyleneimine terminated)
P-ERK	phosphate extracellular signal-regulated kinases

PET/CT	positron emission tomography–computed tomography
PGLA	poly(lactic-co-glycolic acid)
PHMB	polyhexamethylene biguanide
PLL	poly-L-lysine
PMMA	poly(methyl methacrylate)
PPARγ	peroxisome proliferator activated receptor γ
PREF-1	pre-adipocyte factor 1
PSS	polystyrene sulfonate
PVA	polyvinyl alcohol
PVC	polyvinyl chloride
PVK	polyvinyl-N-carbazole
PVP	polyvinylpyrrolidone
Ra	roughness average
RGD	L-arginyl-glycyl-L-aspartyl
rGO	reduced graphene oxide
rGO	reduced graphene oxide
rGONR	reduced graphene oxide nanoribbons
RMS	route mean squared
RNA	ribonucleic acid
ROS	reactive oxygen species
RT-PCR	reverse transcription polymerase chain reaction
Runx2	runt-related transcription factor 2
SBDS	sodium dodecylbenzene sulfonate
SEM	scanning electron microscopy
SMAD	small mothers against decapentaplegic protein
SPR	surface plasmon resonance
ssDNA	single-stranded DNA
STEM	scanning transmission electron microscopy
SWNT	singly walled carbon nanotube
TAZ	transcriptional coactivator
TCF/LEF-1	T-cell factor and lymphoid enhance factor
TEM	transmission electron microscopy
TGA	thermogravimetric analysis
TGF-β	transforming growth factor β
THSPS	3-(trihydroxysilyl) propane-1-sulfonic acid
TNT	trinitrotoluene
TRITC	tetramethylrhodamine
UV	ultraviolet
UV-vis	ultraviolet-visible
VEG-F	vascular endothelial growth factor
wt.%	weight percentage
XPS	x-ray photoelectron spectroscopy

Z	atomic number
β-Gly	β-glycerophosphate

ABSTRACT

Philippa Shellard
The University of Manchester
Doctor of Philosophy
Functionalised graphene for biomedical applications- 2017

There has been increasing interest in the use of pristine graphene in biomedical applications, but its use is limited by its hydrophobicity and lack of functional groups by which to tether molecules, meaning that biological applications of pristine graphene rely on non-specific adsorption of molecules. Furthermore, pristine graphene cannot be used *in-vivo* due to its poor aqueous dispersibility. Functional groups are introduced to graphene to overcome these problems, but many functionalisation methods cause significant disruption to the extended π-system of graphene, from which its favourable properties arise. The aim of this thesis was to address the limitations of using pristine graphene outlined above. The solution proposed was the edge-specific sulfonation and thiol functionalisation of pristine graphene, based upon electrophilic aromatic substitution. The nature of these reactions means that they should cause minimal defect formation, occurring selectively at existing defects and edges of the graphene sheet. The sulfonation of graphene was selected to increase the aqueous dispersibility of pristine graphene, while the thiol functionalisation would provide a means by which to tether molecules covalently to the graphene sheet. The functionalisations were confirmed using a range of analyses, which indicated a low level of new defect formation, as well as demonstrating both the presence of the target functional groups and the change in aqueous dispersibility of the graphene sheets. Furthermore, the functionalisation was shown to be edge-specific by attaching a fluorescent protein to thiol functional groups on the edges.

G-SO_3 was incorporated into a polymer layer-by-layer (LbL) construct, for use in wound healing applications, together with analogous constructs containing graphene oxide (GO) and sulfonate-functionalised GO (GO-SO_3). The constructs were characterised, to assess the effect of different functionalisations on the coverage of graphene. Analysis confirmed the presence of G-SO_3, GO and GO-SO_3 in the constructs, but indicated a lower graphene coverage for the G-SO_3 construct, thought to be a result of the lower number of functional groups in this material. The biocompatibility of G-SO_3, GO and GO-SO_3 LbL constructs was tested on 3T3 Swiss Albino fibroblast cells and human mesenchymal stem cells. In addition, the differentiation of stem cells on these graphene-containing surfaces was monitored and compared to published work on graphene-family nanomaterials. The biocompatibility studies revealed that cell adhesion and proliferation were dictated by extracellular matrix (ECM) protein adsorption on the LbL constructs. The substrates able to bind higher amounts of ECM protein were found to show greater cell adhesion and proliferation, with ECM protein binding correlated to the roughness and surface chemistry of the constructs.

Future applications would be to introduce alternative functional groups to graphene, using the principles outlined in this thesis. In addition, there is potential for the attachment of a variety of biologically relevant molecules to functionalised graphene sheets. This could lead to the use of pristine graphene in many biomedical applications.

DECLARATION

No portion of the work referred to in the thesis has been submitted in support of an application for another degree or qualification of this or any other university or other institute of learning.

COPYRIGHT STATEMENT

ACKNOWLEDGEMENTS

I would like to thank the University of Manchester for giving me the opportunity to undertake this PhD. I would also like to thank Sabine Flitsch and Chris Blanford for agreeing to take me on, for guiding me through the process and supporting me during my time at Manchester.

I would like to thank my work mates, especially Tom McNamara, Joe Butcher and Rebecca Davey, for keeping spirits high through the many challenges of the last few years. I would like to thank all my friends both from home, university, from college and from drama, for keeping me sane and being there for a whinge.

Most importantly, I want to thank my wonderful parents and my partner, Lee, for helping me get through this challenging experience. I could not have completed this thesis without you all and I appreciate all the support you have given me. In addition, I would like to thank my faithful cat, Simba, who has sat by my computer every day during my write up, urging me to keep going!

I would like to thank Ed Lewis and Lan Nguyen for their guidance on the TEM, Ashley Shepherd and Robert Jacobs (Oxford) for running early XPS on our samples and Polly Greensmith for helping with several techniques and facilities. I would also like to than Fan Fei for his contributions to this work. I would like to thank Julie Gough for allowing me to undertake cell culture work, and to Louise Carney for providing training and for her advice on all things cell related. Finally, I would like to extend tremendous gratitude to Deepak Kumar for all his help and guidance over the last year. Getting involved with cell culture was something I'd always wanted to do and Deepak made it an enjoyable experience.

1. INTRODUCTION

Graphene is a novel 2D material, made of sp^2 hybridised carbons in a hexagonal lattice.[1] The desirable properties of graphene such as its high surface area (2630 m^2g^{-1}),[2] high electron mobility (2×10^5 $cm^2 V^{-1} s^{-1}$),[3] high Young's Modulus (1 TPa)[4] and high elastic modulus,[4] have resulted in an increasing interest in graphene and its analogues for biological applications such as drug delivery,[5,6] electrochemical sensors,[7,8] composite materials[9,10] and in tissue engineering.[11,12,13,14]

Pristine graphene is limited in its use in biological settings, largely due to its poor aqueous dispersibility and lack of functional groups by which to tether biologically relevant molecules. Other graphene related materials, such as graphene oxide (GO), graphene with sp^3 carbons and oxygen-containing defects on the basal plane, are used much more widely as they can be dispersed in aqueous solution and have functional groups by which to attach biological molecules.[15] However, the defects present on GO sheets mean that some of the desirable properties of graphene are lost, such as mechanical strength and conductivity.[16,17]

The aim of this thesis was to selectively functionalise pristine graphene at the edges, to provide functional groups on pristine graphene sheets and increase their aqueous dispersibility, while leaving the majority of each graphene sheet intact, thus retaining graphene's favourable properties. The research aims of this thesis are outlined below:

- To develop edge-specific, biologically relevant functionalisations of pristine graphene that do not cause significant damage to the graphene sheet.

- To demonstrate the attachment of selected biologically relevant molecules to the edge-functionalised graphene.
- To incorporate functionalised pristine graphene into a polymer layer-by-layer (LbL) construct.
- To assess the toxicity of the functionalised graphene LbL construct towards 3T3 Swiss albino (3T3 SA) fibroblast cells and compare it to analogous LbL constructs containing GO.
- To compare the viability and differentiation of human mesenchymal stem cells on the functionalised graphene LbL constructs and compare it to analogous LbL constructs containing GO.

The introduction provides a review of the production, characterisation, modification, biological applications and toxicological studies of graphene. The section also provides an overview of cell culture, with particular focus on the cell lines used in this thesis; mouse embryonic fibroblasts and human mesenchymal stem cells. Finally, an experimental outline is provided in Section 1.11.

1.1. Graphene and graphene family nanomaterials

Graphene is, by definition, an atomically thin monolayer of sp^2 -hybridised carbons, arranged in a hexagonal lattice.[1] It was isolated in 2004 and has since been found to possess a range of superlative properties: ultra-high electron mobility (2×10^5 cm^2 V^{-1} S^{-1}),[3] a surface area of approximately 2630 m^2 g^{-1},[2] a high Young's modulus (1 TPa), an intrinsic breaking strength of 42 $N\,m^{-1}$, high elastic modulus,[4] tensile strength of 130 GPa,[4] a thermal conductivity of $5\,kW\,m^{-1}$ K^{-1},[18] and a spring constant ~ 50 eV $Å^{-2}$.[19] Graphene is also the strongest recorded material in elastic

stress-strain response and is approximately one million times more conductive than copper.[4,20]

The favourable characteristics of graphene have been utilised in various scientific applications. The high carrier mobility of graphene has led to its use in sensing and electrochemical applications;[21] adjusting the number of layers of graphene enables tailoring of the band gap, maximising the detection sensitivity.[22] Furthermore, graphene is being set to replace traditional semiconductors in electronic devices.[3,23] The fact that monolayer graphene is almost transparent (approx. 98 %) to visible light, teamed with its flexibility, means that it has great potential for use in devices.[24] The high surface area of graphene has been exploited for drug delivery applications, due to the higher loading capacity achievable in comparison to conventional drug delivery modes.[25,26] Graphene has also been used in the production of composite materials, from polymer fillers to graphene-metal oxide composites.[27,28,29,30]

Several materials exist which are related to 'graphene', or 'graphene-family nanomaterials' (GFNs) and differ in the degree of functionalisation, lateral dimensions and number of layers. Attempts have been made to sub-divide GFNs according to these parameters, an example of which can be seen in Figure 1-1.[31]

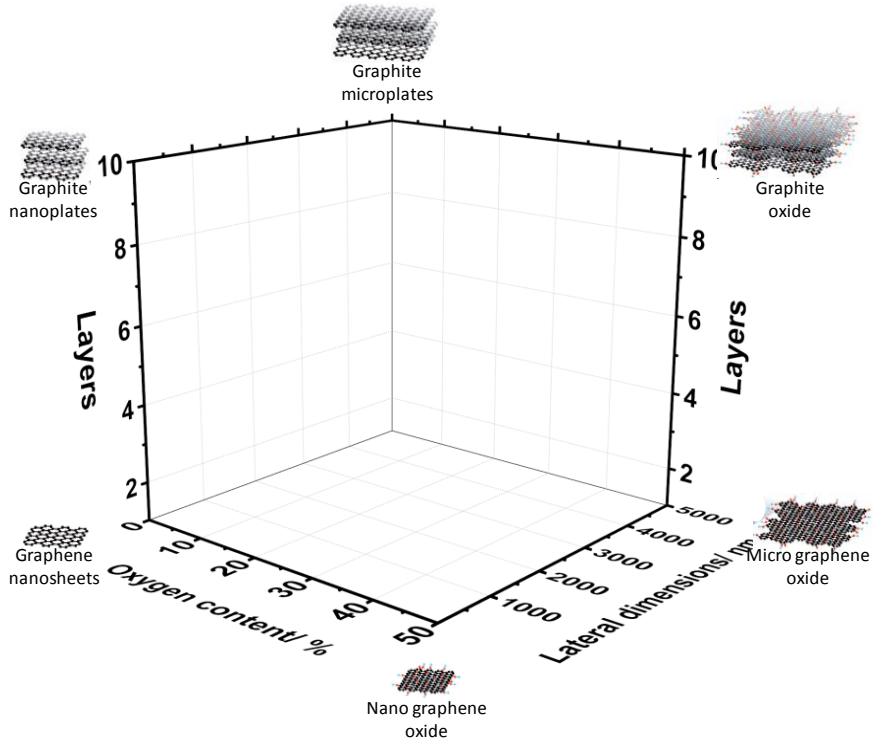

Figure 1-1. Guide to classification of graphene nanomaterials as a function of lateral dimensions, oxygen content and number of layers. Adapted from Wick *et al*.[31]

The size of GFNs span orders of magnitude,[31] with layer number (1-10 layers) and oxygen content (0 % to > 50 %) varying considerably. Understandably, these factors affect the superlative properties of 'graphene'. For example, defects disrupt the electronic properties of graphene,[32] forming sp^3 domains which disrupt conduction across the graphene sheet. The mechanical strength is affected by defects; GO has been reported to show Young's modulus between 200-500 GPa, significantly lower than that of pristine graphene.[16,17] Stiffness of graphene sheets varies with layer number,[4] whilst the lateral dimensions of GFNs have implications in biodistribution.[33,34] Despite attempts to subdivide and categorise GFNs according to these properties, there is no standardised nomenclature for GFNs and thus, though varying considerably, most GFNs are referred to as 'graphene' in the majority of literature, regardless of the sometimes extreme differences in the parameters described above.

An example of a GFN is graphene oxide (GO), produced by exposing graphite to strong acids and oxidants followed by exfoliation (typically sonication).[35] GO can be considered an oxidised form of graphene, which possesses oxygen-containing functional groups including hydroxyl, epoxide and carboxyl groups, which arise from the oxidation process. The precise chemical structure of GO is debated, with early models such as those of Hofman, Reuss and Scholz-Boehm, based upon a regular lattice of repeat units.[36] The Lerf-Klinowsky model, the most widely cited structure for GO, is shown in Figure 1-2 and is based upon NMR studies of GO;[36,37] alternative versions of this model omit carboxylic acids on the periphery.[37,38] A comprehensive review of graphene oxide structures is provided by Dreyer *et al.*[36]

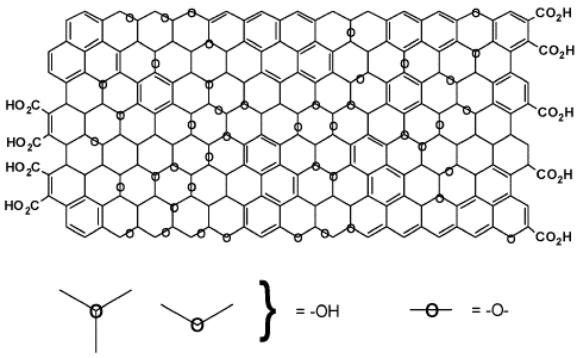

Figure 1-2. The Lerf-Klinowski model of graphene oxide. Reproduced from Dreyer *et al.*[36] Originally from paper by Lerf *et al.*[37]

In GO, a large proportion of the sp^2 carbons are oxidised to sp^3 carbons,[39] with sheets typically containing 30 % to 50 % oxygen, depending on the method of production.[31] GO carries an negative charge, as determined from zeta potential measurements (at physiological pH), thought to arise from the carboxylate functional groups.[40] The negative charge of GO results in electrostatic repulsion between individual sheets, facilitating the separation of layers and resulting in stable aqueous suspensions.[40]

The conductivity of GO is 1–5 × 10^{-3} S cm^{-1},[41, 42] significantly lower than that of pristine graphene, due to the disruption of the sp^2 carbon network. GO is often reduced, therefore, to restore conductivity. Reduced GO (rGO) typically exhibits a conductivity of between 0.05-2 S cm^{-1}, remaining lower than that of pristine graphene.[42,43,44] The restoration of the conductive π-system of graphene is not complete following reduction of GO to rGO, as residual sp^3 hybridised carbons remain on the rGO sheets.[2]

1.2. Synthetic routes to graphene and graphene family nanomaterials

Graphene and graphene-family nanomaterials (GFNs) are fabricated by 'bottom-up' or 'top-down' approaches. In the 'bottom-up' approach, GFNs are fabricated on a substrate from constituent elements while in the 'top-down' approach, graphene is produced from the cleavage of graphite into increasingly thin layers. The following section outlines the most common methods of graphene production and considers their advantages and disadvantages.

1.2.1. Chemical vapour deposition

Chemical vapour deposition (CVD) is a 'bottom-up' method of producing graphene. CVD consists of the pyrolysis of hydrocarbons to form carbon radicals and molecules, following which graphene formation is achieved by the dissolution of these carbon species onto a metal substrate.[45] The metal support is dissolved and the resultant graphene transferred onto an alternative substrate, such as SiO_2. The CVD method is successful in producing large scale, high quality graphene films, with electron mobilities of up to 3700 cm^2 V^{-1} s^{-1}.[46,47]

Transition metals have been used to catalyse the decomposition of hydrocarbons for the formation of graphene-like structures since the 1960s.[48] Ni catalysts were the

first used for production and are still the most commonly employed.[47,49,50] Ni displays high carbon solubility at high temperature but, once the temperature is decreased, carbon solubility decreases, meaning that carbon diffuses out from the Ni-C, forming hexagonal lattices.[51,52] The Ni(111) plane has a similar lattice to that of graphene, making it a good template for graphene growth.[52,53] Figure 1-3 shows the CVD assembly of graphene on Ni.

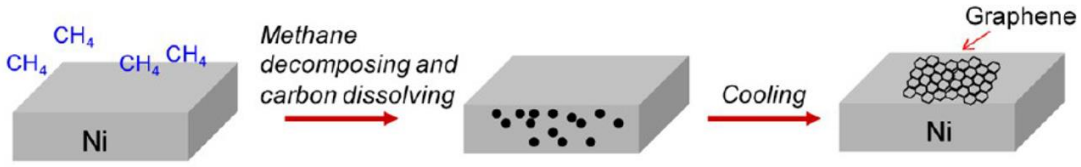

Figure 1-3. Schematic showing the formation of graphene on Ni. Reproduced from Zhang *et al.*[52]

Using Ni catalysts, few-layer graphene is only obtainable over tens of microns, at considerable expense,[46,54] while cooling rate, growth time and hydrocarbon concentration can affect the thickness of graphene films produced.[52,55] Alternative catalysts include Ru,[56] Pt[57] and Cu,[51] with Cu showing the greatest potential for scale-up,[58] as Cu substrates are less expensive than Ni and can produce single-layer graphene sheets of up to ten inches.[46,51] In addition, because Cu has a very low carbon solubility, only a small amount dissolves onto Cu, regardless of the cooling rates or hydrocarbon concentration, meaning that thickness varies little with these parameters, in contrast to Ni catalysis.[52]

Once CVD graphene is produced on metal substrates, it must be transferred to an alternative substrate.[47] Poly-(methyl methacrylate) (PMMA) has been widely used to transfer CVD grown graphene to other substrates.[47,51] Graphene is coated with PMMA before the metal is etched, typically using strong acids such as HNO_3.[47] The PMMA-coated graphene is then transferred onto an alternative substrate. The chemical etching, however, causes a reduction in quality of the graphene product.[47,52]

1.2.2. Epitaxial growth

Epitaxial graphene is grown on SiC (0001) wafers[59] and involves the sublimation of the silicon atoms from SiC (0001) and the annealing of the C atoms, causing graphitisation.[58] During growth of graphene on SiC (0001), the number of layers can be modulated by controlling the sublimation of Si.[59,60] In contrast to the metal substrates used in CVD graphene production, SiC substrates are insulating,[58] meaning that there is no requirement to transfer the graphene to alternate substrates for electronic applications. However, the morphology of graphene sheets is difficult to control in epitaxial growth, and the temperatures required are extremely high.[45]

1.2.3. Sonochemical exfoliation

In sonochemical exfoliation, graphite sheets are dispersed in a solvent and exposed to ultrasonic agitation to force the cleavage of graphitic layers, after which centrifugation is performed to remove heavier, graphitic layers.[61] Sonochemical exfoliation is driven by acoustic cavitations, the formation and implosion of bubbles occurring in a liquid at high ultrasonic intensities, which force apart graphitic layers.[62] Coleman and co-workers demonstrated the production of graphene via sonochemical exfoliation to be strongly dependent on the interaction between the graphitic sheets and the dispersing solvent, as described by Equation 1:[63]

$$\boldsymbol{C_G \propto \left[-\frac{\pi D_G^2}{8\, E_{S,G} kT} \left(E_{S,S} - E_{S,G} \right)^2 \right]} \quad (1)$$

Where $\boldsymbol{C_G}$ is the resultant concentration of the as-produced graphene, $\boldsymbol{D_G}$ is the diameter of the graphene sheet, $\boldsymbol{k}$ is the Boltzmann constant, $\boldsymbol{T}$ is temperature, and $\boldsymbol{E_{S,S}}$ and $\boldsymbol{E_{S,G}}$ are the solvent and graphene surface energies, respectively. Therefore, when the solvent and graphene surface energies are similar, the energetic cost of exfoliating graphite is counteracted by strong graphene-solvent interactions.[61]

Coleman and co-workers performed sonochemical exfoliation of graphite in a variety of solvents, finding that exfoliation was most effective in solvents with surface energies of around 70 mJ m^{-2}.[63] *N*-methyl pyrrolidone (NMP) and dimethyl formamide (DMF) are the most widely used solvents for sonochemical exfoliation of graphite but,[61] due to the high boiling points and relative toxicity of these solvents, graphite has been exfoliated in ionic liquids,[64,65,66,67,68] as well as surfactants such as Pluronic P-123,[69] polyvinylpyrollidone (PVP)[70] and sodium dodecylbenzene sulfonate (SBDS).[71]

Sonochemical exfoliation produces few-layer graphene sheets with few oxygen-containing defects,[61] the low defect density meaning that the electronic properties of graphene are largely conserved.[32] Coleman and co-workers determined trends between the lateral dimensions of sonochemically exfoliated graphene and sonication time, as well as between the number of layers of sonochemically exfoliated graphene and centrifugation parameters.[32,72] These observations provide a means by which to tailor the size and thickness of graphene sheets.

The production rate of sonochemically exfoliated graphene is independent of volume, meaning that scale-up of production by increasing volume is not effective.[73] Theoretical and experimental evidence indicate that vessel shape and size affect acoustic cavitations and thus exfoliation,[74,75,76] which presents an additional obstacle in making sonochemical exfoliation scalable and achieving batch-to-batch consistency. Recently, sonochemically-exfoliated graphene was found to contain more defects than anticipated,[77,78] with Bracamonte *et al*. indicating that shorter sonication times (under 2 hours) produces defects which predominate at edges, but longer sonication times introduce basal plane defects.[78]

1.2.4. Shear exfoliation

The shear exfoliation of graphite was developed as an economical way to produce large quantities of graphene for use in inks, coatings and printed electronics.[79,80] Paton and Liu developed graphene production based on rotor-stator mixing,[81,82] where graphite is suspended in a solvent, after which rotor-stators are placed into the solution and generate local turbulent shear. The rotor stators and set-up for this shear exfoliation is shown in Figure 1-4.

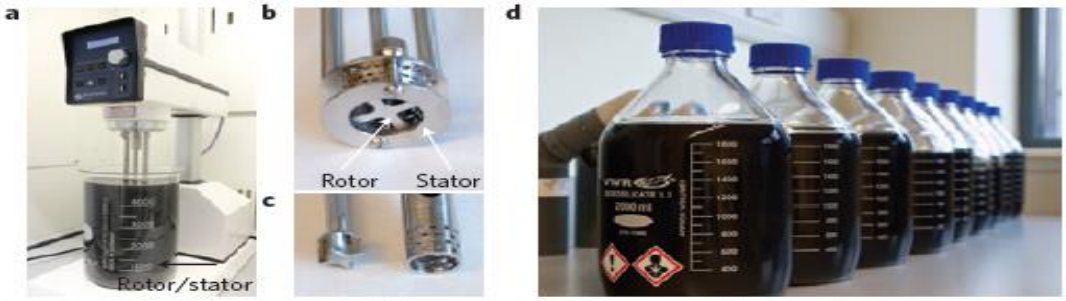

Figure 1-4. (a) Silverson L5M high-shear mixer with mixing head in 5L graphene dispersion. b, c, Close-up view of a D=32mm mixing head (b) and a D=16mm mixing head with rotor (left) separated from stator (c). (d) Graphene–NMP dispersions produced by shear exfoliation. Paton *et al.*[81]

Mixers with shear rates above 10^4 s^{-1} are able to generate graphene,[81] with Varrla *et al*., for example, recording successful exfoliation of graphene, in fairly liquid, using a Kenwood BL370 series kitchen blender fitted with a 400 W motor.[73] Production rates for shear exfoliation scale with volume (as $V^{1.6}$), meaning that scale-up can be achieved by increasing volume.[73, 81] However, low concentrations (approx. 0.1 mg mL^{-1}) are produced by this method, with production rate decreasing as mixing time is increased.[73] In addition, kitchen blenders are not designed to be continuously used at high speeds, meaning that they are only able to be used for short periods, followed by a break, raising concerns about the longevity of the method.[73]

1.2.5. Chemical exfoliation

The chemical oxidation of graphite was first reported in the 19th century, based upon work by Staudenmaier and Brodie.[83,84] This technique was then developed by Hummer and Offeman in the 1950s,[85] using $KMnO_4$ as the oxidant, to produce 'graphene oxide' (GO). The chemical oxidation of graphite, followed by sonication, is able to generate large quantities of homogeneous, colloidal GO suspensions.[35] As the oxidation process reduces the conductivity of GO, reduction is usually performed to restore conductivity, with reducing agents including hydrazine,[86,87,88] sodium borohydride[89] and hydroquinone.[90] Urea, sodium ascorbate, molten halide flux and electrochemical methods have also been used to reduce GO.[91,92,93,94] The reagents used for producing both GO and rGO are hazardous, however, which limits the scalability of this method of production.[95,96]

1.2.6. Thermal exfoliation

Thermal exfoliation of graphite is achieved by the intercalation of graphite, with species such as sulfuric acid and nitric acid,[97,98] followed by rapid heating. Schniepp *et al.* reported the formation of single-layer 'graphene' sheets from thermal exfoliation of graphite and subsequent reduction.[99] Thermally-exfoliated graphene sheets possess similar oxygen content to hydrazine-reduced graphene oxide, and exhibit powder conductivity in the region of $10\ S\ m^{-1}$.[100] Graphite is not fully exfoliated by this method, possessing surface areas of around $100\ m^2\ g^{-1}$ unless sonication is used in combination.[100]

Vacuum assisted thermal exfoliation has been developed by Lv *et al.*,[101] in which the vacuum exerts an outside negative force on graphitic layers, while the inside force of intercalating species pushes layers apart, producing graphene.[101] The vacuum system

means that oxygen-containing functionality can be removed at a lower temperature, with lower temperatures causing fewer defects than for typical thermally-exfoliated graphene.[102]

1.2.7. Electrochemical exfoliation

The electrochemical exfoliation of graphite originates from graphite intercalation complexes,[103,104] such as those with electron donor species like K, Rb and Li and electron acceptors such as Br. Intercalating species are used for the expansion of graphite electrodes,[103] after which applied potentials result in the decomposition of the intercalant, forcing the expanded layers apart and/or the formation of gaseous species from the solution. The process of intercalation and decomposition is repeated to produce graphene, with the number of cycles varying with intercalant and solvent.[105,106,107] Common intercalants include phosphate ions,[108] carboxylates,[109] perchlorates,[110] and nitrates,[111,107] in addition to combinations such as Na^+/DMSO[112] and Et_3NH^+/DMSO/Li^+.[105] Electrochemical exfoliation of graphene takes mins to hours,[32,113,114] is achievable under ambient conditions[103] and is able to produce graphene on a large scale.[115]

The chemistry behind the electrochemical exfoliation processes remains unclear, owing to the high potentials and harsh reagents used. In addition, sonication is often required to achieve full exfoliation, presenting complications for industrial scale-up.[103,107,116,117] The control of lateral size of graphene sheets is challenging and is highly variable, as oxidative processes produce sheets of micrometre size,[114,115,118] while cathodic process can produce sheets reaching hundreds of micrometres in size.[105, 117]

The potentials required for effective intercalation of ions during anodic exfoliation are close to those required to oxidize graphite,[103] meaning that oxygen-containing functionality is generated on the exfoliated graphene sheets, damaging the extended π-structure of graphene.[119] For applications in which the conductivity of the graphene sheets is important, cathodic exfoliation is therefore preferable.[103] For example, Cooper *et al.* produced few-layer graphene with negligible oxidation by cathodic intercalation of tetraalkyl ammonium salts.[120,121] Cathodic exfoliation processes, however, suffer from slow kinetics, which hinders industrial scale-up.[107, 116] Furthermore, the electrolytes used must stabilise the intercalating species, as well as the resultant graphene sheets.[103] Aqueous electrolytes are suitable for anodically exfoliated graphene, as the introduction of hydrophilic, oxygen-containing functionality is able to stabilise sheets.[122] Cathodically exfoliated graphene more closely resembles pristine graphene, meaning that surface energy of the dispersing solvent must be matched to that of graphene.[63,120,123] Dimethyl sulfoxide (DMSO) is the most common solvent for cathodic, electrochemical exfoliation.[103,112,124,125]

1.2.8. Ball milling

Ball milling was originally used to obtain thin graphite,[126] but was developed by Knieke *et al.* to produce graphene.[127] Shear force and the collision of balls during the ball milling process cause the exfoliation.[74] Ball milling is undertaken with the addition of intercalants or stabilising molecules to disperse flakes, avoid agglomeration and increase the exfoliation efficiency. The most common additive is melamine,[128,129] with other examples including 1-pyrene carboxylic acid,[130] sodium dodecyl sulfate[131] and polyurethane,[132] though dry ball milling has been used to exfoliate graphite and is achieved by mixing graphite and chemically inert water-soluble inorganic salts.[133]

The ball milling method integrates the preparation, functionalisation and incorporation processes, and allows the fast production of relatively large quantities of material.[128] Ball milling is dangerous, however, as reactive carbon species are produced inside the ball mill which undergo violent reactions once air is introduced.[134,135,136] In addition, the collision of balls causes fragmentation of large sheets and the formation of amorphous phases,[74] as well as the introduction of basal plane defects.[74] Long milling times and low speeds must be adopted in order to limit damage from ball collisions,[137] but under such conditions sonication is also required to obtain a good degree of exfoliation.[131]

1.2.9. Micromechanical exfoliation

Micromechanical exfoliation of graphene, such as the 'Scotch-tape' method for exfoliation of graphene, originates from the work of Novosolev and co-workers.[43] As the inter-layer interaction energy of graphene sheets is only about 2 eV nm^{-2}, meaning that the force needed to exfoliate graphite is 300 nN μm^{-1}.[45,138] Scotch-tape can provide a force of this magnitude and, when applied to highly ordered pyrolytic graphite (HOPG), exerts a normal force sufficient to cleave apart graphitic layers.[74] This is repeated approximately 12 times (for a 1 μm-thick graphite flake), until single-layer graphene is achieved,[43] after which graphene can be transferred onto alternative substrates by pressing the tape onto the substrate.[45,43,139] The 'Scotch-tape' method produces high-quality sheets, but is labour intensive and produces very small quantities of graphene.[74]

1.2.10. Summary

The highest quality graphene (lowest defect density and oxygen content) would be achieved using the CVD, epitaxial growth or micromechanical exfoliation methods. The drawbacks of these methods are in terms of scale-up; the epitaxial growth and

CVD methods are expensive and micromechanical exfoliation is time consuming and has a low throughput.

The electrochemical exfoliation method is the quickest of the methods outlined, while chemical exfoliation, thermal exfoliation and ball milling can produce gram quantities of graphene. The drawback of these methods arises from the variability in the graphene produced. The electrochemical method is poorly understood and the chemical and thermal exfoliation methods produce highly defected graphene, more close in nature to GO.

The sonochemical and shear exfoliation methods produce relatively large amounts of graphene. The sonochemical exfoliation method also allows for tailoring of graphene properties by altering the duration of sonication. The drawback of these methods is the large amount of solvent required for effective exfoliation. In this thesis, the sonochemical exfoliation method was used, as it can provide good quality graphene without being too expensive, despite the solvent requirement.

1.3. Modification of graphene-family nanomaterials

The modification of graphene-family nanomaterials (GFNs) is employed to alter mechanical[140,141,142] and electronic properties,[143] solubility[89] and biocompatibility.[144,145] Functionalisation can be used to improve the reactivity, covalent attachment, sensing ability or dispersibility of GFNs, or to further enhance the favourable properties of the GFNs.[146] The covalent and non-covalent functionalisation strategies for GFNs are outlined in the following sections.

1.3.1. Non-covalent modifications of graphene-family nanomaterials

The non-covalent modification of GFNs causes little disruption to the electronic properties or structure of the GFNs, while covalent modification introduces sp^3

defects.[146] Pristine graphene has a low defect density and possesses a limited number of binding sites by which to tether molecules. Many modification strategies for pristine graphene therefore centre on non-covalent π-π and CH-π interactions.[146,147] The extended π-system of pristine graphene can interact with aromatic molecules and provides a large surface for π-π interactions.[146] Due to the poor aqueous stability of graphene, non-covalent modification is often used to increase its hydrophilicity. For example, graphene can be functionalised with aromatic molecules containing hydrophilic chains or functional groups, by π-π stacking, with examples including pyrenes,[148] coronenes,[149] porphyrin[150] and anthracenes,[151] as well as polymers with aromatic groups such as poly(styrene sulfonate).[152] For example, Figure 1-5 shows the interaction between graphene and an amphiphilic, pyrene-based compound, including the aqueous dispersion of the resultant graphene/amphiphilic pyrene compound. Biological molecules have also been shown to interact with pristine graphene when aromatic sections are present, through π-π interactions. Examples include glucose oxidase,[153] tryptophan,[154] dopamine[155] singly-stranded DNA (ssDNA)[156] and drugs such as ramisol.[157] Pristine graphene is also able to interact with partially hydrophobic molecules, such as surfactants or ionic liquids species, via hydrophobic interactions[158,66,159,160,161] and, as previously mentioned, the use of ionic liquids has been explored for the sonochemical exfoliation of graphene, to avoid the use of high boiling solvents.

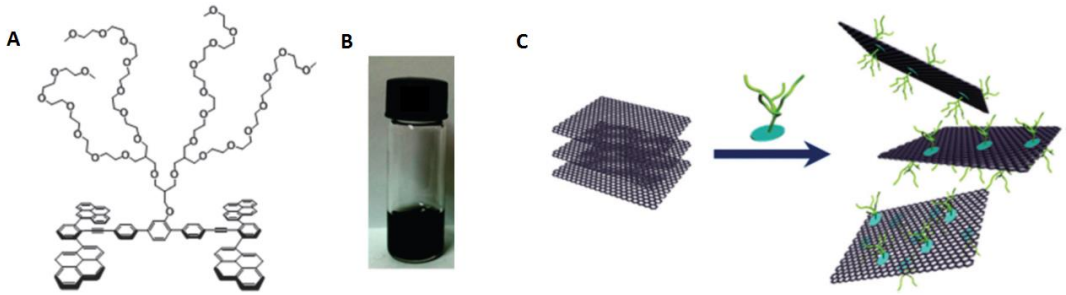

Figure 1-5. (A) Chemical structure of amphiphilic pyrene-based compound (B) Aqueous dispersion of the graphene/amphiphilic pyrene complex. (C) Schematic showing the graphene/amphiphilic pyrene dispersion. Lee *et al.*[148]

Graphene oxide (GO), on the other hand, possesses a high defect density which disrupts the π-system, meaning that π-π interactions are much more limited. In addition, GO is hydrophilic, meaning that small aromatic molecules, which are predominantly hydrophobic, interact less strongly with GO than with pristine graphene.[162] Non-covalent modification of GO with aromatic molecules are limited, but the examples which exist arise from polarity differences,[162,163] or the binding of aromatic molecules to isolated aromatic areas on GO sheets.[146] These polarity differences are used to bind drugs to the hydrophilic GO sheets, such as doxoburicin,[164] ellipticin[165] and hypocrellins, which bind by combination of hydrogen bonding and π-π interactions.[166]

GO possesses hydrogen-bond donors and acceptor groups and the presence of ionic groups such as carboxylates and hydroxyl groups, meaning that it is able to form ionic or hydrogen bonding interactions with molecules, which constitute the most common non-covalent functionalisation strategies for GO.[146] For example, hydrogen bonding has been used to produce GO polymer composites with polymers including polyvinyl alcohol (PVA), epoxy, polyaniline and polyacrylonitrile, improving the mechanical properties of the native polymer.[167,168,169] For example, Rafiee *et al.* performed tensile strength measurements of a graphene platelet (GPL)/epoxy

composite, which showed a 40 % increase in tensile strength in comparison epoxy alone, at only 0.1 wt. % loading.[168]

Figure 1-6 shows the stabilisation of pristine graphene by the addition of PVP and the increased Young's modulus of 0.03 vol % PVP/graphene composite in comparison to PVP alone.[170] GFNs have been used to reinforce many polymers including Kevlar,[171] epoxy,[172] cellulose,[173] polysulfone,[174] poly(vinylidene fluoride)[175] and polyurea.[176]

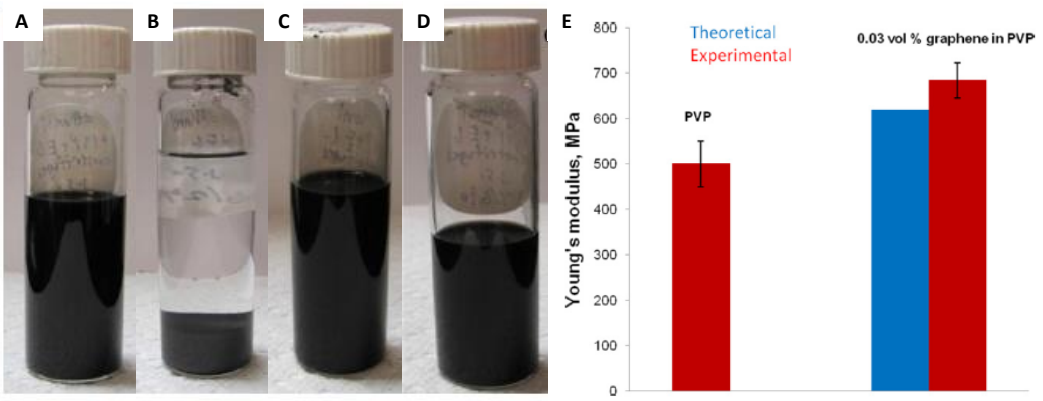

Figure 1-6. Pristine graphene in ethanol A) after sonication B) After centrifugation. PVP-stabilised pristine graphene in ethanol C) After sonication D) After centrifugation. E) Young's modulus of graphene in PVP as determined by stress-strain response under tensile load. From Wajid *et al.*[170]

Due to the desirable mechanical and electronic properties of GFNs, they are commonly combined with polymers in order to improve their native electronic properties.[146] For example, Wajid *et al.* produced a polyvinylpyrrolidone (PVP)/pristine graphene composite, which showed excellent load transfer and improved mechanical and electrical properties.[170] The incorporation of graphene has also been used to enhance the electrochemical performance of polymers, with examples including sulfonated polyaniline,[177] polyaniline,[178,179] poly(vinyl pyrrolidone),[180] polypyrrole,[181] polyethylenedioxythiophene (PEDOT)[182] and a

conducting polypyrrole graft copolymer, poly(styrenesulfonic acid-g-pyrrole)[183] amongst others.[184,185,186]

Reduced graphene oxide (rGO), in which many of the sp^2 domains are restored by reduction, can adsorb aromatic molecules by π-π stacking interactions much more effectively than GO, although the aromatic character remains lower than that of pristine graphene.[2, 187,162,146,163,188] Molecules grafted to rGO include sulfonated aluminium phthalocyanine,[162] 3,4,9,10-perylenetetracarboxylic diimidebisbenzenesulfonic acid (PDI),[189] riboflavin[190] and porphyrin.[191] The presence of residual oxygen-containing groups in rGO means that ionic and hydrogen-bonding interactions are also able to occur and have been used to add sodium lignosulfonate,[192] imidazolium derivatives,[160] polyethylene glycols[193] and aromatic ionic liquids.[66,194]

1.3.2. Covalent modifications of graphene-family nanomaterials

Most of the existing covalent modifications of GFNs are based upon graphene oxide (GO) or reduced graphene oxide (rGO), taking advantage of the oxygen-containing functionality present on GO and, to a lesser extent, rGO.[15] The reactions possible on GO and rGO include nucleophilic substitution, electrophilic addition, condensation and addition.[96] The most common covalent functionalisation is the reaction of amine-terminated groups with epoxy groups of graphene oxide.[96] The advantage to these is that they do not require high temperatures and are often able to proceed in aqueous solutions.[96] Groups added by this method include primary amines,[195,196] silanes,[197] amine-containing biomolecules,[198] poly(norepinephrine),[199] porphyrin,[200] phage-displayed peptides,[201] and amine-containing ionic liquids.[202] Figure 1-7 shows

the amine ionic liquid functionalisation of GO, showing the difference in colour of their dispersions.[202]

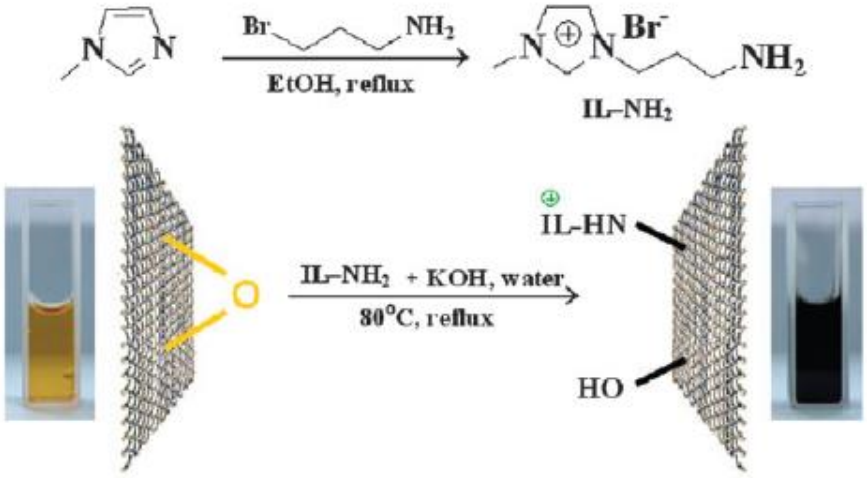

Figure 1-7. Reaction scheme to produce amine-terminated ionic-liquid functionalisation of graphene oxide and the change in colour of their aqueous dispersions. Yang *et al.*[202]

Examples of the electrophilic substitution on GO include the attachment of aryl diazonium salt to graphene.[203] Friedel-Crafts mono-acylation has also been reported on GO, producing ferrocene-functionalised GO.[204] Condensation reactions on GO include the work of Stankovich *et al*., who grafted isocyanate groups onto GO for use in polymer composites.[205] Liu *et al.* reported GO functionalization by amine-terminated poly(ethylene glycol) (PEG-NH_2), which was used in the delivery of hydrophobic drugs,[206] while Chen *et al.* prepared sulfanilic acid functionalized GO as ion-exchange material and studied its electrochemical behaviour towards the detection of hydrogen peroxide.[207] As previously outlined, however, the process of making GO introduces many chemical and topological defects to the graphene structure,[35] which may cause detrimental effects on the electron transfer and structural integrity.[208]

Reduced graphene oxide (rGO), though not containing as many defects as GO, is able to form covalent bonds, using the oxygen-containing functional groups

remaining post-reduction. Manna and Raj demonstrated the grafting of a nitrophenyl group onto rGO and used the complex to sense lactate, which can be an early sign of multiple scleroris.[209] Other examples includes the porphyrin functionalisation of rGO[210] and attachment of a conjugated polyelectrolyte.[211]

Common functionalisations of pristine graphene are based on diazonium chemistry, which occur on the graphene basal plane. Englert *et al*. report the reaction of intercalated graphite with 4-tert-butylphenyldiazonium tetrafluoro borate, which results in the presence of tBu-phenyl groups on the basal planes of the graphene sheet, as seen in Figure 1-8.[212] These groups prevent the reaggregation of the graphene sheets, while the degree of functionalisation can be controlled by changing the 4-tert-butylphenyldiazonium tetrafluoro borate concentration, meaning that sp^3 damage can be limited.[212] Other groups tethered by this method include nitrophenyls,[213,214] polymers[215] and azobenzene.[216]

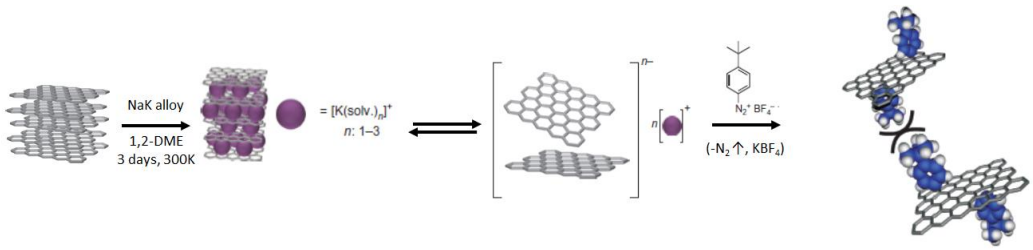

Figure 1-8. Reaction scheme showing the intercalation of a NaK alloy (in 1,2-dimethoxyethane) into graphite, followed by its functionalisation to form 4-tertbutyl-phenyl functionalised graphene. Adapted from Englert *et al*.[212]

Another class of reactions which occur on pristine graphene are nitrene and carbene functionalisations. Nitrene functionalisation has been demonstrated by Liu *et al*., to attach perfluorophenyl azide to graphene,[217] while Sainsbury *et al*. described a carbene functionalisation of graphene.[218] The mechanisms of both functionalisations are shown in Figure 1-9.

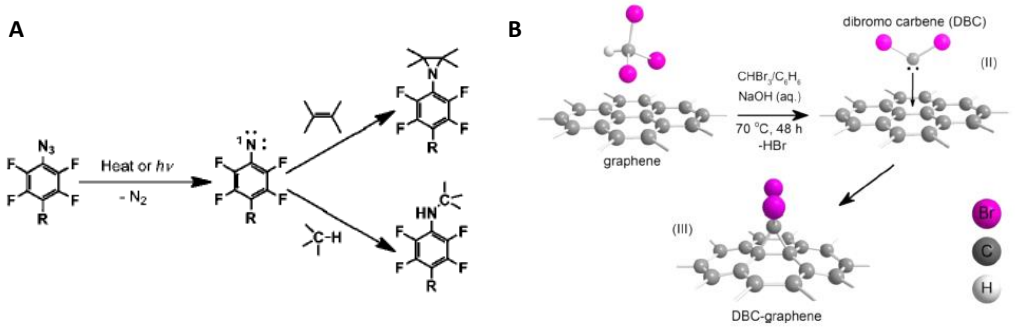

Figure 1-9. A) Nitrene functionalisation mechanism of perfluorophenyl groups on graphene sp^2 and sp^3 sites. From Liu *et al.*[217] B) Carbene functionalisation of graphene by addition of bromoform and hydroxide. From Sainsbury *et al.*[218]

Other common pristine graphene functionalisations are 1,3,dipolar-cycloadditions,[219,220] which generally invoke the use of azomethine ylids, but nitrene cycloaddition and even aryne cycloaddition have been reported.[221,222] This reaction was thought to occur at pre-existing defects sites, but recent work by Daukiya shows that this reaction can be carried out on defect free graphene, at room temperature.[223]

Electrochemistry has been utilised to add functional groups onto graphene.[224] Bjerglund *et al.* describe the intercalation of graphene, grown on Ni, with Bu_4N^+ at a negative potential (-1.9 V vs Ag/AgI). This caused the intercalation of the Bu_4N^+ between graphene sheets. The graphene sheets were then reacted with CO_2 which caused the carboxylation of graphene. This method can be carefully controlled by altering the electrochemical conditions and therefore the degree of carboxylation.[224] Electrochemical diazonium coupling to graphene has also been described.[225]

The disadvantage of these covalent functionalisations of pristine graphene is that they occur on the basal plane of the graphene sheet, therefore causing disruption to the aromatic π-system, hence decreasing the conductivity of the pristine graphene and altering its mechanical properties. The challenge in functionalising pristine

graphene is therefore to develop methods to incorporate functional groups, without altering the favourable properties of pristine graphene

1.3.3. Edge-specific functionalisation of pristine graphene

The current methods and approaches for covalent functionalisation of pristine graphene generally involve the reaction of species with the basal plane, causing disruption of the graphene structure. Covalent functionalisations which occur only at the edges of the graphene sheets consequently leave the basal plane of graphene intact, with ball milling being the predominant approach for achieving the edge-specific functionalisation of graphene. Edge-specific functionalisation is achieved by ball milling graphite in the presence of gases; the ball milling process produces reactive species such as radicals, carbocations and carbanions at the edges of the graphene sheets, which then react with the gases present.[226] Several functional groups have been added using the ball milling technique including carboxylates,[227] sulphonates,[208] hydrogen,[208] antimony,[228] phosphonic acid,[229] fluorine,[230] halogens[231] and nitrogen.[232] These edge-selectively functionalised sheets have been used as fire retardants,[229] lithium-ion batteries[230] and in electrocatalysis.[233]

The ball milling process is dangerous; when the lid is opened of the ball-mill, violent sparking is observed due to remaining 'active carbon species and metallic debris',[136] which react with moisture in the air, as shown in Figure 1-10.[227,231] This raises safety concerns concerning large-scale ball milling. The procedure also introduces metallic residues from the steel balls, which require acidic work up to remove.[136] In addition, in some cases, the calculated surface areas of the exfoliated edge-functionalised graphenes made by this method suggest that the graphene is not fully exfoliated, while the functionalisation percentages were higher than expected for edge only

functionalisation, indicating that graphene sheets become damaged by the ball milling process, undergoing significant fragmentation.[136]

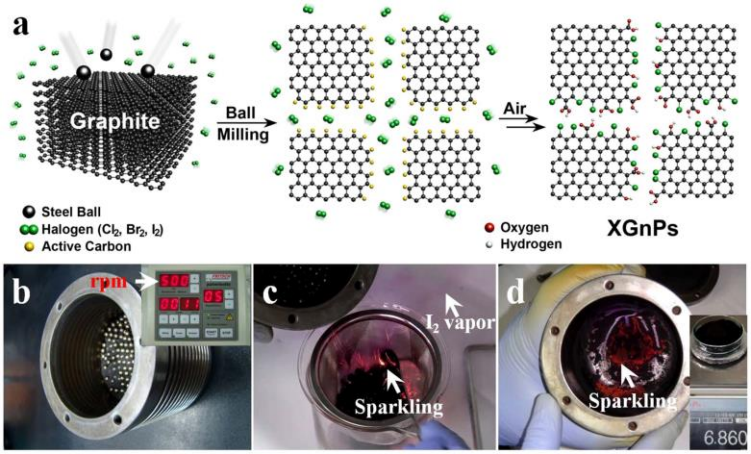

Figure 1-10. a) Schematic of ball-milling edge-halogenation reaction forming edge-halogenated graphene nanoplatelets (XGnPs). b) Ball mill capsule with pristine graphene and stainless steel balls. c) Violent sparking when reaction is exposed to air moisture. d) Continued sparking from residual iodine-functionalised graphene nanoplatelets (IGnPs) after most of the IGnPs and stainless balls were taken out. Jeon *et al*.[231]

Another method of achieving the edge-specific functionalisation of pristine graphene is by the functionalisation of graphite, followed by exfoliation. Sun *et al.* performed diazonium coupling to graphite, after which the functionalised graphite was sonicated, yielding water-dispersible, functionalised graphene. The reaction scheme can be seen in Figure 1-11. Similarly, a Friedl-Crafts acylation of graphene has also been reported.[234] The asymmetric 2D band in the Raman spectrum of these functionalised graphenes, however, suggest that the graphene is not fully exfoliated.[234]

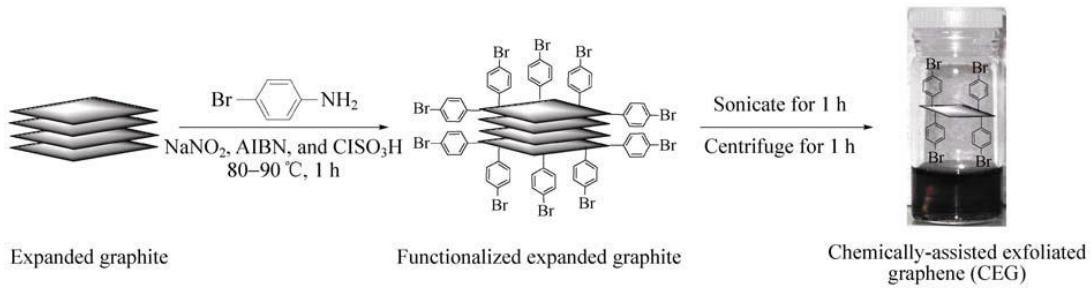

Figure 1-11. Reaction scheme for achieving chemically assisted exfoliated graphene. Sun *et al.*[235]

A wet chemical route to chlorinated nanographenes has been described by Tan *et al.*[236] Nanographenes were produced by dehydrogenation of polyphenylenes,[236,237] with the chlorination following the same principle as the chlorination of hexa-tert-butyl-hexabenzocoronene, as shown in Figure 1-12. The chlorination method, however, only applies to nano-graphenes containing a maximum of 222 carbons.

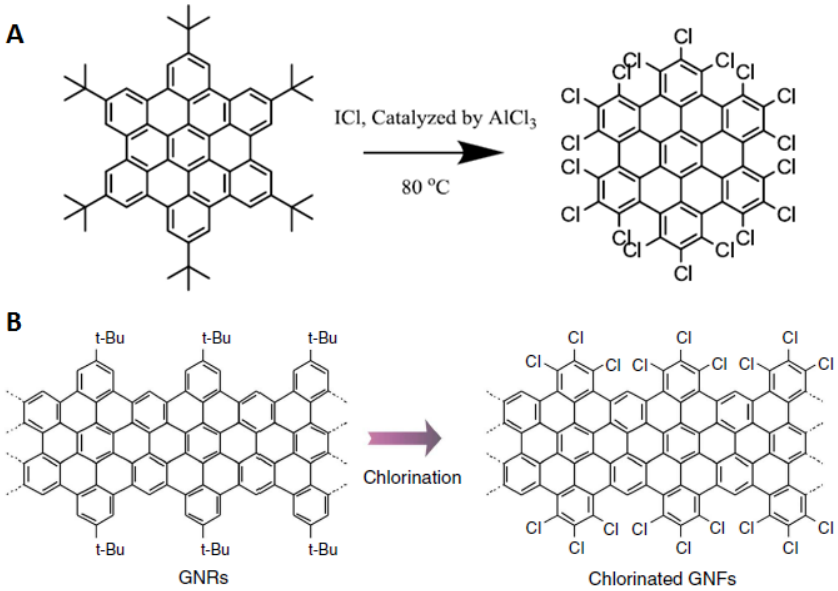

Figure 1-12. A) Chlorination of hexa-tert-butyl-hexabenzocoronene. B) The chlorination of tert-butyl functionalised graphene nanoribbons. Tan *et al.*[236]

1.3.4. Summary

The functionalisations outlined in this section present viable methods by which to modify the properties of graphene for different applications. Non-covalent modification of graphene family nanomaterials (GFNs) cause little structural impairment, meaning that many of the properties of the GFNs remain unaltered.[146]

Pristine graphene functionalisation relies primarily on non-specific adsorption to basal plane, or basal plane covalent functionalisation, which disrupts the graphene sheet while, on the other hand, GO functionalisation can invoke electrostatic, polarity, hydrogen bonding, and covalent attachments, which can be highly specific.

As previously discussed, the production of GO itself causes disruption to many of the favourable properties inherent to 'graphene'. Arguably, rGO has the greatest potential in terms of functionalisation, as it exhibits conductivity between that of GO and pristine graphene,[41, 42,43,44] while possessing residual oxygen-containing groups by which to covalently attach molecules. However, the remaining sp^3 defects present in rGO mean that many of the properties of 'pristine graphene' are still affected.[2, 187]

The most promising functionalisations of pristine graphene are the edge-specific functionalisations, as they leave the majority of the graphene π-system intact. The most widely explored method is ball milling of graphite in the presence of gases, but this method has safety issues and, in some cases, produces graphene which is not fully exfoliated, or is significantly damaged.[208] Other edge functionalisations involve the diazonium functionalisation of graphite, or the wet chemical functionalisation of nanographenes. The work outlined in this thesis is aimed at providing an alternative solution to the existing functionalisation of pristine graphene that preserves the structure of the graphene sheet and can be extended to a variety of functional groups.

1.4. Characterisation of graphene family nanomaterials

1.4.1. Raman spectroscopy of graphene

Graphene possesses two types of carbon atom, A and B,[238] as shown in Figure 1-13. The reciprocal space unit cell of monolayer graphene, with the Γ point in the centre,

M points in the middle of the hexagon sides and K and K' points on the hexagonal corners is also depicted in Figure 1-13.

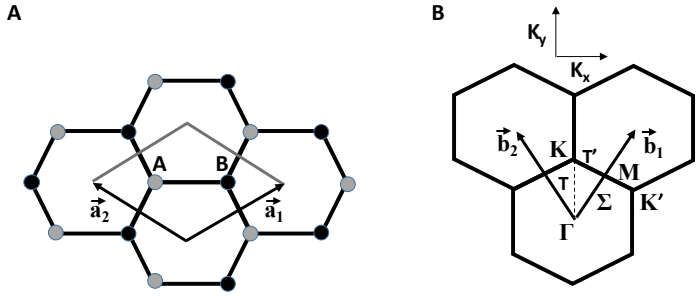

Figure 1-13. A) A top view of the real space unit cell of monolayer graphene with inequivalent atoms A and B and unit vectors $\mathbf{a}_1$ and $\mathbf{a}_2$ and B) Reciprocal space unit cell of the first Brillouin zone, high symmetry points and lines. The two primitive vectors $\vec{b_1}$ and $\vec{b_2}$ are shown and the two vectors on the top of the three hexagons show the reciprocal space coordinate axes. Adapted from Malard *et al*.[238]

Six phonon dispersion bands are present for graphene: three acoustic (coherent movement of atoms of the lattice outside equilibrium positions) and three optic branches (out-of-phase movements of the atoms in the lattice).[238] These branches can be in-plane (i), or out-of-plane (o), corresponding to vibrations parallel to or perpendicular to the graphene plane, respectively. The direction of vibrations is classified as either longitudinal (L) or transverse (T), corresponding to vibrations parallel or perpendicular to the A-B carbon-carbon direction, respectively.[238] The six bands are described in Table 1-1.

Table 1-1. The phonon dispersion bands in graphene and their characteristics.

Band	In-phase/ out-of-phase movement of atoms in the lattice	Parallel/ perpendicular to A-B carbon-carbon bond	In-plane/ out-of-plane
LO	Out-of-phase	Parallel	In plane
iTO	Out-of-phase	Perpendicular	In plane
oTO	Out-of-phase	Perpendicular	Out-of-plane
LA	in-phase	Parallel	In plane
iTA	in-phase	Perpendicular	In plane
oTA	in-phase	Perpendicular	Out-of-plane

Two prominent peaks observed in graphene are the G and 2D (G') peaks, located at around 1580 cm^{-1} and 2700 cm^{-1}, respectively.[239] The G peak arises from the iTO

and LO phonon modes (which are degenerate at the Brillouin centre), and corresponds to the vibration of sublattice A against sublattice B.[240] The G peak possesses E_{2g} symmetry, and is the only first-order Raman process observed in graphene.[238,241] The 2D (or G') band involves two iTO phonons near the K point and originates from a double resonance Raman event.[242,243] An electron around K point absorbs a photon, which is inelastically scattered by a phonon or defect to a point belonging to a circle around the K' point, then is scattered back to a K state, emitting a photon by recombining with a hole,[238] as shown in Figure 1-14.

In defect-containing graphene a further, second-order Raman 'D' peak is observed. The D peak is located at around 1350 cm^{-1},[239] with the process involving one iTO phonon and one defect. One elastic scattering process is caused by the defects in the crystal and another, inelastic process from the emission or absorption of a photon.[238] A smaller band, which is disorder-induced, can be seen at approximately 1620 cm^{-1} called the D' band and is an intra-valley, double-resonance process. These processes are depicted in Figure 1-14.

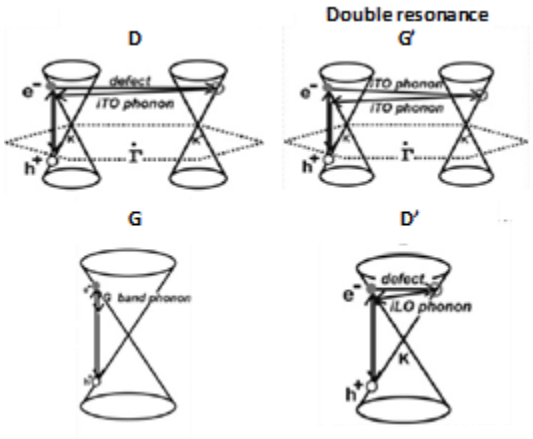

Figure 1-14. Resonance processes for Raman peaks of graphene. Adapted from Malard *et al.*[238]

In graphene, the 2D peak is a single sharp peak, while in graphite it consists of two peaks, as shown in Figure 1-15A. There is correlation between the evolution of the 2D band and the number of graphene layers,[239] as seen in Figure 1-15B, allowing the number of layers in a graphene sample to be determined by analysis of the 2D peak. For turbostratic graphene, in which the stacking of graphene layers is random along the *c* axis, the Raman 2D band is a single Lorentzian, just as in monolayer graphene, but with a larger linewidth, as a result of the relaxation of the Raman selection rules associated with the random orientation of graphene layers.[238,244,245]

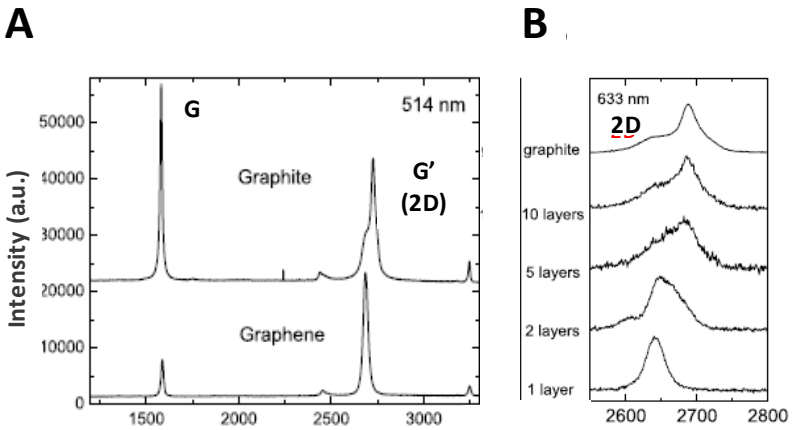

Figure 1-15. A) Raman spectra of graphene and graphite using 514 nm laser irradiation B) Evolution of the 2D band with number of graphene layers, using 633 nm laser irradiation. From Ferrari *et al*.[239]

The ratio of the intensities of the D and G peaks ($\boldsymbol{I_D/I_G}$) was found to scale with the lateral dimensions (width, W and length, L) of sonochemically-exfoliated graphene, according to Equation 2:[32]

$$\boldsymbol{I_D/I_G} \propto (L^{-1} + W^{-1}) \quad (2)$$

Eckmann and co-workers found that the D' peak showed a strong dependence on the type of defect introduced in the lattice. The term C_s represents the Raman cross section of I(x)/I(G) associated with 'the distortion of the crystal lattice after defect introduction per unit of damaged area', where x is either D or D' peak. For the D peak $C_S \sim 0$, independent of defect type, while for the D' peak, $C_S = 0.33$ for sp^3 sites, and $C_S = 0.82$ for vacancies,[246] as seen in Figure 1-16A. Figure 1-16B shows the change in the D to D' ratio with increasing defect concentration. The D band and D' band intensities initially increase as the number of defects increases. This is known as Stage 1. However, Eckmann *et al.* found that, at a certain defect concentration, the D peak reaches a maximum intensity, after which it begins to decrease with the D' peak remaining approximately constant, which is known as stage 2.

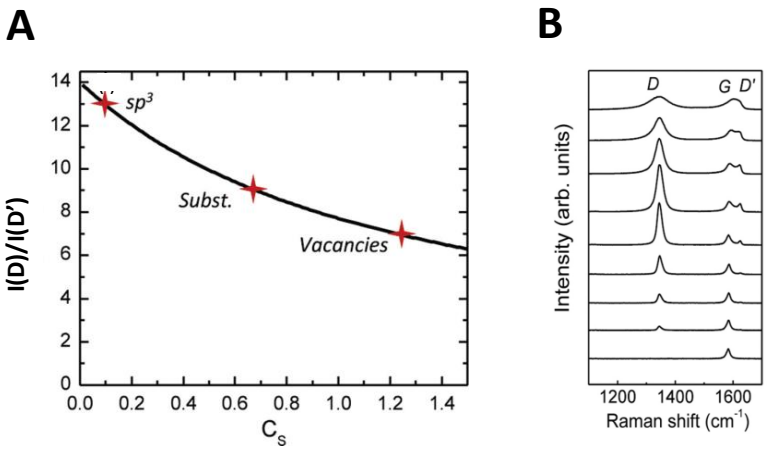

Figure 1-16. A) D/D' ratio correlation to defect type. B) Raman data exemplifying the D/D' ratios in fluorinated graphene with increasing defect concentration (bottom to top). Eckmann *et al.*[246]

Therefore, an increase in D or D' intensity may not occur with an increased defect concentration in stage 2.[247] In stage 1 there are clear patterns in the $I_D/I_{D'}$ ratio between defect types $I_D/I_{D'}$ is maximum (≃13) for defects associated with sp^3 hybridization, it decreases for vacancy-like defects (≃7) and reaches a minimum for boundary-like defects in graphite (≃3.5).

In this work, Raman spectroscopy is used to assess the nature of the graphene produced, including the approximate layer numbers, defect formation and latterly, mapping is used to evaluate the distribution of graphene in layer-by-layer constructs. It is also able to confirm the presence of graphene in mixtures and composites.

1.4.2. Infrared spectroscopy

Infrared (IR) spectroscopy is useful in the identification of functionalised graphene sheets, analysing the disappearance or appearance of peaks. The sample is irradiated which excites vibrations in a molecule. The frequency at which these vibrations are seen is given by Equation 3: [248]

$$\boldsymbol{v} = \frac{\mathbf{1}}{\boldsymbol{\pi}}\sqrt{\frac{\boldsymbol{k}}{\mathbf{2}\boldsymbol{\mu}}} \quad (3)$$

Where $\boldsymbol{v}$ is the frequency (cm^{-1}), $\boldsymbol{k}$ is the force constant (related to the bond strength) and $\boldsymbol{\mu}$ is the reduced mass of the atoms in the bond. IR therefore provides a molecular fingerprint, as different functional groups show IR peaks at different frequencies.

Fourier transform IR (FTIR) has been used to identify functional groups present in GFNs, such as sulfonates,[249] carboxylates[227] and amines.[250] FTIR of GFNs can be difficult to analyse, as the high carbon content of graphene often dominates the spectra, but can be useful when analysed in conjunction with other characterisation methods.

1.4.3. UV-visible spectroscopy

UV-visible spectroscopy (UV-Vis) is a commonly used, non-destructive technique in which light in the visible and UV ranges is absorbed, causing electronic transitions in molecules from a ground state to an excited state. The Beer-Lambert law describes the UV-Vis spectra of compounds by Equation 4:

$$\boldsymbol{A} = \mathbf{log_{10}}\frac{\boldsymbol{I_0}}{\boldsymbol{I}} = \boldsymbol{\varepsilon c l} \quad (4)$$

where $\boldsymbol{A}$ is the absorbance, $\boldsymbol{I}$ is the transmitted intensity and $\boldsymbol{I_0}$ that of incident light, $\boldsymbol{l}$ is the path length through the sample, $\boldsymbol{c}$ the concentration of the sample and $\boldsymbol{\varepsilon}$ the extinction coefficient of the sample. If the UV-visible absorption spectrum is known, it can also be used to assess the concentration of a sample. The extinction coefficient of graphene from sonochemical exfoliation in NMP has been calculated as 2460 $L\ g^{-1}\ m^{-1}$ at 660 nm,[61] meaning that UV-Vis can be used to determine the concentration of GFN dispersions.

1.4.4. Scanning electron microscopy

In scanning electron microscopy (SEM), samples are irradiated with a finely focused electron beam, which interacts with the sample. Analysis can be done by looking at secondary electrons, backscattered electrons, and characteristic X-rays.[251] The secondary electrons and backscattered electrons interact differently to samples of different topography. X-rays are emitted from the material, after electron bombardment of the sample, providing elemental identification and quantitative elemental information from selected regions of the specimen.[251] SEM is therefore able to provide information on the morphology and composition of materials.[252,253] Because SEM is sensitive to surface topology, it is able to provide information on adsorbed species. Back-scattered electrons are sensitive to atomic number and hence can identify where species of a high atomic number lie.

Due to the thin nature of graphene sheets, low accelerating voltages (around 5 kV or lower) must be used to image graphene sheets, because graphene films are nearly electron transparent at higher accelerating voltages, meaning that the electrons pass through the graphene without interacting with the atoms. This limits SEM imaging, because the low accelerating voltages affect the resolution.[254]

1.4.5. Transmission electron microscopy

Transmission electron microscopy (TEM) is used in material characterisation due to the limited image resolution of light microscopes; the Rayleigh criterion for light microscopy states that the smallest distance that can be resolved is given by Equation 5:

$$\boldsymbol{\delta = \frac{0.61\lambda}{\mu \, sin\beta}} \tag{5}$$

where $\boldsymbol{\lambda}$ denotes the wavelength of radiation, $\boldsymbol{\mu}$ is the refractive index, $\boldsymbol{\beta}$ is the semi-angle of collection of the magnifying lens. As $\boldsymbol{\mu\, sin\beta}$ ~ 1, the resolution is around half the wavelength of the light. The wavelength of green light is about 550 nm, leading to a resolution of about 300 nm (about 1000 atom diameters). For a TEM microscope using 100 keV energy electrons, λ ~ 4pm. This is smaller than the diameter of an atom which means that, theoretically, TEM should be able to give atomic resolution,[255] although such resolution is not observed.

When electrons pass through specimen they are scattered by elastic nuclear interactions, with the cross-section for elastic scattering increasing with the atomic number (*Z*) and material thickness, meaning that as thickness increases there is more elastic scattering as the mean free path is fixed.[255] Higher *Z* regions, or thicker regions, scatter more than lower *Z* regions or thinner regions. Electron scatter is then translated into an amplitude by selecting either the direct beam or some of the selected area diffraction pattern.[255] In the diffraction pattern obtained from the specimen, the objective aperture can be set over the central spot (the direct beam), which produces amplitude contrast whether the specimen is crystalline or amorphous, and generates a 'bright-field' image.[255] Alternatively, the aperture is set to a specific spot on the diffraction pattern, in which case only electrons which scattered in that direction will be selected, producing a 'dark-field' image.[255] Dark field images have a much lower intensity, as only a small fraction of the scattered electrons are selected, although dark field imaging produces much greater contrast.[255] Apertures are an important feature of TEM machines, with larger apertures allowing more scattered electrons to contribute to the image, but the contrast between scattering and non-scattering areas is reduced.[255]

Lower accelerating voltages cause both the scattering angle and the cross section to increase, thus increasing the contrast of TEM images, although this in turn affects the image intensity.[255] Though electrons interacting with the sample leads to most of the imaging, secondary signals, which occur from the removal of inner-shell electrons from constituent elements, can also be used in analysis.[255] For example, X-ray spectra can be obtained from TEM specimens, giving information on the identity of elements in a sample.[255]

Electron diffraction patterns from the TEM can provide further information about graphene sheets. When electrons pass through a sample or a lattice they are either scattered by atoms in the sample or pass through. Bragg's law explains the conditions needed for the constructive interference of these electron waves, according to Equation 6:[248]

$$\boldsymbol{n\lambda = 2d\,sin\theta} \quad (6)$$

Where d is the interplane spacing, θ is scattering angle and λ the wavelength of electrons. Therefore, when the path difference between two diffracted waves is an integral multiple of the wavelengths peaks are observed The principal graphene diffraction planes are shown in Figure 1-17, there are two main diffraction planes which are denoted (hk) = 11 and (hk) = 10, according to their Miller-Bravais indices.[256]

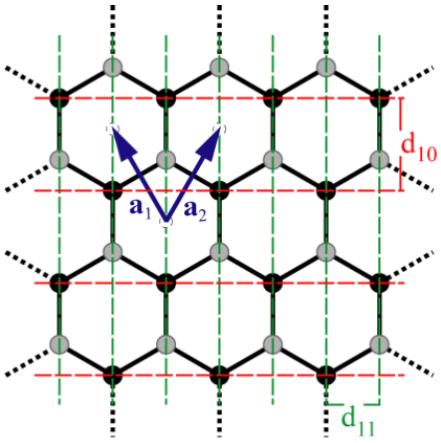

Figure 1-17. Structure of graphene. Inequivalent carbons are labelled in grey and black. Lattice vectors are shown in blue and the (hk) = 11 and (hk) = 10 planes are shown in green and red, respectively, with interplane spacing denoted as d_{11} and d_{10}, respectively. From Wilson *et al.*[256]

The diffraction patterns of graphene are hexagonal diffraction spots, with the spots from diffraction from the (hk) = 10 plane forming a hexagon closer to the central spot and the (hk) = 11 spots forming the outer hexagon. Meyer *et al.* reported that the relative intensities of diffraction spots in the inner and outer hexagons are equivalent in single-layer graphene, while relative intensities of the spots in the outer hexagon were twice those of the spots in the inner hexagon for bilayer graphene.[257] If graphene is restacked, graphene sheets will be randomly orientated with respect to one another, meaning that instead of the hexagonal spots which are well defined, the inner and outer hexagons appear as two circles, from the superposition of hexagonal spots from many orientations. Typical hexagonal selected-area diffraction spots from a graphene flake are shown in Figure 1-18B.

TEM can provide information regarding defect sites[45,258] and can also provide topological information about the nature of graphene sheets. Figure 1-18 shows and example of TEM images of graphene sheets. A disadvantage to TEM is that only small areas are to be looked at, hence limiting the sampling ability of TEM.[255] TEM imaging has a slow sample throughput and is expensive to run, as well as being

difficult to interpret.[255] TEM presents 2D images of 3D specimens which can sometimes lead to incorrect interpretations.[255] Damage can also be presented to the sample from exposing it to ionising radiation, and beam damage limits what we are able to do with TEM, as samples can be destroyed.[255]

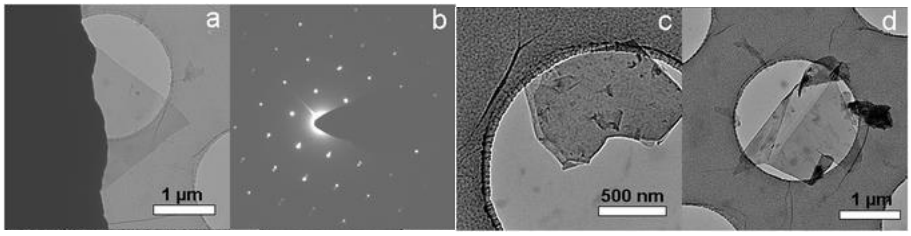

Figure 1-18. TEM images of graphene. TEM images of a) a single-layer graphene sheet b) the corresponding electron diffraction pattern of the sheet c) a bi-layer graphene sheet d) a few-layer graphene sheet. Zhang *et al.*[259]

1.4.6. Atomic force microscopy

Atomic force microscopy (AFM) is a form of imaging samples in which a cantilever tip is scanned over sample surface, first developed by Bining *et al.*[260,261] AFM measurements are acquired by measuring the force on a tip when it is in close proximity to a surface.[261] The tip is mounted onto a cantilever spring,[262] which in turn is mounted onto a piezoelectric actuator.[263] The force on the tip is kept small and remains constant by a feedback mechanism.[261] The topography of the sample is measured by looking at the deflection of the cantilever as a function of its position on the sample.[262] A laser is reflected off the end point of the cantilever, and deflection off the cantilever is measured by the position of the light intensities in the detector.[263] Image contrast comes from changes in short range repulsion which happen when the tip and electrons in the material interact.[262]

In contact mode, the vertical cantilever position is recorded as a function of *x* and *y* coordinates, typically varying between 1-10 μm from the surface, monitoring the forces on the cantilever while in constant contact with the sample.[261] Images are

created by recording the vertical position required to keep the force constant.[264] In tapping mode, the cantilever oscillates at a resonant frequency and amplitude is monitored. When approaching a sample the oscillation amplitude is damped and the feedback signal for keeping the amplitude constant is recorded. This mode causes less damage to samples and reduces dragging forces.[264,265]

AFM generates topological images of GFNs on scale of the order of 1 μm x 1 μm.[45] Layer thickness can be probed by the AFM tapping mode, with singly layered graphene loaded onto a Si/SiOx wafer having a thickness of between 0.8-1.2 nm,[45] with subsequent layers adding approx. 0.35 nm to this number, equating to the van der Waals distance between graphitic layers.[266] Lateral dimensions can be recorded using AFM, meaning that size and thickness distribution profiles can be constructed. Roughness values can also be calculated for composite materials. Representative AFM images of graphene sheets can be seen in Figure 1-19.

For GO the most common AFM preparation is to pre-treat surfaces with poly-L-lysine (PLL) and to drop-cast GO on top of the PLL-coated surfaces.[267] For pristine graphene, preparation is more difficult, as solvents able to stabilise these dispersions generally have a high boiling point.[268] Coleman and co-workers have used both drop-casting onto pre-heated SiO_2 wafers and airbrushing onto SiO_2 wafers, with subsequent annealing, to prepare pristine graphene AFM samples.[81]

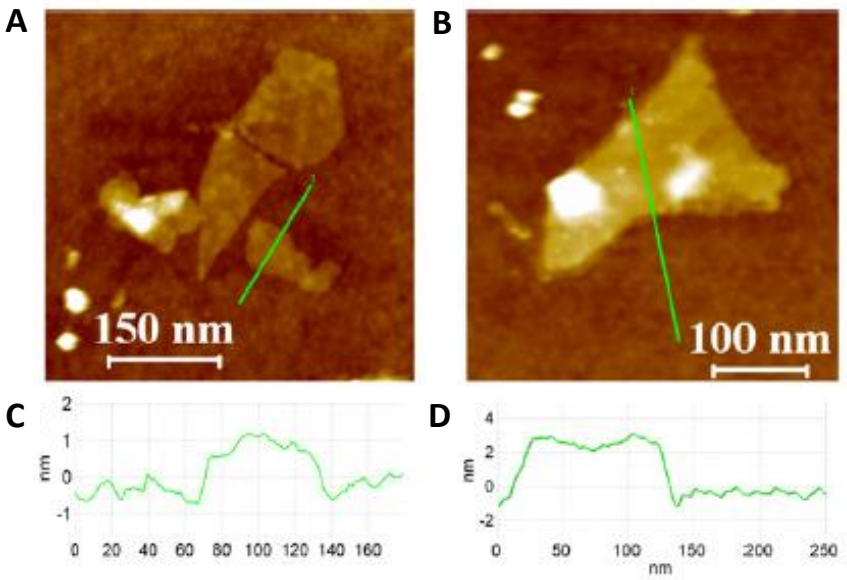

Figure 1-19. A) and B) AFM images of graphene on a Si/SiO_2 substrate. C) and D) corresponding height profiles. From Guardia *et al.*[69]

1.4.7. Nitrogen porosimetry

The adsorption of gas onto a material at different partial pressures provides information about its surface area. In the 1930s, Emmett and Brunauer observed that the physical adsorption of a gas onto a surface does not cease at monolayer coverage if the pressure is increased above a certain threshold, but that molecules adsorbed on one layer helping to adsorb molecules on subsequent layers.[269] From this observation the 'BET' equation, shown in Equation 7, was formulated:

$$\boldsymbol{Q = Q_m}\left(\frac{\boldsymbol{C}\left(\frac{\boldsymbol{P}}{\boldsymbol{P_0}}\right)}{\left\{\boldsymbol{1}-\frac{\boldsymbol{P}}{\boldsymbol{P_0}}+\boldsymbol{C}\left(\frac{\boldsymbol{P}}{\boldsymbol{P_0}}\right)\right\}\cdot\left\{\boldsymbol{1}-\left(\frac{\boldsymbol{P}}{\boldsymbol{P_0}}\right)\right\}}\right) \quad (7)$$

Where $\boldsymbol{Q_m}$ is the adsorbed gas quantity of the monolayer, $\boldsymbol{Q}$ is the adsorbed gas quantity, $\boldsymbol{P}$ is the equilibrium pressure, $\boldsymbol{P_0}$ is the saturation pressure of the adsorbate and $\boldsymbol{C}$ is the BET constant. A 'BET plot' is generated from experimental isotherm data using the linearised form of the BET equation, as shown in Equation 8:

$$\frac{\frac{\boldsymbol{P}}{\boldsymbol{P_0}}}{\boldsymbol{Q}\left(\boldsymbol{1}-\frac{\boldsymbol{P}}{\boldsymbol{P_0}}\right)} = \left(\frac{\boldsymbol{1}}{\boldsymbol{CQ_m}}\right) + \left(\frac{\boldsymbol{C-1}}{\boldsymbol{CQ_m}}\right).\left(\frac{\boldsymbol{P}}{\boldsymbol{P_0}}\right) = \boldsymbol{I} + \boldsymbol{s}\left(\frac{\boldsymbol{P}}{\boldsymbol{P_0}}\right) \quad (8)$$

Where $\boldsymbol{I}$ is the intercept of a straight-line plot of the BET equation and $\boldsymbol{s}$ is the slope of the same plot. From the BET plot, using Equation 9 and Equation 10, the adsorbed gas quantity and BET constant can be calculated.

$$\boldsymbol{Q_m} = \left(\frac{\boldsymbol{1}}{\boldsymbol{I+s}}\right) \quad (9)$$

$$\boldsymbol{C} = \left(\frac{\boldsymbol{I+s}}{\boldsymbol{I}}\right) \quad (10)$$

Once Q_m has been calculated, Equation 11 can be used to calculate the BET surface area.

$$\boldsymbol{S_{BET}} = \frac{\boldsymbol{Q_m N_A A_{CS}}}{\boldsymbol{V_M a}} \quad (11)$$

Where $\boldsymbol{N_A}$ is Avogadro's number, $\boldsymbol{A_{CS}}$ is the cross-sectional surface area of the adsorbing gas, $\boldsymbol{V_M}$ is the molar volume of gas and $\boldsymbol{a}$ is the mass of the sample.

BET analysis can be performed on GFNs to assess the surface area, which can in turn provide an estimate of the average number of layers of the graphene material. This data can be used to support complementary data, such as Raman and AFM, to characterise GFNs. The shape of adsorption isotherms can also provide information about the stacking and porosity of materials, with the different isotherm classifications outlined in the Appendix.

1.4.8. X-ray photoelectron spectroscopy

In X-ray photoelectron spectroscopy (XPS), samples are irradiated with a beam of high energy monochromatic X-ray radiation, such as Al Kα radiation (1486.7 eV) with enough energy to eject electrons from the sample. The kinetic energy of these

electrons is recorded, and the kinetic energy ($\boldsymbol{E_k}$) related to the ionisation energies ($\boldsymbol{I}$) of the electron in its original orbital by Equation 12:[270]

$$\boldsymbol{E_k = h\nu - I - \Phi} \quad (12)$$

where $\boldsymbol{\upsilon}$ is the frequency of incident radiation, $\boldsymbol{h}$ is the Planck constant and $\boldsymbol{\Phi}$ is the work function, which depends on the instrument and the material. The number of electrons in a characteristic peak provides a direct relation to the proportion of the given element in the sample. XPS can reveal the presence of specific carbon states such as C-O C=O and C=C bonds from observed chemical shifts.

XPS is a useful tool in GFN characterisation as chemical shifts can distinguish functional groups. XPS can also be performed on powdered samples and is sensitive to trace amounts of an element.[271,272] Examples of the XPS spectra of graphene are shown in Figure 1-20. This XPS spectra shows the different oxygen-containing species present on the graphene sheet by assessing the C 1s and O 1s peaks.

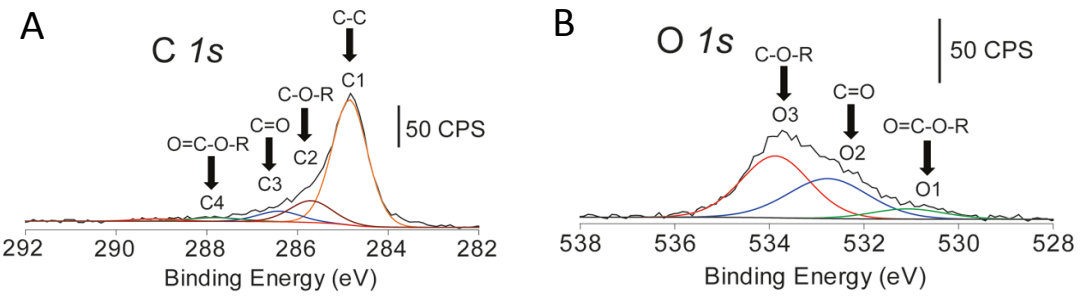

Figure 1-20. XPS spectra for a graphene sheet. A) C1s shell B) O1s shell. Polyakova *et al.*[273]

1.4.9. CHNS analysis

Elemental analysis was developed by Dumas in the 19th Century, where the nitrogen content of substances was determined by the combustion of a known mass of material, at around 900 °C, using a CuO oxidising agent.[274] The combustion generated CO_2, H_2O, and nitrogen oxides, which were passed over special columns

containing KOH solution, which dissolved the CO_2 and H_2O. Metallic copper reduced the nitrogen oxides to elemental N_2 and the volume of liberated gas was measured,[274] while calibration was performed using material of known N_2 content, to allow quantitative analysis to be undertaken.[274]

In CHNS analysis, combustion of C produces CO_2, H_2 forms H_2O, N_2 forms nitrogen oxides and sulfur forms SO_2.[275] The products are swept out of the combustion chamber by inert gases and passed over copper, which gets rid of residual oxygen and reduces nitrogen oxides.[275,276] Gases are then detected by using gas chromatography or quantified by thermal conductivity detectors.[276] CHNS analysis has been used to look at elemental composition of GFNs, and to confirm the functionalisation of GFNs.

1.4.10. Thermogravimetric analysis

Thermogravimetric analysis (TGA) measures the mass changes in materials as a function of increasing temperature (with constant heating rate), or as a function of time (with constant temperature).[277,278] TGA is usually performed under an inert atmosphere like Argon,[279] or in the presence of ~5 % oxygen, in an N_2 or He atmosphere.[280] TGA provides compositional analysis of a sample, by monitoring the decomposition of different functional groups. TGA can aid the characterisation of functionalised graphene, although TGA only provides an indirect measure of the degree of functionalisation unless it is hooked up to a secondary analyser such as gas chromatography.

1.4.11. Contact angle measurements

The contact angle is angle at which a liquid meets a solid surface. It quantifies the wettability of the solid surface by that liquid, and obeys Young's equation, as shown in Equation 13:[248]

$$\mathbf{0} = \boldsymbol{\gamma_{SG}} - \boldsymbol{\gamma_{SL}} - \boldsymbol{\gamma_{LG}}\, \boldsymbol{cos\theta_C} \quad (13)$$

where $\boldsymbol{\gamma_{SG}}$, $\boldsymbol{\gamma_{SL}}$ and $\boldsymbol{\gamma_{LG}}$ are the solid-vapour, solid-liquid and liquid-vapour interfacial energies, respectively, and $\boldsymbol{\theta_C}$ the contact angle. Contact angle measurements provide an indication of the hydrophilicity of materials. Figure 1-21 shows the water contact angle images of GO (A) and graphene (B), indicating the difference in hydrophobicity of the two materials.

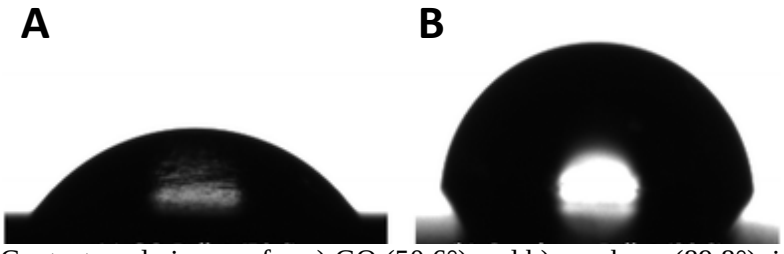

Figure 1-21. Contact angle images for a) GO (50.6°) and b) graphene (89.8°), indicating the differences in hydrophilicity. Samata *et al*.[281]

1.4.12. Zeta potential measurements

For colloidal suspensions to be stable they must possess a net surface charge of > $\boldsymbol{kT/e}$, (25.6 mV at 298 K), where $\boldsymbol{e}$ is the electronic charge.[282,283] The charge can arise from the de-protonation/protonation of surface groups, or from the adsorption of ions from the solvent. The charge draws a layer of counter ions, which forms an electrical double layer, with the diffuse nature of the counter ions creating an overall effective surface charge.[282]

The charges repel other molecules in the solution, which results in stable suspensions. The magnitude and sign of the charge of the double layer is estimated

through the 'zeta potential',[268] which exists at the shear plane of the dispersed particle when moving in the solution.[284] The zeta-potential of a dispersion is estimated using electrophoresis, in which an electric field is applied across the dispersion, causing particles which possess a zeta-potential to migrate toward the electrode of opposite charge. The velocity of the particles toward the electrode is proportional to the magnitude of the zeta-potential.[285] Equation 14, the Smoluchowski equation, describes the relationship between electrophoretic mobility, $\boldsymbol{\mu_e}$ ($m^2\ V^{-1}\ s^{-1}$) and zeta potential ($\boldsymbol{\zeta}$) as:[265]

$$\boldsymbol{\zeta = \frac{4\pi\eta}{\varepsilon_0 \varepsilon_r}.\ \mu_e} \tag{14}$$

Where ζ is the zeta-potential (V), $\boldsymbol{\eta}$ viscocity of the water medium (Pa S), $\boldsymbol{\varepsilon_0}$ is the permittivity of vacuum and $\boldsymbol{\varepsilon_r}$, the dielectric constant of the medium.

Zeta-potential measurements can provide information about the stability of GFN dispersions,[283] as zeta-potentials vary with solvent.[268] It also gives an idea about the charge of GFN dispersions. The pH-dependent zeta-potentials of dispersions are also important to determine, when considering applications *in-vivo*, as the differing pH in organs may cause agglomeration of graphene sheets. As pristine graphene does not disperse in water, it is difficult to measure its zeta-potential in aqueous solution, but the zeta-potential of GO has been recorded and is typically of the order of -40 to -60 mV.[286,287,288]

1.4.13. Light microscopy

The addition of graphene to some substrates causes changes in the visible contrast, providing a means of differentiating single layer from bilayer graphene (BLG) or few-layer graphene (FLG).[289,290] Most commonly SiO_2/Si wafers are used as the substrate for visible light microscopy of graphene,[290] with contrast arising from an

interference effect between the graphene and oxidised silicon.[289,290] The increased interference from the addition of graphene onto the wafer arises because the graphene flakes increase the optical path of light, which therefore changes the interference colour of the wafer, in comparison the bare wafer.[290] Geim and co-workers studied this interference effect on Si substrates with various thicknesses of oxide layer, finding that 300 nm (and 90 nm) oxide layers provide maximum visible contrast under the presence of graphene, using white light.[290] Figure 1-22 shows a visible microscopy image of graphene on a 300 nm SiO_2/Si wafer. Visible light microscopy offers rapid, non-destructive characterisation for large graphene sheets.[291] The limitation of using visible light microscopy is that it is less effective in distinguishing smaller graphene sheets, such as those produced by sonochemical exfoliation, due to resolution limits. It is most suitable for graphene sheets which have sizes of a few microns or larger.[45]

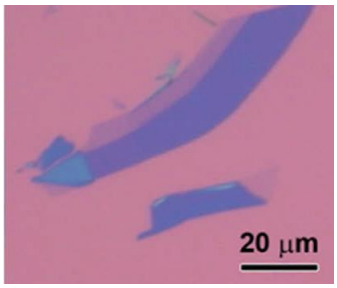

Figure 1-22. A visible light image of few-layer graphene (FLG) and single-layer graphene (lighter purple contrast), on a 300 nm SiO_2 layer. Lighter colour indicates thinner layer. Soldano *et al*.[45]

1.5 Layer-by-layer assemblies

The layer-by-layer (LbL) technique for forming multilayered structures was developed by Decher and co-workers, due to limitations in the Langmuir-Blodgett technique, which was limited to amphiphilic molecules and had to be formed on the surface of water before being transferred to other substrates.[292,293] The LbL technique is based on the immersion of charged surfaces in a solution containing oppositely

charged ions, towards which it experiences an electrostatic attraction. Once the charged species form a layer on top of this surface, the surface is rinsed and exposed to a solution containing ions of the opposite charge to the first layer; the immersion in alternating positively and negatively charged solutions creates the multilayered structure.[294] The LbL technique can produce multilayered structures with a variety of materials, by exploiting electrostatic or hydrogen bonding interactions.[295,296,297,297]

LbL is a low-cost method of fabrication and does not require specialist equipment.[293] In addition, the LbL process can be performed on a variety of surfaces and the thickness of layers can be carefully controlled by altering the solutions in which the surface is immersed. The layer-by-layer method can also be achieved by spraying layers, instead of immersing the surface in alternating solutions, further simplifying the method.[298] A schematic of the LbL assembly of a polyelectrolyte multilayer can be seen in Figure 1-23.[299] Though LbL assemblies commonly involve the use of polyelectrolytes,[300,301,302,303] other species which have been incorporated into LbL assemblies include viruses,[304] dyes,[305] proteins[306,307] DNA[308,309] and carbon nanotubes.[310]

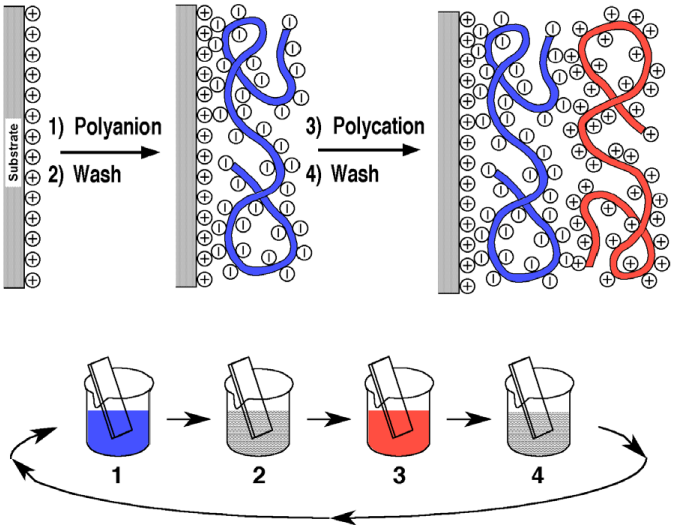

Figure 1-23. Layer-by-layer (LbL) procedure, showing a simplified view of first two layers of a film, deposited on a positively-charged substrate. The charged surface is first immersed in a polyanion solution, washed and then immersed in a polycation solution. Decher *et al.*[293]

LbL assemblies have found use in a variety of biomedical applications. For example, LbL assemblies incorporating laminin and poly-L-glutamine have been used in nerve regeneration applications,[311,312] while polymer LbL constructs have also been widely used in antimicrobial coatings, using both synthetic polymers such as polyhexamethylene biguanide (PHMB) and poly(4-vinylphenol),[313] in addition to naturally found charged species such as lysozyme.[314] Many LbL assemblies have been explored for use in vascular stents, including materials which contain plasmid DNA,[315] collagen/heparin,[316,317] fibronectin/heparin[318] and vascular endothelial growth factor (VEG-F).[318] These examples show the versatility of the LbL method in incorporating a wide range of molecules and the application of LbL assemblies in many biological settings.

GFNs have been incorporated into LbL constructs, with GO commonly used in place of polyanions in the LbL process.[319,320,321,322] For example, Kwon *et al*. assembled polyaniline (PANI)/GO films, by spraying alternating layers of PANI and GO onto glass slides.[323] After reduction of the GO layers, this LbL construct was used as an

electrode.[323] Figure 1-24 shows the change in colour of the PANI/rGO LbL assemblies as a function of layer number, as well as the measured increase in thickness with increasing layer numbers. Chen *et al.* used poly(vinyl alcohol) (PVA)/GO LbL assemblies as electronically conductive films, after the GO layers were reduced.[324]

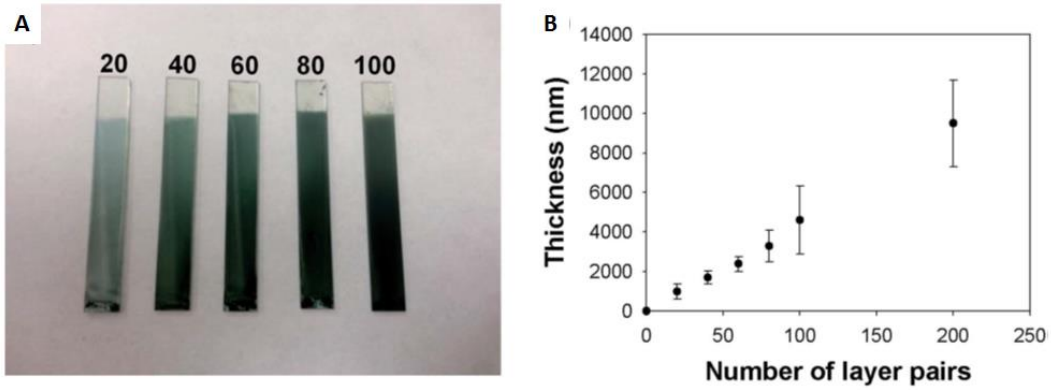

Figure 1-24. A) Digital image of the PANI NF/GO spray-assisted LbL films with varying number of layer pairs. B) Thickness of spray-assisted PANI NF/GO LbL films. Kwon *et al.*[323]

Other examples of GFN LbL assemblies are a poly(diallyldimethylammonium chloride) (PDDA)/GO polymer LbL assembly, which served as a catalyst for the oxygen reduction reaction, as well as GO/PAH LbL assemblies, which were used for drug encapsulation.[325] Chen *et al*. produced a LbL in which GFNs were present in both layers. Reduced graphene oxide was functionalised with, poly(acrylic acid) (PAA) and poly(acryl amide) (PAM) with alternating layers of the rGO/PAA and rGO/PAM forming the LbL assembly.[326] Pristine graphene, on the other hand, is not commonly used in LbL assemblies as it is uncharged, with limited examples invoking surfactant-modified graphene to incorporate the necessary charge for LbL formation.[327]

GFN LbL assemblies have been used in tissue culture applications. For example Shin *et al.* report the encapsulation of 3T3 fibroblasts, human mesenchymal stem cells (hMSCs) and cardiomyocytes in a poly-L-lysine (PLL)/GO LbL construct,

showing good cell adhesion and viability,[328] while Qi *et al*. demonstrated the growth and increased differentiation of stem cells on GO/PLL LbL assemblies.[329] In addition, Qi *et al.* studied fibroblast proliferation on poly(allylamine hydrochloride) (PAH)/GO LbL assemblies, indicating greater proliferation and cell spreading on the PAH/GO LbL assembly than on control substrates.[330]

The LbL process will be used to incorporate G-SO_3, as well as GO and sulfonated GO (GO-SO_3), into scaffolds for use in tissue engineering. The LbL is a straightforward way to incorporate GFNs into multilayer composites and is highly versatile, therefore enabling the incorporation of various counter ions, which could be used to enhance cell binding or alter the properties of the films.

1.6. Biomedical applications of graphene family nanomaterials

In recent literature, there has been a notable shift from the use of carbon nanotubes (CNTs) to GFNs in biological applications due to their higher surface area (~1000 m^2 g^{-1} for CNTs vs. ~2630 m^2 g^{-1} for pristine graphene),[331,332] in addition to concerns about the toxicological effects of CNTs, which are thought to behave in a similar way to asbestos fibres.[333] The favourable characteristics of graphene, such as its electron mobility[3] and high Young's Modulus (1 TPa),[4] have generated interest its use in biological applications. A summary of biomedical applications of graphene is provided in this section.

1.6.1. Electrical biosensors/bio-detectors

The high conductivity and fast electrode kinetics of GFNs, along with the high surface area on which to adsorb or attach biomolecules, have prompted the development of graphene-based electrochemical sensors.[334,335] An example of a GFN electrochemical detector is the detection of glucose by graphene oxide (GO), reported by Liu *et al.*[336] Glucose oxidase (GOx) was attached to GO via a 1-ethyl-

3(3-dimethylaminopropyl)-carbodiimide (EDC) and *N*-hydroxyl succinimide (NHS) coupling. The resulting sensors showed a linear response to glucose concentration and a detection limit of 8 mA cm^{-2} M^{-1}.[336] Mannoor *et al.* reported the use of pristine graphene in the detection of entire bacteria present on tooth enamel, using a peptide-coated graphene sheet.[337] Changes in the electrical resistance of graphene, corresponding to the binding of a single bacterium, gave rise to a bacterial sensor with a detection limit of 1 bacterium μL^{-1}. The graphene-peptide sheet was printed onto water-soluble silk, permitting transfer of graphene nanosensors onto other surfaces or materials. The system is shown in Figure 1-25.

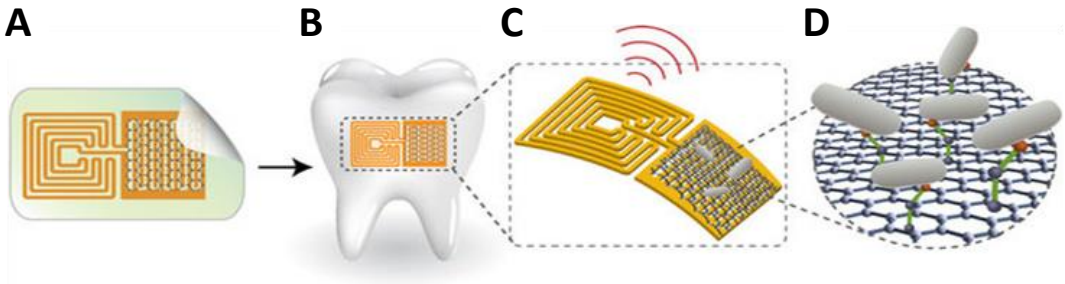

Figure 1-25. A) Graphene printed onto bioresorbable silk and contacts formed with a wireless coil B) Transfer of nanosensing architecture onto tooth C) Magnified sensing element D) binding of pathogenic bacteria by peptides self-assembled on the graphene nanotransducer. Manoor *et al*.[337]

Other GFN sensors include those for the detection of pathogenic virsues,[338] cytochrome *c*,[339] hydrogen peroxide,[340] cytochrome C/hydrogen peroxide,[341] paracetamol,[342] dopamine/serotonin and ascorbic acid[343] DNA decorated sensors,[344] prostate cancer antigens,[345] cancer cells,[346] anthrax,[347] theophylline,[348] peanut allergens,[349] cholesterol,[350] and parathion.[351]

Much of the criticism of GFN-based electrochemical sensors centres on the absence of meaningful control experiments. Materials which display similar characteristics to graphene, such as highly ordered pyrolytic graphite,[352] must be compared to

graphene in sensors. Furthermore, the wide range of GFNs used in electrical biosensors means that it is difficult to determine the true advantage of using 'graphene' in sensors.[353]

1.6.2. Optical sensors

The high fluorescence quenching ability of GFNs have led to their increased use in optical sensing.[354] Fluorescence quenching is sensitive to the proximity of the fluorophore to the quencher,[355] meaning that observing changes in fluorescence intensities under different conditions can sense the binding or release of fluorescent species to graphene. For example, Chang *et al.* produced a GFN-based optical sensor for the detection of thrombin.[356] The binding of a fluorescently-labelled aptamer to graphene resulted in effective florescence quenching, but the binding of thrombin to the aptamer caused a conformational change, which moved the dye further from the graphene sheet, causing a partial restoration of fluorescence, as depicted in Figure 1-26.[356]

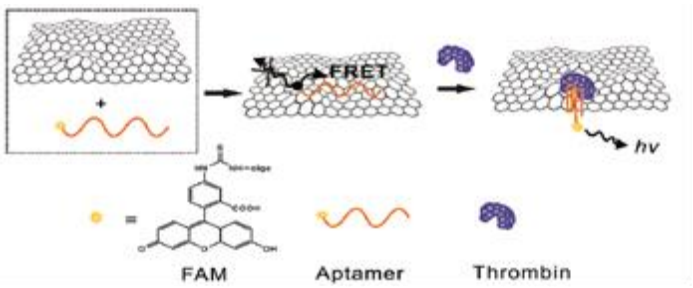

Figure 1-26. FRET graphene-aptamer based thrombin detector. Chang *et al.*[356]

In a paper by Li *et al.*, a GO sensor was developed, using the principle that single-stranded DNA (ssDNA) has a high affinity towards GO and adopts a soft, coiled structure.[357] When a complementary strand binds to ssDNA, the resultant double-stranded DNA (dsDNA) becomes much more rigid. A fluorescently tagged ssDNA was added to GO, with the conformational change associated with complementary DNA binding causing a lowering in fluorescence quenching, due to

the weaker interaction between the dsDNA and the GO sheet.[357] Fluorescence based GFN sensors have also been used in the detection of, amongst others, adenosine triphosphate (ATP), metal ions,[358] hemin,[359] microRNA,[360] TNT,[361] protease[362] and ochratoxin A.[363]

1.6.3. Graphene-family nanomaterials in tissue engineering

1.6.3.1 Antibacterial properties of graphene-family nanomaterials

Much of the interest of GFNs in tissue engineering applications arise from their antibacterial properties. For example, Hu *et al.* fabricated GO and reduced GO (rGO) paper, and found them to inhibit the growth of *E.coli* bacteria,[364] which was thought to be caused by oxidative stress and physical disruption of the bacterial membrane[364] and has been observed in carbon nanotubes and fullerenes.[365,366,367] Similarly, Akhavan *et al.* compared the antibacterial properties of GO and rGO nanowalls, finding that rGO showed greater toxicity towards *Staphylococcus aureus* and *E.coli* bacteria, due to its more sharpened edges which caused greater damage to the bacterial membranes. However, both GO and rGO showed significant antibacterial activity.[368] Liu *et al.* observed the antibacterial action of GFNs and propose that the mechanism of toxicity toward bacteria arises from membrane stress, induced upon contact with sharp GFN sheets causing oxidative stress to the bacteria.[369] Studies have also reported the antibacterial activity of GFNs towards *Enterococcus faecalis*,[370] *Bacillus cereus*,[371] *Staphylococcus epidermis*,[372] *Bacillus subtilis*,[373,374] and *Pseudomonas aeruginosa*.[375]

By assessing the bacterial action of graphene on three substrates: Cu (conductive), Ge (semi-conductive), and SiO_2 (insulating), Li *et al.* proposed that the antibacterial action of graphene could arise from charge transfer between the bacterial membrane

to the graphene sheet, altering the cellular potential and disrupting cell processes.[376] Several other mechanisms have been attributed to the antimicrobial activity of GFNs such as the sharp edges of GFNs acting as 'knives', piercing the cell membrane of bacteria,[368,377] or reactive oxygen species (ROS)-induced oxidative stress, thought to be caused by O_2 adsorption onto defects in GFNs.[378]

A paper by Barbolina *et al.* showed that the purity of GFNs played a crucial role in their antibacterial activity, with non-purified GO causing antibacterial activity arising from the presence of acidic impurities, as they found the antibacterial effect to diminish with an increased number of purification steps.[379] In addition, the adsorption of proteins to GFNs has been found to dampen their antibacterial properties, by preventing GFNs from interacting with microorganisms.[380] This may provide a possible explanation for the difference in cell behaviour between mammalian and bacterial cells, as the adsorption of proteins is favourable for mammalian cell adhesion to surfaces. The structure of different bacteria may also affect the antibacterial action of GFNs as, for example, gram positive bacteria have a thick layer in the cell wall, while gram negative bacteria have only a thin layer, which can affect their interaction with GFNs.[378] In addition, bacteria have different shapes, which can also affect how they interact with GFNs.[378]

1.6.3.2 Wound healing

Motivated by the documented antibacterial activity of GFNs, there has been increased interest in their use in wound healing applications. For example, Deepachitra *et al.* prepared GO-loaded collagen/fibrin films, which showed enhanced fibroblast proliferation and activity, but also accelerated wound healing *in-vivo*.[381] In another study, Dubey *et al.* produced a PEGylated GO-silver nanoparticle-

curcumin nanofiber composite, which showed significant antibacterial property and good cell proliferation of NIH-3T3 mouse embryonic fibroblasts, therefore showing potential as an antibacterial wound dressing.[382]

Curcumin, which is known to aid wound healing but suffers from poor solubility was combined with GO and collagen, with the curcumin-loaded GO/collagen scaffold showing faster wound healing *in-vivo* than collagen scaffolds and exhibiting no toxicity towards NIH-3T3 cell lines.[383] Graphene foams loaded with mesenchymal stem cells have also been shown to enhance wound healing *in-vivo*,[384] while GO has been used in conjunction with laser Nd-YAG laser, on wounds infected with *S. aureus*, causing increased healing of the wound in comparison to laser ablation. The antibacterial action of GO with laser ablation towards various bacteria was also demonstrated by Khan *et al.*.[385]

Sun *et al.* reported the production of 'graphene quantum dot band aids', which enhanced the antibacterial activity of H_2O_2 both *in-vivo* and *in-vitro*. Figure 1-27A shows tissues extracted from wounds in mice after treatment with the graphene quantum dots (GQD) with Figure 1-27B showing the amount of bacteria remaining post-treatment, clearly demonstrating the increased antibacterial action of the GQD + H_2O_2 treatment.[386] Several other GFN-based wound healing materials have been developed, including Ag/graphene polymer hydrogels,[14] Ag nanoparticle-coated graphene[387] and graphene-containing chitosan-PVA nanofibers.[388]

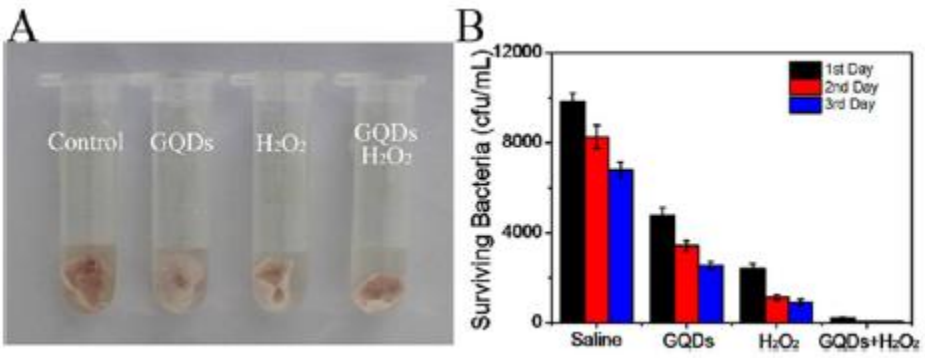

Figure 1-27. A) Tissues from wounds treated with (L-R): control (Saline + band aid), GQD + band aid, H_2O_2 + band aid, GQDs + H_2O_2 + band aid. B) Remaining bacteria in tissues from wounds treated with (L-R): control (Saline + band aid), GQD + band aid, H_2O_2 + band aid, GQDs + H_2O_2 + band aid. Sun *et al.*[386]

1.6.3.3 Stem cell growth and differentiation

Stem cells are progenitor cells which differentiate to adipocytes, osteoblasts, chondrocytes and neurons.[389] Stem cells enable the body to repair organs and tissues and are found in almost every tissue in the body.[390,391] The use of stem cells is of great interest in tissue engineering as they can be used to aid healing and regeneration,[392] significantly reducing the requirement for organ or tissue donation.[393] Stem cells will be described in more detail in Section 1.10. A goal of tissue engineering is therefore to guide the fate of stem cells and to accelerate differentiation.[12]

Lee *et al.* compared proliferation of mesenchymal stem cells (MSCs) on graphene, GO and polydimethylsiloxane (PDMS), a traditional substrate with good proliferation and differentiation-inducing abilities.[394] A higher density of MSCs were found on graphene and GO than on PDMS substrates. Furthermore, after 12 days of osteogenic induction, the extent of mineralisation, as measured by an Alizarin Red stain, was greater on graphene and GO vs. the PDMS control,[389] as seen in Figure 1-28. The Alizarin Red stain detects calcium deposits, which are stained red, indicating a mineralised matrix and thus osteogenesis.

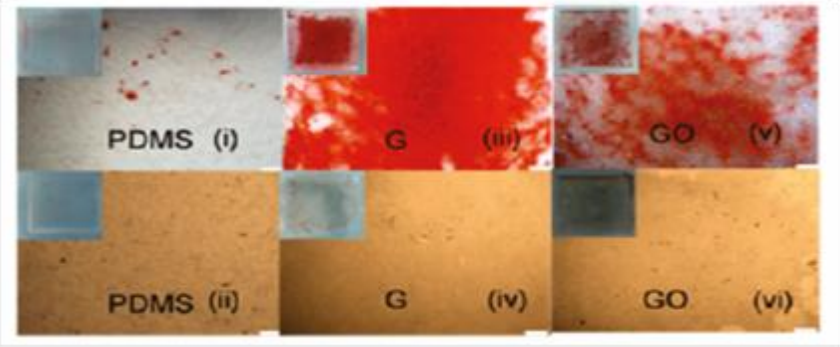

Figure 1-28. Osteogenic differentiation after 12 days, shown using Alizarin Red stain. (i) PDMS with induction. (ii) PDMS without induction (iii) G with induction (iv) G without induction (v) GO with induction and (vi) GO without induction. Enhanced differentiation on G substrate is clearly observed. Lee *et al*.[389]

The increased osteogenic differentiation on the GFNs was attributed to the ability of pristine graphene and, to a lesser extent, GO, to pre-concentrate dexamethasone and β-glycerophosphate, important osteogenic induction molecules, through π-π stacking onto the basal plane. Accelerated osteogenic differentiation on graphene has also been observed by Nayak *et al.*[12] and, in a recent paper by Liu *et al*., CVD graphene enhanced the osteogenic differentiation of hMSCs both *in-vitro* and *in-vivo,* by activating the promoter regions of osteogenesis-associated genes.[395]

Crowder *et al.* demonstrated the osteogenesis of hMSCs, in the absence of chemical cues, in 3D graphene foams.[396] The osteogenesis was attributed to the increased cytoskeletal tension of the hMSCs, caused by the forced elongation across and around the pores of the foams.[396] However, they also found that the large pore size (100 μm) somewhat inhibited cell growth and proliferation, highlighting the importance of regulating pore size to optimise the attachment and spreading of cells, as well as the effect of topology on stem cell growth and differentiation.[396] A paper by Akhavan *et al.* showed a similar effect of topology on differentiation, in which an rGO-nanoribbon (rGONR) grid showed a two-fold enhancement in osteogenesis, in the presence of chemical induction, in comparison to rGO sheets. In the absence of

chemical induction, the nanogrids were still able to show patterned osteogenesis, whereas the rGO sheets showed no significant differentiation.[397]

The synergistic effect of using graphene-based substrates and other molecules known to drive osteogenesis has also been evidenced. Luo *et al.* combined GO and poly (lactic-co-glycolic acid) (PGLA) nanofibers by electrospinning. The PGLA produced a nanofibrous 3D structure, which was complemented by the increase in hydrophilicity, as well as chemical-inducer adsorption, from the addition of GO, which enhanced osteogenesis.[398] In a paper by Nair *et al.* 0.5 wt. % GO was incorporated into a gelatin-hydroxyapatite (GHA) matrix and caused the osteogenic differentiation of adipose derived stem cells without the need for induction media, in contrast to the GHA matrix alone, which only underwent significant osteogenesis in the presence of induction media.[399] Lee *et al*. reported the spontaneous osteogenic differentiation of rGO/hydroxyapatite composites.[400]

GFNs have also been shown to enhance the adipogenesis of stem cells. For example, Lee *et al.* showed that GO promotes adipogenesis, due to the interaction of GO with insulin (required for the induction of fatty acid synthesis), which arises from hydrogen-bonding and electrostatics. In addition, Kim *et al.* reported enhanced adipogenic differentiation of adipose-derived stem cells on GO and hypothesised that a number of characteristics, including roughness, stiffness, reactive oxygen functional groups and the adsorption of different proteins, influences its ability to drive differentiation and the attachment of stem cells.[401] In 3D culture, Patel *et al.* described the production of a GO/polypeptide injectable thermogel, which significantly enhanced the expression of adipogenic markers in comparison to the

polypetide thermogel. They attributed the enhanced adipogenesis to the ability of insulin to bind strongly to GO.[402]

The electronic properties of graphene have been utilised in the neurogenesis of stem cells. For example, Park *et al.* reported the use of a graphene scaffold in the direct neural differentiation of human neural stem cells (hNSCs).[13] After three weeks of incubation in laminin solution and growth factors, twice as many differentiated cells existed on graphene than on a glass substrate. Normally, differentiation of hNSCs favours glial cell formation over neuron formation but, on graphene, a higher proportion of neuron cells (39 %) *vs.* glial cells (22.9 %) was observed. Tang *et al.* also found that CVD graphene promoted the neural differentiation of stem cells, by supporting the growth of neural circuits and by providing a highly conducting surface for electrical signalling.[403] Similarly, Kim *et al.* reported the differentation of MSCs towards neural cells, both with and without induction media.[404]

In addition to pristine graphene, GO based substrates have been used to direct neural differentiation. For example, Weaver *et al.* used a GO/Poly(3,4-ethylenedioxythiophene) (PEDOT) complex to induce neural differentiation. The non-toxic properties of the complex, as well as the ability of GO to crosslink to several induction compounds led to this material showing enhanced neural differentiation.[405] In work by Kim *et al.* the importance of the topography of substrates for neural differentiation was evidenced.[406] GO-nanogrids were fashioned, resulting in a greater conversion of adipose-derived stem cells to neurons in comparison to GO, which was attributed to the shape of the nanogrids, which mimicked the neural networks.[406]

These examples exemplify the promise of GFNs as platforms for accelerated stem cell growth, with selective differentiation arising from the pre-concentration of specific inducers/growth factors,[407] topological cues[408] and material mechanics[409] of the substrates. Surfaces of differing roughness and stiffness exhibiting variances in differentiation, but more extensive investigation into the effect of graphene-based materials must be performed. Another area which must be developed is centred around the idea that the success of implantable and useful cell constructions is dependent on early vascularisation of tissues,[410] meaning that substrates must also be able to drive vascularisation.

1.6.3.4 Bone tissue engineering

Because of the osteogenic differentiation observed on many GFNs, there has been increased interest in the use of GFNs in bone tissue engineering applications. La *et al.* showed that GO-coated Ti delivered sustained release of bone morphogenetic protein 2 (BMP-2), needed for bone formation, leading to higher alkaline phosphatase activity (indicating osteogenesis) than with bare Ti.[411] Another paper from La *et al.* reported the production of an LbL film of alternating negatively-charged GO and positively-charged GO-NH_3^+ on Ti, which encouraged greater bone formation in mice with skull defects, than Ti.[412] Park *et al.* report similar effects in skull defects using GO-coated Ti.[413]

Dinescu *et al.* produced a chitosan/GO 3D-scaffold for bone engineering applications, with well-defined pores, improved mechanical properties and enhanced MC3T3-E1 pre-osteoblast activity in comparison to the chitosan scaffold,[414] while Nishida *et al.* produced GO/collagen sponge scaffolds, shown in Figure 1-29, which showed increased strength, adsorption of calcium and increased MC3T3-E1 activity

in comparison to collagen, as shown in Figure 1-29B. The (1 μg mL^{-1} GO) GO/collagen scaffold was then implanted into canine tooth extraction sockets, with the area of new bone formation increasing five-fold in comparison to the control, as shown in Figure 1-29C.[415]

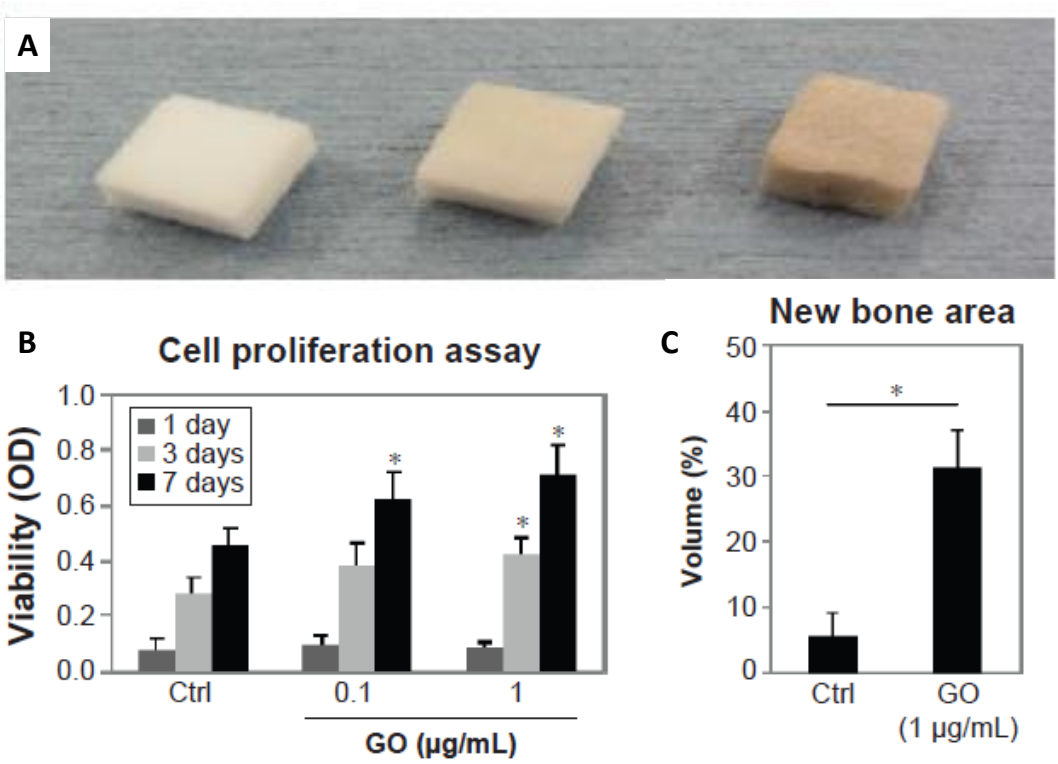

Figure 1-29. A) Pictures of the scaffolds (L-R): collagen sponge, 0.1 μg mL^{-1} GO/collagen scaffold, 1 μg mL^{-1} GO/collagen scaffold B) WST-8 cell proliferation assay (higher OD = higher cell count) of MC-3T3 E1 cells on scaffolds. C) New bone area as taken from histomorphometric measurements. Adapted from Nishida *et al.*[415]

Other graphene based materials which have been explored for bone regeneration applications include a graphene/gold/hydroxyapatite composite,[416] a GO-copper nanocomposite,[417] graphene hydrogel composites,[418,419] a polycaprolactone-graphene scaffold,[420] a rGO/polypyrrole/hydroxyapatite scaffold,[421] a silk fibroin/graphene oxide scaffold[422] and a polyethyleneimine (PEI)/GO scaffold.[423]

1.6.4. Tumour uptake and photothermal therapy

Photothermal therapy uses heat obtained from light absorption to kill unhealthy cells.[424] The high near-IR (NIR) absorbance of graphene has led to its use in

photothermal therapy.[425] Yang *et al.* reported the successful accumulation of fluorescently-labelled nanographene sheets coated with polyethylene glycol (NGS-PEG) to 4T1 (murine breast cancer), KD (human epidermal carcinoma) and U87MG (human glioblastoma) tumours, in mice.[425,426] Figure 1-30 shows the effective localisation of NGS-PEG in 4T1 tumour cells after 24 hours, as indicated by the white arrow. In addition to effective localisation, the high NIR absorbance of graphene was utilised for the photothermal treatment of the tumours.[425] Upon irradiation with an 808 nm NIR laser (power density of 2 W cm^{-2}), NGS-PEG experiences a large increase in temperature.[425]

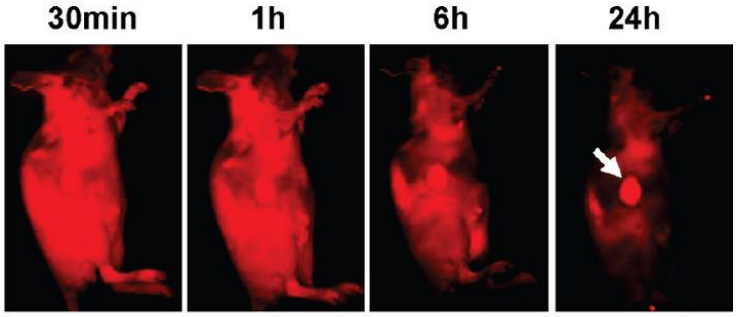

Figure 1-30. Localisation of NGS-PEG sheets into 4T1, tumours *in-vivo*. Yang *et al.*[425]

The treatment of mice with 4T1 tumours with NGS-PEG, subjected to laser irradiation, led to the disappearance of the tumour, leaving a small black scars at the site of the tumour, as seen in Figure 1-31.[425] The tumour site is visibly smaller in the presence of the NGS-PEG, in comparison to the control, in which the tumour remains large. Sheng *et al.* also report the use rGO, for the photothermal treatment of tumours,[427] with laser irradiation decreasing the number of viable cancer cells in the presence of rGO.[427]

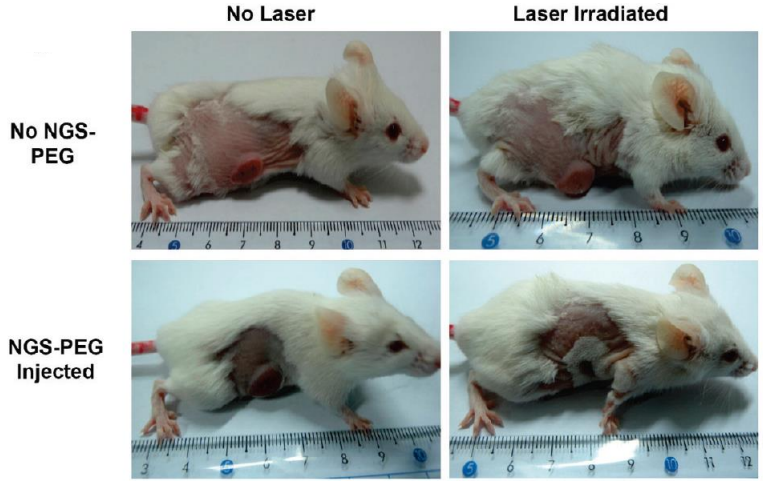

Figure 1-31. The effect of NIR irradiation on 4T1 tumours containing NGS-PEG. Yang *et al.*[425]

1.7 Graphene family nanomaterial biocompatibility and toxicity

With the growing interest in biological applications of GFNs comes a parallel requirement to more fully understand the interaction of GFNs with living tissues and biological systems and to determine the potential health risks of GFNs. Many studies on 'graphene' biocompatibility have been undertaken, but these studies pertain to a wide variety of GFNs which, as previously outlined, vary in lateral dimensions, defect content and number of layers, all of which affect biocompatibility.[31,428] The lack of a standardised nomenclature for GFNs introduces difficulty in drawing conclusions about potential health or toxicological effects of GFNs *in-vitro* and *in-vivo*.

Nevertheless, several reviews have attempted to identify patterns regarding the fate or toxicity of GFNs, by separating studies according to lateral dimensions, defect content (such as C/O ratio) and layers. A literature mining review of GFN studies *in-vivo* from Bussy *et al.* separated studies into four categories: pristine graphene, reduced graphene oxide (rGO), graphene oxide (GO) and functionalised graphene (graphene from one of the first three types but with further functionalisation).[429]

Several parameters were analysed, including the route of administration, the organs in which the highest accumulation of GFNs occurred, adverse effects, mechanisms responsible for adverse effects, the maximum dose administered and the duration of exposure, which revealed several patterns regarding the safety of GFNs.[429]

The most common accumulation of GFNs was in the lungs, with more adverse effects associated with inflammatory responses induced in the pulmonary system than anything other effect.[429] In addition, GFNs which induced the greatest adverse effects were those with the lowest degree of functionalisation, indicating that functionalisation of GFNs may improve their safety profile.[429] One of the other major conclusions from this work was that inadequately dispersed GFNs would be more likely to result in aggregate formation, thus increasing the risk of entrapment in tissues.[429]

In a review of carbon nanotube biocompatibility studies, several patterns were identified which could have implications for graphene biocompatibility.[430] Surface charge was identified as being important for crossing membranes, with positively charged carbon nanotubes more favourable for membrane insertion.[430] In addition, the ability to penetrate the cell membrane was generally lost if nanotube surface was coated with macromolecules.[431] In a review of carbon nanotubes and graphene toxicity studies, Bussy *et al*. produced a set of criteria which likely to minimise the safety risks of graphene.[430] The importance of using small sized, individual sheets which can be internalised by macrophages and removed, was highlighted, as well as the production of stable suspensions of GFNs to reduce aggregation *in-vivo*.[430]

The following section outlines toxicity studies of GFN towards cell lines, in the blood and *in-vivo*. The influence of lateral dimensions of GFN materials will also be outlined as will the effect of protein coating on the fate of GFNs.

1.7.1. Toxicity towards cells and hemocompatibility

There have been many studies of graphene-family nanomaterial (GFN) toxicity on various cell lines. In most studies, graphene is added into the media solution at varying concentrations, and the effects upon cells evaluated. Most studies exhibit a general trend of increased toxicity with increasing nanomaterial concentration and increased exposure time.[432,433,434,435,436,437] In a review of graphene toxicity towards cancer cell lines, oxidative stress and the activation of mitochondria were found to be the common causes of the observed toxicity.[438] A comparison of the toxicity pristine graphene and three commercial sources of GO toward skin keratinocytes showed that the least oxidised sample (pristine graphene) was the least cytotoxic, while the GO with the highest oxygen content showed greater toxicity.[439]

In human glioblastoma cells, graphene platelets localised close to the cells, but were not able to enter. At concentrations over 100 μg mL^{-1}, approximately 50 % cell death occurred and lactate dehydrogenase (LDH) release was detected, indicating membrane integrity loss.[440] Li *et al.* investigated the response of murine macrophages towards pristine graphene, dispersed in 1 % Pluronic F108, finding that the macrophage cells displayed dose-dependent apoptosis, with graphene causing a decrease in the mitochondrial potential and elevated levels of reactive oxygen species (ROS).[441] In contrast, however, Bengtson *et al*. reported no toxicity of graphene or GO towards Murine lung epithelial cells.[442]

GO has been more extensively studied for cellular cytotoxicity due to its high aqueous dispersibility. In many studies GO has been found to show dose-dependent cytotoxicity, although the concentration at which cytotoxicity is induced varied considerably between cell types. For example, in A549 alveolar basal epithelial cells, GO induced oxidative stress at concentrations as low as 10 μg mL^{-1},[443] while Lamel *et al.* reported decreased HepG2 cell activity at GO concentrations as low as 4 μg mL^{-1} and found that GO was able to bind to the cell membrane and enter cells.[444] Similar apoptotic effects and significant oxidative stress towards lung cells and neural stem cells have been reported reported,[445,446] while GO has been reported to causes apoptosis in T-lymphocytes and human fibroblasts at doses above 50 μg mL^{-1}.[432] Other cell lines towards which GO has shown dose-dependent toxicity include RPMI 8226 myeloma cells,[447] ovarian cancer cells[448] and the L929 mice fibroblast cell line.[449] In a paper by Fiorillo *et al.*, GO was found to selectively inhibit tumour-sphere formation and cause cytotoxicity in 6 different cancer cell lines, indicating its potential use for cancer treatment.[450]

Reduced graphene oxide (rGO) has been reported to induce toxic effects in a variety of cell types. For example, neuronal cells exposed to rGO caused the release of LDH and an increase in ROS,[451] with similar effects observed towards macrophages and alveolar epithelial cells.[452] In contrast to GO, rGO only caused moderate changes in cell activity towards HepG2 cells,[453] while both GO and rGO were found to cause dose-dependent toxicity towards MCF7 breast cancer cells, increasing the number of ROS and causing the release of LDH.[454]

As outlined in the review of Bussy *et al*, the functionalisation of GFNs with various molecules is able to reduce the toxicity of GFNs in comparison to the native

material.[429] For example, a common GFN functionalisation is with polyethylene glycol (PEGylation), with PEGylated GO exhibiting no significant toxicity up to concentrations of 100 μg mL^{-1}.[6,206] Another example of the effect of functionalisation upon cytotoxicity is provided by Mu *et al.*, who reported no cytotoxic effects of protein-coated GO, even at doses of 100 μg mL^{-1}.[455] Work by Sasidharan *et al.* found that the internalisation of functionalised graphene into monkey renal epithelial cells caused no obvious toxicity, in contrast to pristine graphene, which accumulated in the cell membrane and led to ROS generation and cell apotosis.[456] The same group found that pristine graphene, localised on the surface of macrophages, caused an increase in ROS, while the same concentration of functionalised graphene showed no toxic effects.[457] No toxicity of biopolymer-functionalized rGO towards human umbilical vein endothelial cells (HUVEC) was observed, even at doses greater than 100 μg mL^{-1}, while a higher level of cytotoxicity was observed for hydrazine-reduced.[458] Romero-Aburto *et al*. found that a fluorinated graphene oxide (FGO) showed no toxicity towards human breast cancer cells (MCF-7), even at the concentration of over 500 μg mL^{-1}.[459]

However, in some cases the functionalisation of graphene was not found to cause increased biocompatibility. For example, PEGylated rGO was found to be toxic toward the MCF-7 human breast cancer cell line and U87MG human glioblastoma cells at concentrations of about 80 μg mL^{-1}.[460] The effect of functionalised GFNs on cytotoxicity is cell dependent, as GO functionalised with 1,2-distearoyl-sn-glycero-3-phosphoethanolamine N-amino-PEG (PEG-DSPE) was found to show high toxicity to HeLa cells, causing significant cell death and LDH release at

concentrations above 10 μg mL^{-1}, while for SKBR3 and MCF-7 cells, almost 80 % of cells were still viable even at concentrations of 400 μg mL^{-1}.[461]

In a hemocompatibility study of GO and graphene, graphene was shown to display higher cytotoxicity, thought to rise from the hydrophobic interaction of graphene with erythrocyte cell membranes. However, in this study neither GO nor graphene showed significant coagulation, even at concentrations of 75 μg mL^{-1}.[435] This contrasts the work from Singh *et al*., which indicated the thrombotoxicity of GO at concentrations as low as 2 μg mL^{-1},[462,463] thus demonstrating the variability in cytotoxicity between similar GFNs, as a result of their production method. Cheng *et al.* reported erythrocyte lysis at rGO concentrations above 100 μg mL^{-1}, but found no significant cytotoxic effects at concentrations less than 10 μg mL^{-1}.[458,464]

The effect of functionalisation on hemocompatibility has also been explored. For example, Singh *et al.* compared the effect of amine-modified graphene, GO and rGO toward platelets.[462] While GO and rGO both caused a strong aggregatory response in platelets, the amine modified graphene displayed no such effect.[462] In addition, when intravenously administered in mice, no pulmonary thromboembolisms were observed, in contrast to other work by Singh *et al*., in which the exposure to rGO caused a strong cumulative response and extensive pulmonary thromboembolism.[462,463] Similarly, while GO caused the formation of an anaphylatoxin which is known to play a major role in inflammatory response, PEGylated-GO displayed significantly lower levels of this toxin.[465] This indicates that functionalisation of GFNs can also affect blood compatibility.

Again, the effect of functionalisation does not always cause increased hemocompatibility. For example, Ding *et al.* investigated the effect of pristine GO,

COOH functionalised GO (GOCOOH) and GO-PEI toward T-lymphocytes, finding that GO and GOCOOH showed good biocompatibility up to 25 μg mL^{-1} and cytotoxicity above 50 μg mL^{-1}, while GO-PEI showed toxicity at concentrations as low as 1.6 μg mL^{-1}.[466] This again highlights the importance of testing parameters such as hemocompatibility upon functionalisation of GFNs.

Akhavan *et al.* demonstrated the difference in cytotoxicity of rGO on stem cells, dependent on the lateral dimensions. The rGO with small lateral dimensions (around 10 nm) caused cell death at about 1 μg mL^{-1}, whereas rGO with larger lateral dimensions (around 4 μm) exhibited no significant cytotoxicity below concentrations of 100 μg mL^{-1}.[467] The difference in toxicity here shows the need for comprehensive understanding of the interaction of the GFN of interest with the specific system in which it will be used, as the effect of lateral dimensions can vary, depending on cell type and the method of administration.

1.7.2. Toxicity *in-vivo*

As well as assessing the response of individual cell types towards GFN, it is also important to understand the interaction of GFNs *in-vivo*, including areas of accumulation, any adverse effects caused by the GFNs and the routes of clearance of GFNs. In addition, the effect of different modes of administration can affect the fate of the GFNs, meaning that testing by specific administration methods is also important. This section describes several studies of GFN toxicity studies *in-vivo.*

Wang *et al.* described a dose-dependent toxicity of graphene oxide in mice.[432] At GO doses of up to 0.25 mg, which were administered intravenously, no significant toxicity was observed. However, once the dose was increased to 0.4 mg, 4 of the 9 test mice died from suffocation, due to the accumulation of GO in the airways,[432]

thus highlighting the extreme difference in bodily response to nanomaterials at differing concentrations and thus the importance of considering concentration when working *in-vivo*. A study by Wang *et al.* demonstrated extensive pulmonary thromboembolism in Swiss male mice only 15 mins after intravenously administrating 250 mg of GO per kg body weight.[468] Sydlik *et al*. compared the compatibility of GO with different levels of oxidation via subcutaneous and intraperitoneal administration in mice, finding that highly-oxidised GO induced a foreign body response in tissues,[469] while GO with a reduced oxidation level led to faster immune cell infiltration and clearance.[469] Yang *et al*. introduced GO into mice by oral ingestion and intraperitoneal injection, finding no uptake of the GO from the oral ingestion and the excretion of almost all the GO. GO which was intraperitoneally injected, however, accumulated in the liver and the spleen, which was thought to be due to ingestion by phagocytes. This evidences the difference in GFN fate, depending on the mode of administration.[470]

Wang *et al*. assessed the toxicity of graphene nanosheets, stabilised by the addition of serum albumin, which were intravenously administered in mice at a mass of 1 mg per kg bodyweight. This material caused site-specific inflammatory responses, pulmonary inflammation, thromboembolisms and immune responses in the lungs.[468] Duch *et al.* tested three different GFNs, administered via intratracheal administration: GO, graphene dispersed in aqueous Pluronic solution, and aggregated graphene.[452] They observed that GO caused persistent lung inflammation, caused by an increased rate of mitochondrial respiration and the generation of ROS in cells, which in turn activated inflammatory and apoptotic pathways.[452] Mice treated with the hydrophobic graphene dispersed in Pluronic, in contrast, presented

no signs of fibrosis, while aggregated graphene was accumulated in the medium or small airways of the lung, inducing peribronchial inflammation and mild fibrosis.[452]

Again, the functionalisation of GFNs serves to improve the response to GFNs *in-vivo*. For example, PEGylated nanographene sheets, administered intravenously, appeared to cause no significant toxicity, with the majority of the material cleared by renal and faecal excretion.[471] Similarly, Yan *et al.* and Yang *et al.* showed that PEGylated GO, administered intravenously, displayed no significant toxicity *in-vivo*.[472,425] In addition, when subcutaneously injected, the incorporation of GO into a Pluronic hydrogel only caused mild inflammation after 3 weeks, which later disappeared.[473] In addition to functionalisation, the importance of purification of GFNs in biocompatibility was shown by Ali-Boucetta *et al*., who found that purified GO, produced by several washings, appeared to decrease the inflammatory effects, following a 50 mg intraperitoneal injection, in comparison to unpurified GO, which caused significant inflammatory responses.[474]

The potential for accidental exposure to GFNs has meant that there has been increased interest in GFN interactions with eyes, skin, or lungs following inhalation. For example, Yan *et al*. administered an intravitreal injection of GO on to the eyes of mice, but found no evidence of ocular change.[475] Inhalation toxicity has also been investigated, due to the potential for this type of exposure during the processing and use of GFNs. Schinwald *et al*., for example, demonstrated that graphene nanoplatelets of up to 25 μm in diameter are respirable. [476] After 24 hours of exposure, there was a large increase in inflammatory cells such as macrophages, granulocytes and pro-inflammatory cytokines in the pleural space and lungs.[476] In addition, there was slower clearance of graphene from the pleural space in

comparison to carbon black, highlighting the effect of shape on clearance and adverse effects.[476] Ma-Hock *et al*. showed that rats suffered no adverse effects when exposed to graphite nanoplatelets or carbon black but, when exposed to pristine graphene, an increase in lymphocytes, cytokines, lactate dehydrogenase (LDH) and microgranuloma in the lungs was observed.[477]

1.7.3. Lateral dimensions

The lateral dimensions of a material have an influence on their internalisation, accumulation and clearance *in-vivo*,[430,478,479] while processes such as endocytosis are also sensitive to lateral dimensions.[480] If GFN flake sizes are too large, this can affect the metabolism of the bio-conjugates within the body, resulting in possible bioaccumulation and subsequent toxicity issues. The number of layers also affects the surface area and stiffness of GFNs, both of which have been investigated by Lee *et al.*[4] The specific surface area is inversely proportional to the number of layers and hence the adsorptive capability of GFNs increases with a decreasing number of layers, while the stiffness of GFNs increases with the number of layers.[4] Poland *et al.* showed a relationship between stiffness and pathological responses in carbon nanotubes.[481] Work by Jasim *et al.* used DOTA-functionalised GO, with ^{64}Cu, to detect the distribution of GO *in-vivo* by positron emission tomography-computed tomography (PET/CT) imaging. They compared thin GO and aggregated GO, monitoring the distribution in mice following intravenous administration. 48 % of the thicker GO sheets remained in the body after 24 hours and were concentrated mostly in the spleen and the liver, while thinner sheets were excreted through the urine with 77 % excreted within 24 hours.[482]

In a report from Yue *et al*. the internalisation of GO with two different lateral dimensions (350 nm and 2 μm) was compared, showing distinctly different interactions with macrophages, the former being wrapped by filopodia, but the latter found 'perpendicular to the membrane'.[483] Mu *et al.* found that the processes of intracellular internalisation differed between GO sheets, with smaller flakes of around 500 nm entering cells though endocytosis, while those with dimensions of around 1 μm were internalised by phagocytosis mechanism.[455] Another study found GO to accumulate in the lungs and liver, with flakes larger than 1 μm mostly ending up in the lungs and smaller flakes (under 500 nm) mostly in the liver.[484] Another study by Ma *et al.* assessed the effect of the lateral dimensions of GO both *in-vitro* and *in-vivo*, finding that larger GO flakes adsorbed onto the plasma membrane and underwent less phagocytosis, while smaller GO flakes were more easily entered into cells. The larger GO caused increased production of inflammatory cytokines and immune cell activation.[34]

1.7.4. Protein corona

A consideration when looking at the use GFNs *in-vivo* is the idea that the GFNs are likely to be coated with a complex mixture of proteins as they enter the body.[485] This is known as a 'protein corona' and can influence the fate of GFNs *in-vivo.* Mao *et al.* argue that, in a biological system, proteins and other biological moieties adhere onto GFN sheets, meaning that in the body the nature of the material may be completely different to that of GFN initially introduced,[486] and that therefore the effect of GFNs *in-vivo* may vary greatly to their behaviour *in-vitro.*

Hu *et al*. assessed the effect of GO nanosheets towards various human cells. At low concentrations of FBS (1 % or lower), a concentration dependent toxicity of GO

towards cells was observed, while when 10 % FBS was used the cytotoxicity was largely mitigated, demonstrating the effect of the 'protein corona' effect of GFNs.[434] Duan *et al.* also demonstrated the protein-corona-related mitigation of cytotoxicity of GO, by reducing its interaction with the plasma membrane of cells.[485] However, Mao *et al*. found that, as the length of incubation of graphene sheets with plasma proteins was increased, there was a reduction in cell count and increase in ROS, in both HeLa and Panc-1 cell lines.[486] This highlights a further consideration for GFN, that an understanding of how they interact with proteins they are likely to encounter is important in predicting toxicological outcomes.

1.7.5. Environmental safety considerations

Biotoxicity studies of GFNs for use in biomedical applications will be extensively tested before their use in humans. However, the large increase in graphene research and production brings with it an increased need for safe disposal, in addition to a requirement to more fully understand the probable effect of GFNs on the environment.

The stability of some GFNs, such as GO, in aqueous solution, means that there is risk of water contamination. For example, Lanphere *et al*. studied the effect of groundwater and surface water on GO nanoparticles, finding them to be stabilised in the presence of natural organic matter, therefore highlighting potential issues with long-term contamination of water.[487] There have been few studies on the effect of aquatic life following exposure to GFNs, meaning that the risk posed is largely unknown. Work by Chen *et al*. assessed the effect of GO on zebrafish, finding them to show resistance to GO, despite GO being distributed throughout the fish.[488] However, work by Pretti *et al.* indicated that monolayer graphene and graphene

powders showed significant toxicity towards algae at concentrations of approximately 1 mg mL^{-1} and 2 mg mL^{-1}, respectively.[489] Therefore, the effect of GFNs on aqueous environments must be more fully understood, as GFN waste could be exposed to marine life, after disposal.

The effect of graphene towards plant life has been evaluated. For example, Begum *et al.* treated several plant types with graphene and found that, at concentrations of 500 μg mL^{-1}, plant growth was significantly inhibited and a reduction in biomass observed.[490] In research by Hu *et al*., GO was found to enhance the phytotoxicity of arsenic, by disrupting fatty acid metabolism and the urea cycle, as well as damaging cells.[491] Begum *et al.* also reported cell membrane damage in the *Arabidopsis thaliana* plant, following exposure to 40 mg L^{-1} GO.[492] However, at concentrations of around 50 μg mL^{-1}, graphene was found to have no negative effect on plant growth of tomato plants.[493] In terms of aqueous leakage of GFNs, however, a review by Zhao *et al*. indicated that the toxicity of GFNs towards aquatic plants, which have larger air spaces and increased numbers of stomata, may be enhanced.[494,495]

1.7.6. Summary

It is important that, before any new GFN-based conjugates are used, a complete understanding of their interactions and impact in the body is reached. General assumptions about the effect of GFNs cannot be made, as even the graphitic starting material and fabrication process affects the characteristics and properties of the final GFN product.[496] The toxicity of GFN-protein complexes is also heavily dependent on cell type,[486] meaning that extensive toxicology investigations must be carried out. In addition, a greater understanding of the environmental impact of GFNs and their composites needs to be reached before they are used in large scale applications.

For this reason, the GFN-containing LbL constructs which will be made in this thesis will be tested for their biocompatibility *in-vitro*. The behaviour of cells on GFNs is likely to be affected be their incorporation into composites, which will affect several parameters such as the roughness, wettability and the attachment of protein to the surface. The cell types that will be initially assessed will be the 3T3 Swiss albino cell line and bone-marrow derived human mesenchymal stem cells.

1.8 Cell adhesion on biomaterials

Before cells adhere to biomaterial surfaces, various extracellular matrix (ECM) proteins deposit onto the surface.[497] Following protein adsorption, integrins within the cells attach to the ECM proteins, which results in cell body attachment to the substrate[498] and the transduction of signals to nucleus.[499,500] Once cells attach to a substrate, the cell body flattens and spreads and the actin cytoskeleton becomes highly organized into microfilament bundles,[501] forming focal adhesions between the cell and the substrate. Focal adhesions are complex, integrin-mediated cell-ECM adhesion sites,[502] which include many proteins such as talin, vinculin, α-actinin, filamin, and paxillin.[503] The roles of ECM proteins, integrins, focal adhesions and cadherins in cell adhesion and proliferation are outlined in the following section.

1.8.1. Protein adsorption onto surfaces

The adsorption of ECM proteins play a crucial role in mediating cell-material surface interaction as they approach the surface, from the serum-containing media, more quickly than cells.[504,505] The cells recognise adsorbed proteins using surface receptors, including integrins,[506] which in turn promote cell proliferation, cell signalling, and the secretion of proteins to replenish the protein layers.[506,507] Therefore, cell attachment occurs as a result of protein adsorption in the initial stages of cell culture *in-vitro*.[497,508] The adsorption of proteins can arise from van der

Waal's, hydrophobic, electrostatic or hydrogen bonding interactions, meaning that the adsorption of different proteins to surfaces is dependent on many factors such as the surface wettability, topography and charge.[509,510] Initial protein adsorption involves serum proteins which are low weight and highly abundant, but over time these proteins are replaced by more strongly binding proteins, known as the Vroman effect.[511,512] Cells also release their own adhesive matrix onto a surface, in order to strengthen the adhesion.[513] Typical serum and ECM proteins which interact with surfaces and cells are outlined in this section.

1.8.1.1. Bovine serum albumin

Bovine serum albumin (BSA) is a 66 kDa plasma protein.[514] BSA is a non-adhesive protein that can 'trigger' the attachment of cells to low levels of adhesion molecules.[515] Although BSA is a non-adhesive protein, it is able to modulate conformation of fibronectin and other adhesion molecules to active forms.[515]

1.8.1.2. Fibronectin

Fibronectin is a dimer of identical subunits of 200 residues,[516] held together by a disulphide bond.[517] It is a major structural component of the filaments surrounding cells.[518] The hydrophilic arginyl-glycyl-aspartic acid (RGD) section of fibronectin binds to cell surfaces.[519] The RGD sequences of fibronectin, as well as vitronectin and other adhesive proteins, forms the initial binding site for integrins.[498,520] The adhesion of fibroblasts to fibronectin via integrins, for example, stimulates spreading and growth.[498] Studies have also found enhanced cell adhesion with RGD-modified surfaces, indicating the importance of RGD binding to integrins on cell attachment.[521, 522]

1.8.1.3. Laminin

Laminin is a basement membrane protein, made of three polypeptide chains arranged in the shape of a cross.[523] Laminin has several domains, two of which bind to perlecan (a basement membrane proteoglycan) and nidogen (a sulphated glycoprotein) and two or more which bind to laminin receptors.[523] The $\alpha_1\beta_1$ $\alpha_3\beta_1$ $\alpha_6\beta_1$ integrin receptors bind to laminin.[524] Laminin is responsible for organising the basement membrane on cell surfaces and forms sheet like extracellular matrices.[523]

1.8.1.4. Vitronectin

Vitronectin is a multifunctional 75 kDa monomer glycoprotein, found in the plasma and the extracellular matrix.[525] The cell attachment activity of vitronectin is via the RGD peptide of vitronectin, which binds to $\alpha_V\beta_1$, $\alpha_V\beta_3$, $\alpha_V\beta_5$ and $\alpha_{IIb}\beta_3$ integrin receptors,[525] activating of the MAPK pathway, consequently initiating cell division and protein expression.[525,526] Vitronectin is therefore involved in cell adhesion and spreading on surfaces.[525]

1.8.1.5 Collagen

Collagens are formed of a triple-stranded structure, where the three α-chains are wound round each other.[523] Several types of collagen exist, which differ in their α-chains. The most common types are I, II, III, V and XI, with type 1 being most abundant and being found in skin and bone. However, type IV collagen form sheet-like networks which forms part of the basal laminae of cells.[523] The mechanical stability of the basal laminae is a result of collagen IV formation.[527] Integrins which bind to collagen IV include $\alpha_1\beta_1$, $\alpha_2\beta_1$, $\alpha_6\beta_1$, $\alpha_v\beta_3$ and $\alpha_v\beta_5$.[528]

1.8.2. Integrins

Cells attach to the extracellular matrix (ECM) by receptors, the most common of which are integrins.[498] Integrins are αβ heterodimers; various combinations of α and

β subunits combine to form different types of integrins. Most ligands of integrins are ECM proteins, which mediate cell-substrate adhesion and include fibronectin, collagen, laminin and vitronectin. The initial binding site of many integrins are the RGD sequences present in fibronectin, vitronectin and other adhesive proteins. When integrins bind to the ECM ligands they undergo a conformational change in which the α and β cytoplasmic domains interact.[529]

The specificity of an integrin for a ligand is dependent upon the α and β constituents of the integrin.[530] For example, the $\alpha_5\beta_1$ integrin recognises the RGD sequence on fibronectin, whereas the $\alpha_2\beta_1$ integrin recognises the Asp-Gly-Glu-Ala (DGEA) sequence on collagen.[530] All integrins, however, contain an extracellular domain, a membrane spanning domain and a cytoplasmic domain.[531] The N-terminal domains of the α and β subunits form a ligand binding head, whilst a stalk from each subunit connects them to the membrane spanning segments.[531] The structure of integrins showing the ligand binding and cytoplasmic domains can be seen in Figure 1-32. Integrins and their adhesion molecules bind to actin filaments within a cell focal adhesion complexes, highly ordered set of proteins and molecules,[501, 532] which transmit adhesive and traction forces.[533,534]

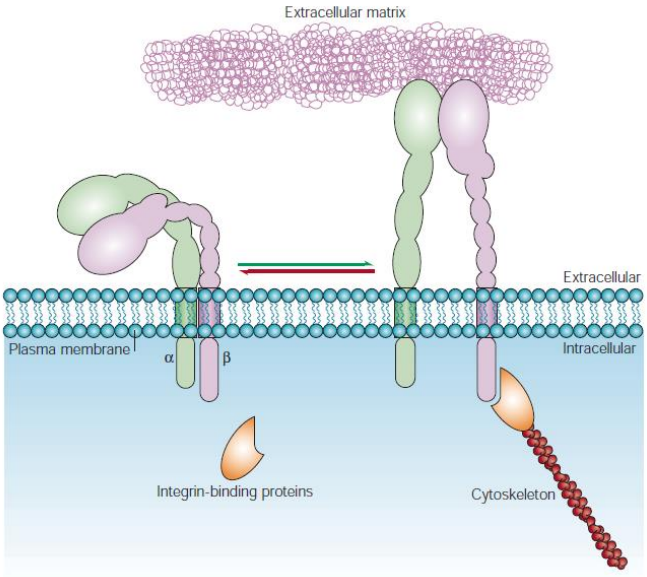

Figure 1-32. The structure of an integrin in an inactive (left) and active (right) state. From Kinbara *et al.*[535]

Once integrins have bound to cytoplasmic regions, they mediate information transfer in cells,[498] initiating signal transduction cascades which ultimately activate transcription factors and thus influence gene expression.[536,537,538] For example, tyrosine phosphorylation has been triggered by integrins in NIH-3T3 fibroblasts; Tyrosine phosphate has been found at cell-substrate and intracellular junctions.[539,540] Guan *et. al* found that adhesion and spreading of NIH-3T3s on fibronectin and anti-integrin antibodies leads to rapid tyrosine phosphorylation.[541] The binding of integrins also activates Rho GTPase, which is involved in cell spreading, migration and the assembly of focal adhesions.[542] Integrins are also responsible for the mediation of cell-cell adhesion.[520]

1.8.3. Integrin-related proteins

The localization of integrins relies on the connection to the actin cytoskeleton, which is formed between the β tail of integrins and actin-binding proteins.[543] Several intracellular proteins, 'effector proteins', are essential to integrin function; the cytoplasmic region of integrins associate with these proteins and transmit

signals.[543,544] Effector proteins include talin, α-actinin, filamin, focal adhesion kinase, paxillin, and vinculin.[543] The interaction between the effector proteins, the actin cytoskeleton and integrins is portrayed in Figure 1-33.

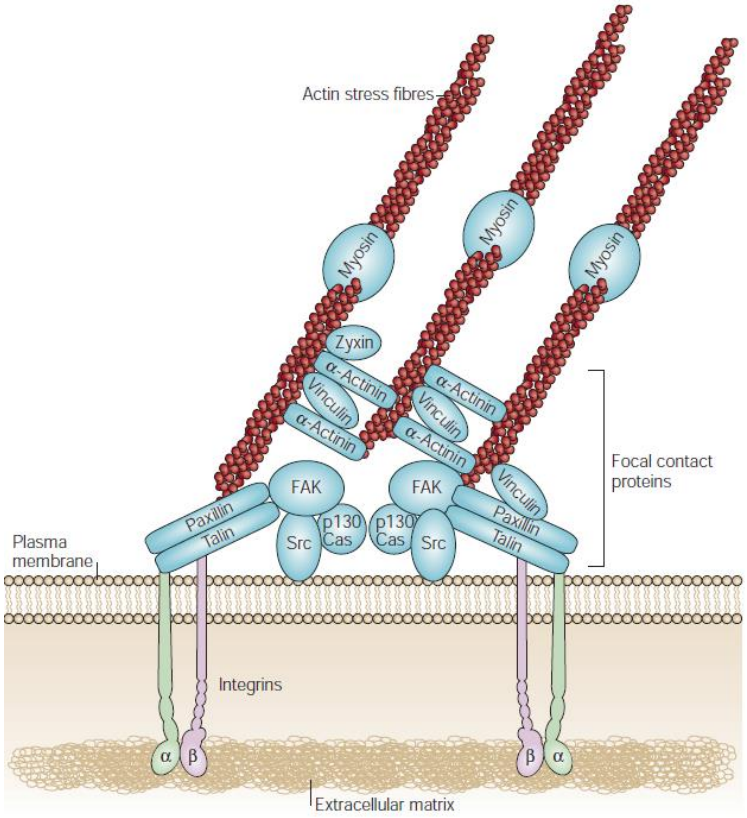

Figure 1-33. The ECM integrins and cell cytoskeleton interact at focal adhesions, which transduce signals to cell interior. Integrin-binding proteins paxillin and talin recruit FAK and vinculin to focal contacts. Actinin is protein which is phosphorylated by FAK, binds to vinculin and crosslinks actomyosin stress fibres, tethering them to focal contacts. Mitra *et al*.[545]

Talin, α-actinin and filamin are 'actin binding proteins' which bind directly to the integrin. Talin is a 270 kDa protein which connects integrin receptors and the cytoskeleton through focal complexes.[546,547] Talin also contains a binding site for focal adhesion kinase (FAK) and substrates for many signaling proteins.[546,547] α-actinin is a modular protein which binds to and cross-links filamentous actin (F-actin) and has binding partners which include vinculin, zyxin and P13Ks (enzymes involved in cell growth and proliferation).[548] It is present both within focal adhesions

and along stress fibres.[548] Filamin is a 280 kDa protein made of immunoglobulin repeat units which is found along stress fibres, as well as in the cortical actin cytoskeleton and in focal adhesions.[549] Filamin, as well as mechanically linking to integrins, behaves as an adaptor protein for signaling proteins involved in the regulation of cytoskeletal dynamics.[543]

Focal adhesion kinase (FAK) is an 125 kDa protein tyrosine kinase,[545] which is localised with integrins at the cell-substrate contact site, through binding to paxillin and talin.[550] FAKs cause the tyrosine phosphorylation of paxillin and talin, which is vital for signal transduction across the cell.[551] Paxillin is a 68-70 kDa phosphotyrosine-containing protein.[552] Paxillin mediates matrix adhesion assembly and matrix signaling, as it contains motifs which assist in protein-protein interactions.[553] Paxillin is thought to recruit signaling molecules to focal adhesions.[553] The association of actin-binding proteins with paxillin anchors the actin cytoskeleton and promotes clustering of molecules.[553]

Vinculin is a 110 kDa protein which is found in integrin-mediated cell–matrix adhesions and cadherin-mediated cell–cell junctions.[554] The active extended form of vinculin exists at focal adhesions, with the folded form in the cytoplasm.[555] Talin is the major protein which activates vinculin,[554] with this interaction playing a crucial role in focal adhesion formation.[556] Vinculin has up to 19 binding partners in its active form, which in turn bind to other proteins and link to a signaling network.[554]

1.8.4. Cadherins

Cadherins are transmembrane proteins found in cell-cell junctions, where they attach to the actin cytoskeleton,[498,557.558] Cadherins possess an extracellular, amino-terminated region to which ligands bind, a transmembrane segment and a

cytoplasmic section.[498] The cytoplasmic section interacts with intracellular proteins called 'catenins'. The subset ‘β-catenins’ bind to the cadherin cytoplasmic region, whilst α-catenins bind both to β-catenins and link the complex to the actin cytoskeleton.[558] Cell-to-cell adhesion, mediated by cadherins, is believed to occur in a 'zip-like manner'; cadherins on one cell form dimers, presenting the N-terminal repeat to complimentary dimers on adjacent cells,[559,560] allowing cells to 'zip up'.[498] The cell-cell adherence junction has additional importance in signalling cascades.[561]

1.9 Embryonic fibroblast cells

Fibroblasts exist in almost all organs the human body and can be defined as adherent cells, which are not originated from the endothelium, epithelium or blood.[562] Fibroblasts are the least specialised cells in the connective tissue family, which secrete extracellular matrix components, containing a high proportion of type I/type III collagen.[523] When tissues are damaged, fibroblasts proliferate and move to the site of injury, producing large amounts of collagenous matrix to help the repair of the damaged tissue.[523]

In addition to providing scaffolding support, fibroblasts also play significant roles in organ development, inflammation and fibrosis.[562,563,564,565] Skin fibroblasts play an important role in wound healing, adopting the contractile properties of smooth muscle cells, which pulls the wound together.[523] Fibroblasts from different tissues possess site-specific molecular identities and topographical memory due to different levels of gene expression.[566]

Mouse embryonic fibroblasts (MEFs) are often used as feeder cells for maintaining mouse/ embryonic stem cells, as they secrete extracellular matrix that affects the

growth of stem cells. They also help these stem cells to remain undifferentiated.[567,568] MEFs and mesenchymal stem cells are both plastic adherent, multipotent cells which adopt a similar morphology.[569] MEFs have been shown to exhibit very similar phenotypes to bone marrow derived stromal cells, displaying cell surface markers such as CD90, CD73, CD105, Vimentin and not expressing hematopoietic markers CD14, CD34 and CD45.[570] Both have the ability to undergo cell differentiation into osteocytes, adipocytes and chondrocytes.[562,569,571,572] For example, NIH-3T3 mouse fibroblast cells have been shown, by Dastagir *et al.*, to differentiate into adipogenic, chondrogenic, and osteogenic lineages expressing typical differentiation markers, though differentiation is not terminal.[569]

Embryonic fibroblast cells have been used in many published papers for conducting initial *in-vitro* biocompatibility screening of graphene nanomaterials. Media containing graphene oxide was found, by Wang *et al*., to display no cytotoxic effects on fibroblast cells below concentrations of 20 μg mL^{-1}. However, above 50 μg mL^{-1} a concentration-dependent toxicity was observed, which caused decreased cell adhesion, cell apoptosis and the presence of GO in many of the cell organelles.[432] Gurunathan *et al*. coated tissue culture plates with GO, hydrazine-reduced GO (H-rGO) and microbially-reduced GO (M-rGO) and found a dose-dependent toxicity of GO and H-rGO surfaces towards mouse embryonic fibroblasts (MEFs) but no significant toxicity of M-rGO.[573] In a second paper by Gurunathan *et al*. spinach-leaf reduced GO surfaces were found to exhibit no significant cytotoxic effects on MEFs.[574] These studies highlight the effect of fabrication method on cytotoxicity and the importance of characterising toxicity, even among similar types of GFN.

The incorporation of GFNs into composites has also been shown to affect biocompatibility, with Qi *et al.* for example, reporting good biocompatibility of a GO/poly(allylamine hydrochloride) layer-by-layer construct toward NIH-3T3 mouse fibroblasts.[330] The work of Qi *et al*. contrasts the findings reported by Guranathan *et al.* (above). Other graphene oxide-polymer composites which have shown good biocompatibility towards 3T3 mouse fibroblasts include a polyvinyl-N-carbazole (PVK)-graphene oxide (GO) nanocomposite[575] and a GO/poly(3,4-ethylenedioxythiophene) (PEDOT) composite.[576] The change in biocompatibility as a result of the incorporation of GO into composites highlights the importance of evaluating biocompatibility after any modification or functionalisation of GFNs, or after their incorporation into a composite.

Comparatively fewer investigations of pristine graphene have been undertaken, primarily due to the difficulty of incorporating graphene into a substrate, due to its hydrophobicity. However, Lin *et al.* used graphene, produced by chemical vapour deposition (CVD), as a substrate for NIH-3T3 mouse fibroblast cells and found that graphene showed good biocompatibility, even if the underlying substrate did not support cell adhesion and proliferation.[577] In contrast, work by Lee *et al.* found a dose-dependent cytotoxicity of pristine graphene towards embryonic fibroblasts.[578]

The cells used in this thesis are 3T3-Swiss Albino (SA) cell line, which was established in 1962 from Swiss albino mouse embryos, by Green and Todaro.[579] 3T3 cell lines are generally mouse embryonic fibroblasts which show 3-day transfer properties.[579] 3T3 SA cells have been used as feeder cells when culturing human epidermis for burns treatments.[580]

1.10 Stem cells

Stem cells are present in many tissues and are used for renewal of cells following illness, injury or ageing.[407] Mesenchymal stem cells (or stromal cells) are derived from bone marrow. The first evidence of mesenchymal stem cells (MSCs) arose from the work of Friedenstein and co-workers who cultured bone marrow in plastic culture and removed non-adherent cells.[581] They observed that the most adherent cells were spindle like in shape and rapidly multiplied after 2-4 days in culture.[581] Bright field images showing the adherence, proliferation and spindle-like morphology of MSCs can be seen in Figure 1-34.

MSCs can be derived from many sources, as most organs in the body contain stem cells.[390,582] The MSCs used in this thesis are derived from bone marrow, which contains hematopoietic stem cells and MSCs. MSCs are isolated from bone marrow after separation by density gradient centrifugation, to remove unwanted cell types.[407,583] They are normally cultured in medium with 10 % foetal bovine serum, with non-adherent cells removed by changes in media.

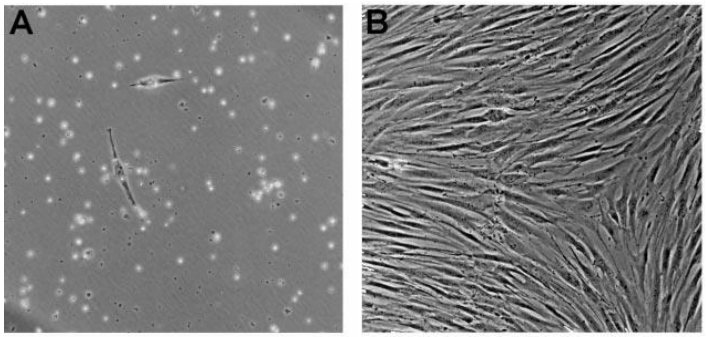

Figure 1-34. isolated marrow stromal cells. At A) 48 hours and B) 10 days after plating. From Pittenger *et al.*[407]

In 2006 Dominici *et al.* and the International Society for Cellular Therapy (ISCT) defined a universal set of criteria to define 'multipotent mesenchymal stromal cells'.[584] The cells must be 'plastic adherent under culture conditions'.[584] The cells must express the CD105, CD73 and CD90 antigens and, to ensure that MSCs are the

only cell type present in the cell population, they must not express antigens observed in other cell types that could be found in MSC culture, including CD45 (pan-leukocyte marker), CD34 (hematopoietic progenitors), CD14 or CD11b (monocytes or macrophages), CD79a or CD19 (B cells) and HLA class II.[584] Typically, MSCs express markers such as CD105 (SH2), CD73 (SH3/4), CD44, CD 90 (Thy-1), CD 71 and stro-1, as well as adhesion molecules such as CD106 (vascular cell adhesion molecule/VCAM-1), CD166 (activated leukocyte cell adhesion molecule (ALCAM)) intercellular adhesion molecule (ICAM)-1 and CD29.[585] The final criterion for MSCs is that they must be able to differentiate to osteoblasts, chondroblast and adipocytes.[584] These three differentiation lineages are described below.

1.10.1. Osteogenic differentiation

Jaiswal *et al.* established a reproducible process for differentiating stem cells into osteogenic lineage by the addition of several factors into Dulbecco's modified Eagle's medium including dexamethasone (optimum concentration of 100 nM), ascorbate-2-phosphate (optimum concentration of 0.05 mM) and β-glycerophosphate (optimum concentration of 10 mM).[586]

Dexamethasone was found by Hamidouch and colleagues to upregulate the four and a half LIM domain 2 protein (FHL2),[587] which leads to the transcription of *Runx2,* a transcription factor which induces the osteoblast phenotype.[588,589] It also regulates the gene for mitogen activated protein kinase (MAPK-1)[587] and dephosphorylates and activates *Runx2.* Ascorbic acid assists in inducing osteogenic differentiation as assists in the formation of collagen I, which is then secreted into the ECM.[587] The collagen 1 and $\alpha_2\beta_1$ integrins interact, also activating MAPK signalling pathways which cause the phosphorylation of *Runx2*.[590] *Runx2* bind to osteocalcin and bone

sialo protein (BSP) gene promoters to induce osteo-specific gene expression.[587] These processes are summarised in Figure 1-35.

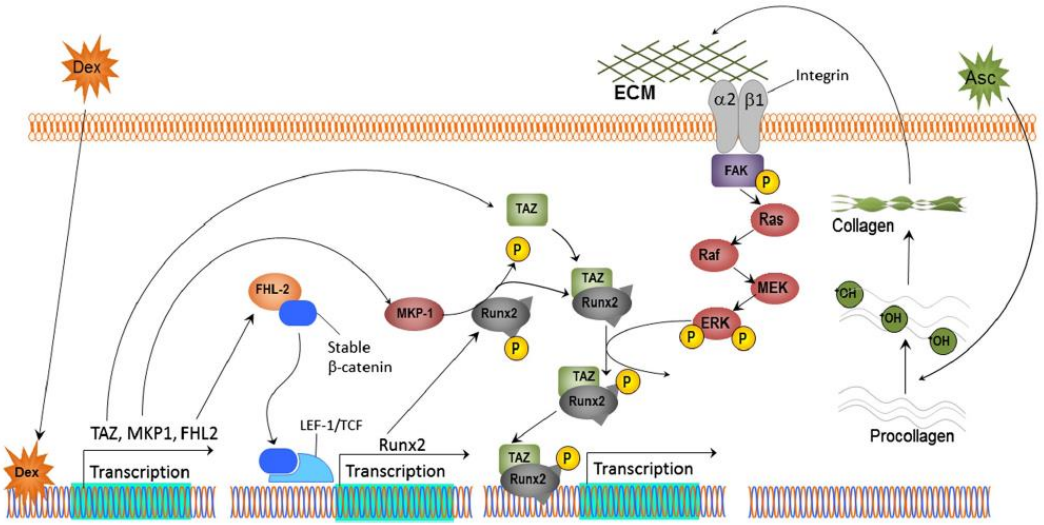

Figure 1-35. Osteogenic differentiation of stem cells by increased transcription of FHL-2. From Lagenbach *et al.*[587]

β-glycerophosphate also plays an important role in inducing osteogenic differentiation. It firstly acts as the phosphate source required to produce hydroxyapatite, a major component of bone. The inorganic phosphate also acts as a signalling molecule to regulate the expression of osteopontin and bone morphogenetic protein 2 (BMP2), which has an important role in bone formation as it is involved in a variety of signalling pathways involved in otseogenesis.[590,591,592]

The extent of osteogenic differentiation of hMSCs can be measured by looking at alkaline phosphatase activity, the increase in mineral deposits of the matrix and osteocalcin production.[586,593] Gene expression which can also indicate osteogenesis include increased expression of BSP, osteopontin and BMP2.

1.10.2. Chondrogenic differentiation

Chondrogenic differentiation can be induced by placing MSCs into pellet cultures with media containing dexamethasone, ascorbic acid, insulin, transferrin, sodium selenite, sodium pyruvate and transforming growth factor β (TGF-β).[594]

Chondrogenesis can be detected by toluidine blue metachromasia and detection of type II collagen.[595]

TGF-β increases the N-Cadherin levels in the cell which assists with cell-cell adhesion and forms the pellet needed for chondrogenesis.[596] TGF-β also stimulates the deposition of cartilage specific molecules such as aggrecan and type II collagen.[597] TGF-β stimulates the initial stages of chondrogenesis but represses chondrocyte terminal differentiation.[596] Ascorbic acid is shown to initiate chondrogenesis through cartilage matrix production.[598]

1.10.3. Adipogenic differentiation.

Adipogenic differentiation can be induced using media containing dexamethasone (0.5-1 mM optimum concentration), indomethacin (60 mM optimum concentration), isobutylmethylxanthine (0.5 mM optimum concentration), and insulin (10 μg mL^{-1}).[407] Signalling pathways for adipogenesis centre around the regulation of peroxisome proliferator activated receptor γ (PPARγ) activity and/or expression,[599] with most adipogenic factors activating PPARγ expression or activity.[599] PPARγ is a nuclear protein which binds to genes involved in adipogenesis, activating transcription.[599] Some of the important pathways involved in adipogenesis are shown in Figure 1-36.

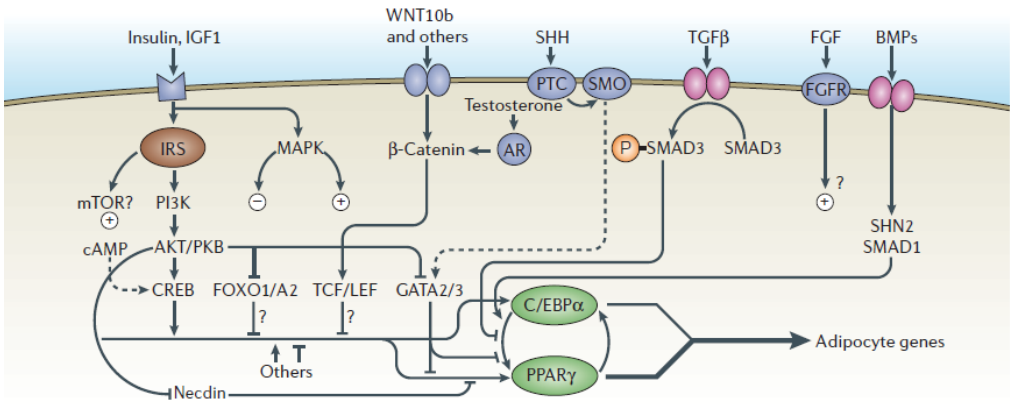

Figure 1-36. Pathways to adipogenesis. From Rosen and MacDougald.[599]

Insulin acts through the insulin growth-factor-1 (IGF1) receptor signalling.[599] Insulin receptor substrates (IRS) are downstream of the IGF1 receptors and the IRS signalling promotes CREB phosphorylation which is important for adipogenesis.[600] Indomethacin has been found to promote adipogenesis by binding to and activating PPARγ, as well as decreasing the amount of β-catenin, a molecule which blocks PPARγ activation.[601,602] Both dexamethasone and isobutylmethylxanthine are thought to regulate the activity of pre-adipocyte factor 1 (PREF-1), a transmembrane protein which inhibits adipocyte differentiation.[603,604] They also help to activate the expression of PPARγ.[604,605]

1.11 Research outline

The extensive use of GO in biological applications arises because of its aqueous stability, but also the presence of oxygen-containing functional groups, which provide sites at which to covalently attach biomolecules. The topological and chemical defects on GO result in the loss of many of the favourable electronic and mechanical properties of graphene. Examples of 'pristine graphene' (with low oxygen content) in biological applications, on the other hand, are limited. The absence of functional groups leads to poor aqueous stability and means that the primary method of decorating pristine graphene sheets is by non-specific, basal-plane adsorption or by functionalising the basal plane of graphene, which causes damage to the graphene sheet.

After analysis of the current literature of functionalised graphene, it became clear that there was a requirement for a functionalisation that would enable greater use of 'pristine graphene' in biological applications, by improving the aqueous dispersibility of the pristine graphene and provide binding sites for the attachment of biological molecules, while preserving the desirable properties of the graphene sheet. The main existing example of such functionalisation, the edge functionalisation via ball milling, causes violent sparking. In addition, the percentage functionalisation is high for some of the ball milled functionalised graphenes, indicating that the graphene sheets have a lot of defects.[233] A novel graphene functionalisation method was investigated as a potential solution to this problem, based upon electrophilic aromatic substitution. This type of functionalisation, by its nature, is only possible at edge or defect sites on graphene sheets, therefore leaving most of the graphene sheet intact. In addition to the graphene functionalisation, the attachment of tracers and

fluorophores was attempted on the functionalised sheets, to demonstrate potential future applications of the functionalisation. As a further investigation, three differently functionalised GFNs were incorporated into layer-by-layer (LbL) constructs, for potential tissue engineering applications. The biocompatibilities of the GFN-LbL constructs towards 3T3 Swiss Albino (3T3 SA) fibroblast cells and human mesenchymal stem cells (hMSCs) were compared., to assess the effect of different functionalisations on cell behaviour. The differentiation of hMSCs on these LbL constructs was also analysed and compared to literature to ascertain the effect of GFN functionalisation on stem cell fate.

The principal research aims were to:

- Create an edge-specific functionalisation of pristine graphene, which leaves the basal plane of graphene intact.
- Attach biologically relevant molecules to functionalised graphene.
- Incorporate different functionalised GFNs into LbL constructs.
- Assess the biocompatibility of functionalised GFN LbL constructs towards a 3T3 SA fibroblast cell line.
- Assess the adhesion, proliferation and differentiation of hMSCs on the functionalised GFN LbL constructs.

2 MATERIALS AND METHODS

2.1. Graphene production

A solution of 4 mg mL^{-1} graphite flakes (Branwell Graphite, Ltd Grade 2369), dispersed in *N*-Methylpyrrolidone (NMP, VWR chemicals, 99 %), was sonicated at 37–100Hz for 48 hours in an ultrasonic bath (Elmasonic PH750EL, Elma), fitted with a copper cooling coil (water cooled copper for BLE-130/220, Fisher Scientific) for temperature regulation. After 48 hours, the solution was transferred to centrifuge tubes and centrifuged at 400 rpm for 20 mins (Eppendorf centrifuge-5810R). After 20 mins' centrifugation, only the top half of the supernatant was retained for subsequent runs, eliminating the denser, multilayered flakes of graphene. The centrifugation/elimination steps were repeated three times. After the final centrifugation run, the resultant graphene suspension was filtered under vacuum through an Anodisc filter (0.02 μm pore size, 47 mm, Whatman) and dried overnight. The graphene powder was then re-suspended in water and freeze dried (HETO Powderdry LL1500 Freeze Dryer, Thermo Electron Corporation) to produce graphene powder.

2.2. Graphene edge-functionalisation

The synthetic route to the thiol functionalisation of graphene is shown in Figure 2-1.

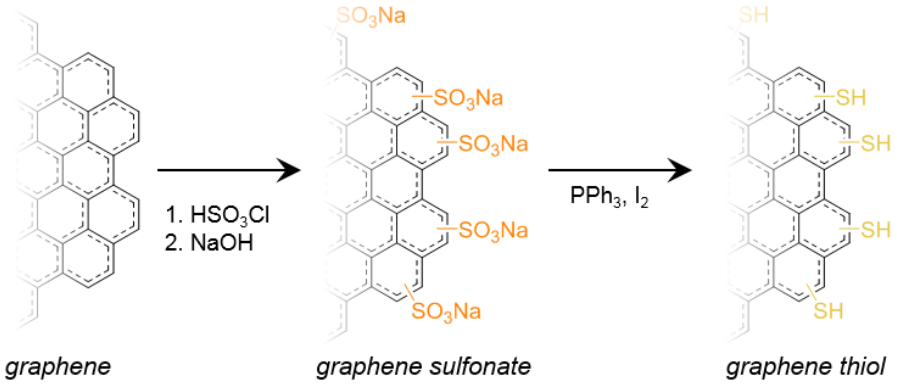

Figure 2-1. Scheme depicting the synthetic steps to graphene thiol.

2.2.1. Synthesis of graphene sulfonate

100 mL graphene dispersion (1 mg mL^{-1} in DMF) and 10 mL chlorosulphonic acid (Fluka, 99 %) were mixed in a 250 mL round-bottomed flask, heated to 55 °C (with stirring) and left to react overnight. The mixture was poured over ice and the conversion from graphene chlorosulfonate to graphene sulfonate (G-SO_3) effected by increasing the pH to 10, by the addition of NaOH (Fisher chemical, ≥ 97 %). The mixture was left to react at room temperature for 30 mins, after which the solution was neutralised, vacuum filtered through an Anodisc filter (0.02 µm pore size, 47 mm, Whatman) and washed with water. The resultant G-SO_3 powder was resonicated into water and freeze dried (HETO Powderdry LL1500 Freeze Dryer, Thermo Electron Corporation).

2.2.2. Reduction of graphene sulfonate to graphene thiol

The freeze-dried graphene sulfonate powder was dissolved into 15 mL anhydrous toluene (Sigma-Aldrich, 99.8 %), and sonicated under a nitrogen atmosphere in a two-necked flask. 2.5 g triphenylphosphine (Sigma, 99 %) and 200 mg iodine (Aldrich, 99.99 %) were added, the reaction mixture heated to 80 °C and the reaction left overnight. The solution was then cooled to room temperature and water added. The solution was vacuum filtered through an Anodisc filter (0.02 µm pore size, 47

mm, Whatman), resonicated into water and freeze dried (HETO Powderdry LL1500 Freeze Dryer, Thermo Electron Corporation).

2.2.3. Characterisation of graphene and functionalised graphene

2.2.3.1 UV-visible spectroscopy

UV-visible spectroscopy was taken on a Cary 300 UV-visible spectrometer using a quartz cuvette. As-prepared graphene samples in NMP (of unknown concentration), obtained from the final centrifugation run of the liquid exfoliation method (laboratory reagent grade, Fluka), were diluted from 25 % to 1 % of the as-produced concentration. The absorbance was recorded at 660 nm and the extinction coefficient of graphene in NMP (2460 L g^{-1} m^{-1} at 660 nm)[61] used to determine the graphene concentration.

2.2.3.2 Transmission electron microscopy

Graphene samples produced by ultrasonic exfoliation were dispersed in ethanol to an approximate concentration of 0.1 mg mL^{-1} and drop casted onto a holey carbon grid (Agar Scientific). Bright field TEM images were recorded using a T2 G2 ChemiSTEM operating at 80 kV.

2.2.3.3 Raman spectroscopy

Raman samples were prepared by vacuum filtration of 10 mL of 1 mg mL^{-1} solution (in ethanol) of graphene onto Anodisc filter. This was left to dry overnight. The Raman used was Renishaw RM MK1 system 200 with Wire 3.3 software, giving 1 cm^{-1} spectral resolution. A 633 nm HeNe laser was used and the laser set at 5 % (0.048 mW), with a Si reference for calibration (520 nm).

2.2.3.4 X-ray photoelectron spectroscopy

X-ray photoelectron spectroscopy samples were prepared from suspension in ethanol, which was vacuum filtered through an Anodisc filter (0.02 µm pore size, 47

mm, Whatman), through a 1.5 cm diameter funnel, to obtain uniform cake sizes. X-ray photoelectron spectroscopy (XPS) data was acquired on a home-built XPS operating at

10^{-9}-10^{-10} Torr, using an Al Kα source (1486.6 eV) at 10 kV anode potential and 10 mA emission current (Oxford University). All peak fitting was done using XPS Peak Fit (v. 4.1) software, using common protocols (e.g., Shirley backgrounds). The reported binding energies have an error of ± 0.25 eV, based on calibration to the C 1s peak.

2.2.3.5 Fourier transform infrared spectroscopy

Fourier transform infrared spectroscopy (FTIR) was performed on a Nicolet 5700 FTIR spectrometer (Thermo Electron Corporation, average spectral resolution 1 cm^{-1}), by mixing ~ 0.1 mg graphene powder with 10 mg KBr powder (FTIR grade, > 99 %, Sigma Aldrich), which was ground and pressed into a pellet. 25 Scans were performed.

2.2.3.6 BET analysis

BET samples were prepared by freeze-drying graphene, G-SO_3 and G-SH powders. BET analysis was performed on a Micromeritics ASAP 2020 Surface area and porosity analyser. Degassing with Ar was undertaken prior to measurement. Adsorption isotherms were measured from 0.01 P/P_0 to 0.955 P/P_0 using a 100-point analysis. Desorption was run from 0.995 to 0.1 P/P_0.

2.2.3.7 Contact angle measurements

10 mL of 1 mg mL^{-1} graphene, G-SO_3 and G-SH solutions were filtered onto Anodisc filters and left to dry overnight. Contact angle measurements were recorded on a Drop Shape Analyser DSA100 (KRUSS) by dropping a ~ 10 μL water droplet onto the powdered graphene sample, with the angle recorded using Sessile analysis.

2.2.3.8 Dispersibility measurements

Dispersibility measurements were performed by dispersing graphene, G-SO_3 and G-SH powders at a concentration of 1 mg mL^{-1} in water, ethanol (VWR chemicals, analytical reagent grade), toluene and cyclohexane (99.5 %, Sigma-Aldrich) and were left overnight. Images were taken using a digital camera.

2.2.3.9 Thermogravimetric analysis

Thermogravimetric analysis was performed on a Q series™ TM Q500 thermogravimetric analyser. 1–3 mg of freeze-dried graphene was heated at 10 °C min^{-1} in an N_2 atmosphere.

2.3. GFN-containing layer-by-layer constructs

For the graphene-family nanomaterial layer-by-layer constructs, commercial source of graphene was used. The justification for the change of source was due to the significant decrease in production time required for the graphene starting material, which generally took up to a week to complete. In addition, the commercial source was more able to allow for any batch-to-batch variation which may occur among researchers using the sonochemical exfoliation method, as vessel sizes, human error and other parameters can affect the quality of graphene produced. The use of commercial source of graphene was considered as an advantage when advancing towards clinical applications, as the solvent usage was a concern in the production of graphene. In addition, the commercial source of graphene was a more economically viable means of producing the large quantities of graphene required for continued research. The selected commercial source was chosen to be comparable to that produced by the sonochemical method in terms of layer number and lateral

dimensions. The starting commercial graphene material was characterised by Raman before use in the LbL constructs to confirm the size and defects.

2.3.1. Synthesis of graphene oxide

Graphene oxide (GO) was synthesized by a modified Hummers method from Thomas *et al.*[606] 85 mL H_2SO_4 (Fisher Scientific, 95 %) was cooled in an ice bath, after which 2.5 g graphite (10 mesh, VWR chemicals) and 2.25 g $NaNO_3$ (Sigma-Aldrich) were added under stirring. 11.25 g $KMnO_4$ (Fluka) was slowly added to the mixture, maintaining the temperature below 10 °C. The mixture was stirred at room temperature for 5 days, after which it was poured slowly into 500 mL 5 wt. % H_2SO_4 (in H_2O) and stirred for 3 hours. 45 mL H_2O_2 (30 % in H_2O, Merck) was added and the mixture stirred for 2 hours, after which it was poured into 500 mL of 3 wt. % H_2SO_4/0.5 wt. % H_2O_2 and stirred for 2 days.

The mixture was centrifuged at 4000 rpm for 20 mins and the solid redispersed in 500 mL 3 wt. % H_2SO_4/0.5 wt. % H_2O_2, before further centrifugation. This redispersion-centrifugation method was repeated 4 times with 3 wt. % H_2SO_4/0.5 wt. % H_2O_2 and 4 times with de-ionised H_2O, the resulting aqueous GO dispersion was freeze-dried and the solid product redispersed into 2L H_2O. 1.2 g NaOH (Fisher Scientific) was added with stirring, after which the mixture was heated to reflux for 30 mins. The mixture was then centrifuged at 12,500 rpm for 30 mins and the collected solid washed in water and redispersed into 2L dilute HCl (37 %, Fisher scientific) and was heated to reflux for 30 mins. The mixture was then centrifuged, washed with water and freeze-dried to obtain the base-washed graphene oxide solid (GO).

2.3.2. Production of sulfonated graphene oxide

100 mg GO was dispersed in 100 mL N-methyl pyrrolidone (NMP, Fluka) and cooled under an ice bath. 4 mL chlorosulfonic acid (98 %, Fluka) was added dropwise, with stirring. The mixture was then heated to 55 °C overnight. The mixture was poured onto ice, filtered and washed with water. The product was redispersed in water and 1 g NaOH added. The mixture was sonicated for 2 hours before being filtered through an Anodisc filter (0.02 µm pore size, 47 mm, Whatman), washed with water and freeze-dried, to produce sulfonated graphene oxide (GO-SO_3).

2.3.3. Production of graphene sulfonate

Graphene sulfonate was prepared using the method outlined in 2.2.1. In this instance, the starting graphene material was purchased from XG sciences (C 750, average surface area 750 m^2 g^{-1}, < 5 layers, submicron lateral dimensions).

2.3.4. Characterisation

2.3.4.1 CHNS analysis

CHNS analysis was conducted at the microanalysis service (dept. Chemistry, University of Manchester) using a Thermo Scientific Flash 2000 Organic Elemental Analyser. A modified Dumas method of dynamic flash combustion was adopted. GO, GO-SO_3 and G-SO_3 were weighed, placed in tin capsules and exposed to a small amount of pure oxygen, at 900-1000 °C, to drive combustion. The combustion resulted in the conversion of the sample into gases (CO_2, H_2O, nitrogen oxides, and SO_2), which were then flowed through separation columns and a thermal conductivity detector used to determine the empirical elemental composition of the samples.

2.3.4.2 Zeta-potential measurements

Aqueous dispersions of GO, GO-SO_3 and G-SO_3 were prepared at 0.1 mg mL^{-1}. Aqueous solutions of polyethyleneimine (PEI, 50 % w/v in H_2O, Fluka) and polystyrene sulfonate (PSS, M_w ca. 70 kDa, Sigma-Aldrich) were prepared at a concentration of 10 mg mL^{-1}. Zeta-potential measurements were performed using a Malvern Zetasizer, Nano series.

2.3.4.3 Raman spectroscopy

Samples were prepared by filtering 10 mL of 1 mg mL^{-1} solutions (in H_2O) onto Anodisc filters. Raman spectroscopy was performed using Renishaw inVia Raman spectrometer with a 633 nm HeNe excitation laser.

2.3.4.4 Infrared spectroscopy

Fourier transform infrared spectroscopy (FTIR) was performed on a Nicolet 5700 FTIR spectrometer (Thermo electron corporation), by mixing < 0.1 mg GO, GO-SO_3 or G-SO_3 powder with 10 mg KBr powder (FTIR grade, > 99 %, Sigma-Aldrich) and grinding into pellet.

2.3.4.5 Dispersibility measurements

Working solutions of polyethyleneimine (PEI) and polystyrene sulfonate (PSS) were prepared at a concentration of 10 mg mL^{-1} in water and solutions of GO, GO-SO_3 and G-SO_3 were made at a concentration of 0.1 mg mL^{-1}. Pictures were taken of the solutions after being left to stand for 24 hours.

2.3.5. Preparation of graphene-containing layer-by-layer constructs.

The positively charged counter layer for the graphene-family nanomaterial (GFN) - containing LbL constructs was polyethyleneimine (PEI), which was selected because of its reported antibacterial properties,[607,608] reported to arise from the perturbation of the negatively charged bacterial membrane upon contact with the positively charged

surface, which is thought to increase the permaeability of the membrane and cause leakage from the cytoplasm.[607,609,610]

meaning that it is suitable for tissue engineering applications. GFN-containing LbL constructs were characterised by various methods including AFM, contact angle measurements, UV-visible spectroscopy, Raman mapping and bright field imaging.

2.3.5.1 Pre-treatment

13 mm circular glass coverslips were cleaned using a mixture of 5:1:1 (v:v:v) water: ammonia (35 % Fisher Scientific): H_2O_2 (30 %, Fisher), heated to 75 °C for 5 mins, rinsed with Milli-Q water, dried under N_2 and placed in a UV/Ozone cleaner for 15 mins. Coverslips were then immersed in 3-(Trihydroxysilyl) propane-1-sulfonic acid THSPS (5 % in EtOH, Fluorochem) overnight, to form a negatively charged THSPS layer

2.3.5.2 Solution preparation

10 mg mL^{-1} solutions of PEI (M_w ca 750,000, branched chain polymer with 1:2:1 ratio of primary:secondary:tertiary amines, with a branching site every 3-3.5 nitrogen atoms, 50 % w/v in H_2O, Fluka) and PSS (M_w ca. 70 kDa, Sigma-Aldrich) were prepared in H_2O. 0.1 mg mL^{-1} dispersions of graphene oxide (GO), sulfonated graphene oxide (GO-SO_3) and graphene sulfonate (G-SO_3) were prepared in H_2O.

2.3.5.3 Layer-by-layer procedure

Coverslips were placed in vertical racks and, for all LbL constructs, were immersed initially in PEI for 5 mins, after which coverslips were washed with H_2O and dried with N_2. Coverslips were immersed in alternating positively and negatively charged solutions in this manner for 5 mins each, with a H_2O wash and N_2 dry between each immersion. The composition of the LbL constructs is outlined in Table 2-1.

NB: The (+) and (-) notation in PEI/PSS(+) and PEI/PSS(-) denote the charge of the terminal layer. PEI/PSS(+) terminates with PEI, thus having a positively charged terminal layer; PEI/PSS(-) terminates with PSS, thus having a negatively charged terminal layer.

Table 2-1. Composition of the layer-by-layer constructs

Surface	Components	Positive layer	Negative Layer	# layers	Terminal layer
Glass	N/A	N/A	N/A	N/A	N/A
PEI/PSS (+)	PEI, PSS	PEI	PSS	7	PEI
PEI/PSS (-)	PEI, PSS	PEI	PSS	6	PSS
PEI/GO	PEI, GO	PEI	GO	6	GO
PEI/GO-SO_3	PEI, GO-SO_3	PEI	GO-SO_3	6	GO-SO_3
PEI/G-SO_3	PEI/ G-SO_3	PEI	G-SO_3	6	G-SO_3

2.3.6. Characterisation of layer-by-layer constructs

2.3.6.1 Images of the as-prepared layer-by-layer constructs

After preparation of the LbL constructs, images were taken of the as-prepared LbL constructs on a white background, to observe the colour change associated with the formation of the LbL constructs. Images were acquired with iPhone camera.

2.3.6.2 Bright field images of the as-prepared layer-by-layer constructs.

Bright field images were taken of the as-prepared LbL constructs using an EVOS*xl* transmitted light microscope (AMG).

2.3.6.3 Raman mapping

GFN-containing LbL constructs were prepared on Si/SiO_2 wafers (300 nm oxide thickness), with 15 bilayers. This was due to the long accumulation time needed for the Raman map. Raman was performed using a Renishaw inVia spectrometer, using a 633 nm HeNe excitation laser set at 5 % power (0.048 mW), with a Si reference for calibration. Raman mapping was performed over an area of 50 μm x 50 μm, with 0.5 μm step, using static scanning centre at a Raman shift of 1400 cm^{-1}.

2.3.6.4 Atomic force microscopy

Atomic force microscopy (AFM) was performed using an Asylum MFP-3D in tapping mode. Images were processed using the Gwyddion software. Data was levelled by a mean plane subtraction, and horizontal scar correction was performed. LbL constructs were prepared on Si/SiO_2 wafers.

2.3.6.5 Contact angle measurements

Contact angle measurements were recorded on a Drop Shape Analyzer DSA100 (KRÜSS*)*, by placing a 20 μL water droplet onto the LbL construct and the angle recorded. Sessile analysis was performed.

2.3.6.6 UV-Visible measurements

UV-Visible measurements were taken using Agilent Cary 60 between 200-800 nm on the LbL constructs after each graphene-containing layer was added.

2.4. Functionalisation of graphene thiol with AllylDO3A

Magnetic resonance imaging (MRI) is based upon the change in distribution of magnetic moments of protons when placed in a magnetic field.[611] The return of magnetic moments to their 'ground state' is what causes the signal.[611] Contrast agents are used to speed up the relaxation time back to the ground state, therefore increasing the signal intensity.[611] In water, relaxation arises from magnetic interactions between neighbouring protons.[612] Many contrast agents are paramagnetic species that bind water molecules, exchanging them with water molecules in solution, thus enabling quicker relaxation of the water molecules.[612] Gd^{3+} is a common contrast agent which has 7 unpaired electrons, so can shorten the relaxation time of water significantly.[612] However, Gd^{3+} is extremely toxic as a naked ion, meaning that, to be used in imaging, it must be stabilised.[613] Cyclen, a

macrocyclic tetraamine, and its derivatives are used to stabilise Gd^{3+} and other lanthanide ions by trapping them within the central cavity, resulting in stable lanthanide ion complexes.[614] Complexes based upon cyclen-1,4,7,10-tetraacetic acid (DOTA) possess high thermodynamic stability and kinetic inertness,[615] as well as long half-lives, which are favourable for MRI.[616,615] The attachment of a DOTA derivative to graphene therefore would provide a means by which to monitor its distribution. A DOTA-derivative, cyclen-1-allyl-4,7,10-triacetic acid (AllylDO3A), was synthesised and attached to G-SH thiol-ene coupling using benzoyl peroxide. In addition, to demonstrate the attachment of AllylDO3A to graphene thiol, Eu^{3+} was added into the AllylDO3A, prior to attachment, as Eu^{3+} shows distinct Laporte forbidden and $\Delta l = \pm 1$ f-f emission bands, which can therefore confirm the addition of Eu^{3+} to the AllylDO3A. The resultant complex was viewed under TEM, as the Eu^{3+} causes high contrast, providing a means by which confirm the presence of Eu^{3+}/AllylDO3A on the G-SH sheet.

Flash silica chromatography was performed using silica gel (Sigma-Aldrich) 40 - 63 μm 60 Å. The solvent mixtures used are reported in individual procedures. All reactions were carried out with under dry conditions in an inert nitrogen atmosphere using a nitrogen balloon, unless otherwise stated. Reaction temperatures of 0 °C were achieved using an ice water bath. Room temperature refers to 20-25 °C.

2.4.1. AllylDO3A synthesis

The AllylDO3A was synthesised according to the paper by Schumann and Kuse.[617] The reaction to produce AllylDO3A and its attachment to G-SH is shown in Figure 2-2.

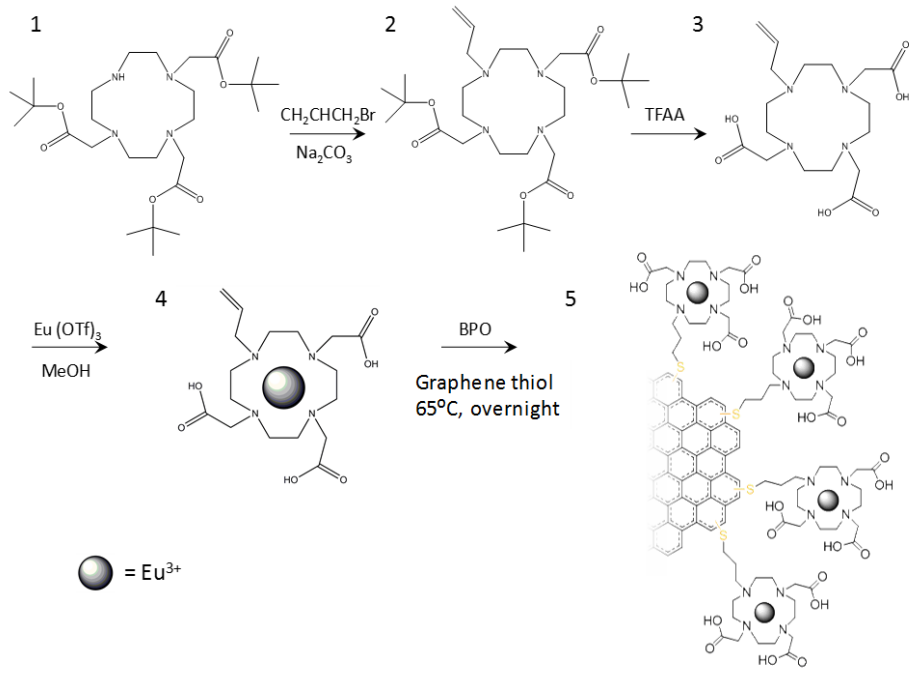

Figure 2-2. Synthetic steps to produce AllylDO3A and attachment to G-SH. 1) DO3A-tBu, 2) AllylDO3A-tBu 3) AllylDO3A 4) Eu^{3+}/AllylDO3A 5) Eu^{3+}/DO3A-$(CH_2)_3$-(G-SH).

2.5.1.1 AllylDO3A-tBu synthesis

100 mg DO3A-tritertbutylester (DO3A-tBu,122555-91-3, CheMatech) was dissolved in 1.5 mL DMF. 21.5 mg CH_2CHCH_2Br (15.4 µL, ReagentPlus, 99 %, Sigma-Aldrich) and 34 mg Na_2CO_3 (BioXtra ≥ 99 %, Sigma-Aldrich) was added and stirred at 80°C. The solution was cooled to room temperature and evaporated in vacuo. Chloroform (Sigma-Aldrich, ACS grade) was added and the solution filtered, after which the solution washed with NH_4Cl (99.998 %, Sigma-Aldrich) three times and once with brine. The filtrate was evaporated in vacuo and crude NMR taken. The product was columned in dichloromethane (DCM, Sigma-Aldrich, analytical standard), moving up to 10 % methanol (ACS grade, Fisher scientific) in DCM.

2.5.1.2 AllylDO3A-tBu deprotection to AllylDO3A

70 mg of AllylDO3A-tBu was dissolved in 1 mL DCM, and 1 mL trifluoroacetic acid (ReagentPlus, 99 %, Sigma-Aldrich) was added and the reaction stirred

overnight. The product was then washed with water and ethanol, before being concentrated *in vacuo*.

2.4.2. Europium insertion to AllylDO3A

48 mg $Eu(OTf)_3$ (from Louise Natrajan group) was added to 30 mg AllylDO3A, in 0.5 mL methanol. The reaction was left to react at 50 °C, overnight. The product was then concentrated in vacuo and added to Et_2O (analytical standard, Sigma-Aldrich) at 0 °C. The resultant solution was concentrated in vacuo to obtain Eu^{3+}/AllylDO3A, which was dissolved in methanol for NMR.

2.4.3. Attachment of Eu^{3+}/Allyl DO3A to graphene thiol

Eu^{3+}/AllylDO3A was added to 2 mL 0.4 mg mL^{-1} G-SH, to obtain a concentration of 1 mM. A spatula of benzoyl peroxide (> 97 %, Sigma-Aldrich) was added and the reaction heated to 55 °C, overnight. The reaction was then quenched with sodium sulphite (BioXtra ≥ 98 %, Sigma-Aldrich) and the solution filtered and redispersed in methanol.

2.4.4. Nuclear magnetic resonance

^1H NMR experiments were carried out using a Bruker Avance 400. Chemical shifts (δ_H) are given in parts per million (ppm) to the nearest 0.01 ppm and referenced to the residual non-deuterated solvent peak. The coupling constants (*J*) are given to the nearest 0.1 Hz. Spectral data is reported as follows: chemical shift, integration, multiplicity, coupling constant(s) and assignment. Multiplicity is described using the following abbreviations: s, singlet; d, doublet; t, triplet; q, quartet; quin, quintet; m, multiplet; or as a combination of these dd, dt etc.

2.4.5. Fluorimetry measurement of Eu^{3+}/ AllylDO3A

Measurements were taken on a LP980 Spectrometer (Edinburgh instruments). Eu^{3+}/AllylDO3A was dissolved at a concentration of 10^{-4} M in methanol. Excitation

was set at 325 nm and emission scanned from 600-800 nm, using 1 nm step, 0.2 secs dwell, Excitation band width: 5 nm, Emission bandwidth: 3 nm, 5 scans.

2.4.6. Transmission electron microscopy images of conjugates

TEM samples were made by preparing samples in ethanol at a concentration of 0.1 mg mL^{-1} and drop casting on to a copper grid (Agar Scientific). TEM measurements were conducted using a T2 G2 ChemiSTEM, operating at 80 kV.

2.5. Production of glycographene and concanavalin A attachment

Lectins are sugar-binding proteins, which can therefore function as cell recognition molecules.[410,411] The attachment of a lectin to functionalised graphene would therefore demonstrate the attachment of a cell-specific targeting molecule to edge-functionalised graphene. The lectin concanavalin-A (conA), which binds glycoproteins,[412] was selected. A fluorescein isothiocyanate (FITC)-labelled-conA was attached to CVD graphene thiol (G-SH) by first attaching mannose groups to CVD G-SH using click chemistry, with the mannose/G-SH complex termed 'glycographene'. FITC-labelled conA was then incubated with CVD glycographene. The glycographene-lectin bioconjugate was then viewed under fluorescence microscopy, to confirm the presence of the bioconjugate on the CVD graphene sheet. The reaction scheme for production of glycographene and concanavalin A attachment are shown in Figure 2-3.

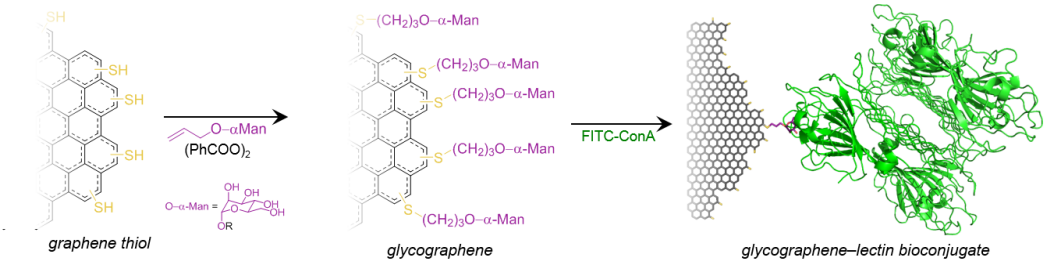

Figure 2-3. Reaction scheme to produce glycographene and concanavalin-A-functionalised graphene.

2.5.1 CVD graphene synthesis

CVD graphene was purchased from 2D tech, Ltd. Uniform polycrystalline films of bilayer graphene (1 cm x 1 cm) were grown by CVD and transferred to Si/SiO_2 wafers (290 nm thickness).

2.5.2 CVD graphene sulfonate functionalisation

8 mL anhydrous DMF (Sigma-Aldrich, 99.8 %) and 2 mL chlorosulfonic acid were mixed in a glass vial. The CVD graphene sample was left to react in the mixture overnight. The CVD graphene sample was rinsed with acetone and water and transferred immediately into the next reaction vial for hydrolysis of the CVD graphene chlorosulfonate. A sodium hydroxide solution (pH 10) was prepared and 10 mL was transferred to a glass vial. The CVD graphene chlorosulfonate sample was left in the sodium hydroxide solution for 15 mins and rinsed immediately with water and acetone. The resultant CVD G-SO_3 sample was dried in an N_2 gas stream and stored at ambient temperature.

2.5.3 CVD graphene thiol

4.6 g (10 mmol) triphenylphosphine (PPh_3, 99 %, Sigma) was dissolved in anhydrous toluene (99.8 %, Sigma-Aldrich) and heated to 90 °C. 300 mg (0.6 mmol) I_2 (99.99 %, Sigma-Aldrich) was added under stirring. The stirrer was stopped, the flask opened under a strong N_2 counter flow and the CVD G-SO_3 added. The

mixture was kept in a nitrogen atmosphere and heated to 90 °C overnight. The CVD 'glycographene' sample was rinsed with acetone, water and ethanol, dried in a nitrogen gas stream and stored at ambient temperature.

2.5.4 'Glycographene' synthesis

Allyl alcohol (125 mL, 1.84 mol, > 95 %, Sigma Aldrich) was cooled to 0 °C, after which acetyl chloride (10 mL, 14.0 mmol, > 99 %, Sigma Aldrich) was added in drops, and the mixture was stirred at 0 °C for 1 h. After heating to 70 °C, mannose (10.0 g, 55.6 mmol, > 99 % Sigma Aldrich) was added and the reaction was stirred under reflux for 5 h. It was neutralized with sodium hydrogen carbonate and filtrated. After three co-distillations with toluene, the solvent was removed and the crude product was purified by flash column chromatography on silica (EtOAc/MeOH, 8:2).

150 mg (682 µmol) allyl mannoside and 1 spatula benzoyl peroxide (> 97 %, Sigma-Aldrich) were dissolved in ethanol. A CVD graphene thiol sample was added to the reaction vial and the mixture was heated to 65 °C overnight. The CVD graphene sample was rinsed with ethanol, water and acetone, dried in a nitrogen gas stream and stored at ambient temperature.

2.5.5 Attachment of FITC-labelled concanavalin A to CVD glycographene

FITC-labelled Concanavalin A (conA, from *Canavalia ensiformis*, Type IV, lyophilised powder, Sigma Aldrich) was dissolved in binding buffer (20 mM Tris, 500 mM NaCl, 1 mM $CaCl_2$, 1 mM $MgCl_2$, pH 7.2) in a glass vial wrapped in aluminium foil. The CVD glycographene sample was added to the vial incubated at 37 °C for 2 hours. The sample was then rinsed with water and dried under N_2 gas.

2.5.6 Removal of FITC-labelled Concanavalin-A from CVD glycographene

CVD glycographene/FITC-conA was incubated in with an excess of methyl mannoside (acquired from the Flitsch group) for 2 hours, after which the sample was washed with water and dried under N_2 gas.

2.5.7 Epifluorescence microscopy images of FITC-conA on CVD glycographene

Fluorescence images were collected on a BX51 microscope using UPlanFLN objectives and captured using a Coolsnap camera (Photometrics) through MetaVue Software (Molecular Devices). A specific band pass filter set for FITC (excitation BP480/40, dichroic Q505LP, emission 535/50) was used.

2.6. 3T3 fibroblast cell viability studies on LbL constructs

2.6.1 Cell growth and delamination

3T3 Swiss Albino (3T3 SA) cells (ECACC 85022108) were purchased from the European Collection of Authenticated Cell cultures. 3T3 SA cells were grown up in Dulbecco's Modified Eagle's medium (DMEM, 4500 mg L^{-1} glucose, sterile filtered, Sigma Aldrich), enriched with 10 % foetal bovine serum (FBS), in T25 and T75 flasks (CELLSTAR). Once approximately 80 % confluence was achieved, media was removed from flasks and the flasks were washed with Dulbecco's Phopshate buffer saline (PBS, sterile filtered, Sigma). 1 mL trypsin (Sigma, 0.05 % trypsin, 0.02 % ethylenediaminetetraacetic acid) was added to the flasks to encourage cell delamination. The flasks were then incubated at 37 °C for 2-3 mins, after which the free cells were suspended in 10 mL of fresh media. The resultant cell solution was centrifuged at 1500 rpm for 5 mins, and the cell pellet suspended in 10 mL fresh media.

2.6.2 Cell counting

The cell membranes of live cells do not allow certain dyes to enter cells.[618] An example is trypan blue, which is negatively charged, meaning that the dye is only able to penetrate cells if the cell membrane is damaged, when they are dying or dead.[618] Cells are stained with trypan blue, after which the cell-containing solution is pipetted into a haemocytometer. Haemocytometers are microscope slides with rectangular indentations. These indentations form a chamber into which the solution moves, and this chamber is a grid of perpendicular lines. The volume of the chamber is known and thus makes it possible to count the number of cells in a small volume of fluid.

10 μL of trypan blue solution (0.4 % in 0.81 % NaCl, 0.06 % Potassium phosphate, dibasic, sterile filtered, Sigma) was combined with 10 μL of the fresh cell/media solution in a sterile Eppendorf tube. 10 μL of this solution was added to either side of a C-Chip haemocytometer and viewed using the 10 x objective lens.

2.6.3 Cell expansion and seeding

After cell counting, the 10 mL cell solution was diluted with the same volume of media and 10 mL of this diluted solution added to two new T25 flasks. For growing into larger flask sizes, recommended seeding densities were used. To expand the cells this procedure was repeated, increasing the number of flasks after each passage, until the required number of cells was achieved. Cells were seeded onto LbL constructs at a density of 50,000 cells per well (~38,000 cells per cm^2) into 24-well plates (CELLSTAR) and incubated at 37 °C, 5 % CO_2.

2.6.4 LIVE/DEAD assay for cell viability

The LIVE/DEAD Assay kit is made up of two components: calcein-AM and ethidium homodimer-1. The calcein-AM component is a marker for intracellular esterase activity. Acetoxymethyl ester hydrolysis is performed by intracellular esterases transforming the calcein-AM, which does not fluoresce to the green fluorescent calcein. As dead cells lack active esterases, only live cells are labelled by calcein-AM. The ester hydrolysis is shown in Figure 2-4.

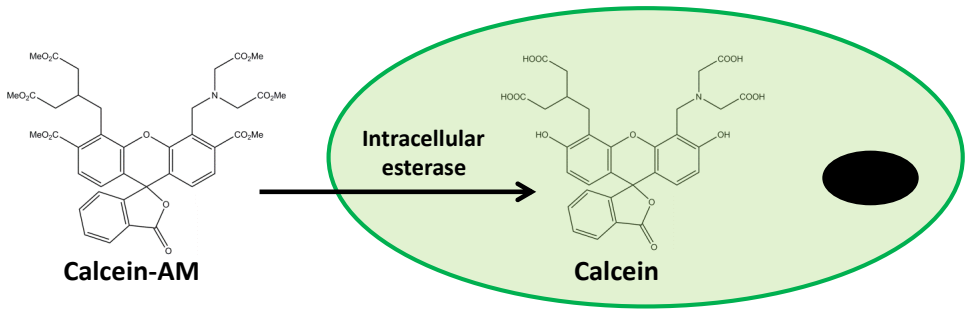

Figure 2-4. Ester hydrolysis of calcein-AM by intracellular esterases.

Ethidium Homodimer-1 (EthD-1) is a weakly fluorescent compound in its native state. Upon binding to DNA, it exhibits strong red fluorescence. Red fluorescence of a cell in this instance indicates the loss of plasma membrane integrity, as EthD-1 is only able to access and bind to DNA if nuclear membrane is degraded, as would be the case for a dead cell. The interaction of EthD-1 with dead cells is shown in Figure 2-5.

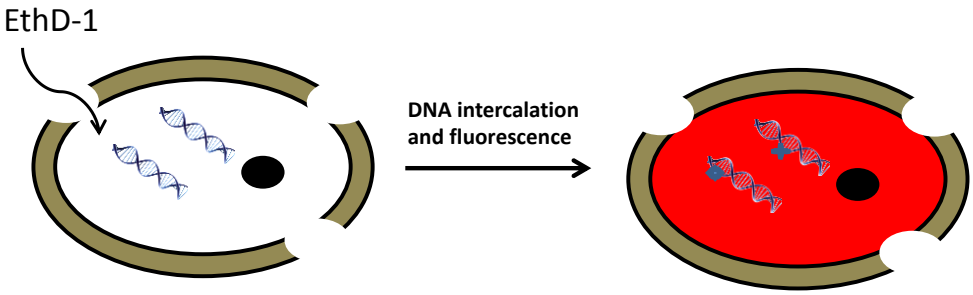

Figure 2-5. The mode of action for ethidium-homodimer-1.

The LIVE/DEAD Viability Assay Kit therefore results in green fluorescence of live cells and red fluorescence of dead cells, therefore making it possible to determine semi-quantitative cell viability percentages, using fluorescence microscopy.

A LIVE/DEAD Viability Assay Kit was purchased from Molecular Probes. The LIVE/DEAD stock solutions were thawed to room temperature. 20 µL of the 2 mM EthD-1 stock solution was added to 10 mL of sterile, tissue culture grade PBS and was vortexed (Vortex Genie 2, Scientific Industries) to ensure thorough mixing (making the solution approximately 4 µM). 5 µL of the 4 mM calcein AM stock solution was added to the 10 mL EthD-1/PBS solution and the resulting solution (2 µM calcein AM, 4 µM EthD-1) vortexed.

Media was removed from the samples and washed with PBS. Approximately 150-200 µL LIVE/DEAD solution was added directly to cells, and incubated for 30-45 mins at room temperature. 10 µL of fresh LIVE/DEAD solution was then added to a clean microscope slide. Fine-tipped forceps were used to mount the wet coverslips onto the microscope slides. LIVE/DEAD stained cells were viewed using a Nikon Eclipse 50*i* fluorescence microscope.

2.6.5 Image J cell counting

After LIVE/DEAD images were obtained, cell counting was performed using the ITCN software plug-in on ImageJ. Colour channels were split and images inverted,

so that cells appeared as dark spots. Estimates of the average size and minimum distance between two cells were input into the software and cell counts performed by recognizing dark spots.

2.6.6 PicoGreen assay

The PicoGreen reagent is an asymmetrical cyanine dye, which does not fluoresce in its native form. When the PicoGreen reagent binds to dsDNA, it exhibits a > 1000-fold enhancement in fluorescence. PicoGreen is 10,000-fold more sensitive than UV absorbance methods, and highly selective for dsDNA over ssDNA and RNA. The structure of the PicoGreen reagent is shown in Figure 2-6. It has an excitation maximum at 480 nm and an emission peak at 520 nm.[619,620]

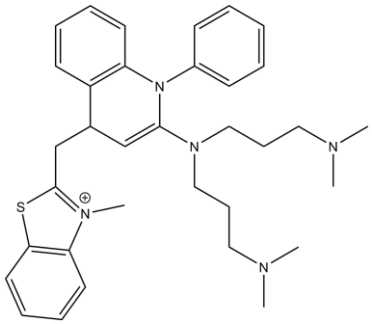

Figure 2-6. Chemical structure of PicoGreen reagent.

A Quant-iT™ PicoGreen dsDNA Assay Kit was purchased from Molecular Probes. Lysis buffer was prepared by adding 1 mL of 20 x TE buffer in 19 mL de-ionised water. 1 % of this solution was removed and replaced with Triton-X (Sigma-Aldrich, molecular biology grade). Working PicoGreen solution was prepared by diluting the stock 200 x PicoGreen solution to 1 x solution using 1 x TE buffer. DNA standards were made by diluting the DNA stock standard 50 x to obtain a working concentration of 2 μg mL^{-1}, from which a dilution series was prepared (in 1 x TE buffer) in the range 0-2 μg mL^{-1} according to Table 2-2.

Table 2-2. Dilutions for the DNA standard curve.

Final concentration/ μg mL^{-1}	Volume of 2 μg mL^{-1} DNA standard/ μL	Vol. 1XTE buffer/ μL
0	0	300
0.005	0.75	299.25
0.01	1.5	298.5
0.05	7.5	292.5
0.1	15	285
0.5	75	225
1	150	150
2	300	0

Media was removed from samples and the cells washed with PBS. 1 mL lysis buffer was added to each well, and cells removed from substrates using a cell scraper. Lysis buffer was left on for a further 5 mins to break up cells, after which cell-containing solutions were transferred to 1.5 mL eppendorfs, and vortexed thoroughly. 100 μL of this solution was added to each well of a black-bottomed 96-well plate, along with 100 μL PicoGreen solution, and fluorescence intensity recorded with λ_{exc} = 480 nm, λ_{em} = 520 nm using a plate reader (FLUOstar OPTIMA, BMG Labtech). Fluorescence intensities were then converted to dsDNA concentration by reference to the DNA standard curve. The DNA standard curve is shown in Figure 2-7.

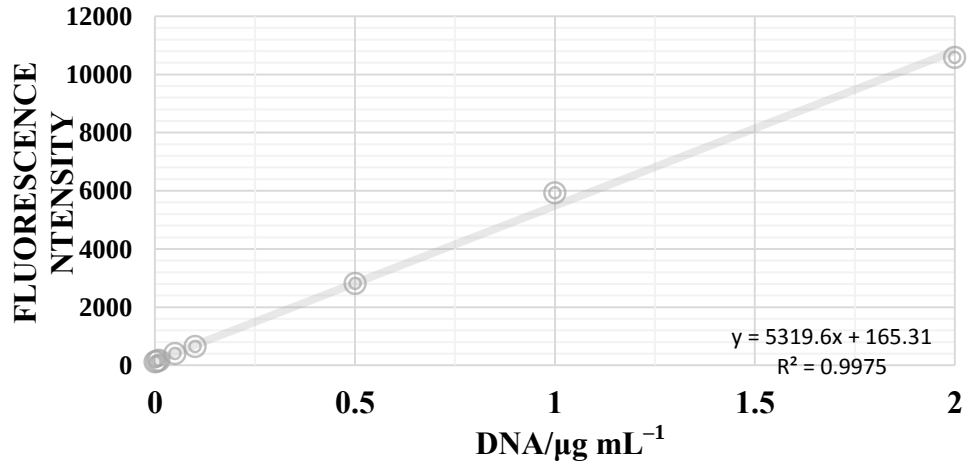

Figure 2-7. PicoGreen DNA standard curve.

2.6.7 AlamarBlue assay

The AlamarBlue reagent is resazurin, a non-toxic, blue, cell-permeable compound. Resazurin does not exhibit fluorescence but, upon entering cells, resazurin is reduced to resorufin, a red compound which is highly fluorescent, as shown in Figure 2-8. Viable cells continuously convert resazurin to resorufin, increasing the overall fluorescence and colour of the media which surrounds the cells, over time. Therefore, the greater the increase in fluorescence, the more active the cells are. This is the basis of the AlamarBlue Assay.

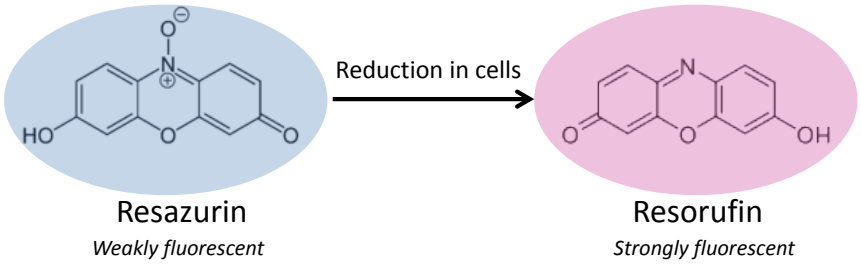

Figure 2-8. Transformation of non-fluorescent resazurin to strongly fluorescent resorufin in active cells

The working 'AlamarBlue' solution was prepared by dissolving 5 mg resazurin salt (Sigma-Aldrich) in 40 mL of tissue culture grade PBS. Media was removed from samples and samples were washed three times with warm PBS. The light to the culture hood was turned off, after which 100 µL of the working AlamarBlue solution was added to each well in, 1 mL fresh culture media. Three additional wells were filled with media and AlamarBlue solution, as controls. Samples were incubated at 37 °C for 2 hours, following which 200 µL of solution was taken from each well and transferred to a 96-well plate (Thermo scientific). Three 200 µL samples were taken from each well in order to take triplicate readings. Fluorescence was recorded using λ_{exc} = 530 nm, λ_{em} = 590 nm using a Plate reader (FLUOstar OPTIMA, BMG Labtech).

2.6.8 NanoOrange assay

A NanoOrange Protein Quantitation Kit was purchased from Molecular Probes. 1 mL of NanoOrange diluent was added to 9 mL de-ionised H_2O to make 1 mL of working diluent solution. Following this, 1 x Stock solution of the NanoOrange reagent was diluted 1:500 into the working diluent solution to make the working NanoOrange solution. The resultant solution was protected from light. Stock protein solutions were diluted in the working NanoOrange solution to a concentration of 10 μg mL^{-1}. LbL constructs were added to a 24-well plate (CELLSTAR) and 500 μL of the working protein/NanoOrange solution added to each well and incubated at 37 °C, 5 % CO_2, to simulate cell incubation conditions. At the designated time points (90 mins and 4 hours), 450 μL of the working protein/NanoOrange solution was transferred from each well to separate sterile eppendorfs and heated to 90-96 °C for 10 mins in a heating mantle, after which they were cooled for 20 mins. 100 μL of the resultant solutions were then transferred (in triplicate) to a 96-well plate and the fluorescence intensity was read at λ_{exc} = 485 nm, λ_{em} = 590 nm using a plate reader (FLUOstar OPTIMA, BMG Labtech). A standard curve was performed using known concentrations of BSA.

2.6.9 Focal adhesion and actin cytoskeleton staining

Focal adhesions contain many integrin-type receptors which attach to the extracellular matrix and are associated with protein complexes such as talin, α-actinin, paxillin, focal adhesion kinase and vinculin. Vinculin is regarded as the universal focal adhesion marker, meaning that anti-vinculin antibodies can be used to visualise focal adhesions. Phalloidin binds to F-actin, meaning that phalloidin staining can be used to visualise the actin cytoskeleton. 4',6-diamidino-2-

phenylindole (DAPI) is a fluorescent dye which binds strongly to A-T regions of DNA, thus staining the cell nuclei.

An FAK100 Actin Cytoskeleton and Focal Adhesion Staining Kit was purchased from Millipore. Additional materials which were prepared or purchased were:

- Fixative 4 % paraformaldehyde (Formalin solution, 10 %, neural buffered, Sigma Aldrich).
- Permeabilization reagent – 1 % Triton X-100 (Sigma Aldrich, molecular biology) in PBS.
- Wash buffer- 0.05 % Tween-20 (VWR Chemicals) in PBS.
- Blocking solution- 1 % BSA (Sigma, 98 % minimum).
- FITC-labelled goat anti-mouse secondary antibody (AP124F, Millipore).
- Pro-long gold antifade mounting solution (Thermo Fisher scientific).

Cells were fixed with 200 μL 4 % paraformaldehyde for 20 mins at room temperature. Cells were then washed twice with wash buffer, after which they were permeabilised by incubation with 200 μL 1 % Triton X-100 for 5 mins. Cells were then washed twice with wash buffer. 200 μL Blocking solution was then added to the cells for 30 mins, after which 200 μL anti-vinculin primary antibody (diluted 1:300 in blocking solution) was added to the cells and left to incubate for 1 hour at room temperature. Cells were washed three times with wash buffer (5 mins each), after which 200 μL PBS, containing both the secondary antibody (AP124F, see above, diluted 1:300) and the TRITC-conjugated Phalloidin (diluted 1:300), was added to each well and incubated for 45 mins at room temperature. Cells were then washed three times with wash buffer (5 mins each), following which nuclei counterstaining was performed by incubating cells with DAPI (diluted 1:500 in PBS) for 5 mins at

room temperature. Cells were then washed three times with wash buffer (5 mins each), followed by one wash with PBS. Coverslips were then mounted onto microscope slides using antifade mounting solution, after which cells were visualised under a Nikon Eclipse 50*i* fluorescence microscope.

2.6.10 Focal adhesion quantification

Cell profiler software was used to quantify focal adhesions and to measure cell shape. Firstly the 'colour to grey' function was used on the green vinculin stained images. A filter was applied to the green channel images to enhance the focal adhesions. An example of this filter can be seen in Figure 2-9B. Once filtered images were obtained, focal adhesions were picked out by using the 'enhance speckles' feature within boundaries set.

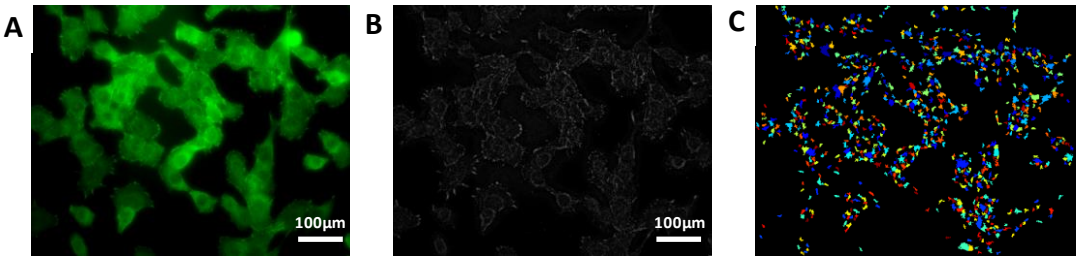

Figure 2-9. Example of CellProfiler filter to identify focal adhesions. A) unfiltered green vinculin image B) Filtered focal adhesions C) Identified focal adhesions

2.6.11 Cell area quantification

Cell profiler was also used to calculate the area per cell. Cells were firstly coloured to grey, as described above, after which individual cells were identified by inputting minimum and maximum approximate sizes of the cells under the 'identify primary objects' feature. As the size of the cells varied between time points and sometimes between substrates, the maximum and minimum was adjusted until all the cells were identified. The 'measure cell shape/size' feature was then used to get information

about cells, as outlined in the appendix. A figure of LIVE/DEAD stained cells and their identification using CellProfiler is shown in Figure 2-10.

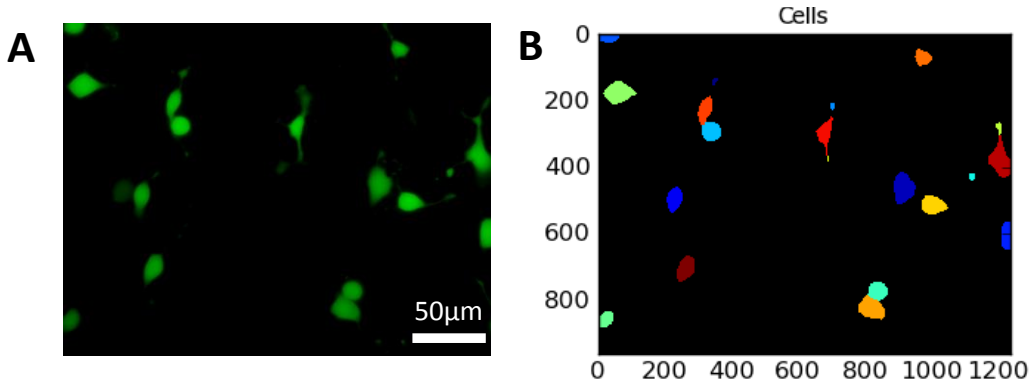

Figure 2-10. A) Original images of 3T3 SA cells B) Processed images, with identified cells coloured

2.6.12 Statistical analysis

Statistical analysis was performed on GraphPad Prism 6 software. Two-way ANOVA tests were performed along with appropriate post hoc test (Tukey's or Dunn's, respectively) to determine the origins of significance. Values reported were: ns ($p > 0.05$), * ($p \leq 0.05$), ** ($p \leq 0.01$), *** ($p \leq 0.001$), **** ($p \leq 0.0001$). Where only one time point was measured, one-way ANOVA tests were performed.

2.7. Mesenchymal stem cell viability on LbL constructs

2.7.1 Stem cell culture

Human mesenchymal stem cells were purchased from PromoCell. Cells were cultured in Dulbecco's Modified Eagles medium, supplemented with 10 % FBS, 1 % antibiotics and antimyotics (A+A), 1 % non-essential amino acids (NEAA). Cells were incubated at 37 °C, 5 % CO_2. Once approximately 80 % confluence was achieved, media was removed from flasks and the flasks were washed with Dulbecco's Phosphate buffer saline (PBS, sterile filtered, Sigma). 1 mL trypsin was added to the flasks to encourage cell delamination. The flasks were then incubated at 37 °C for 2-3 mins, after which the free cells were suspended in 10 mL of fresh

media. The resultant cell solution was centrifuged at 1500 rpm for 5 mins, and the cell pellet suspended in 10 mL fresh media.

2.7.2 Cell seeding

Cells were seeded at a density of 30,000 cells cm^{-2} and incubated 37 °C, 5 % CO_2 for 7 days. Cell viability assays were performed at 4 hours, 1 day and 7 days post-seeding.

2.7.3 LIVE/DEAD assay for cell viability

The LIVE/DEAD Assay was performed as described in Section 2.6.4.

2.7.4 Cell count

Cell count was performed using the same process as that used to calculate the cell area, but in this case only the number of identified objects was recorded, and the analysis did not include information on the shape.

2.7.5 Cell shape

Once cells were outlined using the method outlined in section 2.6.11, the cell eccentricity was calculated by selecting the 'measure object shape and size' option. The parameters measured by this option are outlined in the Appendix.

2.7.6 Cell area

Cell areas were calculated in an analogous way to that described in section 2.6.11.

2.7.7 AlamarBlue assay

The AlamarBlue Assay was performed as described in Section 2.6.6.

2.7.8 Focal adhesion and actin cytoskeleton staining

Focal adhesion and actin cytoskeleton staining was performed as described in Section 2.6.9

2.7.9 Focal adhesion quantification

Cell profiler software was used to quantify focal adhesions and to measure cell shape, as described in 2.6.10 and 2.6.11.

2.7.10 Pre-treatment of LbL constructs

LbL constructs were pre-treated with 200 μL hMSC in-house media (DMEM + 10 % FBS, 1 % NEAA, 1 % A+A) for 90 mins prior to hMSC seeding. Cells were seeded as described in 2.7.2 and the same analysis performed as outlined in Sections 2.7.3 to 2.7.9.

2.8. Stem cell differentiation on GFN-containing LbL constructs

2.8.1 Adipogenesis media

Adipogenesis media was prepared using Dulbecco's Modified Eagle's Medium (DMEM, 4500 mg L^{-1} glucose) supplemented with 10 % FBS, 1 % non-essential amino acids, 1 μM dexamethasone (powder, Bioreagent, suitable for cell culture, ≥ 97 %, Sigma), 6 x 10^{-5} M indomethacin (99 + %, Alfa Aesar), 10 μg mL^{-1} Insulin (Recombinant Human dry powder, Sigma).

2.8.2 Osteogenesis media

Osteogenesis media was prepared using DMEM (4500 mg L^{-1} glucose) supplemented with 10 % FBS, 1 % non-essential amino acids, 10 mM β-glycerophosphate (Bio Ultra, Sigma Aldrich) 10 nM dexamethasone and 50 μg mL^{-1} ascorbic acid (< 98 %, Sigma Aldrich).

2.8.3 Adipogenesis induction procedure

Cells were seeded at density of 20,000 cells cm^{-2} and incubated under standard conditions (37 °C, 5 % CO_2). After 24 hours, post-seeding, media was switched to adipogenic media, after which media was replenished every 3 days.

2.8.4 Osteogenesis induction procedure

Cells were seeded at density of 10,000 cells cm^{-2} and incubated under standard conditions (37 °C, 5 % CO_2) After 24 hours, post-seeding, media was switched to osteogenic media, after which media was replenished every 3 days.

2.8.5 Alizarin red staining

Media was removed from cells and cells washed twice with PBS and once with de-ionised H_2O. Cells were fixed with 4 % formaldehyde for 15-20 mins, after which they were rinsed with 0.05 % Tween-20 (in PBS). Alizarin red solution was produced by dissolving 2 g Alizarin red (Sigma) in 100 mL de-ionised H_2O. pH was then adjusted to 4.2, after which the resultant solution was filtered using 0.2-micron filter. 150 µL working Alizarin red solution was added to each well and left for 25 mins. After this, samples were rinsed with de-ionised H_2O until the solution was clear. Then samples were viewed under 10 x magnification on a EVOS*xl* transmitted light microscope (AMG).

2.8.6 Oil-Red O staining

Media was removed from cells and cells washed twice with PBS and once with de-ionised H_2O. Cells were fixed with 4 % formaldehyde for 15-20 mins, after which they were rinsed with 0.05 % Tween-20 (in PBS). Cells were then rinsed in 60 % isopropanol (BioReagent, 99.5 % Sigma-Aldrich) for 5-10 mins. Stock solution of Oil Red O was made by dissolving 300 mg Oil Red O powder (Sigma Aldrich) in 100 mL of 99 % isopropanol. This solution was diluted 3:2 in de-ionised H_2O and left to stand for 10 mins. The resultant solution was filtered using 0.2-micron filter. 150 µL of working solution was added to each well and left for 5 mins, after which the cells were rinsed with de-ionised water until the solution ran clear. Then samples

were viewed under 10 x magnification on a EVOS*xl* transmitted light microscope (AMG).

2.8.7 Oil-Red O percentage area analysis

Firstly, Oil Red O-stained images were inverted, so that the positively stained areas appeared white against a black background. Cell profiler was then used to 'identify primary objects' and the area of the objects measured. The percentage area of positively stained cells was then calculated in comparison to the total area of each image.

2.9. References

1. Geim, A. K., Graphene: Status and Prospects. *Science* **2009,** *324* (5934), 1530-1534.
2. Zhu, Y.; Murali, S.; Cai, W.; Li, X.; Suk, J. W.; Potts, J. R.; Ruoff, R. S., Graphene and Graphene Oxide: Synthesis, Properties, and Applications. *Advanced Materials* **2010,** *22* (35), 3906-3924.
3. Bolotin, K. I.; Sikes, K. J.; Jiang, Z.; Klima, M.; Fudenberg, G.; Hone, J.; Kim, P.; Stormer, H. L., Ultrahigh electron mobility in suspended graphene. *Solid State Communications* **2008,** *146* (9-10), 351-355.
4. Lee, C.; Wei, X.; Kysar, J. W.; Hone, J., Measurement of the elastic properties and intrinsic strength of monolayer graphene. *Science* **2008,** *321* (5887), 385-388.
5. Zhang, L.; Xia, J.; Zhao, Q.; Liu, L.; Zhang, Z., Functional Graphene Oxide as a Nanocarrier for Controlled Loading and Targeted Delivery of Mixed Anticancer Drugs. *Small* **2010,** *6* (4), 537-544.
6. Sun, X.; Liu, Z.; Welsher, K.; Robinson, J. T.; Goodwin, A.; Zaric, S.; Dai, H., Nano-Graphene Oxide for Cellular Imaging and Drug Delivery. *Nano Research* **2008,** *1* (3), 203-212.
7. Wang, Y.; Shao, Y. Y.; Matson, D. W.; Li, J. H.; Lin, Y. H., Nitrogen-Doped Graphene and Its Application in Electrochemical Biosensing. *ACS Nano* **2010,** *4* (4), 1790-1798.
8. Zhou, M.; Zhai, Y.; Dong, S., Electrochemical Sensing and Biosensing Platform Based on Chemically Reduced Graphene Oxide. *Analytical Chemistry* **2009,** *81* (14) 5603-5613.
9. Li, Y. Q.; Yu, T.; Yang, T. Y.; Zheng, L. X.; Liao, K., Bio-Inspired Nacre-like Composite Films Based on Graphene with Superior Mechanical, Electrical, and Biocompatible Properties. *Advanced Materials* **2012,** *24* (25), 3426-3431.
10. Fan, Z. J.; Wang, J. Q.; Wang, Z. F.; Li, Z. P.; Qiu, Y. N.; Wang, H. G.; Xu, Y.; Niu, L. Y.; Gong, P. W.; Yang, S. R., Casein Phosphopeptide-Biofunctionalized Graphene Biocomposite for Hydroxyapatite Biomimetic Mineralization. *Journal of Physical Chemistry C* **2013,** *117* (20), 10375-10382.
11. Rodriguez-Lozano, F. J.; Garcia-Bernal, D.; Aznar-Cervantes, S.; Ros-Roca, M. A.; Alguero, M. C.; Atucha, N. M.; Lozano-Garcia, A. A.; Moraleda, J. M.; Cenis, J. L., Effects of composite films of silk fibroin and graphene oxide on the proliferation, cell viability and mesenchymal phenotype of periodontal ligament stem cells. *Journal of Materials Science-Materials in Medicine* **2014,** *25* (12), 2731-2741.
12. Nayak, T. R.; Andersen, H.; Makam, V. S.; Khaw, C.; Bae, S.; Xu, X.; Ee, P.-L. R.; Ahn, J.-H.; Hong, B. H.; Pastorin, G.; Oezyilmaz, B., Graphene for Controlled and Accelerated Osteogenic Differentiation of Human Mesenchymal Stem Cells. *ACS Nano* **2011,** *5* (6), 4670-4678.
13. Park, S. Y.; Park, J.; Sim, S. H.; Sung, M. G.; Kim, K. S.; Hong, B. H.; Hong, S., Enhanced Differentiation of Human Neural Stem Cells into Neurons on Graphene. *Advanced Materials* **2011,** *23* (36), 263–267.
14. Fan, Z. J.; Liu, B.; Wang, J. Q.; Zhang, S. Y.; Lin, Q. Q.; Gong, P. W.; Ma, L. M.; Yang, S. R., A Novel Wound Dressing Based on Ag/Graphene Polymer Hydrogel: Effectively Kill Bacteria and Accelerate Wound Healing. *Advanced Functional Materials* **2014,** *24* (25), 3933-3943.
15. Georgakilas, V.; Otyepka, M.; Bourlinos, A. B.; Chandra, V.; Kim, N.; Kemp, K. C.; Hobza, P.; Zboril, R.; Kim, K. S., Functionalization of Graphene: Covalent and Non-Covalent Approaches, Derivatives and Applications. *Chemical Reviews* **2012,** *112* (11), 6156-6214.
16. Liu, L. Z.; Zhang, J. F.; Zhao, J. J.; Liu, F., Mechanical properties of graphene oxides. *Nanoscale* **2012,** *4* (19), 5910-5916.
17. Suk, J. W.; Piner, R. D.; An, J. H.; Ruoff, R. S., Mechanical Properties of Mono layer Graphene Oxide. *ACS Nano* **2010,** *4* (11), 6557-6564.
18. Balandin, A. A.; Ghosh, S.; Bao, W.; Calizo, I.; Teweldebrhan, D.; Miao, F.; Lau, C. N., Superior thermal conductivity of single-layer graphene. *Nano Letters* **2008,** *8* (3), 902-907.
19. Kusminskiy, S. V.; Campbell, D. K.; Castro Neto, A. H., Lenosky's energy and the phonon dispersion of graphene. *Physical Review B* **2009,** *80* (3) 035401/1-5.

20. Moser, J.; Barreiro, A.; Bachtold, A., Current-induced cleaning of graphene. *Applied Physics Letters* **2007,** *91* (16) 163513/1-3.
21. Shao, Y.; Wang, J.; Wu, H.; Liu, J.; Aksay, I. A.; Lin, Y., Graphene Based Electrochemical Sensors and Biosensors: A Review. *Electroanalysis* **2010,** *22* (10) 1027-1036.
22. Park, C.-H.; Louie, S. G., Tunable Excitons in Biased Bilayer Graphene. *Nano Letters* **2010,** *10* (2), 426-431.
23. Geim, A. K.; Novoselov, K. S., The rise of graphene. *Nature Materials* **2007,** *6* (3), 183-191.
24. Nair, R. R.; Blake, P.; Grigorenko, A. N.; Novoselov, K. S.; Booth, T. J.; Stauber, T.; Peres, N. M. R.; Geim, A. K., Fine structure constant defines visual transparency of graphene. *Science* **2008,** *320* (5881), 1308-1308.
25. Liu, J. Q.; Cui, L.; Losic, D., Graphene and graphene oxide as new nanocarriers for drug delivery applications. *Acta Biomaterialia* **2013,** *9* (12), 9243-9257.
26. Goenka, S.; Sant, V.; Sant, S., Graphene-based nanomaterials for drug delivery and tissue engineering. *Journal of Controlled Release* **2014,** *173*, 75-88.
27. Wang, D. H.; Kou, R.; Choi, D.; Yang, Z. G.; Nie, Z. M.; Li, J.; Saraf, L. V.; Hu, D. H.; Zhang, J. G.; Graff, G. L.; Liu, J.; Pope, M. A.; Aksay, I. A., Ternary Self-Assembly of Ordered Metal Oxide-Graphene Nanocomposites for Electrochemical Energy Storage. *ACS Nano* **2010,** *4* (3), 1587-1595.
28. Zhang, L. S.; Jiang, L. Y.; Yan, H. J.; Wang, W. D.; Wang, W.; Song, W. G.; Guo, Y. G.; Wan, L. J., Mono dispersed SnO2 nanoparticles on both sides of single layer graphene sheets as anode materials in Li-ion batteries. *Journal of Materials Chemistry* **2010,** *20* (26), 5462-5467.
29. Wei, T.; Luo, G. L.; Fan, Z. J.; Zheng, C.; Yan, J.; Yao, C. Z.; Li, W. F.; Zhang, C., Preparation of graphene nanosheet/polymer composites using in situ reduction-extractive dispersion. *Carbon* **2009,** *47* (9), 2296-2299.
30. Huang, X.; Qi, X. Y.; Boey, F.; Zhang, H., Graphene-based composites. *Chemical Society Reviews* **2012,** *41* (2), 666-686.
31. Wick, P.; Louw-Gaume, A. E.; Kucki, M.; Krug, H. F.; Kostarelos, K.; Fadeel, B.; Dawson, K. A.; Salvati, A.; Vazquez, E.; Ballerini, L.; Tretiach, M.; Benfenati, F.; Flahaut, E.; Gauthier, L.; Prato, M.; Bianco, A., Classification Framework for Graphene-Based Materials. *Angewandte Chemie-International Edition* **2014,** *53* (30), 7714-7718.
32. Khan, U.; O'Neill, A.; Lotya, M.; De, S.; Coleman, J. N., High-Concentration Solvent Exfoliation of Graphene. *Small* **2010,** *6* (7), 864-871.
33. Mao, L.; Hu, M. J.; Pan, B. C.; Xie, Y. C.; Petersen, E. J., Biodistribution and toxicity of radio-labeled few layer graphene in mice after intratracheal instillation. *Particle and Fibre Toxicology* **2016,** *13,* 1-12.
34. Ma, J.; Liu, R.; Wang, X.; Liu, Q.; Chen, Y. N.; Valle, R. P.; Zuo, Y. Y.; Xia, T.; Liu, S. J., Crucial Role of Lateral Size for Graphene Oxide in Activating Macrophages and Stimulating Pro-inflammatory Responses in Cells and Animals. *ACS Nano* **2015,** *9* (10), 10498-10515.
35. Park, S.; Ruoff, R. S., Chemical methods for the production of graphenes. *Nature Nanotechnology* **2009,** *4* (4) 217-224.
36. Dreyer, D. R.; Park, S.; Bielawski, C. W.; Ruoff, R. S., The chemistry of graphene oxide. *Chemical Society Reviews* **2010,** *39* (1), 228-240.
37. Lerf, A.; He, H. Y.; Forster, M.; Klinowski, J., Structure of graphite oxide revisited. *Journal of Physical Chemistry B* **1998,** *102* (23), 4477-4482.
38. He, H. Y.; Klinowski, J.; Forster, M.; Lerf, A., A new structural model for graphite oxide. *Chemical Physics Letters* **1998,** *287* (1-2), 53-56.
39. Mkhoyan, K. A.; Contryman, A. W.; Silcox, J.; Stewart, D. A.; Eda, G.; Mattevi, C.; Miller, S.; Chhowalla, M., Atomic and Electronic Structure of Graphene-Oxide. *Nano Letters* **2009,** *9* (3), 1058-1063.
40. Li, D.; Mueller, M. B.; Gilje, S.; Kaner, R. B.; Wallace, G. G., Processable aqueous dispersions of graphene nanosheets. *Nature Nanotechnology* **2008,** *3* (2), 101-105.

41. Figueiredo-Filho, L. C. S.; Brownson, D. A. C.; Gomez-Mingot, M.; Iniesta, J.; Fatibello-Filho, O.; Banks, C. E., Exploring the electrochemical performance of graphitic paste electrodes: graphene vs. graphite. *Analyst* **2013,** *138* (21), 6354-6364.
42. Gomez-Navarro, C.; Weitz, R. T.; Bittner, A. M.; Scolari, M.; Mews, A.; Burghard, M.; Kern, K., Electronic transport properties of individual chemically reduced graphene oxide sheets. *Nano Letters* **2007,** *7* (11), 3499-3503.
43. Novoselov, K. S.; Geim, A. K.; Morozov, S. V.; Jiang, D.; Zhang, Y.; Dubonos, S. V.; Grigorieva, I. V.; Firsov, A. A., Electric field effect in atomically thin carbon films. *Science* **2004,** *306* (5696), 666-669.
44. Berger, C.; Song, Z.; Li, X.; Wu, X.; Brown, N.; Naud, C.; Mayou, D.; Li, T.; Hass, J.; Marchenkov, A. N.; Conrad, E. H.; First, P. N.; de Heer, W. A., Electronic confinement and coherence in patterned epitaxial graphene. *Science* **2006,** *312* (5777), 1191-1196.
45. Soldano, C.; Mahmood, A.; Dujardin, E., Production, properties and potential of graphene. *Carbon* **2010,** *48* (8), 2127-2150.
46. Bae, S.; Kim, H.; Lee, Y.; Xu, X.; Park, J.-S.; Zheng, Y.; Balakrishnan, J.; Lei, T.; Kim, H. R.; Song, Y. I.; Kim, Y.-J.; Kim, K. S.; Ozyilmaz, B.; Ahn, J.-H.; Hong, B. H.; Iijima, S., Roll-to-roll production of 30-inch graphene films for transparent electrodes. *Nature Nanotechnology* **2010,** *5* (8), 574-578.
47. Kim, K. S.; Zhao, Y.; Jang, H.; Lee, S. Y.; Kim, J. M.; Kim, K. S.; Ahn, J.-H.; Kim, P.; Choi, J.-Y.; Hong, B. H., Large-scale pattern growth of graphene films for stretchable transparent electrodes. *Nature* **2009,** *457* (7230), 706-710.
48. Banerjee, B. C.; Walker, P. L.; Hirt, T. J., Pyrolytic carbon formation from carbon suboxide. *Nature* **1961,** *192* (480), 450-451.
49. Karu, A. E.; Beer, M., Pyrolytic formation of highly crystalline graphite films. *Journal of Applied Physics* **1966,** *37* (5), 2179.
50. Robertso.Sd, Graphite formation from low temperature pyrolysis of methane over some transition metal surfaces. *Nature* **1969,** *221* (5185), 1044-1046.
51. Li, X.; Cai, W.; An, J.; Kim, S.; Nah, J.; Yang, D.; Piner, R.; Velamakanni, A.; Jung, I.; Tutuc, E.; Banerjee, S. K.; Colombo, L.; Ruoff, R. S., Large-Area Synthesis of High-Quality and Uniform Graphene Films on Copper Foils. *Science* **2009,** *324* (5932), 1312-1314.
52. Zhang, Y.; Zhang, L.; Zhou, C., Review of Chemical Vapor Deposition of Graphene and Related Applications. *Accounts of Chemical Research* **2013,** *46* (10), 2329-2339.
53. Eizenberg, M.; Blakely, J. M., Carbon monolayer phase condensation on Ni(111). *Surface Science* **1979,** *82* (1), 228-236.
54. Obraztsov, A. N.; Obraztsova, E. A.; Tyurnina, A. V.; Zolotukhin, A. A., Chemical vapor deposition of thin graphite films of nanometer thickness. *Carbon* **2007,** *45* (10), 2017-2021.
55. Yu, Q.; Lian, J.; Siriponglert, S.; Li, H.; Chen, Y. P.; Pei, S.-S., Graphene segregated on Ni surfaces and transferred to insulators. *Applied Physics Letters* **2008,** *93* (11), 113103/1-3.
56. Sutter, P. W.; Flege, J.-I.; Sutter, E. A., Epitaxial graphene on ruthenium. *Nature Materials* **2008,** *7* (5), 406-411.
57. Land, T. A.; Michely, T.; Behm, R. J.; Hemminger, J. C.; Comsa, G., STM investigation of single layer graphite structures produced on Pt (111) by hydrocarbon decomposition. *Surface Science* **1992,** *264* (3), 261-270.
58. Mattevi, C.; Kim, H.; Chhowalla, M., A review of chemical vapour deposition of graphene on copper. *Journal of Materials Chemistry* **2011,** *21* (10), 3324-3334.
59. Berger, C.; Song, Z. M.; Li, T. B.; Li, X. B.; Ogbazghi, A. Y.; Feng, R.; Dai, Z. T.; Marchenkov, A. N.; Conrad, E. H.; First, P. N.; de Heer, W. A., Ultrathin epitaxial graphite: 2D electron gas properties and a route toward graphene-based nanoelectronics. *Journal of Physical Chemistry B* **2004,** *108* (52), 19912-19916.
60. Riedl, C.; Coletti, C.; Starke, U., Structural and electronic properties of epitaxial graphene on SiC(0 0 0 1): a review of growth, characterization, transfer doping and hydrogen intercalation. *Journal of Physics D-Applied Physics* **2010,** *43* (37), 374009/1-17.

61. Hernandez, Y.; Nicolosi, V.; Lotya, M.; Blighe, F. M.; Sun, Z.; De, S.; McGovern, I. T.; Holland, B.; Byrne, M.; Gun'ko, Y. K.; Boland, J. J.; Niraj, P.; Duesberg, G.; Krishnamurthy, S.; Goodhue, R.; Hutchison, J.; Scardaci, V.; Ferrari, A. C.; Coleman, J. N., High-yield production of graphene by liquid-phase exfoliation of graphite. *Nature Nanotechnology* **2008,** *3* (9), 563-568.
62. Suslick, K. S., Sonochemistry. *Science* **1990,** *247* (4949), 1439-1445.
63. Coleman, J. N., Liquid Exfoliation of Defect-Free Graphene. *Accounts of Chemical Research* **2013,** *46* (1), 14-22.
64. Wang, X.; Fulvio, P. F.; Baker, G. A.; Veith, G. M.; Unocic, R. R.; Mahurin, S. M.; Chi, M.; Dai, S., Direct exfoliation of natural graphite into micrometre size few layers graphene sheets using ionic liquids. *Chemical Communications* **2010,** *46* (25), 4487-4489.
65. Nuvoli, D.; Valentini, L.; Alzari, V.; Scognamillo, S.; Bon, S. B.; Piccinini, M.; Illescas, J.; Mariani, A., High concentration few-layer graphene sheets obtained by liquid phase exfoliation of graphite in ionic liquid. *Journal of Materials Chemistry* **2011,** *21* (10), 3428-3431.
66. Bari, R.; Tamas, G.; Irin, F.; Aquino, A. J. A.; Green, M. J.; Quitevis, E. L., Direct exfoliation of graphene in ionic liquids with aromatic groups. *Colloids and Surfaces a-Physicochemical and Engineering Aspects* **2014,** *463*, 63-69.
67. Ravula, S.; Baker, S. N.; Kamath, G.; Baker, G. A., Ionic liquid-assisted exfoliation and dispersion: stripping graphene and its two-dimensional layered inorganic counterparts of their inhibitions. *Nanoscale* **2015,** *7* (10), 4338-4353.
68. Lu, J.; Yang, J.-x.; Wang, J.; Lim, A.; Wang, S.; Loh, K. P., One-Pot Synthesis of Fluorescent Carbon Nanoribbons, Nanoparticles, and Graphene by the Exfoliation of Graphite in Ionic Liquids. *ACS Nano* **2009,** *3* (8), 2367-2375.
69. Guardia, L.; Fernandez-Merino, M. J.; Paredes, J. I.; Solis-Fernandez, P.; Villar-Rodil, S.; Martinez-Alonso, A.; Tascon, J. M. D., High-throughput production of pristine graphene in an aqueous dispersion assisted by non-ionic surfactants. *Carbon* **2011,** *49* (5), 1653-1662.
70. Bourlinos, A. B.; Georgakilas, V.; Zboril, R.; Steriotis, T. A.; Stubos, A. K.; Trapalis, C., Aqueous-phase exfoliation of graphite in the presence of polyvinylpyrrolidone for the production of water-soluble graphenes. *Solid State Communications* **2009,** *149* (47-48), 2172-2176.
71. Lotya, M.; Hernandez, Y.; King, P. J.; Smith, R. J.; Nicolosi, V.; Karlsson, L. S.; Blighe, F. M.; De, S.; Wang, Z.; McGovern, I. T.; Duesberg, G. S.; Coleman, J. N., Liquid Phase Production of Graphene by Exfoliation of Graphite in Surfactant/Water Solutions. *Journal of the American Chemical Society* **2009,** *131* (10), 3611-3620.
72. Khan, U.; O'Neill, A.; Porwal, H.; May, P.; Nawaz, K.; Coleman, J. N., Size selection of dispersed, exfoliated graphene flakes by controlled centrifugation. *Carbon* **2012,** *50* (2), 470-475.
73. Varrla, E.; Paton, K. R.; Backes, C.; Harvey, A.; Smith, R. J.; McCauley, J.; Coleman, J. N., Turbulence-assisted shear exfoliation of graphene using household detergent and a kitchen blender. *Nanoscale* **2014,** *6* (20), 11810-11819.
74. Yi, M.; Shen, Z., A review on mechanical exfoliation for the scalable production of graphene. *Journal of Materials Chemistry A* **2015,** *3* (22), 11700-11715.
75. Sutkar, V. S.; Gogate, P. R.; Csoka, L., Theoretical prediction of cavitational activity distribution in sonochemical reactors. *Chemical Engineering Journal* **2010,** *158* (2), 290-295.
76. Yi, M.; Shen, Z.; Zhang, X.; Ma, S., Vessel diameter and liquid height dependent sonication-assisted production of few-layer graphene. *Journal of Materials Science* **2012,** *47* (23), 8234-8244.
77. Skaltsas, T.; Ke, X.; Bittencourt, C.; Tagmatarchis, N., Ultrasonication Induces Oxygenated Species and Defects onto Exfoliated Graphene. *Journal of Physical Chemistry C* **2013,** *117* (44), 23272-23278.
78. Bracamonte, M. V.; Lacconi, G. I.; Urreta, S. E.; Foa Torres, L. E. F., On the Nature of Defects in Liquid-Phase Exfoliated Graphene. *Journal of Physical Chemistry C* **2014,** *118* (28), 15455-15459.

79. Torrisi, F.; Hasan, T.; Wu, W.; Sun, Z.; Lombardo, A.; Kulmala, T. S.; Hsieh, G.-W.; Jung, S.; Bonaccorso, F.; Paul, P. J.; Chu, D.; Ferrari, A. C., Inkjet-Printed Graphene Electronics. *ACS Nano* **2012,** *6* (4), 2992-3006.
80. Finn, D. J.; Lotya, M.; Cunningham, G.; Smith, R. J.; McCloskey, D.; Donegan, J. F.; Coleman, J. N., Inkjet deposition of liquid-exfoliated graphene and MoS2 nanosheets for printed device applications. *Journal of Materials Chemistry C* **2014,** *2* (5), 925-932.
81. Paton, K. R.; Varrla, E.; Backes, C.; Smith, R. J.; Khan, U.; O'Neill, A.; Boland, C.; Lotya, M.; Istrate, O. M.; King, P.; Higgins, T.; Barwich, S.; May, P.; Puczkarski, P.; Ahmed, I.; Moebius, M.; Pettersson, H.; Long, E.; Coelho, J.; O'Brien, S. E.; McGuire, E. K.; Sanchez, B. M.; Duesberg, G. S.; McEvoy, N.; Pennycook, T. J.; Downing, C.; Crossley, A.; Nicolosi, V.; Coleman, J. N., Scalable production of large quantities of defect-free few-layer graphene by shear exfoliation in liquids. *Nature Materials* **2014,** *13* (6), 624-630.
82. Liu, L.; Shen, Z.; Yi, M.; Zhang, X.; Ma, S., A green, rapid and size-controlled production of high-quality graphene sheets by hydrodynamic forces. *Rsc Advances* **2014,** *4* (69), 36464-36470.
83. Staudenmaier, L., Method for the preparation of graphitic acid. *Berichte der Deutschen Chemischen Gesellschaft* **1898,** *31,* 1-3.
84. Brodie, B. C., On the atomic weight of graphite **1859,** *149*, 249-259
85. Hummers, W. S.; Offeman, R. E., Preparation of graphitic oxide. *Journal of the American Chemical Society* **1958,** *80* (6), 1339.
86. Stankovich, S.; Dikin, D. A.; Piner, R. D.; Kohlhaas, K. A.; Kleinhammes, A.; Jia, Y.; Wu, Y.; Nguyen, S. T.; Ruoff, R. S., Synthesis of graphene-based nanosheets via chemical reduction of exfoliated graphite oxide. *Carbon* **2007,** *45* (7), 1558-1565.
87. Tung, V. C.; Allen, M. J.; Yang, Y.; Kaner, R. B., High-throughput solution processing of large-scale graphene. *Nature Nanotechnology* **2009,** *4* (1), 25-29.
88. Park, S.; An, J.; Potts, J. R.; Velamakanni, A.; Murali, S.; Ruoff, R. S., Hydrazine-reduction of graphite- and graphene oxide. *Carbon* **2011,** *49* (9), 3019-3023.
89. Si, Y.; Samulski, E. T., Synthesis of water soluble graphene. *Nano Letters* **2008,** *8* (6), 1679-1682.
90. Wang, G.; Yang, J.; Park, J.; Gou, X.; Wang, B.; Liu, H.; Yao, J., Facile synthesis and characterization of graphene nanosheets. *Journal of Physical Chemistry C* **2008,** *112* (22), 8192-8195.
91. Lei, Z. B.; Lu, L.; Zhao, X. S., The electrocapacitive properties of graphene oxide reduced by urea. *Energy & Environmental Science* **2012,** *5* (4), 6391-6399.
92. Sheng, K. X.; Xu, Y. X.; Li, C.; Shi, G. Q., High-performance self-assembled graphene hydrogels prepared by chemical reduction of graphene oxide. *New Carbon Materials* **2011,** *26* (1), 9-15.
93. Abdelkader, A. M.; Valles, C.; Cooper, A. J.; Kinloch, I. A.; Dryfe, R. A. W., Alkali Reduction of Graphene Oxide in Molten Halide Salts: Production of Corrugated Graphene Derivatives for High-Performance Supercapacitors. *ACS Nano* **2014,** *8* (11), 11225-11233.
94. An, S. J.; Zhu, Y.; Lee, S. H.; Stoller, M. D.; Emilsson, T.; Park, S.; Velamakanni, A.; An, J.; Ruoff, R. S., Thin Film Fabrication and Simultaneous Anodic Reduction of Deposited Graphene Oxide Platelets by Electrophoretic Deposition. *Journal of Physical Chemistry Letters* **2010,** *1* (8), 1259-1263.
95. Dai, L.; Chang, D. W.; Baek, J.-B.; Lu, W., Carbon Nanomaterials for Advanced Energy Conversion and Storage. *Small* **2012,** *8* (8), 1130-1166.
96. Kuila, T.; Bose, S.; Mishra, A. K.; Khanra, P.; Kim, N. H.; Lee, J. H., Chemical functionalization of graphene and its applications. *Progress in Materials Science* **2012,** *57* (7), 1061-1105.
97. Chen, X. M.; Shen, J. W.; Huang, W. Y., Novel electrically conductive polypropylene/graphite nanocomposites. *Journal of Materials Science Letters* **2002,** *21* (3), 213-214.

98. Chen, G. H.; Lu, J. R.; Wu, D. J., PTC effect of polyethylene/foliated graphite nanocomposites. *Journal of Materials Science* **2005,** *40* (18), 5041-5043.
99. Schniepp, H. C.; Li, J. L.; McAllister, M. J.; Sai, H.; Herrera-Alonso, M.; Adamson, D. H.; Prud'homme, R. K.; Car, R.; Saville, D. A.; Aksay, I. A., Functionalized single graphene sheets derived from splitting graphite oxide. *Journal of Physical Chemistry B* **2006,** *110* (17), 8535-8539.
100. McAllister, M. J.; Li, J.-L.; Adamson, D. H.; Schniepp, H. C.; Abdala, A. A.; Liu, J.; Herrera-Alonso, M.; Milius, D. L.; Car, R.; Prud'homme, R. K.; Aksay, I. A., Single sheet functionalized graphene by oxidation and thermal expansion of graphite. *Chemistry of Materials* **2007,** *19* (18), 4396-4404.
101. Lv, W.; Tang, D.-M.; He, Y.-B.; You, C.-H.; Shi, Z.-Q.; Chen, X.-C.; Chen, C.-M.; Hou, P.-X.; Liu, C.; Yang, Q.-H., Low-Temperature Exfoliated Graphenes: Vacuum-Promoted Exfoliation and Electrochemical Energy Storage. *ACS Nano* **2009,** *3* (11), 3730-3736.
102. Wu, Z.-S.; Ren, W.; Gao, L.; Zhao, J.; Chen, Z.; Liu, B.; Tang, D.; Yu, B.; Jiang, C.; Cheng, H.-M., Synthesis of Graphene Sheets with High Electrical Conductivity and Good Thermal Stability by Hydrogen Arc Discharge Exfoliation. *ACS Nano* **2009,** *3* (2), 411-417.
103. Abdelkader, A. M.; Cooper, A. J.; Dryfe, R. A. W.; Kinloch, I. A., How to get between the sheets: a review of recent works on the electrochemical exfoliation of graphene materials from bulk graphite. *Nanoscale* **2015,** *7* (16), 6944-6956.
104. Inagaki, M., Applications of graphite-intercalation compounds. *Journal of Materials Research* **1989,** *4* (6), 1560-1568.
105. Abdelkader, A. M.; Kinloch, I. A.; Dryfe, R. A. W., Continuous Electrochemical Exfoliation of Micrometer-Sized Graphene Using Synergistic Ion Intercalations and Organic Solvents. *ACS Applied Materials & Interfaces* **2014,** *6* (3), 1632-1639.
106. Liu, J.; Poh, C. K.; Zhan, D.; Lai, L.; Lim, S. H.; Wang, L.; Liu, X.; Sahoo, N. G.; Li, C.; Shen, Z.; Lin, J., Improved synthesis of graphene flakes from the multiple electrochemical exfoliation of graphite rod. *Nano Energy* **2013,** *2* (3), 377-386.
107. Wang, J.; Manga, K. K.; Bao, Q.; Loh, K. P., High-Yield Synthesis of Few-Layer Graphene Flakes through Electrochemical Expansion of Graphite in Propylene Carbonate Electrolyte. *Journal of the American Chemical Society* **2011,** *133* (23), 8888-8891.
108. Kim, Y.-R.; Bong, S.; Kang, Y.-J.; Yang, Y.; Mahajan, R. K.; Kim, J. S.; Kim, H., Electrochemical detection of dopamine in the presence of ascorbic acid using graphene modified electrodes. *Biosensors & Bioelectronics* **2010,** *25* (10), 2366-2369.
109. Khanra, P.; Kuila, T.; Bae, S. H.; Kim, N. H.; Lee, J. H., Electrochemically exfoliated graphene using 9-anthracene carboxylic acid for supercapacitor application. *Journal of Materials Chemistry* **2012,** *22* (46), 24403-24410.
110. Xia, Z. Y.; Giambastiani, G.; Christodoulou, C.; Nardi, M. V.; Koch, N.; Treossi, E.; Bellani, V.; Pezzini, S.; Corticelli, F.; Morandi, V.; Zanelli, A.; Palermo, V., Synergic Exfoliation of Graphene with Organic Molecules and Inorganic Ions for the Electrochemical Production of Flexible Electrodes. *Chempluschem* **2014,** *79* (3), 439-446.
111. Lu, X.; Zhao, C., Controlled electrochemical intercalation, exfoliation and in situ nitrogen doping of graphite in nitrate-based protic ionic liquids. *Physical Chemistry Chemical Physics* **2013,** *15* (46), 20005-20009.
112. Zhou, M.; Tang, J.; Cheng, Q.; Xu, G.; Cui, P.; Qin, L.-C., Few-layer graphene obtained by electrochemical exfoliation of graphite cathode. *Chemical Physics Letters* **2013,** *572*, 61-65.
113. Lotya, M.; King, P. J.; Khan, U.; De, S.; Coleman, J. N., High-Concentration, Surfactant-Stabilized Graphene Dispersions. *ACS Nano* **2010,** *4* (6), 3155-3162.
114. Su, C.-Y.; Lu, A.-Y.; Xu, Y.; Chen, F.-R.; Khlobystov, A. N.; Li, L.-J., High-Quality Thin Graphene Films from Fast Electrochemical Exfoliation. *ACS Nano* **2011,** *5* (3), 2332-2339.
115. Wang, G.; Wang, B.; Park, J.; Wang, Y.; Sun, B.; Yao, J., Highly efficient and large-scale synthesis of graphene by electrolytic exfoliation. *Carbon* **2009,** *47* (14), 3242-3246.

116. Huang, H.; Xia, Y.; Tao, X.; Du, J.; Fang, J.; Gan, Y.; Zhang, W., Highly efficient electrolytic exfoliation of graphite into graphene sheets based on Li ions intercalation-expansion-microexplosion mechanism. *Journal of Materials Chemistry* **2012,** *22* (21), 10452-10456.
117. Zhong, Y. L.; Swager, T. M., Enhanced Electrochemical Expansion of Graphite for in Situ Electrochemical Functionalization. *Journal of the American Chemical Society* **2012,** *134* (43), 17896-17899.
118. Parvez, K.; Li, R.; Puniredd, S. R.; Hernandez, Y.; Hinkel, F.; Wang, S.; Feng, X.; Muellen, K., Electrochemically Exfoliated Graphene as Solution-Processable, Highly Conductive Electrodes for Organic Electronics. *ACS Nano* **2013,** *7* (4), 3598-3606.
119. Ambrosi, A.; Pumera, M., Electrochemically Exfoliated Graphene and Graphene Oxide for Energy Storage and Electrochemistry Applications. *Chemistry (Weinheim an der Bergstrasse, Germany)* **2016,** *22* (1), 153-9.
120. Cooper, A. J.; Velicky, M.; Kinloch, I. A.; Dryfe, R. A. W., On the controlled electrochemical preparation of R4N+ graphite intercalation compounds and their host structural deformation effects. *Journal of Electroanalytical Chemistry* **2014,** *730*, 34-40.
121. Cooper, A. J.; Wilson, N. R.; Kinloch, I. A.; Dryfe, R. A. W., Single stage electrochemical exfoliation method for the production of few-layer graphene via intercalation of tetraalkylammonium cations. *Carbon* **2014,** *66*, 340-350.
122. Abdelkader, A. M.; Kinloch, I. A.; Dryfe, R. A. W., High-yield electro-oxidative preparation of graphene oxide. *Chemical Communications* **2014,** *50* (61), 8402-8404.
123. Wang, S.; Zhang, Y.; Abidi, N.; Cabrales, L., Wettability and Surface Free Energy of Graphene Films. *Langmuir* **2009,** *25* (18), 11078-11081.
124. Shih, C.-J.; Lin, S.; Strano, M. S.; Blankschtein, D., Understanding the Stabilization of Liquid-Phase-Exfoliated Graphene in Polar Solvents: Molecular Dynamics Simulations and Kinetic Theory of Colloid Aggregation. *Journal of the American Chemical Society* **2010,** *132* (41), 14638-14648.
125. Yang, Y.; Lu, F.; Zhou, Z.; Song, W.; Chen, Q.; Ji, X., Electrochemically cathodic exfoliation of graphene sheets in room temperature ionic liquids N-butyl, methylpyrrolidinium bis(trifluoromethylsulfonyl)imide and their electrochemical properties. *Electrochimica Acta* **2013,** *113*, 9-16.
126. Antisari, M. V.; Montone, A.; Jovic, N.; Piscopiello, E.; Alvani, C.; Pilloni, L., Low energy pure shear milling: A method for the preparation of graphite nano-sheets. *Scripta Materialia* **2006,** *55* (11), 1047-1050.
127. Knieke, C.; Berger, A.; Voigt, M.; Taylor, R. N. K.; Roehrl, J.; Peukert, W., Scalable production of graphene sheets by mechanical delamination. *Carbon* **2010,** *48* (11), 3196-3204.
128. Leon, V.; Rodriguez, A. M.; Prieto, P.; Prato, M.; Vazquez, E., Exfoliation of Graphite with Triazine Derivatives under Ball-Milling Conditions: Preparation of Few-Layer Graphene via Selective Noncovalent Interactions. *ACS Nano* **2014,** *8* (1), 563-571.
129. Esau Del Rio-Castillo, A.; Merino, C.; Diez-Barra, E.; Vazquez, E., Selective suspension of single layer graphene mechanochemically exfoliated from carbon nanofibres. *Nano Research* **2014,** *7* (7), 963-972.
130. Aparna, R.; Sivakumar, N.; Balakrishnan, A.; Nair, A. S.; Nair, S. V.; Subramanian, K. R. V., An effective route to produce few-layer graphene using combinatorial ball milling and strong aqueous exfoliants. *Journal of Renewable and Sustainable Energy* **2013,** *5* (3), 033123/1-10.
131. Yao, Y.; Lin, Z.; Li, Z.; Song, X.; Moon, K.-S.; Wong, C.-P., Large-scale production of two-dimensional nanosheets. *Journal of Materials Chemistry* **2012,** *22* (27), 13494-13499.
132. Chen, D.; Chen, G., In situ synthesis of thermoplastic polyurethane/graphene nanoplatelets conductive composite by ball milling. *Journal of Reinforced Plastics and Composites* **2013,** *32* (5), 300-307.
133. Lv, Y.; Yu, L.; Jiang, C.; Chen, S.; Nie, Z., Synthesis of graphene nanosheet powder with layer number control via a soluble salt-assisted route. *Rsc Advances* **2014,** *4* (26), 13350-13354.

134. Wu, H.; Zhao, W.; Hu, H.; Chen, G., One-step in situ ball milling synthesis of polymer-functionalized graphene nanocomposites. *Journal of Materials Chemistry* **2011,** *21* (24), 8626-8632.
135. Zhang, D.; Zhang, X.; Sun, X.; Zhang, H.; Wang, C.; Ma, Y., High performance supercapacitor electrodes based on deoxygenated graphite oxide by ball milling. *Electrochimica Acta* **2013,** *109*, 874-880.
136. Jeon, I. Y.; Bae, S. Y.; Seo, J. M.; Baek, J. B., Scalable Production of Edge-Functionalized Graphene Nanoplatelets via Mechanochemical Ball-Milling. *Advanced Functional Materials* **2015,** *25* (45), 6961-6975.
137. Zhao, W.; Fang, M.; Wu, F.; Wu, H.; Wang, L.; Chen, G., Preparation of graphene by exfoliation of graphite using wet ball milling. *Journal of Materials Chemistry* **2010,** *20* (28), 5817-5819.
138. Zhang, Y. B.; Small, J. P.; Pontius, W. V.; Kim, P., Fabrication and electric-field-dependent transport measurements of mesoscopic graphite devices. *Applied Physics Letters* **2005,** *86* (7), 073104/1-3.
139. Novoselov, K. S.; Jiang, D.; Schedin, F.; Booth, T. J.; Khotkevich, V. V.; Morozov, S. V.; Geim, A. K., Two-dimensional atomic crystals. *Proceedings of the National Academy of Sciences of the United States of America* **2005,** *102* (30), 10451-10453.
140. Hong, N. N.; Zhan, J.; Wang, X.; Stec, A. A.; Hull, T. R.; Ge, H.; Xing, W. Y.; Song, L.; Hu, Y., Enhanced mechanical, thermal and flame retardant properties by combining graphene nanosheets and metal hydroxide nanorods for Acrylonitrile-Butadiene-Styrene copolymer composite. *Composites Part a-Applied Science and Manufacturing* **2014,** *64*, 203-210.
141. Li, F.; Liu, Y.; Qu, C. B.; Xiao, H. M.; Hua, Y.; Sui, G. X.; Fu, S. Y., Enhanced mechanical properties of short carbon fiber reinforced polyethersulfone composites by graphene oxide coating. *Polymer* **2015,** *59*, 155-165.
142. Layek, R. K.; Samanta, S.; Chatterjee, D. P.; Nandi, A. K., Physical and mechanical properties of poly(methyl methacrylate) -functionalized graphene/poly(vinylidine fluoride) nanocomposites Piezoelectric beta polymorph formation. *Polymer* **2010,** *51* (24), 5846-5856.
143. Song, B.; Cuniberti, G.; Sanvito, S.; Fang, H. P., Nucleobase adsorbed at graphene devices: Enhance bio-sensorics. *Applied Physics Letters* **2012,** *100* (6), 063101/1-4.
144. Lee, D. Y.; Khatun, Z.; Lee, J.-H.; Lee, Y.-k.; In, I., Blood Compatible Graphene/Heparin Conjugate through Noncovalent Chemistry. *Biomacromolecules* **2011,** *12* (2), 336-341.
145. Wang, Y.; Li, Z.; Wang, J.; Li, J.; Lin, Y., Graphene and graphene oxide: biofunctionalization and applications in biotechnology. *Trends in Biotechnology* **2011,** *29* (5), 205-212.
146. Georgakilas, V.; Tiwari, J. N.; Kemp, K. C.; Perrnan, J. A.; Bourlinos, A. B.; Kim, K. S.; Zboril, R., Noncovalent Functionalization of Graphene and Graphene Oxide for Energy Materials, Biosensing, Catalytic, and Biomedical Applications. *Chemical Reviews* **2016,** *116* (9), 5464-5519.
147. Ceasano, F.; Scarano, D., Carbon for Sensing Devices. Springer Switzerland, 2015.
148. Lee, D. W.; Kim, T.; Lee, M., An amphiphilic pyrene sheet for selective functionalization of graphene. *Chemical Communications* **2011,** *47* (29), 8259-8261.
149. Ghosh, A.; Rao, K. V.; George, S. J.; Rao, C. N. R., Noncovalent Functionalization, Exfoliation, and Solubilization of Graphene in Water by Employing a Fluorescent Coronene Carboxylate. *Chemistry-a European Journal* **2010,** *16* (9), 2700-2704.
150. Geng, J. X.; Jung, H., Porphyrin Functionalized Graphene Sheets in Aqueous Suspensions: From the Preparation of Graphene Sheets to Highly Conductive Graphene Films. *Journal of Physical Chemistry C* **2010,** *114* (18), 8227-8234.
151. Bose, S.; Kuila, T.; Mishra, A. K.; Kim, N. H.; Lee, J. H., Preparation of non-covalently functionalized graphene using 9-anthracene carboxylic acid. *Nanotechnology* **2011,** *22* (40), 405603/1-7.
152. Stankovich, S.; Piner, R. D.; Chen, X. Q.; Wu, N. Q.; Nguyen, S. T.; Ruoff, R. S., Stable aqueous dispersions of graphitic nanoplatelets via the reduction of exfoliated graphite oxide in

the presence of poly(sodium 4-styrenesulfonate). *Journal of Materials Chemistry* **2006,** *16* (2), 155-158.
153. Alwarappan, S.; Boyapalle, S.; Kumar, A.; Li, C. Z.; Mohapatra, S., Comparative Study of Single-, Few-, and Multi layered Graphene toward Enzyme Conjugation and Electrochemical Response. *Journal of Physical Chemistry C* **2012,** *116* (11), 6556-6559.
154. Lian, Q. W.; He, Z. F.; He, Q.; Luo, A.; Yan, K. W.; Zhang, D. X.; Lu, X. Q.; Zhou, X. B., Simultaneous determination of ascorbic acid, dopamine and uric acid based on tryptophan functionalized graphene. *Analytica Chimica Acta* **2014,** *823*, 32-39.
155. Wang, Y.; Li, Y.; Tang, L.; Lu, J.; Li, J., Application of graphene-modified electrode for selective detection of dopamine. *Electrochemistry Communications* **2009,** *11* (4), 889-892.
156. Min, S. K.; Kim, W. Y.; Cho, Y.; Kim, K. S., Fast DNA sequencing with a graphene-based nanochannel device. *Nature Nanotechnology* **2011,** *6* (3), 162-165.
157. Wahid, M. H.; Stroeher, U. H.; Eroglu, E.; Chen, X. J.; Vimalanathan, K.; Raston, C. L.; Boulos, R. A., Aqueous based synthesis of antimicrobial-decorated graphene. *Journal of Colloid and Interface Science* **2015,** *443*, 88-96.
158. Schneider, G. F.; Xu, Q.; Hage, S.; Luik, S.; Spoor, J. N. H.; Malladi, S.; Zandbergen, H.; Dekker, C., Tailoring the hydrophobicity of graphene for its use as nanopores for DNA translocation. *Nature Communications* **2013,** *4,* 1-7.
159. Zeng, Q.; Cheng, J.; Tang, L.; Liu, X.; Liu, Y.; Li, J.; Jiang, J., Self-Assembled Graphene-Enzyme Hierarchical Nanostructures for Electrochemical Biosensing. *Advanced Functional Materials* **2010,** *20* (19), 3366-3372.
160. Yang, Y. K.; He, C. E.; Peng, R. G.; Baji, A.; Du, X. S.; Huang, Y. L.; Xie, X. L.; Mai, Y. W., Non-covalently modified graphene sheets by imidazolium ionic liquids for multifunctional polymer nanocomposites. *Journal of Materials Chemistry* **2012,** *22* (12), 5666-5675.
161. Kim, T.; Lee, H.; Kim, J.; Suh, K. S., Synthesis of Phase Transferable Graphene Sheets Using Ionic Liquid Polymers. *ACS Nano* **2010,** *4* (3), 1612-1618.
162. Zhang, X. F.; Shao, X. N., pi-pi binding ability of different carbon nano-materials with aromatic phthalocyanine molecules: Comparison between graphene, graphene oxide and carbon nanotubes. *Journal of Photochemistry and Photobiology a-Chemistry* **2014,** *278*, 69-74.
163. Yang, X.; Li, J. X.; Wen, T.; Ren, X. M.; Huang, Y. S.; Wang, X. K., Adsorption of naphthalene and its derivatives on magnetic graphene composites and the mechanism investigation. *Colloids and Surfaces a-Physicochemical and Engineering Aspects* **2013,** *422*, 118-125.
164. Balcioglu, M.; Rana, M.; Yigit, M. V., Doxorubicin loading on graphene oxide, iron oxide and gold nanoparticle hybrid. *Journal of Materials Chemistry B* **2013,** *1* (45), 6187-6193.
165. Koninti, R. K.; Sengupta, A.; Gavvala, K.; Ballav, N.; Hazra, P., Loading of an anti-cancer drug onto graphene oxide and subsequent release to DNA/RNA: a direct optical detection. *Nanoscale* **2014,** *6* (5), 2937-2944.
166. Zhou, L.; Jiang, H. J.; Wei, S. H.; Ge, X. F.; Zhou, J. H.; Shen, J., High-efficiency loading of hypocrellin B on graphene oxide for photodynamic therapy. *Carbon* **2012,** *50* (15), 5594-5604.
167. Liang, J. J.; Huang, Y.; Zhang, L.; Wang, Y.; Ma, Y. F.; Guo, T. Y.; Chen, Y. S., Molecular-Level Dispersion of Graphene into Poly(vinyl alcohol) and Effective Reinforcement of their Nanocomposites. *Advanced Functional Materials* **2009,** *19* (14), 2297-2302.
168. Rafiee, M. A.; Rafiee, J.; Wang, Z.; Song, H. H.; Yu, Z. Z.; Koratkar, N., Enhanced Mechanical Properties of Nanocomposites at Low Graphene Content. *ACS Nano* **2009,** *3* (12), 3884-3890.
169. Ramanathan, T.; Abdala, A. A.; Stankovich, S.; Dikin, D. A.; Herrera-Alonso, M.; Piner, R. D.; Adamson, D. H.; Schniepp, H. C.; Chen, X.; Ruoff, R. S.; Nguyen, S. T.; Aksay, I. A.; Prud'homme, R. K.; Brinson, L. C., Functionalized graphene sheets for polymer nanocomposites. *Nature Nanotechnology* **2008,** *3* (6), 327-331.

170. Wajid, A. S.; Das, S.; Irin, F.; Ahmed, H. S. T.; Shelburne, J. L.; Parviz, D.; Fullerton, R. J.; Jankowski, A. F.; Hedden, R. C.; Green, M. J., Polymer-stabilized graphene dispersions at high concentrations in organic solvents for composite production. *Carbon* **2012,** *50* (2), 526-534.
171. Lian, M.; Fan, J. C.; Shi, Z. X.; Li, H.; Yin, J., Kevlar (R)-functionalized graphene nanoribbon for polymer reinforcement. *Polymer* **2014,** *55* (10), 2578-2587.
172. Naebe, M.; Wang, J.; Amini, A.; Khayyam, H.; Hameed, N.; Li, L. H.; Chen, Y.; Fox, B., Mechanical Property and Structure of Covalent Functionalised Graphene/Epoxy Nanocomposites. *Scientific Reports* **2014,** *4,* 1-7.
173. Tian, M. W.; Qu, L. J.; Zhang, X. S.; Zhang, K.; Zhu, S. F.; Guo, X. Q.; Han, G. T.; Tang, X. N.; Sun, Y. N., Enhanced mechanical and thermal properties of regenerated cellulose/graphene composite fibers. *Carbohydrate Polymers* **2014,** *111*, 456-462.
174. Ionita, M.; Pandele, A. M.; Crica, L.; Pilan, L., Improving the thermal and mechanical properties of polysulfone by incorporation of graphene oxide. *Composites Part B-Engineering* **2014,** *59*, 133-139.
175. Maity, N.; Mandal, A.; Nandi, A. K., Synergistic interfacial effect of polymer stabilized graphene via non-covalent functionalization in poly(vinylidene fluoride) matrix yielding superior mechanical and electronic properties. *Polymer* **2016,** *88*, 79-93.
176. Qian, X. D.; Song, L.; Yu, B.; Yang, W.; Wang, B. B.; Hu, Y.; Yuen, R. K. K., One-pot surface functionalization and reduction of graphene oxide with long-chain molecules: Preparation and its enhancement on the thermal and mechanical properties of polyurea. *Chemical Engineering Journal* **2014,** *236*, 233-241.
177. Bai, H.; Xu, Y.; Zhao, L.; Li, C.; Shi, G., Non-covalent functionalization of graphene sheets by sulfonated polyaniline. *Chemical Communications* **2009,** (13), 1667-1669.
178. Wang, H.; Hao, Q.; Yang, X.; Lu, L.; Wang, X., Graphene oxide doped polyaniline for supercapacitors. *Electrochemistry Communications* **2009,** *11* (6), 1158-1161.
179. Sharma, V.; Hynek, D.; Trnkova, L.; Hemzal, D.; Marik, M.; Kizek, R.; Hubalek, J., Electrochemical determination of adenine using a glassy carbon electrode modified with graphene oxide and polyaniline. *Microchimica Acta* **2016,** *183* (4), 1299-1306.
180. Huang, L.; Li, C.; Shi, G. Q., High-performance and flexible electrochemical capacitors based on graphene/polymer composite films. *Journal of Materials Chemistry A* **2014,** *2* (4), 968-974.
181. Chang, H. H.; Chang, C. K.; Tsai, Y. C.; Liao, C. S., Electrochemically synthesized graphene/polypyrrole composites and their use in supercapacitor. *Carbon* **2012,** *50* (6), 2331-2336.
182. Alvi, F.; Ram, M. K.; Basnayaka, P. A.; Stefanakos, E.; Goswami, Y.; Kumar, A., Graphene-polyethylenedioxythiophene conducting polymer nanocomposite based supercapacitor. *Electrochimica Acta* **2011,** *56* (25), 9406-9412.
183. Zhang, J.; Lei, J.; Pan, R.; Xue, Y.; Ju, H., Highly sensitive electrocatalytic biosensing of hypoxanthine based on functionalization of graphene sheets with water-soluble conducting graft copolymer. *Biosensors & Bioelectronics* **2010,** *26* (2), 371-376.
184. Liang, Y. M.; Yu, L. L.; Yang, R.; Li, X.; Qu, L. B.; Li, J. J., High sensitive and selective graphene oxide/molecularly imprinted polymer electrochemical sensor for 2,4-dichlorophenol in water. *Sensors and Actuators B-Chemical* **2017,** *240*, 1330-1335.
185. Dadkhah, S.; Ziaei, E.; Mehdinia, A.; Kayyal, T. B.; Jabbari, A., A glassy carbon electrode modified with amino-functionalized graphene oxide and molecularly imprinted polymer for electrochemical sensing of bisphenol A. *Microchimica Acta* **2016,** *183* (6), 1933-1941.
186. Nguyen, B. H.; Nguyen, B. T.; Vu, H. V.; Nguyen, C. V.; Nguyen, D. T.; Nguyen, L. T.; Vu, T. T.; Tran, L. D., Development of label-free electrochemical lactose biosensor based on graphene/poly(1,5-diaminonaphthalene) film. *Current Applied Physics* **2016,** *16* (2), 135-140.
187. Zhu, Y. W.; Murali, S.; Cai, W. W.; Li, X. S.; Suk, J. W.; Potts, J. R.; Ruoff, R. S., Graphene and Graphene Oxide: Synthesis, Properties, and Applications (vol 22, pg 3906, 2010). *Advanced Materials* **2010,** *22* (46), 5226-5226.

188. Wang, J.; Chen, Z. M.; Chen, B. L., Adsorption of Polycyclic Aromatic Hydrocarbons by Graphene and Graphene Oxide Nanosheets. *Environmental Science & Technology* **2014,** *48* (9), 4817-4825.
189. Su, Q.; Pang, S. P.; Alijani, V.; Li, C.; Feng, X. L.; Mullen, K., Composites of Graphene with Large Aromatic Molecules. *Advanced Materials* **2009,** *21* (31), 3191-3195.
190. Iliut, M.; Gabudean, A. M.; Leordean, C.; Simon, T.; Teodorescu, C. M.; Astilean, S., Riboflavin enhanced fluorescence of highly reduced graphene oxide. *Chemical Physics Letters* **2013,** *586*, 127-131.
191. Lv, M. J.; Mei, T.; Zhang, C. A.; Wang, X. B., Selective and sensitive electrochemical detection of dopamine based on water-soluble porphyrin functionalized graphene nanocomposites. *Rsc Advances* **2014,** *4* (18), 9261-9270.
192. Yang, Q.; Pan, X. J.; Huang, F.; Li, K. C., Fabrication of High-Concentration and Stable Aqueous Suspensions of Graphene Nanosheets by Noncovalent Functionalization with Lignin and Cellulose Derivatives. *Journal of Physical Chemistry C* **2010,** *114* (9), 3811-3816.
193. Zhang, J. Z.; Xu, Y. H.; Cui, L.; Fu, A. P.; Yang, W. R.; Barrow, C.; Liu, J. Q., Mechanical properties of graphene films enhanced by homo-telechelic functionalized polymer fillers via pi-pi It stacking interactions. *Composites Part a-Applied Science and Manufacturing* **2015,** *71*, 1-8.
194. Zhang, B. Q.; Ning, W.; Zhang, J. M.; Qiao, X.; Zhang, J.; He, J. S.; Liu, C. Y., Stable dispersions of reduced graphene oxide in ionic liquids. *Journal of Materials Chemistry* **2010,** *20* (26), 5401-5403.
195. Bourlinos, A. B.; Gournis, D.; Petridis, D.; Szabo, T.; Szeri, A.; Dekany, I., Graphite oxide: Chemical reduction to graphite and surface modification with primary aliphatic amines and amino acids. *Langmuir* **2003,** *19* (15), 6050-6055.
196. Chua, C. K.; Sofer, Z.; Luxa, J.; Pumera, M., Selective Nitrogen Functionalization of Graphene by Bucherer-Type Reaction. *Chemistry-a European Journal* **2015,** *21* (22), 8090-8095.
197. Yang, H.; Li, F.; Shan, C.; Han, D.; Zhang, Q.; Niu, L.; Ivaska, A., Covalent functionalization of chemically converted graphene sheets via silane and its reinforcement. *Journal of Materials Chemistry* **2009,** *19* (26), 4632-4638.
198. Laaksonen, P.; Kainlauri, M.; Laaksonen, T.; Shchepetov, A.; Jiang, H.; Ahopelto, J.; Linder, M. B., Interfacial Engineering by Proteins: Exfoliation and Functionalization of Graphene by Hydrophobins. *Angewandte Chemie-International Edition* **2010,** *49* (29), 4946-4949.
199. Kang, S. M.; Lee, H., Surface Modification of Highly Ordered Pyrolytic Graphite (HOPG) by a Mussel-Inspired Poly(norepinephrine) Coating: Characterizations and Cell Adhesion Test. *Bulletin of the Korean Chemical Society* **2013,** *34* (3), 960-962.
200. Xu, Y. F.; Liu, Z. B.; Zhang, X. L.; Wang, Y.; Tian, J. G.; Huang, Y.; Ma, Y. F.; Zhang, X. Y.; Chen, Y. S., A Graphene Hybrid Material Covalently Functionalized with Porphyrin: Synthesis and Optical Limiting Property. *Advanced Materials* **2009,** *21* (12), 1275-1279.
201. Cui, Y.; Kim, S. N.; Jones, S. E.; Wissler, L. L.; Naik, R. R.; McAlpine, M. C., Chemical Functionalization of Graphene Enabled by Phage Displayed Peptides. *Nano Letters* **2010,** *10* (11), 4559-4565.
202. Yang, H.; Shan, C.; Li, F.; Han, D.; Zhang, Q.; Niu, L., Covalent functionalization of polydisperse chemically-converted graphene sheets with amine-terminated ionic liquid. *Chemical Communications* **2009,** (26), 3880-3882.
203. Bekyarova, E.; Itkis, M. E.; Ramesh, P.; Berger, C.; Sprinkle, M.; de Heer, W. A.; Haddon, R. C., Chemical Modification of Epitaxial Graphene: Spontaneous Grafting of Aryl Groups. *Journal of the American Chemical Society* **2009,** *131* (4), 1336-1337.
204. Avinash, M. B.; Subrahmanyam, K. S.; Sundarayya, Y.; Govindaraju, T., Covalent modification and exfoliation of graphene oxide using ferrocene. *Nanoscale* **2010,** *2* (9), 1762-1766.
205. Stankovich, S.; Dikin, D. A.; Dommett, G. H. B.; Kohlhaas, K. M.; Zimney, E. J.; Stach, E. A.; Piner, R. D.; Nguyen, S. T.; Ruoff, R. S., Graphene-based composite materials. *Nature* **2006,** *442* (7100), 282-286.

206. Liu, Z.; Robinson, J. T.; Sun, X.; Dai, H., PEGylated nanographene oxide for delivery of water-insoluble cancer drugs. *Journal of the American Chemical Society* **2008,** *130* (33), 10876–10877.
207. Chen, G.; Zhai, S.; Zhai, Y.; Zhang, K.; Yue, Q.; Wang, L.; Zhao, J.; Wang, H.; Liu, J.; Jia, J., Preparation of sulfonic-functionalized graphene oxide as ion-exchange material and its application into electrochemiluminescence analysis. *Biosensors & Bioelectronics* **2011,** *26* (7), 3136-3141.
208. Jeon, I.-Y.; Choi, H.-J.; Jung, S.-M.; Seo, J.-M.; Kim, M.-J.; Dai, L.; Baek, J.-B., Large-Scale Production of Edge-Selectively Functionalized Graphene Nanoplatelets via Ball Milling and Their Use as Metal-Free Electrocatalysts for Oxygen Reduction Reaction. *Journal of the American Chemical Society* **2013,** *135* (4), 1386-1393.
209. Manna, B.; Raj, C. R., Covalent functionalization and electrochemical tuning of reduced graphene oxide for the bioelectrocatalytic sensing of serum lactate. *Journal of Materials Chemistry B* **2016,** *4* (26), 4585-4593.
210. Wang, A. J.; Yu, W.; Huang, Z. P.; Zhou, F.; Song, J. B.; Song, Y. L.; Long, L. L.; Cifuentes, M. P.; Humphrey, M. G.; Zhang, L.; Shao, J. D.; Zhang, C., Covalent functionalization of reduced graphene oxide with porphyrin by means of diazonium chemistry for nonlinear optical performance. *Scientific Reports* **2016,** *6,* 1-12.
211. Qi, X. Y.; Pu, K. Y.; Zhou, X. Z.; Li, H.; Liu, B.; Boey, F.; Huang, W.; Zhang, H., Conjugated-Polyelectrolyte-Functionalized Reduced Graphene Oxide with Excellent Solubility and Stability in Polar Solvents. *Small* **2010,** *6* (5), 663-669.
212. Englert, J. M.; Dotzer, C.; Yang, G.; Schmid, M.; Papp, C.; Gottfried, J. M.; Steinrueck, H.-P.; Spiecker, E.; Hauke, F.; Hirsch, A., Covalent bulk functionalization of graphene. *Nature Chemistry* **2011,** *3* (4), 279-286.
213. Lomeda, J. R.; Doyle, C. D.; Kosynkin, D. V.; Hwang, W.-F.; Tour, J. M., Diazonium Functionalization of Surfactant-Wrapped Chemically Converted Graphene Sheets. *Journal of the American Chemical Society* **2008,** *130* (48), 16201-16206.
214. Niyogi, S.; Bekyarova, E.; Itkis, M. E.; McWilliams, J. L.; Hamon, M. A.; Haddon, R. C., Solution properties of graphite and graphene. *Journal of the American Chemical Society* **2006,** *128* (24), 7720-7721.
215. Fang, M.; Wang, K.; Lu, H.; Yang, Y.; Nutt, S., Covalent polymer functionalization of graphene nanosheets and mechanical properties of composites. *Journal of Materials Chemistry* **2009,** *19* (38), 7098-7105.
216. Saini, D., Covalent functionalisation of graphene: novel approach to change electronic structure of graphene. *Materials Research Innovations* **2015,** *19* (4), 287-294.
217. Liu, L. H.; Yan, M. D., Functionalization of pristine graphene with perfluorophenyl azides. *Journal of Materials Chemistry* **2011,** *21* (10), 3273-3276.
218. Sainsbury, T.; Passarelli, M.; Naftaly, M.; Gnaniah, S.; Spencer, S. J.; Pollard, A. J., Covalent Carbene Functionalization of Graphene: Toward Chemical Band-Gap Manipulation. *ACS Applied Materials & Interfaces* **2016,** *8* (7), 4870-4877.
219. Quintana, M.; Spyrou, K.; Grzelczak, M.; Browne, W. R.; Rudolf, P.; Prato, M., Functionalization of Graphene via 1,3-Dipolar Cycloaddition. *ACS Nano* **2010,** *4* (6), 3527-3533.
220. Georgakilas, V.; Bourlinos, A. B.; Zboril, R.; Steriotis, T. A.; Dallas, P.; Stubos, A. K.; Trapalis, C., Organic functionalisation of graphenes. *Chemical Communications* **2010,** *46* (10), 1766-1768.
221. He, H.; Gao, C., General Approach to Individually Dispersed, Highly Soluble, and Conductive Graphene Nanosheets Functionalized by Nitrene Chemistry. *Chemistry of Materials* **2010,** *22* (17), 5054-5064.
222. Zhong, X.; Jin, J.; Li, S.; Niu, Z.; Hu, W.; Li, R.; Ma, J., Aryne cycloaddition: highly efficient chemical modification of graphene. *Chemical Communications* **2010,** *46* (39), 7340-7342.
223. Daukiya, L.; Mattioli, C.; Aubel, D.; Hajjar-Garreau, S.; Vonau, F.; Denys, E.; Reiter, G.; Fransson, J.; Perrin, E.; Bocquet, M.-L.; Bena, C.; Gourdon, A.; Simon, L., Covalent

Functionalization by Cycloaddition Reactions of Pristine Defect-Free Graphene. *ACS Nano* **2017,** *11* (1), 627–634.
224. Bjerglund, E.; Kongsfelt, M.; Shimizu, K.; Jensen, B. B. E.; Koefoed, L.; Ceccato, M.; Skrydstrup, T.; Pedersen, S. U.; Daasbjerg, K., Controlled Electrochemical Carboxylation of Graphene To Create a Versatile Chemical Platform for Further Functionalization. *Langmuir* **2014,** *30* (22), 6622-6628.
225. Xia, Z. Y.; Leonardi, F.; Gobbi, M.; Liu, Y.; Bellani, V.; Liscio, A.; Kovtun, A.; Li, R. J.; Feng, X. L.; Orgiu, E.; Samori, P.; Treossi, E.; Palermo, V., Electrochemical Functionalization of Graphene at the Nanoscale with Self-Assembling Diazonium Salts. *ACS Nano* **2016,** *10* (7), 7125-7134.
226. Won Cho, D.; Parthasarathi, R.; Pimentel, A. S.; Maestas, G. D.; Park, H. J.; Yoon, U. C.; Dunaway-Mariano, D.; Gnanakaran, S.; Langan, P.; Mariano, P. S., Nature and Kinetic Analysis of Carbon-Carbon Bond Fragmentation Reactions of Cation Radicals Derived from SET-Oxidation of Lignin Model Compounds. *Journal of Organic Chemistry* **2010,** *75* (19), 6549-6562.
227. Jeon, I.-Y.; Shin, Y.-R.; Sohn, G.-J.; Choi, H.-J.; Bae, S.-Y.; Mahmood, J.; Jung, S.-M.; Seo, J.-M.; Kim, M.-J.; Chang, D. W.; Dai, L.; Baek, J.-B., Edge-carboxylated graphene nanosheets via ball milling. *Proceedings of the National Academy of Sciences of the United States of America* **2012,** *109* (15), 5588-5593.
228. Jeon, I.-Y.; Choi, M.; Choi, H.-J.; Jung, S.-M.; Kim, M.-J.; Seo, J.-M.; Bae, S.-Y.; Yoo, S.; Kim, G.; Jeong, H. Y.; Park, N.; Baek, J.-B., Antimony-doped graphene nanoplatelets. *Nature Communications* **2015,** *6,* 1-8.
229. Kim, M.-J.; Jean, I.-Y.; Seo, J.-M.; Dai, L.; Baek, J.-B., Graphene Phosphonic Acid as an Efficient Flame Retardant. *ACS Nano* **2014,** *8* (3), 2820-2825.
230. Jeon, I.-Y.; Ju, M. J.; Xu, J.; Choi, H.-J.; Seo, J.-M.; Kim, M.-J.; Choi, I. T.; Kim, H. M.; Kim, J. C.; Lee, J.-J.; Liu, H. K.; Kim, H. K.; Dou, S.; Dai, L.; Baek, J.-B., Edge-Fluorinated Graphene Nanoplatelets as High Performance Electrodes for Dye-Sensitized Solar Cells and Lithium Ion Batteries. *Advanced Functional Materials* **2015,** *25* (8), 1170-1179.
231. Jeon, I.-Y.; Choi, H.-J.; Choi, M.; Seo, J.-M.; Jung, S.-M.; Kim, M.-J.; Zhang, S.; Zhang, L.; Xia, Z.; Dai, L.; Park, N.; Baek, J.-B., Facile, scalable synthesis of edge-halogenated graphene nanoplatelets as efficient metal-free eletrocatalysts for oxygen reduction reaction. *Scientific Reports* **2013,** *3,* 1810/1-7.
232. Jeon, I.-Y.; Choi, H.-J.; Ju, M. J.; Choi, I. T.; Lim, K.; Ko, J.; Kim, H. K.; Kim, J. C.; Lee, J.-J.; Shin, D.; Jung, S.-M.; Seo, J.-M.; Kim, M.-J.; Park, N.; Dai, L.; Baek, J.-B., Direct nitrogen fixation at the edges of graphene nanoplatelets as efficient electrocatalysts for energy conversion. *Scientific Reports* **2013,** *3,* 2260/1-7.
233. Jeon, I.-Y.; Zhang, S.; Zhang, L.; Choi, H.-J.; Seo, J.-M.; Xia, Z.; Dai, L.; Baek, J.-B., Edge-Selectively Sulfurized Graphene Nanoplatelets as Efficient Metal-Free Electrocatalysts for Oxygen Reduction Reaction: The Electron Spin Effect. *Advanced Materials* **2013,** *25* (42), 6138-6145.
234. Liu, K.; Chen, S.; Luo, Y.; Jia, D.; Gao, H.; Hu, G.; Liu, L., Edge-functionalized graphene as reinforcement of epoxy-based conductive composite for electrical interconnects. *Composites Science and Technology* **2013,** *88*, 84-91.
235. Sun, Z.; Kohama, S.-i.; Zhang, Z.; Lomeda, J. R.; Tour, J. M., Soluble graphene through edge-selective functionalization. *Nano Research* **2010,** *3* (2), 117-125.
236. Tan, Y.-Z.; Yang, B.; Parvez, K.; Narita, A.; Osella, S.; Beljonne, D.; Feng, X.; Muellen, K., Atomically precise edge chlorination of nanographenes and its application in graphene nanoribbons. *Nature Communications* **2013,** *4,* 2646/1-7.
237. Wu, J. S.; Pisula, W.; Mullen, K., Graphenes as potential material for electronics. *Chemical Reviews* **2007,** *107* (3), 718-747.
238. Malard, L. M.; Pimenta, M. A.; Dresselhaus, G.; Dresselhaus, M. S., Raman spectroscopy in graphene. *Physics Reports-Review Section of Physics Letters* **2009,** *473* (5-6), 51-87.

239. Ferrari, A. C.; Meyer, J. C.; Scardaci, V.; Casiraghi, C.; Lazzeri, M.; Mauri, F.; Piscanec, S.; Jiang, D.; Novoselov, K. S.; Roth, S.; Geim, A. K., Raman spectrum of graphene and graphene layers. *Physical Review Letters* **2006,** *97* (18), 187401/1-4.
240. Wang, K.-A.; Rao, A. M.; Eklund, P. C.; Dresselhaus, M.; Dresselhaus, G., Observation of higher-order infrared modes in solid C60films. *Phys. Rev. B* **1993,** *48,* 11375-11380.
241. Tuinstra, F.; Koenig, J. L., Raman spectrum of graphite. *Journal of Chemical Physics* **1970,** *53* (3), 1126.
242. Reich, S.; Thomsen, C., Raman spectroscopy of graphite. *Philosophical Transactions of the Royal Society a-Mathematical Physical and Engineering Sciences* **2004,** *362* (1824), 2271-2288.
243. Saito, R.; Jorio, A.; Souza, A. G.; Dresselhaus, G.; Dresselhaus, M. S.; Pimenta, M. A., Probing phonon dispersion relations of graphite by double resonance Raman scattering. *Physical Review Letters* **2002,** *88* (2), 027401/1-4.
244. Cancado, L. G.; Pimenta, M. A.; Saito, R.; Jorio, A.; Ladeira, L. O.; Grueneis, A.; Souza, A. G.; Dresselhaus, G.; Dresselhaus, M. S., Stokes and anti-Stokes double resonance Raman scattering in two-dimensional graphite. *Physical Review B* **2002,** *66* (3), 035415/1-5.
245. Cancado, L. G.; Takai, K.; Enoki, T.; Endo, M.; Kim, Y. A.; Mizusaki, H.; Speziali, N. L.; Jorio, A.; Pimenta, M. A., Measuring the degree of stacking order in graphite by Raman spectroscopy. *Carbon* **2008,** *46* (2), 272-275.
246. Eckmann, A.; Felten, A.; Verzhbitskiy, I.; Davey, R.; Casiraghi, C., Raman study on defective graphene: Effect of the excitation energy, type, and amount of defects. *Physical Review B* **2013,** *88* (3), 035426/1-11.
247. Eckmann, A.; Felten, A.; Mishchenko, A.; Britnell, L.; Krupke, R.; Novoselov, K. S.; Casiraghi, C., Probing the Nature of Defects in Graphene by Raman Spectroscopy. *Nano Letters* **2012,** *12* (8), 3925-3930.
248. Atkins, P. W., *Physical Chemistry*. 6th Edition ed.; Oxford University Press: Oxford, UK., 1998.
249. Zhang, L. Y.; Shi, T. J.; Wu, S. L.; Zhou, H. O., Sulfonated graphene oxide: the new and effective material for synthesis of polystyrene-based nanocomposites. *Colloid and Polymer Science* **2013,** *291* (9), 2061-2068.
250. Jang, J.; Pham, V. H.; Rajagopalan, B.; Hur, S. H.; Chung, J. S., Effects of the alkylamine functionalization of graphene oxide on the properties of polystyrene nanocomposites. *Nanoscale Research Letters* **2014,** *9,* 265/1-6.
251. Goldstein, J.; Newbury, D.; Joy, D.; Lyman, C.; Echlin, P.; Lifshin, E.; Sawyer, L.; Michael, J. R., *Scanning Electron Microscopy and X-ray Microanalysis: Third Edition*. Third ed.; Springer Science & Business Media: Berlin, Germany, 2012.
252. Chescoe, D.; Peterhew, P. J., *The Operation of Transmission and Scanning Electron Microscopes*. Oxford University Press: Oxford, United Kingdom, 1990.
253. Goldstein, J. I.; Newbury, D. E.; Echlin, P.; Joy, D. C.; Romig, A. D.; Lyman, C. E.; Fiori, C.; Lifshin, E., Scanning Electron Microscopy and X-ray Microanalysis. Plenum Press: New York, 1992.
254. Zhou, W.; Apkarian, R. P.; Wang, Z.; Joy, D., *Scanning Microscopy for Nanotechnology: Techniques and Applications*. Springer Science and Business Media, LLC: New York, 2006.
255. Williams, D. B.; Carter, B. C., *Transmission Electron MicroscopyA textbook for Materials Science*. Plenum Press: New York, 1996.
256. Wilson, N. R.; Pandey, P. A.; Beanland, R.; Rourke, J. P.; Lupo, U.; Rowlands, G.; Romer, R. A., On the structure and topography of free-standing chemically modified graphene. *New Journal of Physics* **2010,** *12,* 125010/1-22.
257. Meyer, J. C.; Kisielowski, C.; Erni, R.; Rossell, M. D.; Crommie, M. F.; Zettl, A., Direct Imaging of Lattice Atoms and Topological Defects in Graphene Membranes. *Nano Letters* **2008,** *8* (11), 3582-3586.
258. Hashimoto, A.; Suenaga, K.; Gloter, A.; Urita, K.; Iijima, S., Direct evidence for atomic defects in graphene layers. *Nature* **2004,** *430* (7002), 870-873.

259. Zhang, X. Y.; Coleman, A. C.; Katsonis, N.; Browne, W. R.; van Wees, B. J.; Feringa, B. L., Dispersion of graphene in ethanol using a simple solvent exchange method. *Chemical Communications* **2010,** *46* (40), 7539-7541.
260. Lapshin, R. V., Feature-oriented scanning methodology for probe microscopy and nanotechnology. *Nanotechnology* **2004,** *15* (9), 1135-1151.
261. Binnig, G.; Quate, C. F.; Gerber, C., ATOMIC FORCE MICROSCOPE. *Physical Review Letters* **1986,** *56* (9), 930-933.
262. Butt, H. J.; Cappella, B.; Kappl, M., Force measurements with the atomic force microscope: Technique, interpretation and applications. *Surface Science Reports* **2005,** *59* (1-6), 1-152.
263. Jalili, N.; Laxminarayana, K., A review of atomic force microscopy imaging systems: application to molecular metrology and biological sciences. *Mechatronics* **2004,** *14* (8), 907-945.
264. Alessandrini, A.; Facci, P., AFM: a versatile tool in biophysics. *Measurement Science and Technology* **2005,** *16* (6), 65-92.
265. Tamayo, J.; Garcia, R., Deformation, contact time, and phase contrast in tapping mode scanning force microscopy. *Langmuir* **1996,** *12* (18), 4430-4435.
266. Novoselov, K. S.; Geim, A. K.; Morozov, S. V.; Jiang, D.; Katsnelson, M. I.; Grigorieva, I. V.; Dubonos, S. V.; Firsov, A. A., Two-dimensional gas of massless Dirac fermions in graphene. *Nature* **2005,** *438* (7065), 197-200.
267. Jasim, D. A.; Lozano, N.; Kostarelos, K., Synthesis of few-layered, high-purity graphene oxide sheets from different graphite sources for biology. *2d Materials* **2016,** *3* (1).
268. Coleman, J. N., Liquid-Phase Exfoliation of Nanotubes and Graphene. *Advanced Functional Materials* **2009,** *19* (23), 3680-3695.
269. Hubbard, A. T., *Encyclopedia of Surface and Colloid science - Volume 1*. Marcel Dekker, Inc.: New York, 2002; Vol. 1.
270. Shriver, D. F.; Atkins, P. W.; Overton, T. I.; Rourke, J. P.; Weller, M. T.; Armstrong, F. A., *Inorganic Chemistry (4th edition)*. Oxford University Press: Oxford, 2006.
271. Webb, M. J.; Palmgren, P.; Pal, P.; Karis, O.; Grennberg, H., A simple method to produce almost perfect graphene on highly oriented pyrolytic graphite. *Carbon* **2011,** *49* (10), 3242-3249.
272. Sobon, G.; Sotor, J.; Jagiello, J.; Kozinski, R.; Zdrojek, M.; Holdynski, M.; Paletko, P.; Boguslawski, J.; Lipinska, L.; Abramski, K. M., Graphene Oxide vs. Reduced Graphene Oxide as saturable absorbers for Er-doped passively mode-locked fiber laser. *Optics Express* **2012,** *20* (17), 19463-19473.
273. Polyakova, E. Y.; Rim, K. T.; Eom, D.; Douglass, K.; Opila, R. L.; Heinz, T. F.; Teplyakov, A. V.; Flynn, G. W., Scanning Tunneling Microscopy and X-ray Photoelectron Spectroscopy Studies of Graphene Films Prepared by Sonication-Assisted Dispersion. *ACS Nano* **2011,** *5* (8), 6102-6108.
274. Rosenfeld, L., *Origins of Clinical Chemistry: The Evolution of Protein Analysis*. Academic Press Inc.: New York, 1982.
275. Olmsted, J.; Williams, G. M., *Chemistry: The Molecular Science*. Second ed.; Wm. C. Brown: Iowa, USA, 1997.
276. Rouessac, F.; Rouessac, A., Chemical Analysis: Modern Instrumentation Methods and Techniques. Second ed.; John Wiley and Sons: Chichester, England, 2013.
277. Robinson, J. W.; Skelly Frame, E. M.; Frame II, G. M., *Undergraduate Instrumental Analysis, Sixth Edition*. Marcel Dekker: New York, 2005.
278. Arepalli, S.; Nikolaev, P.; Gorelik, O.; Hadjiev, V. G.; Bradlev, H. A.; Holmes, W.; Files, B.; Yowell, L., Protocol for the characterization of single-wall carbon nanotube material quality. *Carbon* **2004,** *42* (8-9), 1783-1791.
279. Liu, W. W.; Chai, S. P.; Mohamed, A. R.; Hashim, U., Synthesis and characterization of graphene and carbon nanotubes: A review on the past and recent developments. *Journal of Industrial and Engineering Chemistry* **2014,** *20* (4), 1171-1185.

280. Alvarez, W. E.; Kitiyanan, B.; Borgna, A.; Resasco, D. E., Synergism of Co and Mo in the catalytic production of single-wall carbon nanotubes by decomposition of CO. *Carbon* **2001,** *39* (4), 547-558.
281. Samanta, S.; Singh, S.; Sahoo, R. R., Simultaneous chemical reduction and surface functionalization of graphene oxide for efficient lubrication of steel-steel contact. *Rsc Advances* **2015,** *5* (76), 61888-61899.
282. Hunter, R. J., Introduction to modern colloid science. Oxford Science publications: Oxford, 1994.
283. Shaw, D. J., Introduction to colloid and surface chemistry. Butterworth Heinemann. : London, 1992.
284. Pradeep, T.; Ashokreddy, A.; Buergi, B. R.; Chainani, A.; Chakrabarti, J.; Das, S. K., *A textbook of Nanoscience and Nanotechnology*. Tata McGraw-Hill: New Delhi, 2012.
285. Kissa, E., *Dispersions: Characterization, Testing and Measurement*. Marcel Dekker: Basel, Switzerland, 1999.
286. Xu, Z.; Gao, C., Aqueous Liquid Crystals of Graphene Oxide. *ACS Nano* **2011,** *5* (4), 2908-2915.
287. Chen, J. T.; Fu, Y. J.; An, Q. F.; Lo, S. C.; Huang, S. H.; Hung, W. S.; Hu, C. C.; Lee, K. R.; Lai, J. Y., Tuning nanostructure of graphene oxide/polyelectrolyte LbL assemblies by controlling pH of GO suspension to fabricate transparent and super gas barrier films. *Nanoscale* **2013,** *5* (19), 9081-9088.
288. Wu, S. L.; Zhao, X. D.; Li, Y. H.; Du, Q. J.; Sun, J. K.; Wang, Y. H.; Wang, X.; Xia, Y. Z.; Wang, Z. H.; Xia, L. H., Adsorption Properties of Doxorubicin Hydrochloride onto Graphene Oxide: Equilibrium, Kinetic and Thermodynamic Studies. *Materials* **2013,** *6* (5), 2026-2042.
289. Ni, Z. H.; Wang, H. M.; Kasim, J.; Fan, H. M.; Yu, T.; Wu, Y. H.; Feng, Y. P.; Shen, Z. X., Graphene thickness determination using reflection and contrast spectroscopy. *Nano Letters* **2007,** *7* (9), 2758-2763.
290. Blake, P.; Hill, E. W.; Neto, A. H. C.; Novoselov, K. S.; Jiang, D.; Yang, R.; Booth, T. J.; Geim, A. K., Making graphene visible. *Applied Physics Letters* **2007,** *91* (6), 063124/1-3.
291. Jung, I.; Pelton, M.; Piner, R.; Dikin, D. A.; Stankovich, S.; Watcharotone, S.; Hausner, M.; Ruoff, R. S., Simple approach for high-contrast optical imaging and characterization of graphene-based sheets. *Nano Letters* **2007,** *7* (12), 3569-3575.
292. Blodgett, K. B., Monomolecular films of fatty acids on glass. *Journal of the American Chemical Society* **1934,** *56*, 495-495.
293. Decher, G., Fuzzy nanoassemblies: Toward layered polymeric multicomposites. *Science* **1997,** *277* (5330), 1232-1237.
294. Decher, G.; Hong, J. D., Buildup of ultrathin multilayer films by a self-assembly process .2. Consecutive adsorption of anionic and cationic bipolar amphiphiles and polyelectrolytes on charged surfaces. *Berichte Der Bunsen-Gesellschaft-Physical Chemistry Chemical Physics* **1991,** *95* (11), 1430-1434.
295. Cheung, J. H.; Stockton, W. B.; Rubner, M. F., Molecular-level processing of conjugated polymers .3. Layer-by-layer manipulation of polyaniline via electrostatic interactions. *Macromolecules* **1997,** *30* (9), 2712-2716.
296. Chen, W.; McCarthy, T. J., Layer-by-layer deposition: A tool for polymer surface modification. *Macromolecules* **1997,** *30* (1), 78-86.
297. Stockton, W. B.; Rubner, M. F., Molecular-level processing of conjugated polymers .4. Layer-by-layer manipulation of polyaniline via hydrogen-bonding interactions. *Macromolecules* **1997,** *30* (9), 2717-2725.
298. Bruening, M.; Dotzauer, D., Just spray it. *Nature Materials* **2009,** *8* (6), 449-450.
299. Decher, G.; Hong, J. D.; Schmitt, J., Buildup of ultrathin multilayer films by a self-assembly process .3. Consecutively alternating adsorption of anionic and cationic polyelectrolytes on charged surfaces. *Thin Solid Films* **1992,** *210* (1-2), 831-835.

300. Sukhorukov, G. B.; Donath, E.; Lichtenfeld, H.; Knippel, E.; Knippel, M.; Budde, A.; Mohwald, H., Layer-by-layer self assembly of polyelectrolytes on colloidal particles. *Colloids and Surfaces a-Physicochemical and Engineering Aspects* **1998,** *137* (1-3), 253-266.
301. Kotov, N. A.; Dekany, I.; Fendler, J. H., Layer-by-layer self-assembly of polyelectrolyte-semiconductor nanoparticle composite films. *Journal of Physical Chemistry* **1995,** *99* (35), 13065-13069.
302. Lvov, Y.; Decher, G.; Mohwald, H., Assembly, structural characterization, and thermal-behavior of layer-by-layer deposited ultrathin films of poly(vinyl sulfate) and poly(allylamine). *Langmuir* **1993,** *9* (2), 481-486.
303. Tang, Z. Y.; Wang, Y.; Podsiadlo, P.; Kotov, N. A., Biomedical applications of layer-by-layer assembly: From biomimetics to tissue engineering. *Advanced Materials* **2006,** *18* (24), 3203-3224.
304. Lvov, Y.; Haas, H.; Decher, G.; Mohwald, H.; Mikhailov, A.; Mtchedlishvily, B.; Morgunova, E.; Vainshtein, B., Successive deposition of alternate layers of polyelectrolytes and a charged virus. *Langmuir* **1994,** *10* (11), 4232-4236.
305. Linford, M. R.; Auch, M.; Mohwald, H., Nonmonotonic effect of ionic strength on surface dye extraction during dye-polyelectrolyte multilayer formation. *Journal of the American Chemical Society* **1998,** *120* (1), 178-182.
306. Lvov, Y.; Ariga, K.; Kunitake, T., Layer-by-layer assembly of alternate protein polyion ultrathin films. *Chemistry Letters* **1994,** (12), 2323-2326.
307. Lehnert, M.; Rosin, C.; Knoll, W.; Veith, M., Layer-by-Layer Assembly of a Streptavidin-Fibronectin Multilayer on Biotinylated TiOx. *Langmuir* **2013,** *29* (6), 1732-1737.
308. Roh, Y. H.; Lee, J. B.; Shopsowitz, K. E.; Dreaden, E. C.; Morton, S. W.; Poon, Z.; Hong, J.; Yamin, I.; Bonner, D. K.; Hammond, P. T., Layer-by-Layer Assembled Antisense DNA Microsponge Particles for Efficient Delivery of Cancer Therapeutics. *ACS Nano* **2014,** *8* (10), 9767-9780.
309. Saurer, E. M.; Flessner, R. M.; Sullivan, S. P.; Prausnitz, M. R.; Lynn, D. M., Layer-by-Layer Assembly of DNA- and Protein-Containing Films on Microneedles for Drug Delivery to the Skin. *Biomacromolecules* **2010,** *11* (11), 3136-3143.
310. Correa-Duarte, M. A.; Kosiorek, A.; Kandulski, W.; Giersig, M.; Liz-Marzan, L. M., Layer-by-layer assembly of multiwall carbon nanotubes on spherical colloids. *Chemistry of Materials* **2005,** *17* (12), 3268-3272.
311. He, L. M.; Tang, S.; Prabhakaran, M. P.; Liao, S.; Tian, L. L.; Zhang, Y. M.; Xue, W.; Ramakrishna, S., Surface Modification of PLLA Nano-scaffolds with Laminin Multilayer by LbL Assembly for Enhancing Neurite Outgrowth. *Macromolecular Bioscience* **2013,** *13* (11), 1601-1609.
312. Ai, H.; Meng, H. D.; Ichinose, I.; Jones, S. A.; Mills, D. K.; Lvov, Y. M.; Qiao, X. X., Biocompatibility of layer-by-layer self-assembled nanofilm on silicone rubber for neurons. *Journal of Neuroscience Methods* **2003,** *128* (1-2), 1-8.
313. Mei, Y.; Yao, C.; Li, X. S., A simple approach to constructing antibacterial and anti-biofouling nanofibrous membranes. *Biofouling* **2014,** *30* (3), 313-322.
314. Zhou, B.; Li, Y.; Deng, H. B.; Hu, Y.; Li, B., Antibacterial multilayer films fabricated by layer-by-layer immobilizing lysozyme and gold nanoparticles on nanofibers. *Colloids and Surfaces B-Biointerfaces* **2014,** *116*, 432-438.
315. Jewell, C. M.; Zhang, J. T.; Fredin, N. J.; Wolff, M. R.; Hacker, T. A.; Lynn, D. M., Release of plasmid DNA from intravascular stents coated with ultrathin multilayered polyelectrolyte films. *Biomacromolecules* **2006,** *7* (9), 2483-2491.
316. Chou, C. C.; Zeng, H. J.; Yeh, C. H., Blood compatibility and adhesion of collagen/heparin multilayers coated on two titanium surfaces by a layer-by-layer technique. *Thin Solid Films* **2013,** *549*, 117-122.

317. Lin, Q. K.; Van, J. J.; Qiu, F. Y.; Song, X. X.; Fu, G. S.; Ji, J. A., Heparin/collagen multilayer as a thromboresistant and endothelial favorable coating for intravascular stent. *Journal of Biomedical Materials Research Part A* **2011,** *96A* (1), 132-141.
318. Wang, H. G.; Yin, T. Y.; Ge, S. P.; Zhang, Q.; Dong, Q. L.; Lei, D. X.; Sun, D. M.; Wang, G. X., Biofunctionalization of titanium surface with multilayer films modified by heparin-VEGF-fibronectin complex to improve endothelial cell proliferation and blood compatibility. *Journal of Biomedical Materials Research Part A* **2013,** *101* (2), 413-420.
319. Lee, D. W.; Hong, T.-K.; Kang, D.; Lee, J.; Heo, M.; Kim, J. Y.; Kim, B.-S.; Shin, H. S., Highly controllable transparent and conducting thin films using layer-by-layer assembly of oppositely charged reduced graphene oxides. *Journal of Materials Chemistry* **2011,** *21* (10), 3438-3442.
320. Zhu, J. Y.; He, J. H., Assembly and benign step-by-step post-treatment of oppositely charged reduced graphene oxides for transparent conductive thin films with multiple applications. *Nanoscale* **2012,** *4* (11), 3558-3566.
321. Choi, W.; Choi, J.; Bang, J.; Lee, J. H., Layer-by-Layer Assembly of Graphene Oxide Nanosheets on Polyamide Membranes for Durable Reverse-Osmosis Applications. *ACS Applied Materials & Interfaces* **2013,** *5* (23), 12510-12519.
322. Tang, Y.; Wu, N.; Luo, S.; Liu, C.; Wang, K.; Chen, L., One-Step Electrodeposition to Layer-by-Layer Graphene-Conducting-Polymer Hybrid Films. *Macromolecular Rapid Communications* **2012,** *33* (20), 1780-1786.
323. Kwon, S. R.; Jeon, J. W.; Lutkenhaus, J. L., Sprayable, paintable layer-by-layer polyaniline nanofiber/graphene electrodes. *Rsc Advances* **2015,** *5* (20), 14994-15001.
324. Chen, D.; Wang, X. Y.; Liu, T. X.; Wang, X. D.; Li, J., Electrically Conductive Poly(vinyl alcohol) Hybrid Films Containing Graphene and Layered Double Hydroxide Fabricated via Layer-by-Layer Self-Assembly. *ACS Applied Materials & Interfaces* **2010,** *2* (7), 2005-2011.
325. Kurapati, R.; Raichur, A. M., Graphene oxide based multilayer capsules with unique permeability properties: facile encapsulation of multiple drugs. *Chemical Communications* **2012,** *48* (48), 6013-6015.
326. Shen, J.; Hu, Y.; Li, C.; Qin, C.; Shi, M.; Ye, M., Layer-by-Layer Self-Assembly of Graphene Nanoplatelets. *Langmuir* **2009,** *25* (11), 6122-6128.
327. Sham, A. Y. W.; Notley, S. M., Layer-by-Layer Assembly of Thin Films Containing Exfoliated Pristine Graphene Nanosheets and Polyethyleneimine. *Langmuir* **2014,** *30* (9), 2410-2418.
328. Shin, S. R.; Aghaei-Ghareh-Bolagh, B.; Gao, X. G.; Nikkhah, M.; Jung, S. M.; Dolatshahi-Pirouz, A.; Kim, S. B.; Kim, S. M.; Dokmeci, M. R.; Tang, X. W.; Khademhosseini, A., Layer-by-Layer Assembly of 3D Tissue Constructs with Functionalized Graphene. *Advanced Functional Materials* **2014,** *24* (39), 6136-6144.
329. Qi, W.; Yuan, W.; Yan, J.; Wang, H., Growth and accelerated differentiation of mesenchymal stem cells on graphene oxide/poly-L-lysine composite films. *Journal of Materials Chemistry B* **2014,** *2* (33), 5461-5467.
330. Qi, W.; Xue, Z.; Yuan, W.; Wang, H., Layer-by-layer assembled graphene oxide composite films for enhanced mechanical properties and fibroblast cell affinity. *Journal of Materials Chemistry B* **2014,** *2* (3), 325-331.
331. Bacsa, R. R.; Laurent, C.; Peigney, A.; Bacsa, W. S.; Vaugien, T.; Rousset, A., High specific surface area carbon nanotubes from catalytic chemical vapor deposition process. *Chemical Physics Letters* **2000,** *323* (5-6), 566-571.
332. Peigney, A.; Laurent, C.; Flahaut, E.; Bacsa, R. R.; Rousset, A., Specific surface area of carbon nanotubes and bundles of carbon nanotubes. *Carbon* **2001,** *39* (4), 507-514.
333. Huczko, A.; Lange, H.; Calko, E.; Grubek-Jaworska, H.; Droszcz, P., Physiological testing of carbon nanotubes: Are they asbestos-like? *Fullerene Science and Technology* **2001,** *9* (2), 251-254.
334. Weiss, N. O.; Zhou, H. L.; Liao, L.; Liu, Y.; Jiang, S.; Huang, Y.; Duan, X. F., Graphene: An Emerging Electronic Material. *Advanced Materials* **2012,** *24* (43), 5782-5825.

335. Brownson, D. A. C.; Banks, C. E., Graphene electrochemistry: an overview of potential applications. *Analyst* **2010,** *135* (11), 2768-2778.
336. Liu, Y.; Yu, D.; Zeng, C.; Miao, Z.; Dai, L., Biocompatible Graphene Oxide-Based Glucose Biosensors. *Langmuir* **2010,** *26* (9), 6158-6160.
337. Mannoor, M. S.; Tao, H.; Clayton, J. D.; Sengupta, A.; Kaplan, D. L.; Naik, R. R.; Verma, N.; Omenetto, F. G.; McAlpine, M. C., Graphene-based wireless bacteria detection on tooth enamel. *Nature Communications* **2012,** *3* (763), 1-8.
338. Liu, F.; Choi, K. S.; Park, T. J.; Lee, S. Y.; Seo, T. S., Graphene-based electrochemical biosensor for pathogenic virus detection. *Biochip Journal* **2011,** *5* (2), 123-128.
339. Wu, J.-F.; Xu, M.-Q.; Zhao, G.-C., Graphene-based modified electrode for the direct electron transfer of Cytochrome c and biosensing. *Electrochemistry Communications* **2010,** *12* (1), 175-177.
340. Lu, Q.; Dong, X.; Li, L.-J.; Hu, X., Direct electrochemistry-based hydrogen peroxide biosensor formed from single-layer graphene nanoplatelet-enzyme composite film. *Talanta* **2010,** *82* (4), 1344-1348.
341. Xu, X.; Yan, S. C.; Wang, B. J.; Qu, P.; Wang, J. Z.; Wu, J. S., Graphene Aerogel/Platinum Nanoparticle Nanocomposites for Direct Electrochemistry of Cytochrome c and Hydrogen Peroxide Sensing. *Journal of Nanoscience and Nanotechnology* **2016,** *16* (12), 12299-12306.
342. Kang, X.; Wang, J.; Wu, H.; Liu, J.; Aksay, I. A.; Lin, Y., A graphene-based electrochemical sensor for sensitive detection of paracetamol. *Talanta* **2010,** *81* (3), 754-759.
343. Alwarappan, S.; Erdem, A.; Liu, C.; Li, C.-Z., Probing the Electrochemical Properties of Graphene Nanosheets for Biosensing Applications. *Journal of Physical Chemistry C* **2009,** *113* (20), 8853-8857.
344. Lu, Y.; Goldsmith, B. R.; Kybert, N. J.; Johnson, A. T. C., DNA-decorated graphene chemical sensors. *Applied Physics Letters* **2010,** *97* (8), 083107/1-3.
345. Kim, D.-J.; Sohn, I. Y.; Jung, J.-H.; Yoon, O. J.; Lee, N. E.; Park, J.-S., Reduced graphene oxide field-effect transistor for label-free femtomolar protein detection. *Biosensors & Bioelectronics* **2013,** *41*, 621-626.
346. Feng, L. Y.; Chen, Y.; Ren, J. S.; Qu, X. G., A graphene functionalized electrochemical aptasensor for selective label-free detection of cancer cells. *Biomaterials* **2011,** *32* (11), 2930-2937.
347. Kim, D.-J.; Park, H.-C.; Sohn, I. Y.; Jung, J.-H.; Yoon, O. J.; Park, J.-S.; Yoon, M.-Y.; Lee, N.-E., Electrical graphene aptasensor for ultra-sensitive detection of anthrax toxin with amplified signal transduction. *Small (Weinheim an der Bergstrasse, Germany)* **2013,** *9* (19), 3352-60.
348. Ling, K.; Jiang, H. Y.; Li, Y.; Tao, X. J.; Qiu, C.; Li, F. R., A self-assembling RNA aptamer-based graphene oxide sensor for the turn-on detection of theophylline in serum. *Biosensors & Bioelectronics* **2016,** *86*, 8-13.
349. Weng, X.; Neethirajan, S., A microfluidic biosensor using graphene oxide and aptamer-functionalized quantum dots for peanut allergen detection. *Biosensors & Bioelectronics* **2016,** *85*, 649-656.
350. Lakshmi, G.; Sharma, A.; Solanki, P. R.; Avasthi, D. K., Mesoporous polyaniline nanofiber decorated graphene micro-flowers for enzyme-less cholesterol biosensors. *Nanotechnology* **2016,** *27* (34), 345101/1-10.
351. Mehta, J.; Vinayak, P.; Tuteja, S. K.; Chhabra, V. A.; Bhardwaj, N.; Paul, A. K.; Kim, K. H.; Deep, A., Graphene modified screen printed immunosensor for highly sensitive detection of parathion. *Biosensors & Bioelectronics* **2016,** *83*, 339-346.
352. Kampouris, D. K.; Banks, C. E., Exploring the physicoelectrochemical properties of graphene. *Chemical Communications* **2010,** *46* (47), 8986-8988.
353. Yang, W.; Ratinac, K. R.; Ringer, S. P.; Thordarson, P.; Gooding, J. J.; Braet, F., Carbon Nanomaterials in Biosensors: Should You Use Nanotubes or Graphene? *Angewandte Chemie-International Edition* **2010,** *49* (12), 2114-2138.

354. Kasry, A.; Ardakani, A. A.; Tulevski, G. S.; Menges, B.; Copel, M.; Vyklicky, L., Highly Efficient Fluorescence Quenching with Graphene. *Journal of Physical Chemistry C* **2012,** *116* (4), 2858-2862.
355. Gomez-Santos, G.; Stauber, T., Fluorescence quenching in graphene: A fundamental ruler and evidence for transverse plasmons. *Physical Review B* **2011,** *84* (16), 165438/1-6.
356. Chang, H.; Tang, L.; Wang, Y.; Jiang, J.; Li, J., Graphene Fluorescence Resonance Energy Transfer Aptasensor for the Thrombin Detection. *Analytical Chemistry* **2010,** *82* (6), 2341-2346.
357. Li, F.; Pei, H.; Wang, L.; Lu, J.; Gao, J.; Jiang, B.; Zhao, X.; Fan, C., Nanomaterial-Based Fluorescent DNA Analysis: A Comparative Study of the Quenching Effects of Graphene Oxide, Carbon Nanotubes, and Gold Nanoparticles. *Advanced Functional Materials* **2013,** *23* (33), 4140-4148.
358. Wei, W. L.; Xu, C.; Ren, J. S.; Xu, B. L.; Qu, X. G., Sensing metal ions with ion selectivity of a crown ether and fluorescence resonance energy transfer between carbon dots and graphene. *Chemical Communications* **2012,** *48* (9), 1284-1286.
359. Shi, Y.; Huang, W. T.; Luo, H. Q.; Li, N. B., A label-free DNA reduced graphene oxide-based fluorescent sensor for highly sensitive and selective detection of hemin. *Chemical Communications* **2011,** *47* (16), 4676-4678.
360. Yang, L.; Liu, C. H.; Ren, W.; Li, Z. P., Graphene Surface-Anchored Fluorescence Sensor for Sensitive Detection of MicroRNA Coupled with Enzyme-Free Signal Amplification of Hybridization Chain Reaction. *ACS Applied Materials & Interfaces* **2012,** *4* (12), 6450-6453.
361. Fan, L. S.; Hu, Y. W.; Wang, X.; Zhang, L. L.; Li, F. H.; Han, D. X.; Li, Z. G.; Zhang, Q. X.; Wang, Z. X.; Niu, L., Fluorescence resonance energy transfer quenching at the surface of graphene quantum dots for ultrasensitive detection of TNT. *Talanta* **2012,** *101*, 192-197.
362. Wang, H. B.; Zhang, Q.; Chu, X.; Chen, T. T.; Ge, J.; Yu, R. Q., Graphene Oxide-Peptide Conjugate as an Intracellular Protease Sensor for Caspase-3 Activation Imaging in Live Cells. *Angewandte Chemie-International Edition* **2011,** *50* (31), 7065-7069.
363. Sheng, L. F.; Ren, J. T.; Miao, Y. Q.; Wang, J. H.; Wang, E. K., PVP-coated graphene oxide for selective determination of ochratoxin A via quenching fluorescence of free aptamer. *Biosensors & Bioelectronics* **2011,** *26* (8), 3494-3499.
364. Hu, W.; Peng, C.; Luo, W.; Lv, M.; Li, X.; Li, D.; Huang, Q.; Fan, C., Graphene-Based Antibacterial Paper. *ACS Nano* **2010,** *4* (7), 4317-4323.
365. Kang, S.; Pinault, M.; Pfefferle, L. D.; Elimelech, M., Single-walled carbon nanotubes exhibit strong antimicrobial activity. *Langmuir* **2007,** *23* (17), 8670-8673.
366. Tang, Y. J. J.; Ashcroft, J. M.; Chen, D.; Min, G. W.; Kim, C. H.; Murkhejee, B.; Larabell, C.; Keasling, J. D.; Chen, F. Q. F., Charge-associated effects of fullerene derivatives on microbial structural integrity and central metabolism. *Nano Letters* **2007,** *7* (3), 754-760.
367. Narayan, R. J.; Berry, C. J.; Brigmon, R. L., Structural and biological properties of carbon nanotube composite films. *Materials Science and Engineering B-Solid State Materials for Advanced Technology* **2005,** *123* (2), 123-129.
368. Akhavan, O.; Ghaderi, E., Toxicity of Graphene and Graphene Oxide Nanowalls Against Bacteria. *ACS Nano* **2010,** *4* (10), 5731-5736.
369. Liu, S.; Zeng, T. H.; Hofmann, M.; Burcombe, E.; Wei, J.; Jiang, R.; Kong, J.; Chen, Y., Antibacterial Activity of Graphite, Graphite Oxide, Graphene Oxide, and Reduced Graphene Oxide: Membrane and Oxidative Stress. *ACS Nano* **2011,** *5* (9), 6971-6980.
370. Nanda, S. S.; Yi, D. K.; Kim, K., Study of antibacterial mechanism of graphene oxide using Raman spectroscopy. *Scientific Reports* **2016,** *6,* 128-136.
371. Nguyen, V. H.; Kim, B. K.; Jo, Y. L.; Shim, J. J., Preparation and antibacterial activity of silver nanoparticles-decorated graphene composites. *Journal of Supercritical Fluids* **2012,** *72*, 28-35.
372. Yadav, S. K.; Jung, Y. C.; Kim, J. H.; Ko, Y. I.; Ryu, H. J.; Yadav, M. K.; Kim, Y. A.; Cho, J. W., Mechanically Robust, Electrically Conductive Biocomposite Films Using Antimicrobial Chitosan-Functionalized Graphenes. *Particle & Particle Systems Characterization* **2013,** *30* (8), 721-727.

373. Das, M. R.; Sarma, R. K.; Borah, S. C.; Kumari, R.; Saikia, R.; Deshmukh, A. B.; Shelke, M. V.; Sengupta, P.; Szunerits, S.; Boukherroub, R., The synthesis of citrate-modified silver nanoparticles in an aqueous suspension of graphene oxide nanosheets and their antibacterial activity. *Colloids and Surfaces B-Biointerfaces* **2013,** *105*, 128-136.
374. Krishnamoorthy, K.; Veerapandian, M.; Zhang, L. H.; Yun, K.; Kim, S. J., Antibacterial Efficiency of Graphene Nanosheets against Pathogenic Bacteria via Lipid Peroxidation. *Journal of Physical Chemistry C* **2012,** *116* (32), 17280-17287.
375. Pham, V. T. H.; Vi Khanh, T.; Quinn, M. D. J.; Notley, S. M.; Guo, Y.; Baulin, V. A.; Al Kobaisi, M.; Crawford, R. J.; Ivanova, E. P., Graphene Induces Formation of Pores That Kill Spherical and Rod-Shaped Bacteria. *ACS Nano* **2015,** *9* (8), 8458-8467.
376. Li, J. H.; Wang, G.; Zhu, H. Q.; Zhang, M.; Zheng, X. H.; Di, Z. F.; Liu, X. Y.; Wang, X., Antibacterial activity of large-area monolayer graphene film manipulated by charge transfer. *Scientific Reports* **2014,** *4,* 4359/1-8.
377. Szunerits, S.; Boukherroub, R., Antibacterial activity of graphene-based materials. *Journal of Materials Chemistry B* **2016,** *4* (43), 6892-6912.
378. Zou, X. F.; Zhang, L.; Wang, Z. J.; Luo, Y., Mechanisms of the Antimicrobial Activities of Graphene Materials. *Journal of the American Chemical Society* **2016,** *138* (7), 2064-2077.
379. Barbolina, I.; Woods, C. R.; Lozano, N.; Kostarelos, K.; Novoselov, K. S.; Roberts, I. S., Purity of graphene oxide determines its antibacterial activity. *2d Materials* **2016,** *3* (2), 69103-69116.
380. Hui, L. W.; Piao, J. G.; Auletta, J.; Hu, K.; Zhu, Y. W.; Meyer, T.; Liu, H. T.; Yang, L. H., Availability of the Basal Planes of Graphene Oxide Determines Whether It Is Antibacterial. *ACS Applied Materials & Interfaces* **2014,** *6* (15), 13183-13190.
381. Deepachitra, R.; Ramnath, V.; Sastry, T. P., Graphene oxide incorporated collagen-fibrin biofilm as a wound dressing material. *Rsc Advances* **2014,** *4* (107), 62717-62727.
382. Dubey, P.; Gopinath, P., PEGylated graphene oxide-based nanocomposite-grafted chitosan/polyvinyl alcohol nanofiber as an advanced antibacterial wound dressing. *Rsc Advances* **2016,** *6* (73), 69103-69116.
383. Mitra, T.; Manna, P. J.; Raja, S. T. K.; Gnanamani, A.; Kundu, P. P., Curcumin loaded nano graphene oxide reinforced fish scale collagen - a 3D scaffold biomaterial for wound healing applications. *Rsc Advances* **2015,** *5* (119), 98653-98665.
384. Li, Z. H.; Wang, H. Q.; Yang, B.; Sun, Y. K.; Huo, R., Three-dimensional graphene foams loaded with bone marrow derived mesenchymal stem cells promote skin wound healing with reduced scarring. *Materials Science & Engineering C-Materials for Biological Applications* **2015,** *57*, 181-188.
385. Khan, M. S.; Abdelhamid, H. N.; Wu, H. F., Near infrared (NIR) laser mediated surface activation of graphene oxide nanoflakes for efficient antibacterial, antifungal and wound healing treatment. *Colloids and Surfaces B-Biointerfaces* **2015,** *127*, 281-291.
386. Sun, H. J.; Gao, N.; Dong, K.; Ren, J. S.; Qu, X. G., Graphene Quantum Dots-Band-Aids Used for Wound Disinfection. *ACS Nano* **2014,** *8* (6), 6202-6210.
387. Zhou, Y. Z.; Chen, R.; He, T. T.; Xu, K.; Du, D.; Zhao, N.; Cheng, X. N.; Yang, J.; Shi, H. F.; Lin, Y. H., Biomedical Potential of Ultrafine Ag/AgCl Nanoparticles Coated on Graphene with Special Reference to Antimicrobial Performances and Burn Wound Healing. *ACS Applied Materials & Interfaces* **2016,** *8* (24), 15067-15075.
388. Lu, B. G.; Li, T.; Zhao, H. T.; Li, X. D.; Gao, C. T.; Zhang, S. X.; Xie, E. Q., Graphene-based composite materials beneficial to wound healing. *Nanoscale* **2012,** *4* (9), 2978-2982.
389. Lee, W. C.; Lim, C.; Shi, H.; Tang, L. A. L.; Wang, Y.; Lim, C. T.; Loh, K. P., Origin of Enhanced Stem Cell Growth and Differentiation on Graphene and Graphene Oxide. *ACS Nano* **2011,** *5* (9), 7334-7341.
390. Marion, N. W.; Mao, J. J., Mesenchymal stem cells and tissue engineering. *Stem Cell Tools and Other Experimental Protocols* **2006,** *420*, 339-361.

391. Crisan, M.; Yap, S.; Casteilla, L.; Chen, C. W.; Corselli, M.; Park, T. S.; Andriolo, G.; Sun, B.; Zheng, B.; Zhang, L.; Norotte, C.; Teng, P. N.; Traas, J.; Schugar, R.; Deasy, B. M.; Badylak, S.; Buhring, H. J.; Giacobino, J. P.; Lazzari, L.; Huard, J.; Peault, B., A perivascular origin for mesenchymal stem cells in multiple human organs. *Cell Stem Cell* **2008,** *3* (3), 301-313.
392. Eberli, D.; Atala, A., Tissue engineering using adult stem cells. *Stem Cell Tools and Other Experimental Protocols* **2006,** *420*, 287-302.
393. Griffith, L. G.; Naughton, G., Tissue engineering - Current challenges and expanding opportunities. *Science* **2002,** *295* (5557), 1009-1014.
394. Kim, S.-J.; Lee, J. K.; Kim, J. W.; Jung, J.-W.; Seo, K.; Park, S.-B.; Roh, K.-H.; Lee, S.-R.; Hong, Y. H.; Kim, S. J.; Lee, Y.-S.; Kim, S. J.; Kang, K.-S., Surface modification of polydimethylsiloxane (PDMS) induced proliferation and neural-like cells differentiation of umbilical cord blood-derived mesenchymal stem cells. *Journal of Materials Science-Materials in Medicine* **2008,** *19* (8), 2953-2962.
395. Liu, Y. S.; Chen, T.; Du, F.; Gu, M.; Zhang, P.; Zhang, X.; Liu, J. Z.; Lv, L. W.; Xiong, C. Y.; Zhou, Y. S., Single-Layer Graphene Enhances the Osteogenic Differentiation of Human Mesenchymal Stem Cells In Vitro and In Vivo. *Journal of Biomedical Nanotechnology* **2016,** *12* (6), 1270-1284.
396. Crowder, S. W.; Prasai, D.; Rath, R.; Balikov, D. A.; Bae, H.; Bolotin, K. I.; Sung, H.-J., Three-dimensional graphene foams promote osteogenic differentiation of human mesenchymal stem cells. *Nanoscale* **2013,** *5* (10), 4171-4176.
397. Alzhavan, O.; Ghaderi, E.; Shahsavar, M., Graphene nanogrids for selective and fast osteogenic differentiation of human mesenchymal stem cells. *Carbon* **2013,** *59*, 200-211.
398. Luo, Y.; Shen, H.; Fang, Y. X.; Cao, Y. H.; Huang, J.; Zhang, M. X.; Dai, J. W.; Shi, X. Y.; Zhang, Z. J., Enhanced Proliferation and Osteogenic Differentiation of Mesenchymal Stem Cells on Graphene Oxide-Incorporated Electrospun Poly(lactic-co-glycolic acid) Nanofibrous Mats. *ACS Applied Materials & Interfaces* **2015,** *7* (11), 6331-6339.
399. Nair, M.; Nancy, D.; Krishnan, A. G.; Anjusree, G. S.; Vadukumpully, S.; Nair, S. V., Graphene oxide nanoflakes incorporated gelatin-hydroxyapatite scaffolds enhance osteogenic differentiation of human mesenchymal stem cells. *Nanotechnology* **2015,** *26* (16), 161001/1-10.
400. Lee, J. H.; Shin, Y. C.; Jin, O. S.; Kang, S. H.; Hwang, Y. S.; Park, J. C.; Hong, S. W.; Han, D. W., Reduced graphene oxide-coated hydroxyapatite composites stimulate spontaneous osteogenic differentiation of human mesenchymal stem cells. *Nanoscale* **2015,** *7* (27), 11642-11651.
401. Kim, J.; Choi, K. S.; Kim, Y.; Lim, K. T.; Seonwoo, H.; Park, Y.; Kim, D. H.; Choung, P. H.; Cho, C. S.; Kim, S. Y.; Choung, Y. H.; Chung, J. H., Bioactive effects of graphene oxide cell culture substratum on structure and function of human adipose-derived stem cells. *Journal of Biomedical Materials Research Part A* **2013,** *101* (12), 3520-3530.
402. Patel, M.; Moon, H. J.; Ko, D. Y.; Jeong, B., Composite System of Graphene Oxide and Polypeptide Thermogel As an Injectable 3D Scaffold for Adipogenic Differentiation of Tonsil-Derived Mesenchymal Stem Cells. *ACS Applied Materials & Interfaces* **2016,** *8* (8), 5160-5169.
403. Tang, M. L.; Song, Q.; Li, N.; Jiang, Z. Y.; Huang, R.; Cheng, G. S., Enhancement of electrical signaling in neural networks on graphene films. *Biomaterials* **2013,** *34* (27), 6402-6411.
404. Kim, J.; Park, S.; Kim, Y. J.; Jeon, C. S.; Lim, K. T.; Seonwoo, H.; Cho, S. P.; Chung, T. D.; Choung, P. H.; Choung, Y. H.; Hong, B. H.; Chung, J. H., Monolayer Graphene-Directed Growth and Neuronal Differentiation of Mesenchymal Stem Cells. *Journal of Biomedical Nanotechnology* **2015,** *11* (11), 2024-2033.
405. Weaver, C. L.; Cui, X. T., Directed Neural Stem Cell Differentiation with a Functionalized Graphene Oxide Nanocomposite. *Advanced Healthcare Materials* **2015,** *4* (9), 1408-1416.
406. Kim, T. H.; Shah, S.; Yang, L. T.; Yin, P. T.; Hossain, M. K.; Conley, B.; Choi, J. W.; Lee, K. B., Controlling Differentiation of Adipose-Derived Stem Cells Using Combinatorial Graphene Hybrid-Pattern Arrays. *ACS Nano* **2015,** *9* (4), 3780-3790.

407. Pittenger, M. F.; Mackay, A. M.; Beck, S. C.; Jaiswal, R. K.; Douglas, R.; Mosca, J. D.; Moorman, M. A.; Simonetti, D. W.; Craig, S.; Marshak, D. R., Multilineage potential of adult human mesenchymal stem cells. *Science* **1999,** *284* (5411), 143-147.
408. Dalby, M. J.; Gadegaard, N.; Tare, R.; Andar, A.; Riehle, M. O.; Herzyk, P.; Wilkinson, C. D. W.; Oreffo, R. O. C., The control of human mesenchymal cell differentiation using nanoscale symmetry and disorder. *Nature Materials* **2007,** *6* (12), 997-1003.
409. Engler, A. J.; Sen, S.; Sweeney, H. L.; Discher, D. E., Matrix elasticity directs stem cell lineage specification. *Cell* **2006,** *126* (4), 677-689.
410. Auger, F. A.; Gibot, L.; Lacroix, D., The Pivotal Role of Vascularization in Tissue Engineering. *Annual Review of Biomedical Engineering, Vol 15* **2013,** *15*, 177-200.
411. La, W. G.; Jin, M.; Park, S.; Yoon, H. H.; Jeong, G. J.; Bhang, S. H.; Park, H.; Char, K.; Kim, B. S., Delivery of bone morphogenetic protein-2 and substance P using graphene oxide for bone regeneration. *International Journal of Nanomedicine* **2014,** *9*, 107-116.
412. La, W. G.; Park, S.; Yoon, H. H.; Jeong, G. J.; Lee, T. J.; Bhang, S. H.; Han, J. Y.; Char, K.; Kim, B. S., Delivery of a Therapeutic Protein for Bone Regeneration from a Substrate Coated with Graphene Oxide. *Small* **2013,** *9* (23), 4051-4060.
413. Park, K. O.; Lee, J. H.; Park, J. H.; Shin, Y. C.; Huh, J. B.; Bae, J. H.; Kang, S. H.; Hong, S. W.; Kim, B.; Yang, D. J.; Han, D. W.; Yeum, J. H., Graphene oxide-coated guided bone regeneration membranes with enhanced osteogenesis: Spectroscopic analysis and animal study. *Applied Spectroscopy Reviews* **2016,** *51* (7-9), 540-551.
414. Dinescu, S.; Ionita, M.; Pandele, A. M.; Galateanu, B.; Iovu, H.; Ardelean, A.; Costache, M.; Hermenean, A., In vitro cytocompatibility evaluation of chitosan/graphene oxide 3D scaffold composites designed for bone tissue engineering. *Bio-Medical Materials and Engineering* **2014,** *24* (6), 2249-2256.
415. Nishida, E.; Miyaji, H.; Kato, A.; Takita, H.; Iwanaga, T.; Momose, T.; Ogawa, K.; Murakami, S.; Sugaya, T.; Kawanami, M., Graphene oxide scaffold accelerates cellular proliferative response and alveolar bone healing of tooth extraction socket. *International Journal of Nanomedicine* **2016,** *11*, 2265-2277.
416. Biris, A. R.; Mahmood, M.; Lazar, M. D.; Dervishi, E.; Watanabe, F.; Mustafa, T.; Baciut, G.; Baciut, M.; Bran, S.; Ali, S.; Biris, A. S., Novel Multicomponent and Biocompatible Nanocomposite Materials Based on Few-Layer Graphenes Synthesized on a Gold/Hydroxyapatite Catalytic System with Applications in Bone Regeneration. *Journal of Physical Chemistry C* **2011,** *115* (39), 18967-18976.
417. Zhang, W. J.; Chang, Q.; Xu, L.; Li, G. L.; Yang, G. Z.; Ding, X.; Wang, X. S.; Cui, D. X.; Jiang, X. Q., Graphene Oxide-Copper Nanocomposite-Coated Porous CaP Scaffold for Vascularized Bone Regeneration via Activation of Hif-1. *Advanced Healthcare Materials* **2016,** *5* (11), 1299-1309.
418. Lu, J. Y.; Cheng, C.; He, Y. S.; Lyu, C. Q.; Wang, Y. F.; Yu, J.; Qiu, L.; Zou, D. R.; Li, D., Multilayered Graphene Hydrogel Membranes for Guided Bone Regeneration. *Advanced Materials* **2016,** *28* (21), 4025-4031.
419. Lu, J. Y.; He, Y. S.; Cheng, C.; Wang, Y.; Qiu, L.; Li, D.; Zou, D. R., Self-Supporting Graphene Hydrogel Film as an Experimental Platform to Evaluate the Potential of Graphene for Bone Regeneration. *Advanced Functional Materials* **2013,** *23* (28), 3494-3502.
420. Wang, W. G.; Caetano, G.; Ambler, W. S.; Blaker, J. J.; Frade, M. A.; Mandal, P.; Diver, C.; Bartolo, P., Enhancing the Hydrophilicity and Cell Attachment of 3D Printed PCL/Graphene Scaffolds for Bone Tissue Engineering. *Materials* **2016,** *9* (12), 992/1-11.
421. Song, F. X.; Jie, W. B.; Zhang, T.; Li, W.; Jiang, Y. J.; Wan, L.; Liu, W. J.; Li, X. C.; Liu, B., Room-temperature fabrication of a three-dimensional reduced-graphene oxide/polypyrrole/ hydroxyapatite composite scaffold for bone tissue engineering. *Rsc Advances* **2016,** *6* (95), 92804-92812.

422. Wang, L.; Lu, C. X.; Li, Y. H.; Wu, F.; Zhao, B.; Dong, X. Z., Green fabrication of porous silk fibroin/graphene oxide hybrid scaffolds for bone tissue engineering. *Rsc Advances* **2015,** *5* (96), 78660-78668.
423. Kumar, S.; Raj, S.; Sarkar, K.; Chatterjee, K., Engineering a multi-biofunctional composite using poly(ethylenimine) decorated graphene oxide for bone tissue regeneration. *Nanoscale* **2016,** *8* (12), 6820-6836.
424. Zou, L. L.; Wang, H.; He, B.; Zeng, L. J.; Tan, T.; Cao, H. Q.; He, X. Y.; Zhang, Z. W.; Guo, S. R.; Li, Y. P., Current Approaches of Photothermal Therapy in Treating Cancer Metastasis with Nanotherapeutics. *Theranostics* **2016,** *6* (6), 762-772.
425. Yang, K.; Zhang, S.; Zhang, G.; Sun, X.; Lee, S.-T.; Liu, Z., Graphene in Mice: Ultrahigh In Vivo Tumor Uptake and Efficient Photothermal Therapy. *Nano Letters* **2010,** *10* (9), 3318-3323.
426. Yang, K.; Feng, L.; Shi, X.; Liu, Z., Nano-graphene in biomedicine: theranostic applications. *Chemical Society Reviews* **2012,** *42*, 530-547.
427. Sheng, Z.; Song, L.; Zheng, J.; Hu, D.; He, M.; Zheng, M.; Gao, G.; Gong, P.; Zhang, P.; Ma, Y.; Cai, L., Protein-assisted fabrication of nano-reduced graphene oxide for combined in vivo photoacoustic imaging and photothermal therapy. *Biomaterials* **2013,** *34* (21), 5236-5243.
428. Bianco, A.; Cheng, H.-M.; Enoki, T.; Gogotsi, Y.; Hurt, R. H.; Koratkar, N.; Kyotani, T.; Monthioux, M.; Park, C. R.; Tascon, J. M. D.; Zhang, J., All in the graphene family - A recommended nomenclature for two-dimensional carbon materials. *Carbon* **2013,** *65*, 1-6.
429. Bussy, C.; Jasim, D.; Lozano, N.; Terry, D.; Kostarelos, K., The current graphene safety landscape - a literature mining exercise. *Nanoscale* **2015,** *7* (15), 6432-6435.
430. Bussy, C.; Ali-Boucetta, H.; Kostarelos, K., Safety Considerations for Graphene: Lessons Learnt from Carbon Nanotubes. *Accounts of Chemical Research* **2013,** *46* (3), 692-701.
431. Ali-Boucetta, H.; Al-Jamal, K. T.; McCarthy, D.; Prato, M.; Bianco, A.; Kostarelos, K., Multiwalled carbon nanotube-doxorubicin supramolecular complexes for cancer therapeutics. *Chemical Communications* **2008,** (4), 459-461.
432. Wang, K.; Ruan, J.; Song, H.; Zhang, J. L.; Wo, Y.; Guo, S. W.; Cui, D. X., Biocompatibility of Graphene Oxide. *Nanoscale Research Letters* **2011,** *6,* 1-8.
433. Gollavelli, G.; Ling, Y. C., Multi-functional graphene as an in vitro and in vivo imaging probe. *Biomaterials* **2012,** *33* (8), 2532-2545.
434. Hu, W. B.; Peng, C.; Lv, M.; Li, X. M.; Zhang, Y. J.; Chen, N.; Fan, C. H.; Huang, Q., Protein Corona-Mediated Mitigation of Cytotoxicity of Graphene Oxide. *ACS Nano* **2011,** *5* (5), 3693-3700.
435. Liao, K. H.; Lin, Y. S.; Macosko, C. W.; Haynes, C. L., Cytotoxicity of Graphene Oxide and Graphene in Human Erythrocytes and Skin Fibroblasts. *ACS Applied Materials & Interfaces* **2011,** *3* (7), 2607-2615.
436. Pinto, A. M.; Moreira, S.; Goncalves, I. C.; Gama, F. M.; Mendes, A. M.; Magalhaes, F. D., Biocompatibility of poly(lactic acid) with incorporated graphene-based materials. *Colloids and Surfaces B-Biointerfaces* **2013,** *104*, 229-238.
437. Cai, X.; Tan, S. Z.; Yu, A. L.; Zhang, J. L.; Liu, J. H.; Mai, W. J.; Jiang, Z. Y., Sodium 1-Naphthalenesulfonate-Functionalized Reduced Graphene Oxide Stabilizes Silver Nanoparticles with Lower Cytotoxicity and Long-Term Antibacterial Activity. *Chemistry-an Asian Journal* **2012,** *7* (7), 1664-1670.
438. Jarosz, A.; Skoda, M.; Dudek, I.; Szukiewicz, D., Oxidative Stress and Mitochondrial Activation as the Main Mechanisms Underlying Graphene Toxicity against Human Cancer Cells. *Oxidative Medicine and Cellular Longevity* **2016,** .
439. Pelin, M.; Fusco, L.; Leon, V.; Martin, C.; Criado, A.; Sosa, S.; Vazquez, E.; Tubaro, A.; Prato, M., Differential cytotoxic effects of graphene and graphene oxide on skin keratinocytes. *Scientific Reports* **2017,** *7,* 40572/1-12.
440. Jaworski, S.; Sawosz, E.; Grodzik, M.; Winnicka, A.; Prasek, M.; Wierzbicki, M.; Chwalibog, A., In vitro evaluation of the effects of graphene platelets on glioblastoma multiforme cells. *International Journal of Nanomedicine* **2013,** *8*, 413-420.

441. Li, Y.; Liu, Y.; Fu, Y.; Wei, T.; Le Guyader, L.; Gao, G.; Liu, R.-S.; Chang, Y.-Z.; Chen, C., The triggering of apoptosis in macrophages by pristine graphene through the MAPK and TGF-beta signaling pathways. *Biomaterials* **2012,** *33* (2), 402-411.
442. Bengtson, S.; Kling, K.; Madsen, A. M.; Noergaard, A. W.; Jacobsen, N. R.; Clausen, P. A.; Alonso, B.; Pesquera, A.; Zurutuza, A.; Ramos, R.; Okuno, H.; Dijon, J.; Wallin, H.; Vogel, U., No cytotoxicity or genotoxicity of graphene and graphene oxide in murine lung epithelial FE1 cells in vitro. *Environmental and Molecular Mutagenesis* **2016,** *57* (6), 469-482.
443. Chang, Y. L.; Yang, S. T.; Liu, J. H.; Dong, E.; Wang, Y. W.; Cao, A. N.; Liu, Y. F.; Wang, H. F., In vitro toxicity evaluation of graphene oxide on A549 cells. *Toxicology Letters* **2011,** *200* (3), 201-210.
444. Lammel, T.; Boisseaux, P.; Fernandez-Cruz, M. L.; Navas, J. M., Internalization and cytotoxicity of graphene oxide and carboxyl graphene nanoplatelets in the human hepatocellular carcinoma cell line Hep G2. *Particle and Fibre Toxicology* **2013,** *10,* 27/1-21.
445. Vallabani, N. V. S.; Mittal, S.; Shukla, R. K.; Pandey, A. K.; Dhakate, S. R.; Pasricha, R.; Dhawan, A., Toxicity of Graphene in Normal Human Lung Cells (BEAS-2B). *Journal of Biomedical Nanotechnology* **2011,** *7* (1), 106-107.
446. Kang, S. M.; Kim, T. H.; Choi, J. W., Cell Chip to Detect Effects of Graphene Oxide Nanopellet on Human Neural Stem Cell. *Journal of Nanoscience and Nanotechnology* **2012,** *12* (7), 5185-5190.
447. Wang, Y. Z.; Wu, S. L.; Zhao, X. D.; Su, Z.; Du, L.; Sui, A. H., In vitro toxicity evaluation of graphene oxide on human RPMI 8226 cells. *Bio-Medical Materials and Engineering* **2014,** *24* (6), 2007-2013.
448. Choi, Y. J.; Kim, E.; Han, J. W.; Kim, J. H.; Gurunathan, S., A Novel Biomolecule-Mediated Reduction of Graphene Oxide: A Multifunctional Anti-Cancer Agent. *Molecules* **2016,** *21* (3), 1-10.
449. Wojtoniszak, M.; Chen, X.; Kalenczuk, R. J.; Wajda, A.; Lapczuk, J.; Kurzewski, M.; Drozdzik, M.; Chu, P. K.; Borowiak-Palen, E., Synthesis, dispersion, and cytocompatibility of graphene oxide and reduced graphene oxide. *Colloids and Surfaces B-Biointerfaces* **2012,** *89*, 79-85.
450. Fiorillo, M.; Verre, A. F.; Iliut, M.; Peiris-Pages, M.; Ozsvari, B.; Gandara, R.; Cappello, A. R.; Sotgia, F.; Vijayaraghavan, A.; Lisanti, M. P., Graphene oxide selectively targets cancer stem cells, across multiple tumor types: Implications for non-toxic cancer treatment, via "differentiation-based nano-therapy". *Oncotarget* **2015,** *6* (6), 3553-3562.
451. Zhang, Y. B.; Ali, S. F.; Dervishi, E.; Xu, Y.; Li, Z. R.; Casciano, D.; Biris, A. S., Cytotoxicity Effects of Graphene and Single-Wall Carbon Nanotubes in Neural Phaeochromocytoma-Derived PC12 Cells. *ACS Nano* **2010,** *4* (6), 3181-3186.
452. Duch, M. C.; Budinger, G. R. S.; Liang, Y. T.; Soberanes, S.; Urich, D.; Chiarella, S. E.; Campochiaro, L. A.; Gonzalez, A.; Chandel, N. S.; Hersam, M. C.; Mutlu, G. M., Minimizing Oxidation and Stable Nanoscale Dispersion Improves the Biocompatibility of Graphene in the Lung. *Nano Letters* **2011,** *11* (12), 5201-5207.
453. Yuan, J. F.; Gao, H. C.; Ching, C. B., Comparative protein profile of human hepatoma HepG2 cells treated with graphene and single-walled carbon nanotubes: An iTRAQ-coupled 2D LC-MS/MS proteome analysis. *Toxicology Letters* **2011,** *207* (3), 213-221.
454. Gurunathan, S.; Han, J. W.; Eppakayala, V.; Kim, J. H., Green synthesis of graphene and its cytotoxic effects in human breast cancer cells. *International Journal of Nanomedicine* **2013,** *8*, 1015-1027.
455. Mu, Q. X.; Su, G. X.; Li, L. W.; Gilbertson, B. O.; Yu, L. H.; Zhang, Q.; Sun, Y. P.; Yan, B., Size-Dependent Cell Uptake of Protein-Coated Graphene Oxide Nanosheets. *ACS Applied Materials & Interfaces* **2012,** *4* (4), 2259-2266.
456. Sasidharan, A.; Panchakarla, L. S.; Chandran, P.; Menon, D.; Nair, S.; Rao, C. N. R.; Koyakutty, M., Differential nano-bio interactions and toxicity effects of pristine versus functionalized graphene. *Nanoscale* **2011,** *3* (6), 2461-2464.

457. Sasidharan, A.; Panchakarla, L. S.; Sadanandan, A. R.; Ashokan, A.; Chandran, P.; Girish, C. M.; Menon, D.; Nair, S. V.; Rao, C. N. R.; Koyakutty, M., Hemocompatibility and Macrophage Response of Pristine and Functionalized Graphene. *Small* **2012,** *8* (8), 1251-1263.
458. Cheng, C.; Nie, S. Q.; Li, S.; Peng, H.; Yang, H.; Ma, L.; Sun, S. D.; Zhao, C. S., Biopolymer functionalized reduced graphene oxide with enhanced biocompatibility via mussel inspired coatings/anchors. *Journal of Materials Chemistry B* **2013,** *1* (3), 265-275.
459. Romero-Aburto, R.; Narayanan, T. N.; Nagaoka, Y.; Hasumura, T.; Mitcham, T. M.; Fukuda, T.; Cox, P. J.; Bouchard, R. R.; Maekawa, T.; Kumar, D. S.; Torti, S. V.; Mani, S. A.; Ajayan, P. M., Fluorinated Graphene Oxide; a New Multimodal Material for Biological Applications. *Advanced Materials* **2013,** *25* (39), 5632-5637.
460. Chaudhari, N. S.; Pandey, A. P.; Patil, P. O.; Tekade, A. R.; Bari, S. B.; Deshmukh, P. K., Graphene oxide based magnetic nanocomposites for efficient treatment of breast cancer. *Materials Science & Engineering C-Materials for Biological Applications* **2014,** *37*, 278-285.
461. Chowdhury, S. M.; Lalwani, G.; Zhang, K. V.; Yang, J. Y.; Neville, K.; Sitharaman, B., Cell specific cytotoxicity and uptake of graphene nanoribbons. *Biomaterials* **2013,** *34* (1), 283-293.
462. Singh, S. K.; Singh, M. K.; Kulkarni, P. P.; Sonkar, V. K.; Gracio, J. J. A.; Dash, D., Amine-Modified Graphene. Thrombo-Protective Safer Alternative to Graphene Oxide for Biomedical Applications. *ACS Nano* **2012,** *6* (3), 2731-2740.
463. Singh, S. K.; Singh, M. K.; Nayak, M. K.; Kumari, S.; Shrivastava, S.; Gracio, J. J. A.; Dash, D., Thrombus Inducing Property of Atomically Thin Graphene Oxide Sheets. *ACS Nano* **2011,** *5* (6), 4987-4996.
464. Zhang, X. Y.; Yin, J. L.; Peng, C.; Hu, W. Q.; Zhu, Z. Y.; Li, W. X.; Fan, C. H.; Huang, Q., Distribution and biocompatibility studies of graphene oxide in mice after intravenous administration. *Carbon* **2011,** *49* (3), 986-995.
465. Tan, X. F.; Feng, L. Z.; Zhang, J.; Yang, K.; Zhang, S.; Liu, Z.; Peng, R., Functionalization of Graphene Oxide Generates a Unique Interface for Selective Serum Protein Interactions. *ACS Applied Materials & Interfaces* **2013,** *5* (4), 1370-1377.
466. Ding, Z.; Zhang, Z.; Ma, H.; Chen, Y., In Vitro Hemocompatibility and Toxic Mechanism of Graphene Oxide on Human Peripheral Blood T Lymphocytes and Serum Albumin. *ACS Applied Materials & Interfaces* **2014,** *6* (22), 19797-19807.
467. Akhavan, O.; Ghaderi, E.; Akhavan, A., Size-dependent genotoxicity of graphene nanoplatelets in human stem cells. *Biomaterials* **2012,** *33* (32), 8017-8025.
468. Wang, X. J.; Podila, R.; Shannahan, J. H.; Rao, A. M.; Brown, J. M., Intravenously delivered graphene nanosheets and multiwalled carbon nanotubes induce site-specific Th2 inflammatory responses via the IL-33/ST2 axis. *International Journal of Nanomedicine* **2013,** *8*, 1733-1748.
469. Sydlik, S. A.; Jhunjhunwala, S.; Webber, M. J.; Anderson, D. G.; Langer, R., In Vivo Compatibility of Graphene Oxide with Differing Oxidation States. *ACS Nano* **2015,** *9* (4), 3866-3874.
470. Yang, K.; Gong, H.; Shi, X. Z.; Wan, J. M.; Zhang, Y. J.; Liu, Z., In vivo biodistribution and toxicology of functionalized nano-graphene oxide in mice after oral and intraperitoneal administration. *Biomaterials* **2013,** *34* (11), 2787-2795.
471. Yang, K.; Wan, J. M.; Zhang, S. A.; Zhang, Y. J.; Lee, S. T.; Liu, Z. A., In Vivo Pharmacokinetics, Long-Term Biodistribution, and Toxicology of PEGylated Graphene in Mice. *ACS Nano* **2011,** *5* (1), 516-522.
472. Yan, L.; Zhao, F.; Li, S.; Hu, Z.; Zhao, Y., Low-toxic and safe nanomaterials by surface-chemical design, carbon nanotubes, fullerenes, metallofullerenes, and graphenes. *Nanoscale* **2011,** *3* (2), 362-382.
473. Sahu, A.; Choi, W. I.; Tae, G., A stimuli-sensitive injectable graphene oxide composite hydrogel. *Chemical Communications* **2012,** *48* (47), 5820-5822.
474. Ali-Boucetta, H.; Bitounis, D.; Raveendran-Nair, R.; Servant, A.; Van den Bossche, J.; Kostarelos, K., Purified Graphene Oxide Dispersions Lack In Vitro Cytotoxicity and In Vivo Pathogenicity. *Advanced Healthcare Materials* **2013,** *2* (3), 433-441.

475. Yan, L.; Wang, Y. P.; Xu, X.; Zeng, C.; Hou, J. P.; Lin, M. M.; Xu, J. Z.; Sun, F.; Huang, X. J.; Dai, L. M.; Lu, F.; Liu, Y., Can Graphene Oxide Cause Damage to Eyesight? *Chemical Research in Toxicology* **2012,** *25* (6), 1265-1270.
476. Schinwald, A.; Murphy, F. A.; Jones, A.; MacNee, W.; Donaldson, K., Graphene-Based Nanoplatelets: A New Risk to the Respiratory System as a Consequence of Their Unusual Aerodynamic Properties. *ACS Nano* **2012,** *6* (1), 736-746.
477. Ma-Hock, L.; Strauss, V.; Treumann, S.; Kuttler, K.; Wohlleben, W.; Hofmann, T.; Groters, S.; Wiench, K.; van Ravenzwaay, B.; Landsiedel, R., Comparative inhalation toxicity of multi-wall carbon nanotubes, graphene, graphite nanoplatelets and low surface carbon black. *Particle and Fibre Toxicology* **2013,** *10,* 23/1-19.
478. Sanchez, V. C.; Jachak, A.; Hurt, R. H.; Kane, A. B., Biological Interactions of Graphene-Family Nanomaterials: An Interdisciplinary Review. *Chemical Research in Toxicology* **2012,** *25* (1), 15-34.
479. Aillon, K. L.; Xie, Y.; El-Gendy, N.; Berkland, C. J.; Forrest, M. L., Effects of nanomaterial physicochemical properties on in vivo toxicity. *Advanced Drug Delivery Reviews* **2009,** *61* (6), 457-466.
480. Yue, H.; Wei, W.; Yue, Z.; Wang, B.; Luo, N.; Gao, Y.; Ma, D.; Ma, G.; Su, Z., The role of the lateral dimension of graphene oxide in the regulation of cellular responses. *Biomaterials* **2012,** *33* (16), 4013-4021.
481. Poland, C. A.; Duffin, R.; Kinloch, I.; Maynard, A.; Wallace, W. A. H.; Seaton, A.; Stone, V.; Brown, S.; MacNee, W.; Donaldson, K., Carbon nanotubes introduced into the abdominal cavity of mice show asbestos-like pathogenicity in a pilot study. *Nature Nanotechnology* **2008,** *3* (7), 423-428.
482. Jasim, D. A.; Boutin, H.; Fairclough, M.; Menard-Moyon, C.; Prenant, C.; Bianco, A.; Kostarelos, K., Thickness of functionalized graphene oxide sheets plays critical role in tissue accumulation and urinary excretion: A pilot PET/CT study. *Applied Materials Today* **2016,** *4*, 24-30.
483. Yue, H.; Wei, W.; Yue, Z. G.; Wang, B.; Luo, N. N.; Gao, Y. J.; Ma, D.; Ma, G. H.; Su, Z. G., The role of the lateral dimension of graphene oxide in the regulation of cellular responses. *Biomaterials* **2012,** *33* (16), 4013-4021.
484. Liu, J. H.; Yang, S. T.; Wang, H. F.; Chang, Y. L.; Cao, A. N.; Liu, Y. F., Effect of size and dose on the biodistribution of graphene oxide in mice. *Nanomedicine* **2012,** *7* (12), 1801-1812.
485. Duan, G. X.; Kang, S. G.; Tian, X.; Garate, J. A.; Zhao, L.; Ge, C. C.; Zhou, R. H., Protein corona mitigates the cytotoxicity of graphene oxide by reducing its physical interaction with cell membrane. *Nanoscale* **2015,** *7* (37), 15214-15224.
486. Mao, H.; Chen, W.; Laurent, S.; Thirifays, C.; Burtea, C.; Rezaee, F.; Mahmoudi, M., Hard corona composition and cellular toxicities of the graphene sheets. *Colloids and Surfaces B-Biointerfaces* **2013,** *109*, 212-218.
487. Lanphere, J. D.; Rogers, B.; Luth, C.; Bolster, C. H.; Walker, S. L., Stability and Transport of Graphene Oxide Nanoparticles in Groundwater and Surface Water. *Environmental Engineering Science* **2014,** *31* (7), 350-359.
488. Chen, L. Q.; Hu, P. P.; Zhang, L.; Huang, S. Z.; Luo, L. F.; Huang, C. Z., Toxicity of graphene oxide and multi-walled carbon nanotubes against human cells and zebrafish. *Science China-Chemistry* **2012,** *55* (10), 2209-2216.
489. Pretti, C.; Oliva, M.; Di Pietro, R.; Monni, G.; Cevasco, G.; Chiellini, F.; Pomelli, C.; Chiappe, C., Ecotoxicity of pristine graphene to marine organisms. *Ecotoxicology and Environmental Safety* **2014,** *101*, 138-145.
490. Begurn, P.; Ikhtiari, R.; Fugetsu, B., Graphene phytotoxicity in the seedling stage of cabbage, tomato, red spinach, and lettuce. *Carbon* **2011,** *49* (12), 3907-3919.
491. Hu, X. G.; Kang, J.; Lu, K. C.; Zhou, R. R.; Mu, L.; Zhou, Q. X., Graphene oxide amplifies the phytotoxicity of arsenic in wheat. *Scientific Reports* **2014,** *4,* 6122/1-10.

492. Begum, P.; Fugetsu, B., Induction of cell death by graphene in Arabidopsis thaliana (Columbia ecotype) T87 cell suspensions. *Journal of Hazardous Materials* **2013,** *260*, 1032-1041.
493. Khodakovskaya, M. V.; de Silva, K.; Nedosekin, D. A.; Dervishi, E.; Biris, A. S.; Shashkov, E. V.; Galanzha, E. I.; Zharov, V. P., Complex genetic, photothermal, and photoacoustic analysis of nanoparticle-plant interactions. *Proceedings of the National Academy of Sciences of the United States of America* **2011,** *108* (3), 1028-1033.
494. Zhao, J.; Wang, Z. Y.; White, J. C.; Xing, B. S., Graphene in the Aquatic Environment: Adsorption, Dispersion, Toxicity and Transformation. *Environmental Science & Technology* **2014,** *48* (17), 9995-10009.
495. Ma, S.; Lin, D. H., The biophysicochemical interactions at the interfaces between nanoparticles and aquatic organisms: adsorption and internalization. *Environmental Science-Processes & Impacts* **2013,** *15* (1), 145-160.
496. Bianco, A.; Kostarelos, K.; Prato, M., Making carbon nanotubes biocompatible and biodegradable. *Chemical Communications* **2011,** *47* (37), 10182-10188.
497. Kasemo, B., Biological surface science. *Current Opinion in Solid State & Materials Science* **1998,** *3* (5), 451-459.
498. Aplin, A. E.; Howe, A.; Alahari, S. K.; Juliani, R. L., Signal transduction and signal modulation by cell adhesion receptors: The role of integrins, cadherins, immunoglobulin-cell adhesion molecules, and selectins. *Pharmacological Reviews* **1998,** *50* (2), 197-263.
499. Ostuni, E.; Chapman, R. G.; Liang, M. N.; Meluleni, G.; Pier, G.; Ingber, D. E.; Whitesides, G. M., Self-assembled monolayers that resist the adsorption of proteins and the adhesion of bacterial and mammalian cells. *Langmuir* **2001,** *17* (20), 6336-6343.
500. Chen, C. S.; Mrksich, M.; Huang, S.; Whitesides, G. M.; Ingber, D. E., Geometric control of cell life and death. *Science* **1997,** *276* (5317), 1425-1428.
501. Khalili, A. A.; Ahmad, M. R., A Review of Cell Adhesion Studies for Biomedical and Biological Applications. *International Journal of Molecular Sciences* **2015,** *16* (8), 18149-18184.
502. Jockusch, B. M.; Bubeck, P.; Giehl, K.; Kroemker, M.; Moschner, J.; Rothkegel, M.; Rudiger, M.; Schluter, K.; Stanke, G.; Winkler, J., The molecular architecture of focal adhesions. *Annual Review of Cell and Developmental Biology* **1995,** *11*, 379-416.
503. Horton, E. R.; Humphries, J. D.; James, J.; Jones, M. C.; Askari, J. A.; Humphries, M. J., The integrin adhesome network at a glance. *Journal of Cell Science* **2016,** *129* (22), 4159-4163.
504. Ruoslahti, E.; Pierschbacher, M. D., New perspectives in cell-adhesion - RGD and integrins. *Science* **1987,** *238* (4826), 491-497.
505. Wilson, C. J.; Clegg, R. E.; Leavesley, D. I.; Pearcy, M. J., Mediation of biomaterial-cell interactions by adsorbed proteins: A review. *Tissue Engineering* **2005,** *11* (1-2), 1-18.
506. Zelzer, M.; Albutt, D.; Alexander, M. R.; Russell, N. A., The Role of Albumin and Fibronectin in the Adhesion of Fibroblasts to Plasma Polymer Surfaces. *Plasma Processes and Polymers* **2012,** *9* (2), 149-156.
507. Ostuni, E.; Yan, L.; Whitesides, G. M., The interaction of proteins and cells with self-assembled monolayers of alkanethiolates on gold and silver. *Colloids and Surfaces B-Biointerfaces* **1999,** *15* (1), 3-30.
508. Kasemo, B., Biological surface science. *Surface Science* **2002,** *500* (1-3), 656-677.
509. Roach, P.; Farrar, D.; Perry, C. C., Surface tailoring for controlled protein adsorption: Effect of topography at the nanometer scale and chemistry. *Journal of the American Chemical Society* **2006,** *128* (12), 3939-3945.
510. Roach, P.; Farrar, D.; Perry, C. C., Interpretation of protein adsorption: Surface-induced conformational changes. *Journal of the American Chemical Society* **2005,** *127* (22), 8168-8173.
511. Vroman, L., Effect of adsorbed proteins on wettability of hydrophilic and hydrophobic solids. *Nature* **1962,** *196* (4853), 476-477.
512. Hirsh, S. L.; McKenzie, D. R.; Nosworthy, N. J.; Denman, J. A.; Sezerman, O. U.; Bilek, M. M. M., The Vroman effect: Competitive protein exchange with dynamic multilayer protein aggregates. *Colloids and Surfaces B-Biointerfaces* **2013,** *103*, 395-404.

513. Morla, A.; Zhang, Z. H.; Ruoslahti, E., Superfibronectin is a functionally distinct form of fibronectin. *Nature* **1994,** *367* (6459), 193-196.
514. Maddipati, K. R.; Marnett, L. J., Characterization of the major hydroperoxide-reducing activity of human-plasma - purification and properties of a selenium-dependent glutathione-peroxidasE. *Journal of Biological Chemistry* **1987,** *262* (36), 17398-17403.
515. Koblinski, J. E.; Wu, M.; Demeler, B.; Jacob, K.; Kleinman, H. K., Matrix cell adhesion activation by non-adhesion proteins. *Journal of Cell Science* **2005,** *118* (13), 2965-2974.
516. Mosher, D. F.; McKeownlongo, P. J., Assembly of fibronectin-containing extracellular-matrix - a glimpse of the machinery. *Biopolymers* **1985,** *24* (1), 199-210.
517. Petersen, T. E.; Thogersen, H. C.; Skorstengaard, K.; Vibepedersen, K.; Sahl, P.; Sottrupjensen, L.; Magnusson, S., Partial primary structure of bovine plasma fibronectin - 3 types of internal homology. *Proceedings of the National Academy of Sciences of the United States of America-Biological Sciences* **1983,** *80* (1), 137-141.
518. Singer, II; Kawka, D. W.; Kazazis, D. M.; Clark, R. A. F., *Invivo* co-distribution of fibronectin and actin fibers in granulation-tissue - immunofluorescence and electron-microscope studies of the fibronexus at the myofibroblast surface. *Journal of Cell Biology* **1984,** *98* (6), 2091-2106.
519. Rubin, K.; Hook, M.; Obrink, B.; Timpl, R., Substrate adhesion of rat hepatocytes - mechanism of attachment to collagen substrates. *Cell* **1981,** *24* (2), 463-470.
520. Hynes, R. O., Integrins - versatility, modulation, and signaling in cell-adhesion. *Cell* **1992,** *69* (1), 11-25.
521. Berg, M. C.; Yang, S. Y.; Hammond, P. T.; Rubner, M. F., Controlling mammalian cell interactions on patterned polyelectrolyte multilayer surfaces. *Langmuir* **2004,** *20* (4), 1362-1368.
522. Hersel, U.; Dahmen, C.; Kessler, H., RGD modified polymers: biomaterials for stimulated cell adhesion and beyond. *Biomaterials* **2003,** *24* (24), 4385-4415.
523. Alberts, B.; Johnson, A.; Lewis, J.; Roberts, K.; Raff, M.; Walter, P., Molecular Biology of the Cell. 4th edition ed.; Garland Science: New York, 2002.
524. Sonnenberg, A.; Modderman, P. W.; Hogervorst, F., Laminin receptor on platelets is the integrin VLA-6. *Nature* **1988,** *336* (6198), 487-489.
525. Habermann, B. F.; Cheresh, D. A., Vitronectin and its receptors. *Current Opinion in Cell Biology* **1993,** *5* (5), 864-868.
526. Braam, S. R.; Tertoolen, L.; van de Stolpe, A.; Meyer, T.; Passier, R.; Mummery, C. L., Prediction of drug-induced cardiotoxicity using human embryonic stem cell-derived cardiomyocytes. *Stem Cell Research* **2010,** *4* (2), 107-116.
527. Kruegel, J.; Miosge, N., Basement membrane components are key players in specialized extracellular matrices. *Cellular and Molecular Life Sciences* **2010,** *67* (17), 2879-2895.
528. Khoshnoodi, J.; Pedchenko, V.; Hudson, B. G., Mammalian collagen IV. *Microscopy Research and Technique* **2008,** *71* (5), 357-370.
529. Schwartz, M. A., Integrin signaling revisited. *Trends in Cell Biology* **2001,** *11* (12), 466-470.
530. Bacakova, L.; Filova, E.; Parizek, M.; Ruml, T.; Svorcik, V., Modulation of cell adhesion, proliferation and differentiation on materials designed for body implants. *Biotechnology Advances* **2011,** *29* (6), 739-767.
531. Ruoslahti, E., INTEGRINS. *Journal of Clinical Investigation* **1991,** *87* (1), 1-5.
532. Horwitz, A. F., Integrins and health. *Scientific American* **1997,** *276* (5), 68-75.
533. Beningo, K. A.; Dembo, M.; Kaverina, I.; Small, J. V.; Wang, Y. L., Nascent focal adhesions are responsible for the generation of strong propulsive forces in migrating fibroblasts. *Journal of Cell Biology* **2001,** *153* (4), 881-887.
534. Dumbauld, D. W.; Lee, T. T.; Singh, A.; Scrimgeour, J.; Gersbach, C. A.; Zamir, E. A.; Fu, J.; Chen, C. S.; Curtis, J. E.; Craig, S. W.; Garcia, A. J., How vinculin regulates force transmission.

Proceedings of the National Academy of Sciences of the United States of America **2013,** *110* (24), 9788-9793.
535. Kinbara, K.; Goldfinger, L. E.; Hansen, M.; Chou, F. L.; Ginsberg, M. H., Ras GTPases: Integrins' friends or foes? *Nature Reviews Molecular Cell Biology* **2003,** *4* (10), 767-776.
536. Webb, K.; Hlady, V.; Tresco, P. A., Relative importance of surface wettability and charged functional groups on NIH 3T3 fibroblast attachment, spreading, and cytoskeletal organization. *Journal of Biomedical Materials Research* **1998,** *41* (3), 422-430.
537. Clark, E. A.; Brugge, J. S., Integrins and signal-transduction pathways - the road taken. *Science* **1995,** *268* (5208), 233-239.
538. Schwartz, M. A.; Schaller, M. D.; Ginsberg, M. H., Integrins: Emerging paradigms of signal transduction. *Annual Review of Cell and Developmental Biology* **1995,** *11*, 549-599.
539. Maher, P. A.; Pasquale, E. B.; Wang, J. Y. J.; Singer, S. J., Phosphotyrosine-containing proteins are concentrated in focal adhesions and intercellular-junctions in normal-cells. *Proceedings of the National Academy of Sciences of the United States of America* **1985,** *82* (19), 6576-6580.
540. Tsukita, S.; Oishi, K.; Akiyama, T.; Yamanashi, Y.; Yamamoto, T., Specific protooncogenic tyrosine kinases of src family are enriched in cell-to-cell adherens junctions where the level of tyrosine phosphorylation is elevated. *Journal of Cell Biology* **1991,** *113* (4), 867-879.
541. Guan, J. L.; Trevithick, J. E.; Hynes, R. O., Fibronectin integrin interaction induces tyrosine phosphorylation of a 120-KDa protein. *Cell Regulation* **1991,** *2* (11), 951-964.
542. Hall, A., Rho GTPases and the actin cytoskeleton. *Science* **1998,** *279* (5350), 509-514.
543. Liu, S. C.; Calderwood, D. A.; Ginsberg, M. H., Integrin cytoplasmic domain-binding proteins. *Journal of Cell Science* **2000,** *113* (20), 3563-3571.
544. Wiesner, S.; Legate, K. R.; Fassler, R., Integrin-actin interactions. *Cellular and Molecular Life Sciences* **2005,** *62* (10), 1081-1099.
545. Mitra, S. K.; Hanson, D. A.; Schlaepfer, D. D., Focal adhesion kinase: In command and control of cell motility. *Nature Reviews Molecular Cell Biology* **2005,** *6* (1), 56-68.
546. Goldmann, W. H., Kinetic determination of focal adhesion protein formation. *Biochemical and Biophysical Research Communications* **2000,** *271* (2), 553-557.
547. Horwitz, A.; Duggan, K.; Buck, C.; Beckerle, M. C.; Burridge, K., Interaction of plasma-membrane fibronectin receptor with talin - a transmembrane linkage. *Nature* **1986,** *320* (6062), 531-533.
548. Otey, C. A.; Pavalko, F. M.; Burridge, K., An interaction between alpha-actinin and the beta-1 integrin subunit *invitro*. *Journal of Cell Biology* **1990,** *111* (2), 721-729.
549. Pavalko, F. M.; Otey, C. A.; Burridge, K., Identification of a filamin isoform enriched at the ends of stress fibers in chicken-embryo fibroblastS. *Journal of Cell Science* **1989,** *94*, 109-118.
550. Schlaepfer, D. D.; Mitra, S. K.; Ilic, D., Control of motile and invasive cell phenotypes by focal adhesion kinase. *Biochimica Et Biophysica Acta-Molecular Cell Research* **2004,** *1692* (2-3), 77-102.
551. Parsons, J. T., Focal adhesion kinase: the first ten years. *Journal of Cell Science* **2003,** *116* (8), 1409-1416.
552. Glenney, J. R.; Zokas, L., Novel tyrosine kinase substrates from rous-sarcoma virus-transformed cells are present in the membrane skeleton. *Journal of Cell Biology* **1989,** *108* (6), 2401-2408.
553. Schaller, M. D., Paxillin: a focal adhesion-associated adaptor protein. *Oncogene* **2001,** *20* (44), 6459-6472.
554. Carisey, A.; Ballestrem, C., Vinculin, an adapter protein in control of cell adhesion signalling. *European Journal of Cell Biology* **2011,** *90* (2-3), 157-163.
555. Chen, H.; Cohen, D. M.; Choudhury, D. M.; Kioka, N.; Craig, S. W., Spatial distribution and functional significance of activated vinculin in living cells. *Journal of Cell Biology* **2005,** *169* (3), 459-470.

556. Humphries, J. D.; Wang, P.; Streuli, C.; Geiger, B.; Humphries, M. J.; Ballestrem, C., Vinculin controls focal adhesion formation by direct interactions with talin and actin. *Journal of Cell Biology* **2007,** *179* (5), 1043-1057.
557. Suzuki, S. T., Structural and functional diversity of cadherin superfamily: Are new members of cadherin superfamily involved in signal transduction pathway? *Journal of Cellular Biochemistry* **1996,** *61* (4), 531-542.
558. Cowin, P.; Burke, B., Cytoskeleton-membrane interactions. *Current Opinion in Cell Biology* **1996,** *8* (1), 56-65.
559. Shapiro, L.; Fannon, A. M.; Kwong, P. D.; Thompson, A.; Lehmann, M. S.; Grubel, G.; Legrand, J. F.; Alsnielsen, J.; Colman, D. R.; Hendrickson, W. A., Structural basis of cell-cell adhesion by cadherins. *Nature* **1995,** *374* (6520), 327-337.
560. Aberle, H.; Schwartz, H.; Kemler, R., Cadherin-catenin complex: Protein interactions and their implications for cadherin function. *Journal of Cellular Biochemistry* **1996,** *61* (4), 514-523.
561. Peifer, M., Regulating cell proliferation: As easy as APC. *Science* **1996,** *272* (5264), 974-975.
562. Haniffa, M. A.; Collin, M. P.; Buckley, C. D.; Dazzi, F., Mesenchymal stem cells: the fibroblasts' new clothes? *Haematologica-the Hematology Journal* **2009,** *94* (2), 258-263.
563. Fries, K. M.; Blieden, T.; Looney, R. J.; Sempowski, G. D.; Silvera, M. R.; Willis, R. A.; Phipps, R. P., Evidence of fibroblast heterogeneity and the role of fibroblast subpopulations in fibrosis. *Clinical Immunology and Immunopathology* **1994,** *72* (3), 283-292.
564. Mebius, R. E., Organogenesis of lymphoid tissues. *Nature Reviews Immunology* **2003,** *3* (4), 292-303.
565. Serhan, C. N.; Brain, S. D.; Buckley, C. D.; Gilroy, D. W.; Haslett, C.; O'Neill, L. A. J.; Perretti, M.; Rossi, A. G.; Wallace, J. L., Resolution of inflammation: state of the art, definitions and terms. *Faseb Journal* **2007,** *21* (2), 325-332.
566. Chang, H. Y.; Chi, J. T.; Dudoit, S.; Bondre, C.; van de Rijn, M.; Botstein, D.; Brown, P. O., Diversity, topographic differentiation, and positional memory in human fibroblasts. *Proceedings of the National Academy of Sciences of the United States of America* **2002,** *99* (20), 12877-12882.
567. Thomson, J. A.; Itskovitz-Eldor, J.; Shapiro, S. S.; Waknitz, M. A.; Swiergiel, J. J.; Marshall, V. S.; Jones, J. M., Embryonic stem cell lines derived from human blastocysts. *Science* **1998,** *282* (5391), 1145-1147.
568. Reubinoff, B. E.; Pera, M. F.; Fong, C. Y.; Trounson, A.; Bongso, A., Embryonic stem cell lines from human blastocysts: somatic differentiation in vitro. *Nature Biotechnology* **2000,** *18* (4), 399-404.
569. Yusuf, B.; Gopurappilly, R.; Dadheech, N.; Gupta, S.; Bhonde, R.; Pal, R., Embryonic fibroblasts represent a connecting link between mesenchymal and embryonic stem cells. *Development Growth & Differentiation* **2013,** *55* (3), 330-340.
570. Covas, D. T.; Panepucci, R. A.; Fontes, A. M.; Silva, W. A.; Orellana, M. D.; Freitas, M. C. C.; Neder, L.; Santos, A. R. D.; Peres, L. C.; Jamur, M. C.; Zago, M. A., Multipotent mesenchymal stromal cells obtained from diverse human tissues share functional properties and gene-expression profile with CD146(+) perivascular cells and fibroblasts. *Experimental Hematology* **2008,** *36* (5), 642-654.
571. Horwitz, E. M.; Le Blanc, K.; Dominici, M.; Mueller, I.; Slaper-Cortenbach, I.; Marini, F. C.; Deans, R. J.; Krause, D. S.; Keating, A., Clarification of the nomenclature for MSC: The international society for cellular therapy position statement. *Cytotherapy* **2005,** *7* (5), 393-395.
572. Haniffa, M. A.; Wang, X. N.; Holtick, U.; Rae, M.; Isaacs, J. D.; Dickinson, A. M.; Hilkens, C. M. U.; Collin, M. P., Adult human fibroblasts are potent immunoregulatory cells and functionally equivalent to mesenchymal stem cells. *Journal of Immunology* **2007,** *179* (3), 1595-1604.

573. Gurunathan, S.; Han, J. W.; Eppakayala, V.; Kim, J. H., Biocompatibility of microbially reduced graphene oxide in primary mouse embryonic fibroblast cells. *Colloids and Surfaces B-Biointerfaces* **2013,** *105*, 58-66.
574. Gurunathan, S.; Han, J. W.; Eppakayala, V.; Dayem, A. A.; Kwon, D. N.; Kim, J. H., Biocompatibility effects of biologically synthesized graphene in primary mouse embryonic fibroblast cells. *Nanoscale Research Letters* **2013,** *8,* .
575. Carpio, I. E. M.; Santos, C. M.; Wei, X.; Rodrigues, D. F., Toxicity of a polymer-graphene oxide composite against bacterial planktonic cells, biofilms, and mammalian cells. *Nanoscale* **2012,** *4* (15), 4746-4756.
576. Tian, H. C.; Liu, J. Q.; Wei, D. X.; Kang, X. Y.; Zhang, C.; Du, J. C.; Yang, B.; Chen, X.; Zhu, H. Y.; NuLi, Y. N.; Yang, C. S., Graphene oxide doped conducting polymer nanocomposite film for electrode-tissue interface. *Biomaterials* **2014,** *35* (7), 2120-2129.
577. Lin, F.; Du, F.; Huang, J. Y.; Chau, A.; Zhou, Y. S.; Duan, H. L.; Wang, J. X.; Xiong, C. Y., Substrate effect modulates adhesion and proliferation of fibroblast on graphene layer. *Colloids and Surfaces B-Biointerfaces* **2016,** *146*, 785-793.
578. Lee, J. H.; Shin, Y. C.; Jin, O. S.; Lee, E. J.; Han, D. W.; Kang, S. H.; Hong, S. W.; Ahn, J. Y.; Kim, S. H., Cytotoxicity evaluations of pristine graphene and carbon nanotubes in fibroblastic cells. *Journal of the Korean Physical Society* **2012,** *61* (6), 873-877.
579. Todaro, G. J.; Green, H., Quantitative studies of the growth of mouse embryo cells in culture and their development into established lines. *The Journal of Cell Biology* **1963,** *17* (1), 299-313.
580. Takeuchi, T.; Wang, L.; Mori, S.; Nakagawa, K.; Yoshikura, H.; Kanda, T., Characterization of mouse 3T3-Swiss albino cells available in Japan: Necessity of quality control when used as feeders. *Japanese Journal of Infectious Diseases* **2008,** *61* (1), 9-12.
581. Friedenstein, A.; Chailakhyan, R.; UV, G., Bone marrow osteogenic stem cells: in vitro cultivation and transplantation in diffusion chambers. *Cell and Tissue Kinetics* **1987,** *20* (3), 263-272.
582. Mao, J. J., Stem-cell-driven regeneration of synovial joints. *Biology of the Cell* **2005,** *97* (5), 289-301.
583. Colter, D. C.; Class, R.; DiGirolamo, C. M.; Prockop, D. J., Rapid expansion of recycling stem cells in cultures of plastic-adherent cells from human bone marrow. *Proceedings of the National Academy of Sciences of the United States of America* **2000,** *97* (7), 3213-3218.
584. Dominici, M.; Le Blanc, K.; Mueller, I.; Slaper-Cortenbach, I.; Marini, F. C.; Krause, D. S.; Deans, R. J.; Keating, A.; Prockop, D. J.; Horwitz, E. M., Minimal criteria for defining multipotent mesenchymal stromal cells. The International Society for Cellular Therapy position statement. *Cytotherapy* **2006,** *8* (4), 315-317.
585. Chamberlain, G.; Fox, J.; Ashton, B.; Middleton, J., Concise review: Mesenchymal stem cells: Their phenotype, differentiation capacity, immunological features, and potential for homing. *Stem Cells* **2007,** *25* (11), 2739-2749.
586. Jaiswal, N.; Haynesworth, S. E.; Caplan, A. I.; Bruder, S. P., Osteogenic differentiation of purified, culture-expanded human mesenchymal stem cells in vitro. *Journal of Cellular Biochemistry* **1997,** *64* (2), 295-312.
587. Langenbach, F.; Handschel, J., Effects of dexamethasone, ascorbic acid and beta-glycerophosphate on the osteogenic differentiation of stem cells in vitro. *Stem Cell Research & Therapy* **2013,** *4,* 117/1-7.
588. Hamidouche, Z.; Hay, E.; Vaudin, P.; Charbord, P.; Schule, R.; Marie, P. J.; Fromigue, O., FHL2 mediates dexamethasone-induced mesenchymal cell differentiation into osteoblasts by activating Wnt/beta-catenin signaling-dependent Runx2 expression. *Faseb Journal* **2008,** *22* (11), 3813-3822.
589. Gaur, T.; Lengner, C. J.; Hovhannisyan, H.; Bhat, R. A.; Bodine, P. V. N.; Komm, B. S.; Javed, A.; van Wijnen, A. J.; Stein, J. L.; Stein, G. S.; Lian, J. B., Canonical WNT signaling promotes osteogenesis by directly stimulating Runx2 gene expression. *Journal of Biological Chemistry* **2005,** *280* (39), 33132-33140.

590. Tada, H.; Nemoto, E.; Foster, B. L.; Somerman, M. J.; Shimauchi, H., Phosphate increases bone morphogenetic protein-2 expression through cAMP-dependent protein kinase and ERK1/2 pathways in human dental pulp cells. *Bone* **2011,** *48* (6), 1409-1416.
591. Foster, B. L.; Nociti, F. H.; Swanson, E. C.; Matsa-Dunn, D.; Berry, J. E.; Cupp, C. J.; Zhang, P.; Somerman, M. J., Regulation of cementoblast gene expression by inorganic phosphate in vitro. *Calcified Tissue International* **2006,** *78* (2), 103-112.
592. Fatherazi, S.; Matsa-Dunn, D.; Foster, B. L.; Rutherford, R. B.; Somerman, M. J.; Presland, R. B., Phosphate Regulates Osteopontin Gene Transcription. *Journal of Dental Research* **2009,** *88* (1), 39-44.
593. Bruder, S. P.; Jaiswal, N.; Haynesworth, S. E., Growth kinetics, self-renewal, and the osteogenic potential of purified human mesenchymal stem cells during extensive subcultivation and following cryopreservation. *Journal of Cellular Biochemistry* **1997,** *64* (2), 278-294.
594. Mackay, A. M.; Beck, S. C.; Murphy, J. M.; Barry, F. P.; Chichester, C. O.; Pittenger, M. F., Chondrogenic differentiation of cultured human mesenchymal stem cells from marrow. *Tissue Engineering* **1998,** *4* (4), 415-428.
595. Johnstone, B.; Hering, T. M.; Caplan, A. I.; Goldberg, V. M.; Yoo, J. U., In vitro chondrogenesis of bone marrow-derived mesenchymal progenitor cells. *Experimental Cell Research* **1998,** *238* (1), 265-272.
596. van der Kraan, P. M.; Davidson, E. N. B.; Blom, A.; van den Berg, W. B., TGF-beta signaling in chondrocyte terminal differentiation and osteoarthritis Modulation and integration of signaling pathways through receptor-Smads. *Osteoarthritis and Cartilage* **2009,** *17* (12), 1539-1545.
597. Worster, A. A.; Nixon, A. J.; Brower-Toland, B. D.; Williams, J., Effect of transforming growth factor beta 1 on chondrogenic differentiation of cultured equine mesenchymal stem cells. *American Journal of Veterinary Research* **2000,** *61* (9), 1003-1010.
598. Farquharson, C.; Berry, J. L.; Mawer, E. B.; Seawright, E.; Whitehead, C. C., Ascorbic acid-induced chondrocyte terminal differentiation: the role of the extracellular matrix and 1,25-dihydroxyvitamin D. *European Journal of Cell Biology* **1998,** *76* (2), 110-118.
599. Rosen, E. D.; MacDougald, O. A., Adipocyte differentiation from the inside out. *Nature Reviews Molecular Cell Biology* **2006,** *7* (12), 885-896.
600. Klemm, D. J.; Leitner, J. W.; Watson, P.; Nesterova, A.; Reusch, J. E. B.; Goalstone, M. L.; Draznin, B., Insulin-induced adipocyte differentiation - Activation of CREB rescues adipogenesis from the arrest caused by inhibition of prenylation. *Journal of Biological Chemistry* **2001,** *276* (30), 28430-28435.
601. Lehmann, J. M.; Lenhard, J. M.; Oliver, B. B.; Ringold, G. M.; Kliewer, S. A., Peroxisome proliferator-activated receptors alpha and gamma are activated by indomethacin and other non-steroidal anti-inflammatory drugs. *Journal of Biological Chemistry* **1997,** *272* (6), 3406-3410.
602. Styner, M.; Sen, B.; Xie, Z. H.; Case, N.; Rubin, J., Indomethacin Promotes Adipogenesis of Mesenchymal Stem Cells Through a Cyclooxygenase Independent Mechanism. *Journal of Cellular Biochemistry* **2010,** *111* (4), 1042-1050.
603. Smas, C. M.; Sul, H. S., PREF-1, a protein containing EGF-like repeats, inhibits adipocyte differentiation. *Cell* **1993,** *73* (4), 725-734.
604. Gregoire, F. M.; Smas, C. M.; Sul, H. S., Understanding adipocyte differentiation. *Physiological Reviews* **1998,** *78* (3), 783-809.
605. Wu, Z. D.; Xie, Y. H.; Bucher, N. L. R.; Farmer, S. R., Conditional ectopic expression of C/EBP-beta in NIH-3T3 cells induces PPAR-gamma and stimulates adipogenesis. *Genes & Development* **1995,** *9* (19), 2350-2363.
606. Thomas, H. R.; Valles, C.; Young, R. J.; Kinloch, I. A.; Wilson, N. R.; Rourke, J. P., Identifying the fluorescence of graphene oxide. *Journal of Materials Chemistry C* **2013,** *1* (2), 338-342.

607. He, T.; Chan, V., Covalent layer-by-layer assembly of polyethyleneimine multilayer for antibacterial applications. *Journal of Biomedical Materials Research Part A* **2010,** *95A* (2), 454-464.
608. Shvero, D. K.; Davidi, M. P.; Weiss, E. I.; Srerer, N.; Beyth, N., Antibacterial effect of polyethyleneimine nanoparticles incorporated in provisional cements against Streptococcus mutans. *Journal of Biomedical Materials Research Part B-Applied Biomaterials* **2010,** *94B* (2), 367-371.
609. Beyth, N.; Yudovin-Farber, I.; Bahir, R.; Domb, A. J.; Weissa, E., Antibacterial activity of dental composites containing quaternary ammonium polyethylenimine nanoparticles against Streptococcus mutans. *Biomaterials* **2006,** *27* (21), 3995-4002.
610. Kugler, R.; Bouloussa, O.; Rondelez, F., Evidence of a charge-density threshold for optimum efficiency of biocidal cationic surfaces. *Microbiology-Sgm* **2005,** *151*, 1341-1348.
611. Merbach , A. S.; Helm , L.; Tóth, É., The Chemistry of Contrast Agents in Medical Magnetic Resonance Imaging. Second ed.; John Wiley and Sons: Chichester, United Kingdom, 2013.
612. Carr, D. H.; Gadian, D. G., Contrast agents in magnetic-resonance imaging. *Clinical Radiology* **1985,** *36* (6), 561-568.
613. Gries, H., *Extracellular MRI Contrast Agents Based on Gadolinium*. Springer-Verlag: Berlin, 2002.
614. Rashid, H. U.; Martines, M. A. U.; Jorge, J.; de Moraes, P. M.; Umar, M. N.; Khan, K.; Rehman, H. U., Cyclen-based Gd3+ complexes as MRI contrast agents: Relaxivity enhancement and ligand design. *Bioorganic & Medicinal Chemistry* **2016,** *24* (22), 5663-5684.
615. Cakic, N.; Gunduz, S.; Rengarasu, R.; Angelovski, G., Synthetic strategies for preparation of cyclen-based MRI contrast agents. *Tetrahedron Letters* **2015,** *56* (6), 759-765.
616. Geraldes, C.; Laurent, S., Classification and basic properties of contrast agents for magnetic resonance imaging. *Contrast Media & Molecular Imaging* **2009,** *4* (1), 1-23.
617. Schumann, H.; Kuse, K., Lanthanide Complexes of 1-(2-Propenyl)- and 1-(3-Butenyl)-1,4,7,10-tetraazacyclododecane-4,7,10-tris-Acetic Acid. *Zeitschrift Fur Anorganische Und Allgemeine Chemie* **2008,** *634* (15), 2954-2958.
618. Tran, S. L.; Puhar, A.; Ngo-Camus, M.; Ramarao, N., Trypan Blue Dye Enters Viable Cells Incubated with the Pore-Forming Toxin HlyII of Bacillus cereus. *Plos One* **2011,** *6* (9), 22876/1-5.
619. Ahn, S. J.; Costa, J.; Emanuel, J. R., PicoGreen quantitation of DNA: Effective evaluation of samples pre- or post-PCR. *Nucleic Acids Research* **1996,** *24* (13), 2623-2625.
620. Singer, V. L.; Jones, L. J.; Yue, S. T.; Haugland, R. P., Characterization of PicoGreen reagent and development of a fluorescence-based solution assay for double-stranded DNA quantitation. *Analytical Biochemistry* **1997,** *249* (2), 228-238.

3. GRAPHENE FUNCTIONALISATION AND GRAPHENE-CONTAINING LAYER-BY-LAYER CONSTRUCTS.

One of the principal research aims was to develop a graphene functionalisation which causes minimal damage to the graphene sheet, thus preserving its physical properties. The functionalisation should be able to modulate the dispersibility of graphene, as well as providing groups by which to tether biomolecules. The functionalisations presented in this chapter are based upon electrophilic aromatic substitution. By its nature, it should specifically target edges and defect sites, resulting in limited disturbance of the extended π-system of the pristine graphene sheet. The functionalisation outlined in this chapter are the sulfonate and thiol functionalisations of pristine graphene, to produce graphene sulfonate (G-SO_3) and graphene thiol (G-SH), respectively. The thiol functionalisation gives rise to the possibility of tethering biomolecules by redox-cleavable disulphide linkages, maleimido coupling, radical addition to alkenes and gold-thiol bonds. In addition, the sulfonate functionalisations would increase the polarity of graphene, therefore increasing its aqueous dispersibility.

In this chapter, the characterisation of as-prepared graphene, G-SO_3 and G-SH is presented via UV-visible spectroscopy, transmission electron microscopy, Raman spectroscopy, X-ray photoelectron spectroscopy, Fourier transform infrared (FTIR) spectroscopy, Brunauer-Emmett-Teller (BET) surface area analysis, water contact angles, thermogravimetric analysis and dispersibility measurements. In addition, the attachment of biologically-relevant molecules to G-SH is evidenced. Finally, G-SO_3, graphene oxide (GO) and sulfonated graphene oxide (GO-SO_3) were incorporated

into layer-by-layer (LbL) constructs with polyethyleneimine (PEI) and are compared to assess the effect of different graphene functionalisations on LbL assemblies.

3.1. Research aims

The aims of the research discussed in this chapter were to:

- Develop edge-selective graphene functionalisations that can alter the dispersibility of graphene and provide functional groups, while conserving the graphene sheet dimensions, defect density and conductivity.
- Demonstrate the tethering of molecules to functionalised graphene thiol (G-SH).
- Incorporate G-SO_3, GO and GO-SO_3 into PEI LbL constructs and to compare the graphene distribution and properties.

3.2. Characterisation of graphene, graphene sulfonate and graphene thiol

Graphene was produced as outlined in Section 2.1.1 of the Materials and Methods chapter. Briefly, graphite flakes were sonicated in NMP for 48 hours, followed by centrifugation steps to remove denser graphitic flakes. The target functionalisations of as-prepared graphene was were sulfonation and thiol functionalisation. The target materials, graphene sulfonate (G-SO_3) and graphene thiol (G-SH), along with the corresponding reaction schemes, are depicted in Figure 3-1. The following section outlines the characterisations performed to confirm the presence of these functional groups on graphene.

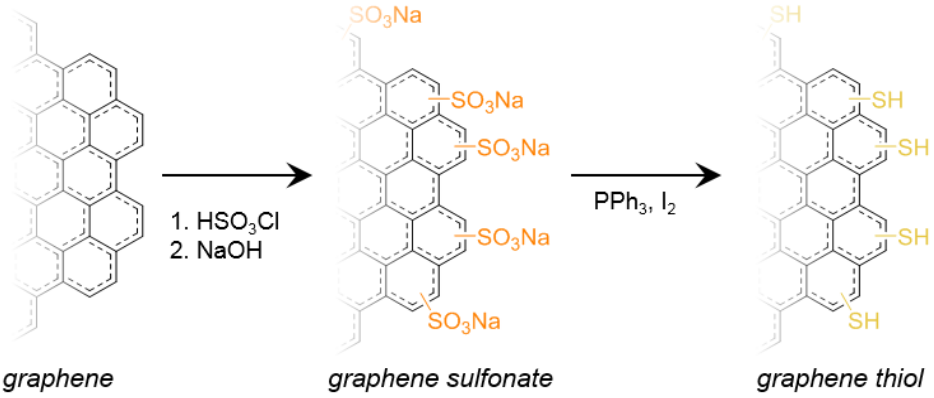

Figure 3-1. Reaction scheme for producing graphene sulfonate (G-SO_3) and graphene thiol (G-SH). Figure rendered by Christopher Blanford.

3.2.1. UV-visible spectroscopy

As-produced graphene, of unknown concentration, was diluted in NMP and the UV-visible absorbance (at 660 nm) recorded as a function of the percentage graphene in NMP. For example, the ’25 % graphene in NMP’ was graphene, diluted fourfold in NMP from the original solution. The resultant UV-visible data is shown in Figure 3-2.

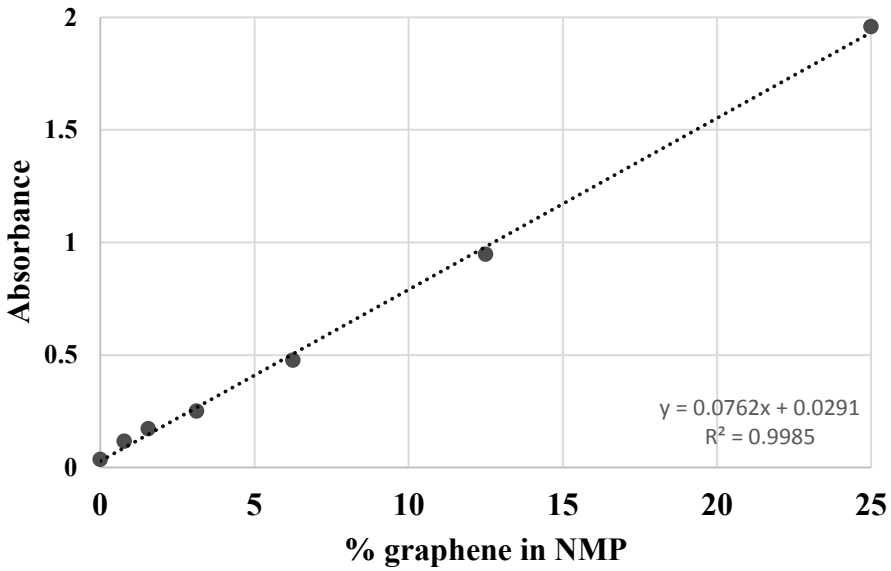

Figure 3-2. UV-visible absorbance as a function of graphene percentage in NMP. $R^2 = 0.9985$

Using the graphene extinction coefficient (660 nm) of 2460 L g^{-1} m^{-1},[1] with path length of 1 cm (0.01 m), the concentration of the produced graphene dispersion was calculated by extrapolation of the graph in Figure 3-2 and using the Beer-Lambert Law. The calculated 'as-produced' graphene concentration was therefore approximately 0.31 mg mL^{-1}, indicating a graphene yield of approximately 8 % (as-produced concentration graphene/ starting concentration of graphite). This value is in good agreement with sonochemically exfoliated graphene produced by Khan *et al*.[2]

3.2.2. Transmission electron microscopy

Transmission electron microscopy (TEM) was used to visualise the as-produced graphene flakes and to confirm the exfoliation. NMP could not be used as the dispersing solvent for TEM measurements, as the boiling point is above 200 °C, meaning that it would be difficult to remove all residual solvent, even with heating. The as-produced graphene was therefore re-dispersed into ethanol and pipetted on to a holey carbon grid under mild heating, to evaporate off the ethanol.

Figure **3-3** shows representative TEM images (A and B) and electron diffraction pattern (C) of sonochemically exfoliated graphene flakes, as well as a TEM image of a graphene thiol (G-SH) flake.

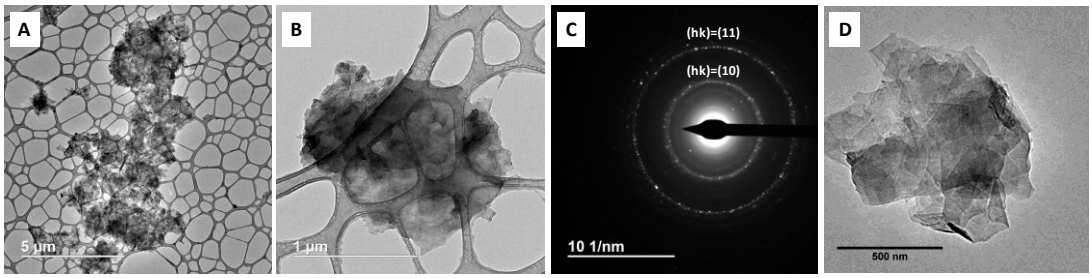

Figure 3-3. TEM images of graphene (dispersed in ethanol) on a holey carbon grid A) Zoomed out B) Zoomed in on single agglomeration of flakes and C) Selected area electron diffraction pattern of as-produced graphene D) A G-SH flake.

In both the lower magnification image (Figure 3-3A) and higher magnification image (Figure 3-3B), it is evident that the graphene flakes have re-agglomerated.

Though ethanol has been reported to disperse graphene, significant sedimentation occurs over time and sonication is required to re-disperse the graphene flakes.[3] The selected-area electron diffraction pattern (Figure 3-3C) does not display the typical hexagonal diffraction spots normally observed for graphene,[4] instead showing a superposition of several hexagonal diffraction spots forming two rings for the (hk) = (10) and hk = (11) planes on the inner and outer ring, respectively.[4] The calculated d-spacings were 0.127 nm and 0.219 nm for d_{11} and d_{10}, respectively. This electron diffraction pattern indicates turbostratic graphene layers, stacked in multiple orientations.[5,6,7] Raman was used in conjunction with the TEM data to confirm the presence of turbostratic graphene and to determine the average number of layers, by reference to the 2D peak.[8]

Figure 3-3D shows the TEM image of G-SH. Again, the image shows some re-stacked flakes. The lateral size of the flakes is around 1 micron, which indicates that the flakes are not ripped apart significantly by the functionalisation process.

3.2.3. Raman spectroscopy

Raman spectra were recorded for graphite and the as-prepared sonochemically exfoliated graphene to confirm the exfoliation and are shown in Figure 3-4.

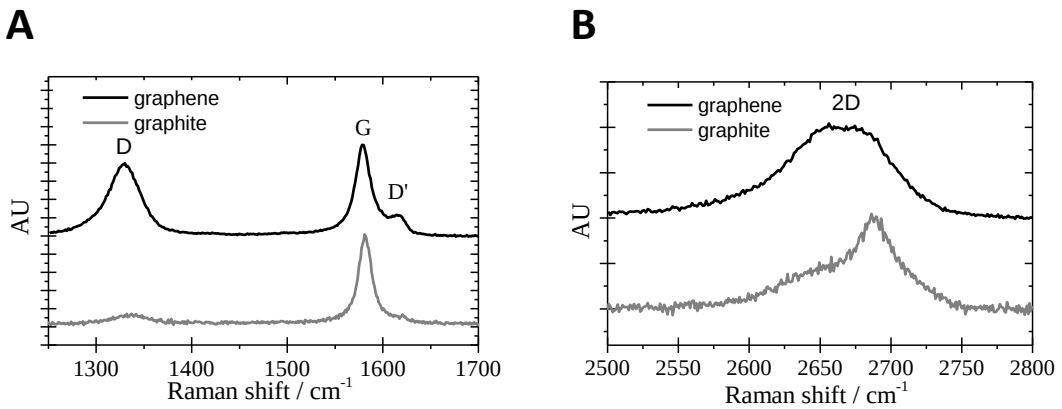

Figure 3-4. Raman spectra of graphite (grey) and graphene (black). A) D and G region B) 2D region.

For graphite, there are no discernible defect-induced D or D' peaks, which are both present in the graphene sample. The appearance of the D and D' peaks for graphene indicate a decrease in flake size upon sonochemical exfoliation, which has been reported by Coleman and co-workers.[9] The 2D peak which is asymmetric for graphite is broader and symmetrical for graphene and is shifted to lower Raman shift, indicating the exfoliation of graphite to sheets of 5 layers and lower. This is consistent with reported Raman spectra for sonochemically exfoliated graphene.[2,8,9] The increase in the full width half maximum (FWHM) of the 2D peak has been shown to arise from turbostratic graphene, in which the larger linewidth arises from the relaxation of the Raman selection rules due to the random orientation of graphene layers.[10,11,12] This evidence supports the TEM findings that the sonochemical exfoliation of graphene produces exfoliated graphene sheets.

Raman spectra were compared on as-prepared graphene, G-SO_3 and G-SH powder filter cakes, as described in the materials and methods. Raman spectra are displayed in Figure 3-5A (D,G and D' peaks) and Figure 3-5B (2D peak). All graphene materials show the characteristic G and 2D peaks observed in graphene.[10,13,14] In addition, all show the defect-induced D and D' peaks,[8,10,15] which are formally

forbidden by Raman selection rules, but occur via a single-phonon intervalley and intravalley process, with the defects providing the additional momentum, so that momentum is conserved.[15]

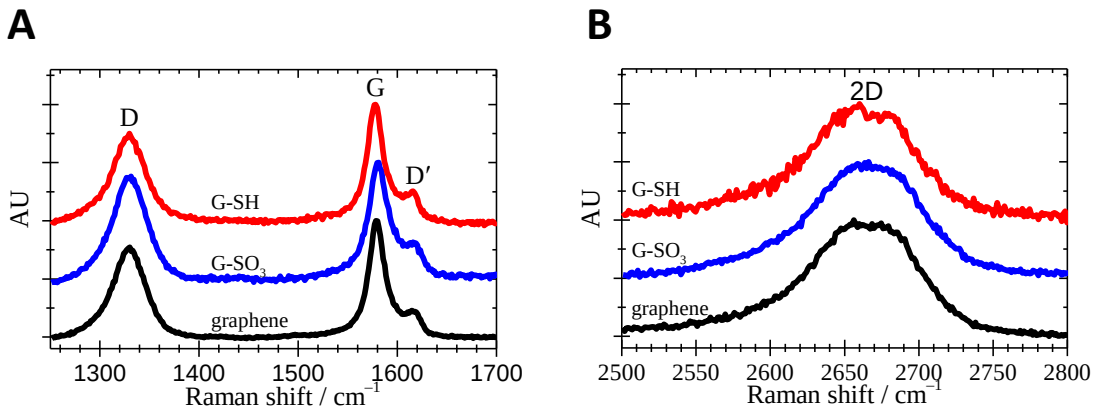

Figure 3-5. Raman spectra for graphene (black), graphene sulfonate (blue) and graphene thiol (red) A) D and G region B) 2D region.

The position of the 2D peak has been reported, both by Park *et al*. and Ferrari *et al.*, to increase with an increasing number of layers, as has the full width at half maximum (FWHM) of the peak.[8,16] The position and FWHM for the 2D peaks of graphene, G-SO_3 and G-SH are reported in Table 3-1 and are consistent with graphene between 3-5 layers, as the 2D band were located at 2662 cm^{-1}, 2664 cm^{-1} and 2660 cm^{-1}, respectively.[2,8,10] These results are consistent with Raman spectra for sonochemically-exfoliated graphene reported by Coleman *et al*.[2]

Table 3-1. Tabulated data for Raman spectra of graphene, G-SO_3 and G-SH.

Material	$I_D/I_{D'}$	Position of 2D peak/ cm^{-1}	FWHM (2D)/ cm^{-1}	I_D/I_G	$I_{D'}/I_G$	G peak position/ cm^{-1}
graphene	3.3	2662	82.1	0.78	0.24	1579
G-SO_3	2.7	2664	84.5	0.86	0.32	1580
G-SH	2.9	2660	78.1	0.75	0.26	1578

Work by Hernandez *et al.* reported the absence of a significant D peak for sonochemically exfoliated flakes greater than 1 micron in size, but the appearance of a D peak for flakes smaller than 1 μm, which they attributed to an increased number

of edge defects.[1,8] In addition, Coleman and co-workers found the I_D/I_G to scale with the lateral dimensions of the flakes, with Khan *et al.* observing the evolution of the D band with increasing sonication time.[2] The hypothesis of Coleman papers, which is substantiated by complementary methods, is that the increase in D band intensity with sonication time and rotation rate is solely from the introduction of new edges as graphene sheets are cut.[2] The appearance of a significant D peak for graphene, G-SO_3 and G-SH indicates that the graphene lateral dimensions are smaller than 1 micron, supporting the evidence from the TEM images. This also supports that the TEM agglomerates are not a result of incomplete exfoliation to graphene, but instead are a result of the TEM sample preparation which causes re-stacking and agglomeration of graphene.

The ratio of the D and G peaks also gives an indication of the number of defects in the graphene material, as the D peak increases with increasing defect concentration. Because the functionalisation should occur at edges, which are already 'defect sites', there should be not be a large change in the concentration of defects. There is a small increase in the I_D/I_G ratio increases after the sulfonation of graphene from 0.78 to 0.86, which decreases to 0.75 after the reduction to G-SH. The I_D/I_G change from graphene to G-SO_3 can be attributed to new defects forming in the G-SO_3 sheet, most likely from a small number of oxygen-containing defects. The change in I_D/I_G is not due to the decrease in size of flakes upon functionalisation (from tearing of graphene sheets), as the I_D/I_G ratio would have remained higher for G-SH, which is not the case. However, there is little shift in the G peak position, which suggests that the level of oxygen-containing defects is small. The G peak shifts, when graphene is oxidised, to a higher wavenumber, due to the single and double carbon bonds, made

as a result of the formation of sp^3 domains.[17] In addition, there is no significant reduction in intensity of the 2D peak, which would not be disappear or be significantly reduced in oxidised graphene, as oxygen-containing groups between the graphitic layers would lead to reduced ordering along the axis perpendicular to the graphene.[18,19]

As outlined in the Introduction, the D' peak is induced by disorder, with the ratio of the D' and G peaks varying considerably with the type of defect introduced. The $I_D/I_{D'}$ ratios can give more precise information about defect types and, though the $I_D/I_{D'}$ ratios varied amongst the three species, in all cases the $I_D/I_{D'}$ ratio remain around 3, which is nearest to the typical values for 'boundary-like defects', with typical values for sp^3 hybridisation at about 13 and for vacancies at about 7. Therefore, it can be concluded that the increase in sp^3 defects is minimal.[15]

3.2.4. X-ray photoelectron spectroscopy

X-ray photoelectron spectroscopy (XPS) of graphene, G-SO_3 and G-SH was performed to identify the presence of sulfonate and thiol functional groups. The survey scan can be seen in Figure 3-6, showing the presence of a S 2p peak in the G-SO_3 and G-SH, which is not present in the pristine graphene sample.

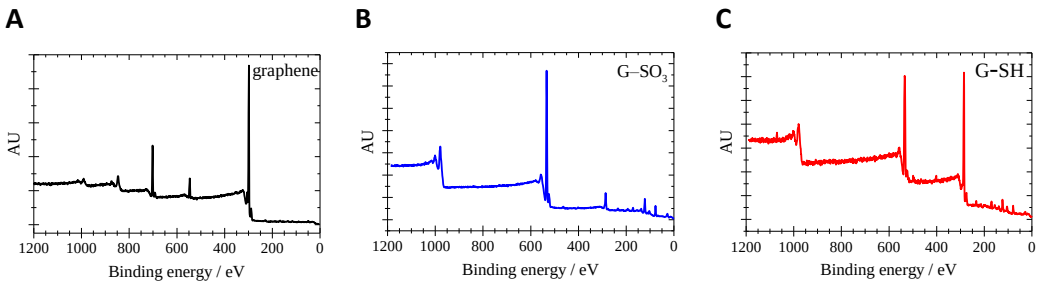

Figure 3-6. XPS survey spectra for A) graphene B) graphene sulfonate C) graphene thiol. Data acquired by Ashley Shepherd (Oxford University).

C 1s peaks can be seen in Figure 3-7, with peak fittings shown in Table 3-2. For unfunctionalised graphene there is a small degree of oxygen containing functionality,

consistent with findings from Coleman *et al*. for sonochemically exfoliated graphene, who report small defect formation.[20] A C-F peak was observed in the graphene C 1s spectrum, at a binding energy consistent with aliphatic fluorine. The aliphatic nature of this peak indicates that it is not a species directly bound to graphene, but rather an artefact or contaminant. Likely sources of contamination include the vacuum grease used in the filtration set up, or fluorine-containing compounds present inside the Schott bottles in which the graphene was stored. This peak was not observed in any other material, indicating that it was a contaminant in the graphene sample. The C1s peak, situated close to 300 eV in this figure, appears to decrease in intensity for G-SO_3. However, the apparent change in magnitude of this peak is not from the loss of any carbon material, but due to the corresponding increase in the magnitude of the O1s peak. The increased O1s peak is due to the increased hydrophilicity of the G-SO_3 material as a result of the sulfonation process. The increase in this peak is not likely to be caused by oxidation of the graphene, as the Raman spectra suggests little change in defects between the unfunctionalised graphene and G-SO_3. The C1s spectra, with corresponding C-O fittings, can be seen in Figure 3-7, and show the increase in the C-O peak for G-SO_3.

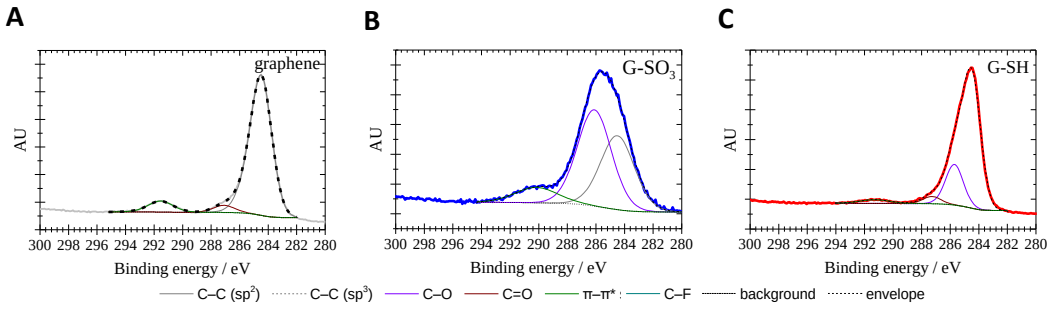

Figure 3-7. C 1s spectra for A) graphene B) graphene sulfonate C) graphene thiol. Data acquired by Ashley Shepherd (Oxford University).

Table 3-2. Peak fitting results for XPS for C1s from pristine and edge-modified graphene.

Material	C–C (sp^2)/ eV	C–C (sp^3)/ eV	C–O/ eV	C=O/ eV	π–π*/ eV
graphene	284.5	—	—	287.1	291.6
G-SO_3	284.5	—	286.1	—	290.1
G-SH	284.6	—	285.8	287.3	291.3

Upon transformation to G-SO_3, the magnitude of the C-O peak fit is larger, most likely due to a small degree of oxidation introduced by the sulphonation. The C-O peak from G-SO_3 to G-SH decreases in amplitude, due the reducing conditions used to achieve G-SH, which would also reduce any oxygen-containing defects on the graphene sheets. However, graphene, G-SO_3 and G-SH, there were no fits for the sp^3 carbons and, in addition, the C-O peaks are close to those for adventitious C-O. The S 2p spectra of G-SO_3 and G-SH are shown in Figure 3-8, with peak positions shown in Table 3-3. The presence of S 2p peaks in G-SO_3 and G-SH is evidence of the functionalisation of the pristine graphene.

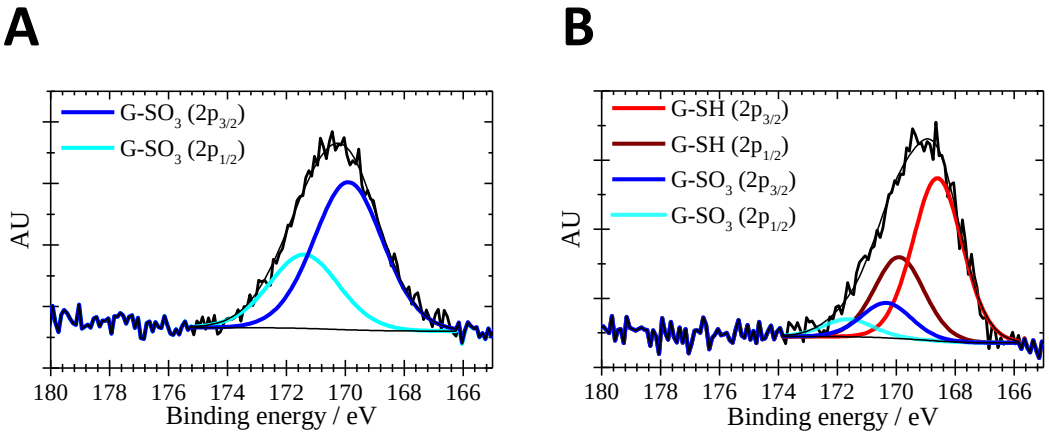

Figure 3-8. S 2p XPS spectra for A) Graphene sulfonate B) Graphene thiol. Data acquired by Ashley Shepherd (Oxford University).

The S 2p spectra of G-SO_3 and G-SH indicate the presence of C-S bonded species which are split, by spin-orbit coupling, into S $2p_{3/2}$ and S $2p_{1/2}$ lines. The G-SO_3 2p spectra consists of two peaks corresponding to the S $2p_{3/2}$ and S $2p_{1/2}$ lines for the

C-SO_3^- bond. For G-SH, the presence of two sets of S $2p_{3/2}$ and S $2p_{1/2}$ peaks indicates that there are residual unreduced C-SO_3^- groups remaining after reduction. The fraction of -SO_3^- groups remaining after reduction was calculated to be 0.18, indicating an 82 % conversion to G-SH.

Table 3-3. Peak fitting results for XPS for S 2p from pristine and sulfur-containing edge-modified graphene. The right-most column gives the ratio of the areas of SO_3 peaks to total S 2p peak area.

Material	-SH ($2p_{3/2}$)/ eV	-SH ($2p_{1/2}$)/ eV	-SO_3 /($2p_{3/2}$) eV	-SO_3 ($2p_{1/2}$)/ eV	Fraction SO_3
G-SO_3	—	—	169.9	171.4	1.00
G-SH	168.6	169.9	170.4	171.7	0.18

For the -SO_3^- groups, the sulfur is attached to oxygens, which are electron withdrawing groups, causing the S 2p electrons to possess increased binding energies. Upon reduction, there is a smaller deshielding effect, as the oxygen-containing groups are replaced by hydrogen, leading to a decreased binding energy for the -SH sulfur. The second set of S $2p_{3/2}$ and S $2p_{1/2}$ lines, arising from the C-SH species, therefore appear at lower binding energy. The XPS data above confirms the conversion of pristine graphene into G-SO_3 and the reduction to G-SH. The approximate percentage of sulfur in G-SO_3 was calculated to be 2.2 % with G-SH containing approximately 3 % sulfur.

3.2.5. Fourier transform infrared spectroscopy

Figure 3-9 shows the Fourier Transform Infrared (FTIR) spectra of graphene, G-SO_3 and G-SH. In the low energy spectra (Figure 3-9B) peaks at 1124 and 1034 cm^{-1} for G-SO_3 can be attributed to the two ν(S-O) stretches of the -SO_3H bond,[21,22] which are not observed in the unfunctionalised graphene FTIR spectra.[23] It is difficult to see

whether these peaks have disappeared in the case of G-SH, as there is a strong, broad absorbance centred at 1097 cm^{-1}.

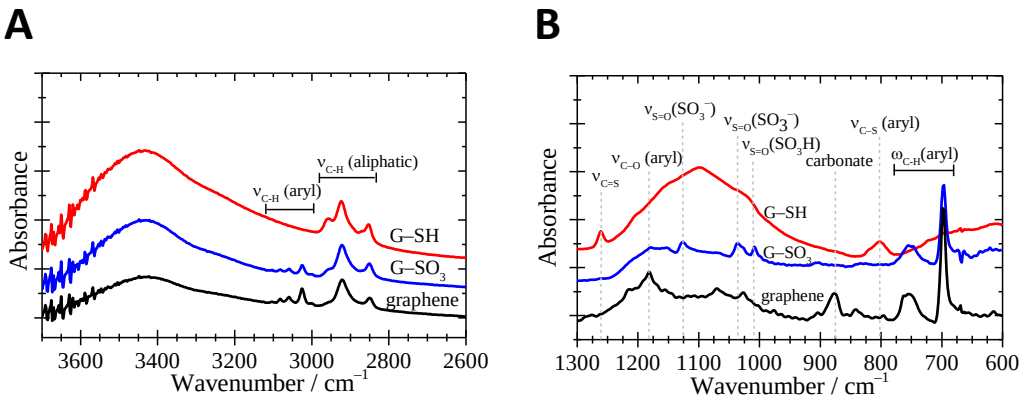

Figure 3-9. Baseline-corrected FTIR spectra for graphene (black), graphene sulfonate (blue) and graphene thiol (red). Graphene and graphene thiol spectra were shifted by -30 and +30 mAU, respectively, for clearer representation. A) High energy B) low energy spectra. Dotted lines represent peaks of interest.

Peaks at 1261 cm^{-1} and approximately 800 cm^{-1} for G-SH, which are not present in either graphene or G-SO_3, can be assigned to C=S bond and C-S bonds, respectively, which have been observed in thiol groups grafted to GO.[24] The S-H stretch of thiol group should be at around 2550-2600 cm^{-1}, but is not observed in G-SH. However, this stretch is known to be weak and can be obscured by any carboxyl absorptions in the same region.[25] Peaks between 675 cm^{-1} and 775 cm^{-1}, present in both unfunctionalized graphene and G-SO_3, can be attributed to C-H aryl stretches, although the peaks decrease in intensity from graphene to G-SO_3, indicating the replacement of hydrogens with sulfonate groups. In addition, the C-H aryl region between 3000 cm^{-1} and 3100 cm^{-1} is present in pristine graphene and is still present, but is weaker for G-SO_3. The FTIR spectra supports the XPS data in confirming the presence of C-S bonded functional groups.

3.2.6. Brunauer–Emmett–Teller (BET) surface area analysis

To confirm the surface area and number of layers in graphene, G-SO_3 and G-SH, surface area analysis was conducted by analysis of their N_2 adsorption isotherms, which are presented in Figure 3-10. All three materials exhibit a Type IIb isotherms, indicating aggregates of materials with slit-shaped pores.[26] Type IIb isotherms are normal Type II adsorption isotherms with H3 hysteresis (see appendix for hysteresis classifications) and no plateau at high P/P_0.[27]

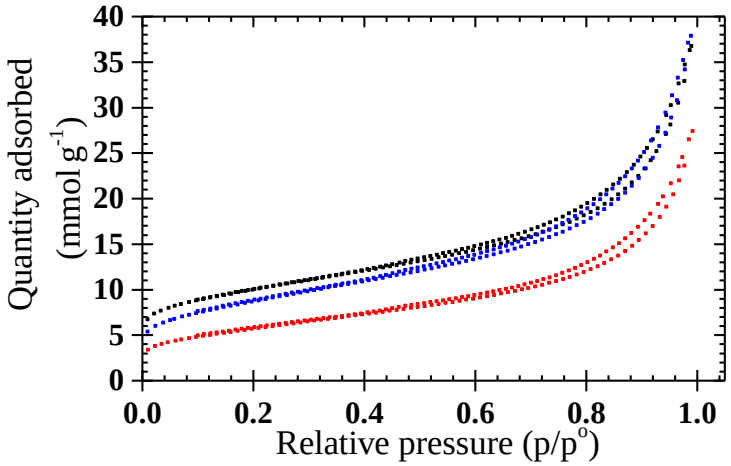

Figure 3-10. Isotherm for N_2 adsorption for graphene (black), G-SO_3 (blue) and G-SH (red).

To determine surface area information, the linearised form of the BET equation was used, with linearised BET plots for graphene, G-SO_3 and G-SH shown in Figure 3-11A. Rouquerol developed a method by which to determine the data to include for fitting of the linearised BET equation; The BET constant, C, should be positive and the BET equation should only be applicable for the pressure range in which the term $Q\ (1 - P_0)$ continuously increases as a function of P/P_0.[28] Rouquerol plots for each of the graphene materials are shown in Figure 3-11B. The P/P_0 cut off for the BET data, as determined by the Rouquerol plots, were 0.17 for graphene, 0.25 for G-SO_3 and 0.27 G-SH, which therefore determined the points to be used for surface area analysis.

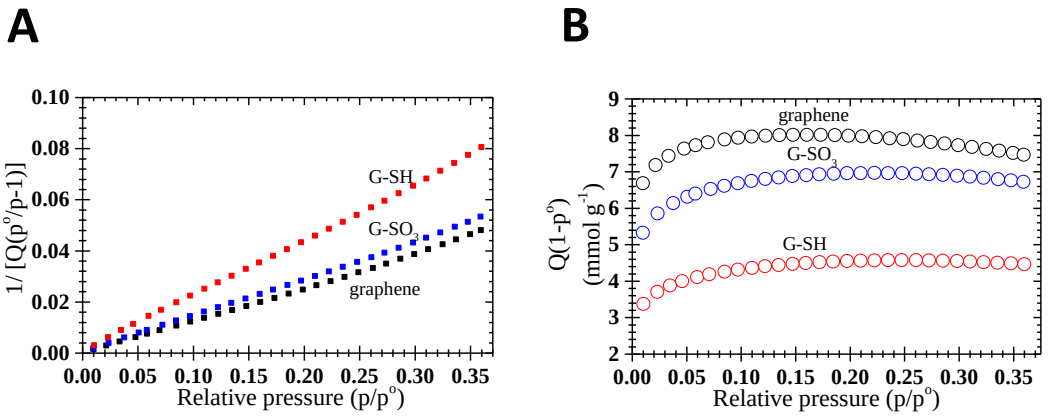

Figure 3-11. BET analysis on graphene (black), G-SO_3 (blue) and G-SH (red). A) Linearised BET plot. B) Rouquerol BET plot.

After the calculation of $\boldsymbol{Q_m}$, the monolayer adsorbed gas quantity, the BET surface area was calculated using Equation 4:

$$\boldsymbol{S_{BET} = \frac{Q_m N_A A_{CS}}{V_M m}} \quad (1)$$

Where $\boldsymbol{N_A}$ is Avogadro's number, $\boldsymbol{A_{CS}}$ is the cross-sectional surface area of the adsorbing gas, $\boldsymbol{V_M}$ is the molar volume of gas and $\boldsymbol{m}$ the mass of the sample. The cross-sectional surface area of N_2 was set to 0.162 nm^2.[29] The BET constant, monolayer adsorbed gas quantity and calculated BET surfaces areas resulting from the BET measurements are summarised in Table 3-4.

Table 3-4. BET values obtained from analysis of BET isotherm plots

Material	C	Q_m / mmol g^{-1}	Surface area / $m^2 g^{-1}$
graphene	335.3	8.2	794.9 ± 1.6
G-SO_3	169.9	7.1	693.4 ± 2.0
G-SH	133.1	4.7	456.0 ± 1.5

Using the calculated surface area of monolayer pristine graphene of (2630 m^2g^{-1}),[30] the average layer number for the unfunctionalised graphene is between 3-4 layers, which is consistent with the Raman data, outlined in Section 3.2.3. The decrease in specific surface area for both G-SO_3 and G-SH may be a result of the increase in

mass of the graphene flakes due to the functionalisations, leading to an apparent lowering in surface area.

Other explanations could be some re-stacking of graphene sheets, especially for G-SH. For G-SO_3 the average number of layers is around 4, and for G-SH is 6, by reference to the calculated surface area of monolayer graphene of 2630 $m^2 g^{-1}$.[30] This compares to the BET surface area of 2.9 m^2 g^{-1} for edge-sulfonated 'graphene' produced by Jeon *et al.*,[31] meaning that the edge functionalised graphene presented in this thesis has an area over 100 times greater. For comparison the edge-carboxylated GNPs (cGNPs) produced in the same group had a surface area of 389 $m^2 g^{-1}$.[32]

3.2.7. Contact angle measurements

The wettability of graphene, G-SO_3 and G-SH was assessed by looking at water contact angles of powder filter cakes. Water droplets were placed onto graphene filter cakes and the resultant contact angles measured. The concentration and area on which the graphene materials were filtered was the same in each case, meaning that the topological properties would be similar on each surface. The differences in contact angle would therefore indicate differing properties of the graphene materials. Figure 3-12 shows the images of contact angle measurements, with average contact angles are shown in Table 3-5.

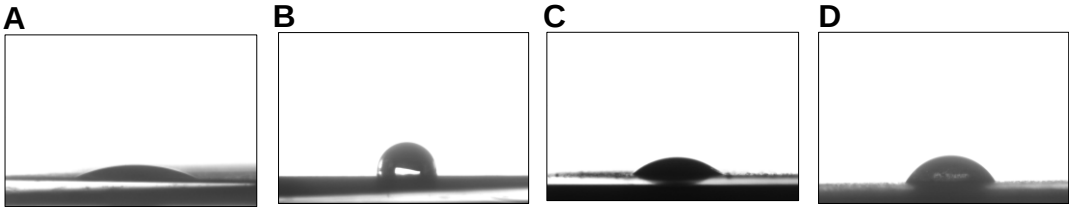

Figure 3-12. Contact angle measurements of water on Anodisc filters coated with a thin film of functionalised graphene. A) Anodisc control B) graphene C) graphene sulfonate D) graphene thiol.

Table 3-5. Contact angle measurements of water on Anodisc filter coated with a laminate of graphene powders. Errors are from repeated measurements.

Material	Contact angle
graphene	105.1° ± 7.7°
G-SO_3	45.9° ± 5.7°
G-SH	66.2° ± 3.6°
anodisc control	26° ± 8.3°

The contact angle for the as-prepared graphene was in good agreement with the published value for few-layered graphene, showing graphene to be hydrophobic.[33] However, the texture of these surfaces may have an impact on the observed contact angle, as the filter cake is made up of many small graphene flakes, rather than a continuous sheet, such as those in CVD graphene. The contact angle for G-SO_3 is much lower than for unfunctionalised graphene (45.9° vs. 105.1°), which is consistent with the expected increase in hydrophilicity by the introduction of oxygen-containing sulfonate groups, which increase the polarity and hydrogen bonding to water. The calculated contact angle here is higher than the 23.2° contact angle reported by Jeon *et al*. for sulfonated graphene produced by ball milling. However, the wt. % of sulfur in the ball-milled graphene was 9 %.[31] The contact angle increases for G-SH in comparison to G-SO_3 (66.2° vs. 45.9°), due to the removal of the sulfonate oxygen groups. However, the contact angle remains lower than for unfunctionalised graphene, indicating an increase in hydrophilicity for both functionalisations.

3.2.8. Dispersibility assessment

The dispersibility of the functionalised graphene materials was assessed in protic and aprotic solvents of differing polarities and levels of aromaticity. Graphene, G-SO_3 and G-SH were dispersed in water (dipole moment: 1.85 D, protic, non-aromatic), ethanol (dipole moment: 1.69 D, protic, non-aromatic), toluene (dipole moment: 0.36

D, aprotic, aromatic) and cyclohexane (non-polar, aprotic, non-aromatic), with images of the dispersions, after 24 hours, shown in Figure 3-13. G-SO_3 disperses well in water, in contrast to unfunctionalised graphene. G-SH is poorly dispersible in water, but shows better dispersion than unfunctionalised graphene. This follows the trends observed in the contact angle measurements, which indicate that the hydrophilicity of the graphene materials is in the order G-SO_3 > G-SH > graphene.

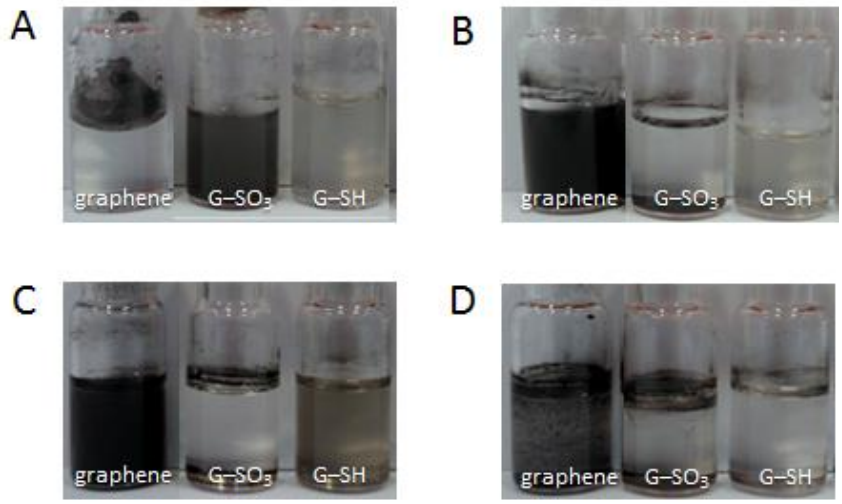

Figure 3-13. Dispersibility studies of functionalised graphene in A) water B) ethanol C) toluene D) cyclohexane. Concentration: 0.1 mg mL^{-1}

As seen in Figure 3-13C, unfunctionalised graphene disperses well in the relatively less polar, aromatic toluene (dipole moment: 0.36 D). However, toluene does not disperse G-SO_3, which is likely due to the increased polarity of G-SO_3 from the introduction of sulfonate functional groups. The G-SH shows dispersibility in toluene between these two extremes, again indicating that it is still more polar than unfunctionalised graphene, but less polar than G-SO_3. The same pattern was observed in ethanol (dipole moment: 1.69 D), as seen in Figure 3-13B. None of the graphene materials disperse well in cyclohexane (dipole moment: 0), as shown in Figure 3-13D since it is non-polar and non-aromatic.

The dispersibility images clearly indicate that upon functionalisation, the dispersibility of graphene in different solvents changes significantly, providing a further indication that the graphene, G-SO_3 and G-SH materials are chemically different and supports the XPS and FTIR evidence, which indicate the functionalisation of graphene.

3.2.9. Thermogravimetric analysis

Figure 3-14 displays the thermogravimetric analysis (TGA) traces for graphene, G-SO_3 and G-SH. TGA was used for compositional analysis, by assessing the decomposition of different functional groups with increasing temperature. Freeze-dried graphene was heated at 10 °C min^{-1} in a N_2 atmosphere, with mass loss recorded as a function of temperature, as shown in Figure 3-14A. The derivative weight, shown in Figure 3-14B, shows the points at which largest mass changes occurred in the samples.

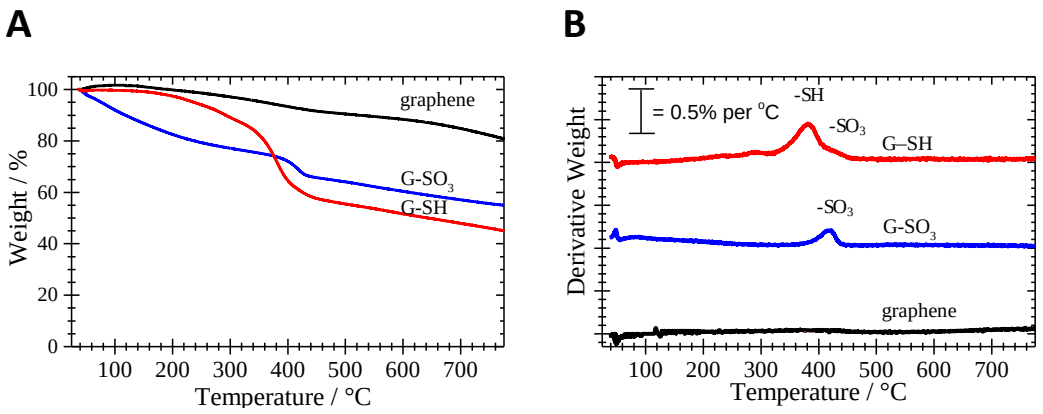

Figure 3-14. TGA plots for graphene (black), G-SO_3 (blue) and G-SH (red). Experimental conditions: heating rate 10 °C min^{-1}, N_2 atmosphere. A) Weight loss as a function of temperature B) Derivative weight as a function of temperature.

The functionalisation of graphene results in the lowering of thermal stability, with G-SO_3 and G-SH undergo significant mass loss below 800 °C, in contrast to the steady mass loss for graphene over the temperature range. The mass losses for both G-SO_3 and G-SH are larger than expected for just the loss of the functional groups,

so it is likely that the presence of these groups labilises the remaining graphene and allows it to decompose at a lower temperature. The temperature of the maximum mass loss in G-SO_3 occurs at 422 °C and at 380 °C for G-SH, indicating that the two samples are different. However, a shoulder can be seen in the derivative mass loss peak for G-SH, which is consistent with a small amount of remaining G-SO_3, as observed in the XPS data.

3.3. Attachment of biologically relevant molecules to graphene thiol

3.3.1. Glycographene and lectin-bioconjugate

The attachment of a lectin to edge-functionalised graphene was achieved by first attaching a mannose sugar to G-SH by click chemistry, to produce ‘glycographene’, followed by the attachment of the lectin to glycographene. The reaction scheme for the attachment of the fluorescently labelled Concanavalin A lectin (FITC-ConA), to mannose-functionalised CVD G-SH (or ‘glycographene’), is shown in Figure 3-15.

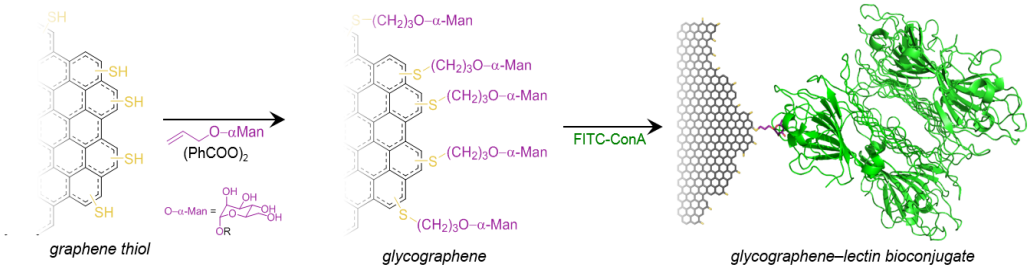

Figure 3-15. Reaction scheme to produce glycographene and a graphene-lectin bioconjugate. Figure produced by Christopher Blanford.

The attachment of FITC-ConA to glycographene was visualised using fluorescence microscopy and compared to a control, in which pristine CVD graphene and FITC-conA were incubated together. CVD graphene was used to more clearly visualise the edges of the sheet. Figure 3-16 shows the fluorescence images of CVD pristine graphene and CVD glycographene, incubated with FITC-conA (panels A and B, respectively). The CVD pristine graphene shows only background fluorescence,

whereas the CVD glycographene shows increased fluorescence round the edges of the sheet, indicating the attachment of FITC-conA to the mannose groups present at the edges of the CVD glycographene. However, once methyl mannoside, which provides a stronger interaction with FITC-conA, is added to the CVD glycographene/FITC-conA conjugate, the FITC-conA is removed from the edges and therefore there is no longer a discernible increase in fluorescence intensity around the edges of the CVD glycographene sheet, as shown in Figure 3-16D.

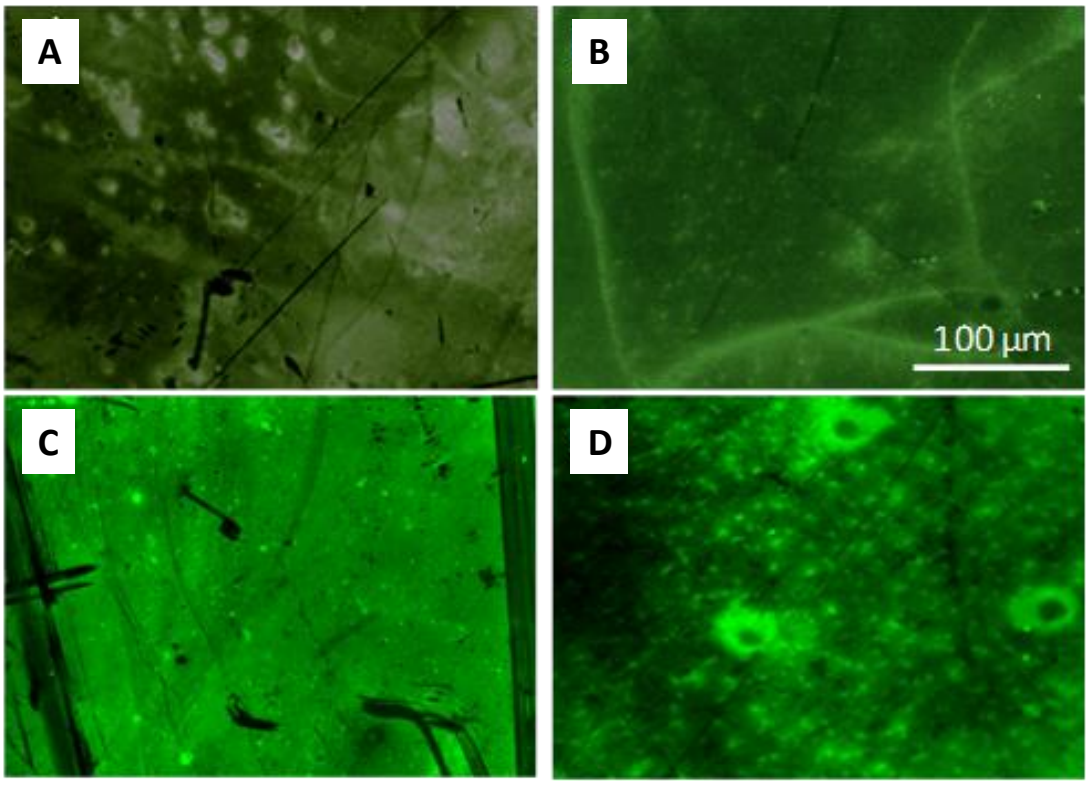

Figure 3-16. A) CVD graphene + FITC-conA, exhibiting only background fluorescence B) CVD glycographene + FITC-conA. C) CVD graphene + FITC-conA, following incubation with excess methyl mannoside D) CVD glycographene +FITC-conA, after incubation with excess methyl mannoside. Data acquired by Mirja Hartmann (previously of Blanford group).

These images both confirm the presence of FITC-ConA on the edges of the CVD 'glycographene' sheet, and also show that this can be removed once a competitive interaction is provided. This attachment also confirms the edge-selectivity of the thiol functionalisation, as the increased fluorescence is visible on the sharp, well-defined edges of the CVD sheet.

3.3.2. Attachment of cyclen derivatives to graphene thiol

Cyclen-1,4,7,10-tetraacetic acid (DOTA) is a chelator, used to enhance the sensitivity of Gd^{3+}, a magnetic resonance imaging (MRI) contrast agent, whilst also rendering Gd^{3+} ion safe for use in the body.[34,35] A DOTA analogue, AllylDO3A, was chosen to tether to G-SH, by click chemistry. To confirm the presence of a lanthanide ion in the cavity of AllylDO3A, Eu^{3+} was added to the AllylDO3A. Eu^{3+} displays luminescence and so the presence can be detected by fluorimetry. The synthetic scheme to produce AllylDO3A is revisited in Figure 3-17.

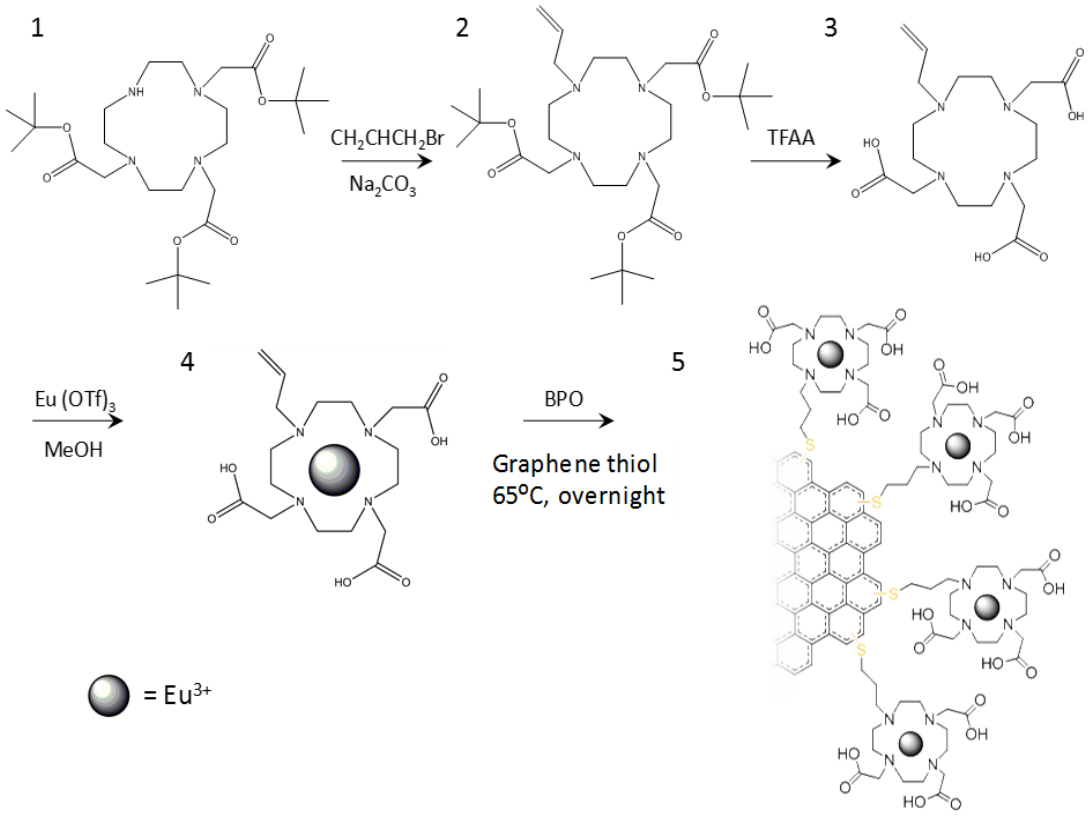

Figure 3-17. The synthesis of AllylDO3A and its tethering to graphene thiol. 1. DO3A-tBu, 2. AllylDO3A-tBu, 3. AllylDO3A, 4. Eu^{3+}/AllylDO3A, 5. Eu^{3+}/DO3A-$(CH_2)_3$-(G-SH)

3.3.2.1.[1]HNMR characterisation of AllylDO3A

AllylDO3A-tBu - [1]HNMR (400MHz, $CDCl_3$): 1.43 (9H, s, $C(C\underline{H}_3)_3$), 1.48 (18H, s, 2x $C(C\underline{H}_3)_3$), 2.18-3.31 (24H, m, 12x CH_2), 5.17-5.25 (2H, m, $CH=C\underline{H}_2$), 5.75-5.5 (1H, m, $C\underline{H}=CH_2$)

AllylDO3A- [1]HNMR (400MHz, MeOD): 2.94-3.1 (8H, m, 4x CH_2), 3.33-3.62 (12H, m, 6 x CH_2), 3.84 (2H, d, *J 6.8*, CH2), 4.14 (2H, s, CH_2), 5.61-5.65 (2H, m, $CH=C\underline{H}_2$), 5.98-6.09 (1H, m $C\underline{H}=CH_2$)

These [1]HNMR spectra confirm the production of AllylDO3A and match with literature spectra.[36]

3.3.2.2 Insertion of Eu^{3+} into AllylDO3A

The insertion of the Eu^{3+} ion into AllylDO3A was confirmed by recording a luminescence spectrum of the Eu^{3+}/AllylDO3A. The luminescence spectra of Eu^{3+}/AllylDO3A is shown in Figure 3-18, confirming the successful incorporation of the Eu^{3+} ion.

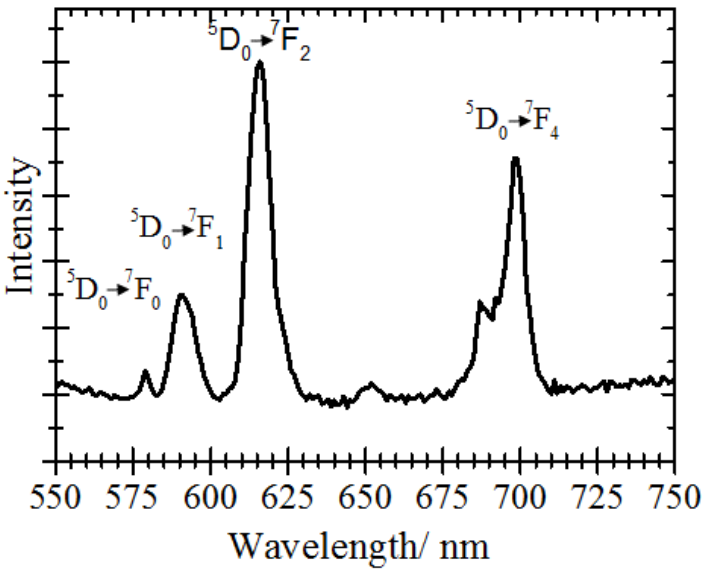

Figure 3-18. Eu^{3+} emission spectra for Eu^{3+}/AllylDO3A.

3.3.2.3 Transmission electron microscopy

TEM images of the conjugated Eu^{3+}/DO3A-$(CH_2)_3$-(G-SH) complex are shown in Figure 3-19 (A-C) and shows the presence of the high contrast areas which contain Eu^{3+}/DO3A-$(CH_2)_3$-(G-SH) complex, as indicated by red arrows. However, these species do not seem to be distributed around all the edges of the G-SH sheets. The control image in Figure 3-19 shows pristine graphene, physically mixed with Eu^{3+}/AllylDO3A. There are no similar areas of high contrast in the control image, indicating that the Eu^{3+}/AllylDO3A has not attached non-specifically to the pristine graphene sheet.

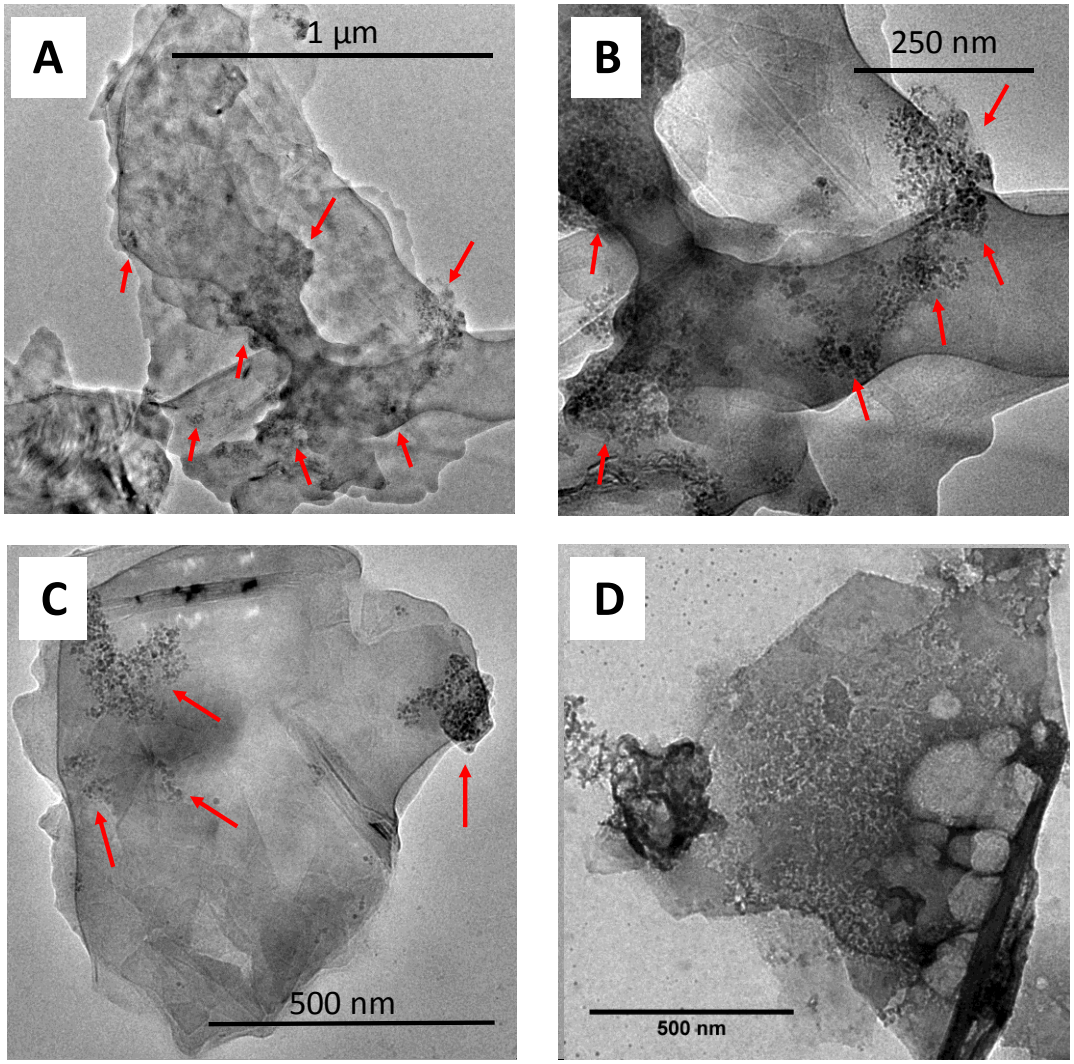

Figure 3-19. A-C: Bright-field TEM images of Eu^{3+}/DO3A-$(CH_2)_3$-(G-SH) complex. Red arrows indicate areas covered by Eu^{3+}/DO3A-$(CH_2)_3$-(G-SH) as indicated by areas of higher contrast, arising from the higher mass of Eu^{3+} ion. D) Control image of pristine graphene + Eu^{3+}/AllylDO3A.

The binding of the cyclen analogue needs to be further investigated using CVD graphene, on which the basal plane can be masked and the edges exposed to the Eu^{3+}/AllylDO3A. This would enable further modification of the attachment protocol to enable a greater amount of Eu^{3+}/AllylDO3A to attach. XPS spectra should also be taken of the Eu^{3+}/DO3A-$(CH_2)_3$-(G-SH) complex to confirm the presence of Eu^{3+}. Initial luminescence measurements and luminescence lifetimes of the Eu^{3+}/DO3A-$(CH_2)_3$-(G-SH) complex are shown in the future work section.

3.4. Graphene-containing layer-by-layer constructs

The effect of different graphene-family nanomaterials (GFNs) on the formation of layer-by-layer (LbL) constructs was assessed. Pristine graphene is uncharged, meaning that it is not possible to incorporate it into LbL constructs without first combining with charged species. G-SO_3 was selected as a target material for incorporation into a LbL construct, due to the presence of the negatively charged sulfonate groups.

The incorporation of G-SO_3 into a LbL construct, serves as the first example, to my knowledge, of a pristine graphene-LbL which has not first been combined with solubilising agents or charged polymers prior to the process. The incorporation of G-SO_3 into a LbL construct could have potential applications in tissue engineering. Pristine graphene has higher mechanical strength than GO,[37,38] meaning that it is favourable to use pristine graphene to modulate the mechanical strength of composites. As outlined in the Introduction, PEI was selected as the positively charged polymer layer, due to its antibacterial properties. The PEI/G-SO_3 LbL construct was produced along with analogous LbL constructs containing graphene oxide (GO) and sulfonated graphene oxide (GO-SO_3), to assess the effect different functionalisations on the formation of LbL constructs and, latterly, to compare their biocompatibilities.

The starting graphene material used for the G-SO_3 LbL construct was bought from XG Sciences (average surface area 750 m^2 g^{-1}, < 5 layers, submicron lateral dimensions), while GO was produced from the modified Hummer's oxidation of graphite, as described by Thomas *et al.*[39] GO-SO_3 was prepared from GO in an analogous way to G-SO_3. The production of G-SO_3, GO and GO-SO_3 are described

in the materials and methods. The as-prepared GFNs (G-SO_3, GO and GO-SO_3) were characterised by CHNS analysis, zeta potential, Raman and FTIR. The as-GFNs were then incorporated into LbL constructs with polyethyleneimine (PEI). LbL constructs were made by immersing 3-(trihydroxysilyl) propane-1-sulfonic acid (THSPS)-coated coverslips in alternating solutions of PEI, followed by either G-SO_3, GO or GO-SO_3, after which the resultant PEI/GFN LbL constructs were characterised.

3.4.1. CHNS analysis

CHNS analysis was recorded for the as-prepared GFNs, with the results shown in Table 3-6. Both G-SO_3 and GO-SO_3 were found to contain 1 % and 0.7 % sulfur, respectively, while the GO and GO-SO_3 contained a much higher oxygen wt. % than G-SO_3 (although this cannot be quantitatively compared as other elements are included in this group).

Table 3-6. CHNS analysis of as-prepared GO, GO-SO_3 and G-SO_3.

	wt. %				
Material	C	H	N	S	Other (O, Na etc.…)
graphene	90	0.3	0.5	0	9.2
GO	50	2.6	0	trace	>47
GO-SO_3	51	0.7	0.9	0.7	>46
G-SO_3	76	0.7	1.2	1	21.1

3.4.2. Zeta potential

The measured zeta potential (ζ-potential) of the prepared GO, GO-SO_3 and G-SO_3 were measured at a concentration of 0.1 mg mL^{-1} in water, while PEI and polystyrene sulfonate (PSS) were measured at a concentration of 10 g L^{-1}, as these were the working concentrations for the LbL process. The zeta-potential values are summarised in Table 3-7.

Table 3-7. Zeta potential values of prepared graphene materials and polymers.

Material	Zeta potential/ mV
PEI	9 mV (± 1 mV)
PSS	-37 mV (± 5 mV)
GO	-37 mV (± 6 mV)
GO-SO_3	-38 mV (± 4 mV)
G-SO_3	-42 mV (± 1 mV)

Reported zeta-potential values for graphene oxide vary somewhat but are reported to be of the order of -40 mV, which is in good agreement with the value reported here.[19,40,41] The zeta-potential of G-SO_3 is comparable to the calculated -39 mV from Jeon *et al.* for sulfonated graphene, at 0.14 mg mL^{-1}.[31]

3.4.3. Raman spectroscopy

The Raman spectra of graphite, graphene, GO, GO-SO_3 and G-SO_3 are shown in Figure 3-20, with peak positions and intensity ratios shown in Table 3-8. The 2D peak of graphite is shifted to a lower energy for graphene and G-SO_3 than for graphite,[8] and is symmetrical for graphene and G-SO_3, which is typical for pristine graphene of around 5 layers.[8,10] The disappearance of the 2D peak for GO and GO-SO_3, in contrast to the starting material (graphite), arises due to the highly defective structure of GO and GO-SO_3, which consists of functional groups between the graphitic layers and therefore a lack of ordering along the axis perpendicular to the graphene sheet.[18,19] There is no reduction in 2D peak for G-SO_3 in comparison to graphene, also indicating that the functionalisation does not introduce much oxidation.

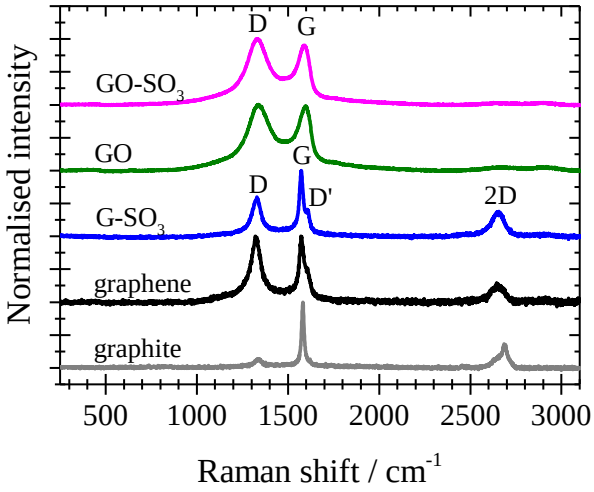

Figure 3-20. Raman spectra of as-prepared GFNs. Data provided by Fan Fei (Blanford group)

Table 3-8. Raman peak positions and intensity ratios.

Material	I_D/I_G	G peak position/ cm^{-1}	2D peak position/ cm^{-1}	2D peak FWHM/ cm^{-1}
GO-SO_3	1.1	1585	-	-
GO	1	1591	-	-
G-SO_3	0.6	1574	2650	80
graphene	1	1578	2647	89
graphite	0.1	1581	2682	57

The ratio of the D peak and G peak intensities (I_D/I_G) can give an indication of the defects in GFNs. The value of I_D/I_G is much higher for GO and GO-SO_3 than for graphite. However, the I_D/I_G ratio of G-SO_3 is not increased in comparison to graphene, indicating that there is no significant increase in defects as a result of the functionalisation, such as the introduction of sp^3 domains. The G peak of graphite (1581 cm^{-1}) is shifted to a higher energy for GO and GO-SO_3 (1591 cm^{-1} and 1585 cm^{-1} respectively), which can be attributed to the structure of GO, with alternating single and double carbon bonds, made as a result of the formation of sp^3 domains.[17] The G peak also undergoes a red shift with increased layer number,[8,42] meaning that the peak shift between graphene and G-SO_3 indicates a small decrease in the number

of layers upon functionalisation. This may be due to the production of the sulfonate groups at the edges of the graphene, forcing apart the remaining layers.

3.4.4. Fourier transform infrared spectroscopy

FTIR characterisation of GO, GO-SO_3 and G-SO_3 can be seen in Figure 3-21 and show featureless spectra for the starting materials (graphite and graphene). C=O stretches (1600-1700 cm^{-1}) can be seen for GO and GO-SO_3 and the anti-symmetric O=S=O vibrations (around 1035 cm^{-1} and 1224 cm^{-1} and symmetric O=S=O stretches at about 1039 cm^{-1} are observed in G-SO_3 and GO-SO_3.[43]

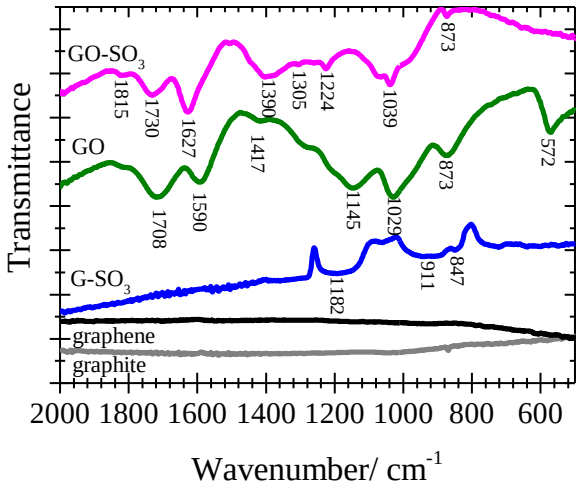

Figure 3-21. FTIR spectra of prepared GFNs. Data provided by Fan Fei (Blanford group).

3.4.5. Composition of LbL constructs

The composition of the different LbL constructs are outlined in Table 3-9.

Table 3-9. Composition of the layer-by-layer constructs

Surface	Components	Positive layer	Negative Layer	# layers	Terminal layer
Glass	N/A	N/A	N/A	N/A	N/A
PEI/PSS (+)	PEI, PSS	PEI	PSS	7	PEI
PEI/PSS (-)	PEI, PSS	PEI	PSS	6	PSS
PEI/GO	PEI, GO	PEI	GO	6	GO
PEI/GO-SO_3	PEI, GO-SO_3	PEI	GO-SO_3	6	GO-SO_3
PEI/G-SO_3	PEI/ G-SO_3	PEI	G-SO_3	6	G-SO_3

3.4.6. Images of the as-prepared LbL constructs

Images of the as-prepared graphene-containing LbL constructs can be seen in Figure 3-22. The brown tinge of the PEI/GO and PEI/GO-SO_3 is characteristic of oxidised graphene, showing its incorporation into the LbL construct, while the PEI/G-SO_3 has a grey/black tint, indicative of the incorporation of pristine graphene into the LbL construct.

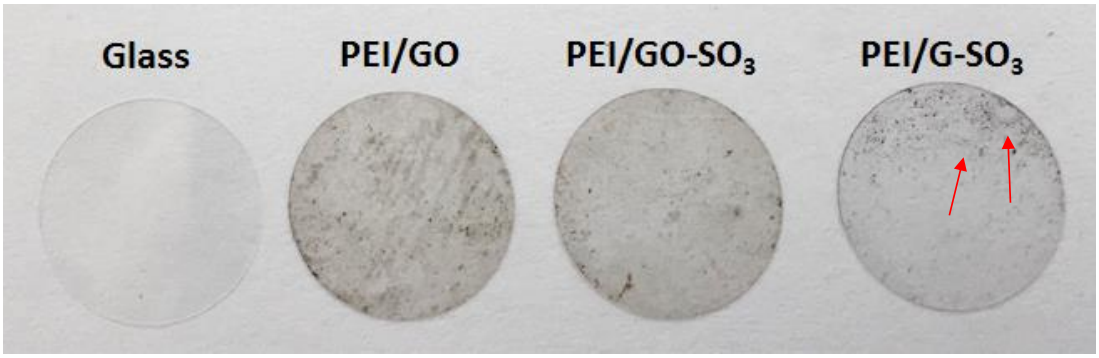

Figure 3-22. Images of as-prepared LbL constructs, grown on glass coverslips, taken on a white background. L-R: Glass, PEI/GO, PEI/GO-SO_3 and PEI/G-SO_3 (3 bilayers, GFN terminated surfaces).

Note that the PEI/GO and PEI/GO-SO_3 LbL constructs appear to have a greater coverage than the PEI/G-SO_3, which was consistently observed across samples; PEI/G-SO_3 constructs appeared visually lighter. This was investigated using UV-visible spectroscopy (3.3.7). The G-SO_3 in the PEI/G-SO_3 LbL construct is more unevenly distributed, with the red arrows indicating areas with much denser coverage than the rest of the construct. This may arise from the interaction of graphene and remaining, unbound PEI, which causes agglomeration.

3.4.7. UV-visible spectroscopy

To estimate the amount of GFNs in the GFN-containing LbL constructs, UV-visible measurements were performed after the deposition of each bilayer. The recorded UV-visible absorbance values up to 15 bilayers is shown in Figure 3-23A, showing an increase in UV absorbance as a function of increasing number of bilayers for PEI/GO, PEI/GO-SO_3 and PEI/G-SO_3. The increase in UV absorbance is approximately linear for the PEI/GO and PEI/GO-SO_3 LbL constructs, but appears to show non-linear growth for the PEI/G-SO_3 LbL construct, indicating the weaker interaction between the PEI and G-SO_3 layers. Figure 3-23B shows the UV-visible absorbance up to 3 bilayers, clearly showing the lower UV-visible absorbance of the PEI/G-SO_3 LbL construct in comparison to the PEI/GO and PEI/GO-SO_3 LbL constructs. 3 bilayers (6 layers in total) was selected as the initial target, as this number of layers produced LbL constructs which showed a visual colour change, enabling swift and facile confirmation of LbL formation. In addition, at this point the G-SO_3 LbL construct still has a linear increase in UV-vis absorbance, incidating that the layers are still quite well associated at this stage.

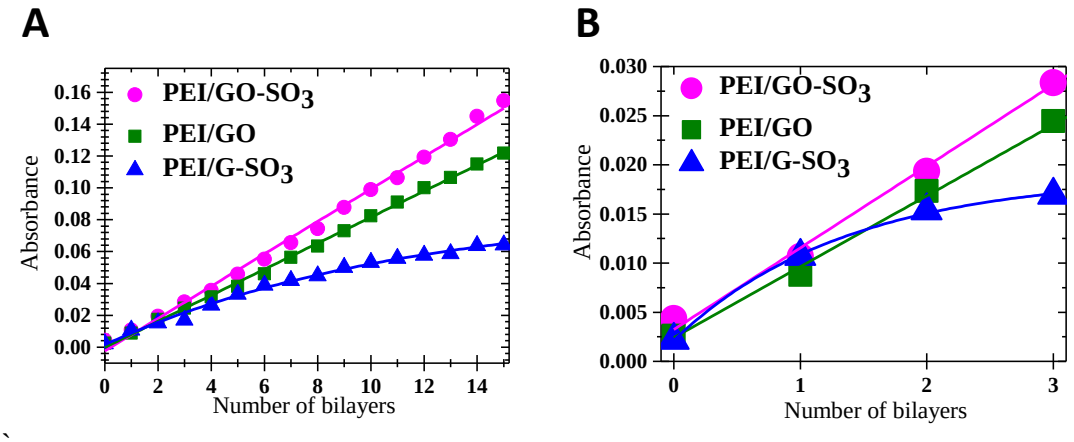

Figure 3-23. A) UV- visible absorbance at 650 nm of graphene-based LbL constructs as a function of layer, up to 15 bilayers. B) UV-visible absorbance up to 3 bilayers. Data provided by Fan Fei (Blanford group)

3.4.8. Bright field images

Bright field images of the PEI/GO, PEI/GO-SO_3 and PEI/G-SO_3 LbL constructs are shown in Figure 3-24. The PEI/GO-SO_3 appears to be most densely covered with GO-SO_3, while the PEI/G-SO_3 appears to have the least dense coverage. Agglomerates, which are indicated by the red arrows, occurred in many samples. The interaction of the GO, GO-SO_3 and G-SO_3 with residual PEI solution was found to cause agglomeration, when mixed in solution. The coverslips were washed thoroughly between each immersion to prevent agglomeration from this interaction. However, agglomeration of the GFNs on the coverslips was still found. The likely origin of this effect is from the drying step of the LbL process. The drying of GFNs from aqueous solutions onto surfaces has been known to cause a coffee-staining effect, and it is likely that when the GFN layers are dried there may be agglomeration which results during the the drying process. The agglomerates are not likely to be due to the agglomeration of the GFN dispersions, as the zeta potential measurments suggest that the dispersions are stable, and no agglomerates were observed in the dispersions, which were also sonicated briefly before use.

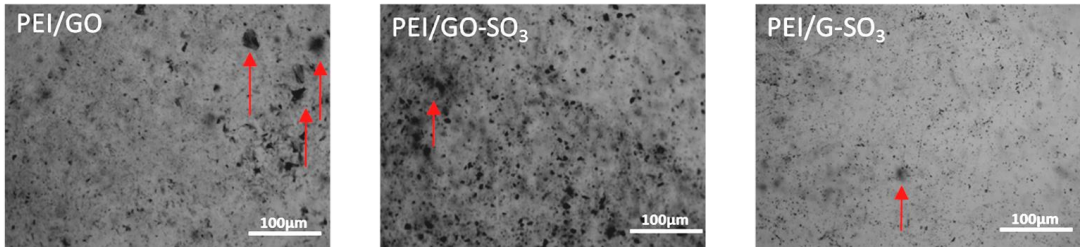

Figure 3-24. Bright field images of LbL constructs. L to R: PEI/GO, PEI/GO-SO_3, PEI/G-SO_3. Red arrows indicate areas with large agglomerates.

3.4.9. Raman mapping

To quantitatively compare the distribution of G-SO_3, GO and GO-SO_3 in LbL constructs, PEI/GO, PEI/GO-SO_3 and PEI/G-SO_3 LbL constructs, containing 15 bilayers, were produced to give an indication of the distribution of GFNs in the

constructs and to assess the homogeneity of GFN coverage. Raman maps of the D band intensity (centred 1330 cm^{-1}) and the G band intensity (centred at 1593 cm^{-1}) were recorded and are shown in Figure 3-25, with colour bars to the right of each map indicate the intensity range of the peaks. These peaks are specific to GFNs therefore indicating the locations of GFNs in the mapped area. By reference to the colour bars, the D and G band intensities are lower for PEI/G-SO_3 than for either PEI/GO or PEI/GO-SO_3. In addition, the PEI/GO-SO_3 LbL construct appears to have the highest D and G band intensities and a greater coverage of graphene across the substrate, as indicated by the red and green coloured areas in the Raman maps. This is consistent with the bright field image of the PEI/GO-SO_3 substrate.

It is important to note, however, that the Raman can penetrate further than the first layer, so these maps may also incorporate graphene in the layers below. Again, there are areas in which the GFNs have agglomerated, meaning that the LbL constructs are not completely homogeneously distributed.

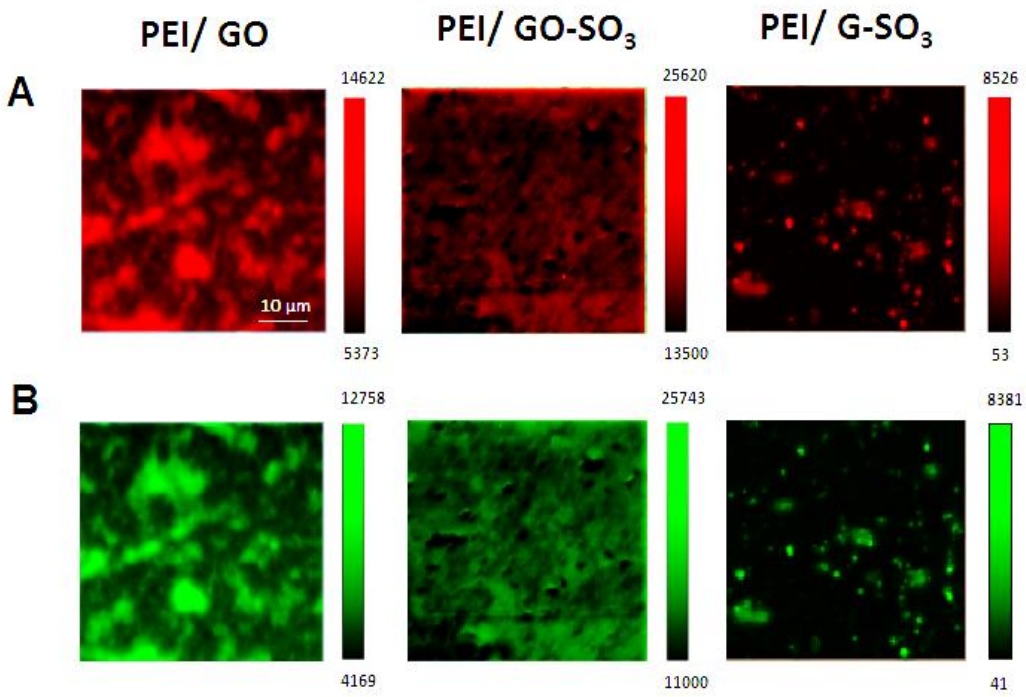

Figure 3-25. A) D peak (1330 cm^{-1}) Raman intensity maps. B) G peak (1593 cm^{-1}) Raman intensity maps. L-R: PEI/GO, PEI/GO-SO_3 and PEI/G-SO_3 (15 bilayers). Area 50 µm x 50 µm, step: 0.5 µm. Static scan centred at 1400 cm^{-1}.

3.4.10. Atomic force microscopy

To assess the roughness of the prepared LbL constructs, atomic force microscopy (AFM) images were recorded and are displayed in Figure 3-26. The roughness average (Ra) of the peaks and troughs of the surface and the route mean square (RMS) of the peaks and troughs were calculated and are reported in Table 3-10.

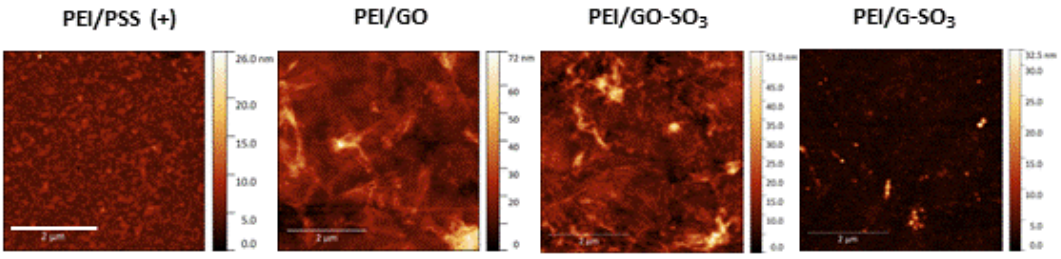

Figure 3-26. AFM (tapping mode) images of LbL constructs L to R: PEI/PSS(+), PEI/GO, PEI/GO-SO_3 and PEI/G-SO_3. Scale bar represents 2 µm.

Table 3-10. Roughness values of LbL constructs, as recorded by AFM measurements

Material	R_{RMS}/ nm	R_a/ nm
PEI/PSS(+)	1.2	0.9
PEI/GO	7.4	4.9
PEI/GO-SO_3	5.4	3.7
PEI/G-SO_3	1.5	0.7

The R_a and R_{RMS} values of the PEI/GO, PEI/GO-SO_3 and PEI/G-SO_3 LbL constructs are higher than that of the PEI/PSS(+) LbL construct, which was used as comparison to demonstrate the difference in the roughness by incorporation of GFNs into LbL constructs. The higher R_a and R_{RMS} roughness values for the PEI/GO and PEI/GO-SO_3 LbL constructs in comparison to the PEI/G-SO_3 indicates a greater loading of graphene into the PEI/GO and PEI/GO-SO_3 constructs, which is in agreement with the bright field images and Raman maps, which also suggest a lower coverage for the PEI/G-SO_3 LbL construct.

3.4.11. Water contact angle measurements

The wettability of the LbL constructs was assessed using water contact angle measurements. Contact angle images of the prepared LbL constructs (3 bilayers) are shown in Figure 3-27 and average contact angles are shown in Table 3-11.

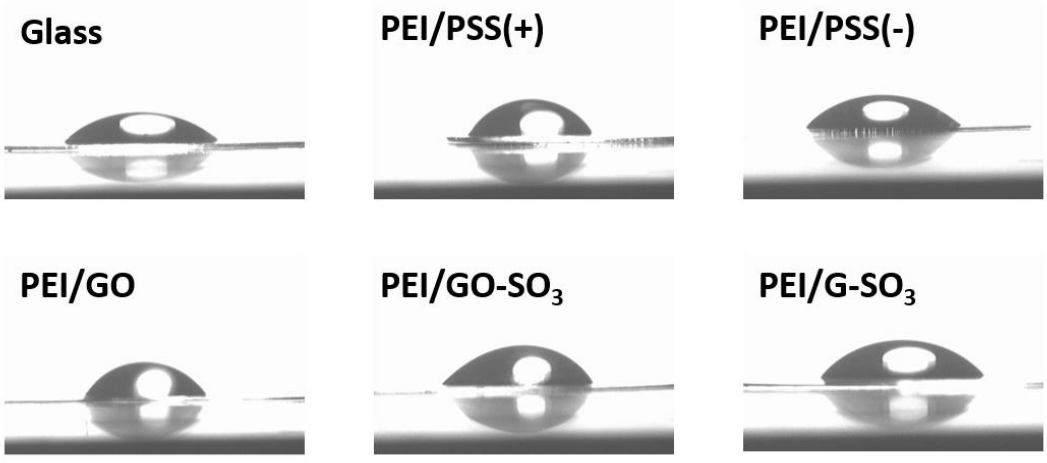

Figure 3-27. Water contact angle images on LbL constructs.

Table 3-11. Contact angles of the LbL constructs. Error bars are from repeats.

LbL construct	Contact angle
Glass	42.5° ± 1.8°
PEI/PSS(+)	57.4° ± 2°
PEI/PSS(-)	41.9° ± 7.7°
PEI/GO	58.3° ± 3.5°
PEI/GO-SO_3	44.1° ± 7.4°
PEI/G-SO_3	48.7° ± 3.6°

The wettability of all LbL constructs is lower than that of glass, with the exception of the PEI/PSS(-) LbL construct. However, all constructs display moderate wettability. The water contact angles values for PEI/PSS(+) and PEI/PSS(-) are consistent with studies by Chen *et al.*, who found the contact angle of PEI/PSS LbL construct to varying as each layer was deposited, with the angle decreasing with a PSS layer and increasing with the deposition of a PEI layer.[44] PEI/GO LbL constructs were made in paper by Zhao *et al*. who report a contact angle of 48°, although the preparation method of the GO was not specified.[45]

3.5. Discussion

3.5.1. Edge-selective functionalisation of pristine graphene

The XPS data and FTIR stretches presented in this chapter confirm the presence of sulfur-containing functional groups, bonded to graphene, in both G-SO_3 and G-SH samples, as well as indicating their chemical identity. Furthermore, TEM, Raman and BET data show that the pristine graphene sheet remains relatively unchanged after functionalisation, with only a small amount of oxygen-containing functionality introduced into the G-SO_3 material. The TGA, contact angle and dispersibility measurements indicate that graphene, G-SO_3 and G-SH have different wettability, decomposition profiles and solvent dispersibilities, which provides further evidence of the functionalisations. The thiol functionalisation of pristine graphene, presented in this chapter is the first edge-specific, thiol functionalisation of pristine graphene

and provides the possibility of developing redox-cleavable links to pristine graphene by disulphide bonds or attaching molecules covalently to graphene edges.

The production of G-SO_3 can be compared to an analogous compound made by ball milling.[31] The approximate wt. % of sulfur for the G-SO_3 produced in this thesis, as calculated by XPS, was 2 %. This compares to 9 % reported by Jeon *et al.* for edge-sulfonated graphene nanoplatelets (SGnP) produced by ball milling.[31] The percentage sulfur in the SGnPs indicates either very small graphene flakes or the introduction of a significant number of new defects, which could arise from damage to sheets from the ball milling process. The reported Raman spectra for the SGnPs confirms this, as the I_D/I_G ratio was 2.3, in comparison to a ratio of 0.86 for the G-SO_3 characterised in this chapter. Therefore, the ball milling process introduces significant defects to the graphene sheet, to the extent that the defect-induced D peak is larger in magnitude than the G peak, while the sulfonation presented here causes little change in defect density. Furthermore, the calculated surface area of SGnPs produced by Jeon *et al.* was 2.9 $m^2\ g^{-1}$ (for comparison, the calculated BET surface area for the graphite starting material was 2.8 $m^2\ g^{-1}$),[31] suggesting the SGnPs contain are over 100 layers thick, meaning this method is not able to produce graphene. In comparison the surface area of the G-SO_3 produced in this thesis was 693 $m^2\ g^{-1}$ which, using the surface are of monolayer graphene of 2630 $m^2\ g^{-1}$,[2] gives an approximate number of layers between 3 and 4. Therefore, the edge functionalisation presented here produces less defected edge-functionalised, with a lower layer number.

3.5.2. Attachment of species to edge-functionalised graphene

The attachment of a cyclen derivative, Eu^{3+}/AllylDO3A, as well as a fluorescently-labelled lectin, were characterised in this chapter. The CVD glycographene/FITC-conA conjugate was identified on the edges of the CVD glycographene sheets by an increase in fluorescence around the edges. The competitive binding of this lectin and its consequent removal from the glycographene sheet was also demonstrated. This attachment both demonstrated the attachment of a cell localising molecule to graphene edges, but also enabled the visualisation of the edge-specificity of the functionalisation, by virtue of the enhanced fluorescence on the edges of the glycographene sheet. Now that the attachment of a protein has been demonstrated on CVD G-SH, further proteins can be tethered by making use of, for example, cysteine residues, which can be introduced by genetic modification.

The attachment of Eu^{3+}/AllylDO3A to G-SH was observed, by TEM, in isolated areas of the G-SH sheet, but did not show very high coverage. CVD G-SH should be used to further characterise this attachment, as it is difficult to visualise the edges of the agglomerated, powdered graphene samples and thus to make conclusions about where the complex is distributed. Elemental mapping should also be used to examine the distribution of different species and will be discussed in the future work section.

3.5.3. GFN-containing layer-by-layer constructs

G-SO_3, GO and GO-SO_3 were incorporated into LbL constructs, containing PEI counter-layers. The PEI/G-SO_3 LbL construct was found to have a lower coverage than analogous PEI/GO and PEI/GO-SO_3 LbL constructs containing, as shown using Raman mapping, UV-visible spectroscopy and bright field images, but is the first example of the incorporation of edge-functionalised pristine graphene into a polymer

LbL construct. The R_a and R_{RMS} roughness values of the PEI/GO, PEI/GO-SO_3 and PEI/G-SO_3 were found to follow the order PEI/GO > PEI/GO-SO_3 >> PEI/G-SO_3. Hu *et al.* investigated the formation of GO/poly(allylamine hydrochloride) (PAH) LbL constructs using a quartz crystal microbalance and found multiple layers of GO existing in each GO/PAH bilayer, attributing this to the higher mass to charge ratio of GO versus the PAH.[46] This could explain the difference in roughness between the LbL constructs, as the mass-to-charge ratio of GO and GO-SO_3, which are both oxidised forms of graphene, will be higher than G-SO_3, which is functionalised only at the edges.

This work provides a basis for future pristine graphene composites. The degree of functionalisation can now be tailored to try to increase the amount of G-SO_3 in the LbL constructs, while the increased hydrophilicity of the G-SO_3 in comparison to pristine graphene presents opportunities to use functionalised graphene in the production of hydrophilic composite materials. The future scope of this work is outlined in the future work section.

3.6. References

1. Hernandez, Y.; Nicolosi, V.; Lotya, M.; Blighe, F. M.; Sun, Z.; De, S.; McGovern, I. T.; Holland, B.; Byrne, M.; Gun'ko, Y. K.; Boland, J. J.; Niraj, P.; Duesberg, G.; Krishnamurthy, S.; Goodhue, R.; Hutchison, J.; Scardaci, V.; Ferrari, A. C.; Coleman, J. N., High-yield production of graphene by liquid-phase exfoliation of graphite. *Nature Nanotechnology* **2008,** *3* (9), 563-568.
2. Khan, U.; O'Neill, A.; Lotya, M.; De, S.; Coleman, J. N., High-Concentration Solvent Exfoliation of Graphene. *Small* **2010,** *6* (7), 864-871.
3. Zhang, X. Y.; Coleman, A. C.; Katsonis, N.; Browne, W. R.; van Wees, B. J.; Feringa, B. L., Dispersion of graphene in ethanol using a simple solvent exchange method. *Chemical Communications* **2010,** *46* (40), 7539-7541.
4. Meyer, J. C.; Geim, A. K.; Katsnelson, M. I.; Novoselov, K. S.; Booth, T. J.; Roth, S., The structure of suspended graphene sheets. *Nature* **2007,** *446* (7131), 60-63.
5. Fu, Y.; Zhang, J. W.; Liu, H.; Hiscox, W. C.; Gu, Y., Ionic liquid-assisted exfoliation of graphite oxide for simultaneous reduction and functionalization to graphenes with improved properties. *Journal of Materials Chemistry A* **2013,** *1* (7), 2663-2674.
6. Lavanya, J.; Gomathi, N.; Neogi, S., Electrochemical performance of nitrogen and oxygen radio-frequency plasma induced functional groups on tri-layered reduced graphene oxide. *Materials Research Express* **2014,** *1* (2) 1-18.

7. Cui, T. X.; Lv, R. T.; Huang, Z. H.; Zhu, H. W.; Jia, Y.; Chen, S. X.; Wang, K. L.; Wu, D. H.; Kang, F. Y., Low-temperature synthesis of multilayer graphene/amorphous carbon hybrid films and their potential application in solar cells. *Nanoscale Research Letters* **2012,** *7* 453/1-7.
8. Ferrari, A. C.; Meyer, J. C.; Scardaci, V.; Casiraghi, C.; Lazzeri, M.; Mauri, F.; Piscanec, S.; Jiang, D.; Novoselov, K. S.; Roth, S.; Geim, A. K., Raman spectrum of graphene and graphene layers. *Physical Review Letters* **2006,** *97* (18), 187401/1-4.
9. Coleman, J. N., Liquid-Phase Exfoliation of Nanotubes and Graphene. *Advanced Functional Materials* **2009,** *19* (23), 3680-3695.
10. Malard, L. M.; Pimenta, M. A.; Dresselhaus, G.; Dresselhaus, M. S., Raman spectroscopy in graphene. *Physics Reports-Review Section of Physics Letters* **2009,** *473* (5-6), 51-87.
11. Cancado, L. G.; Pimenta, M. A.; Saito, R.; Jorio, A.; Ladeira, L. O.; Grueneis, A.; Souza, A. G.; Dresselhaus, G.; Dresselhaus, M. S., Stokes and anti-Stokes double resonance Raman scattering in two-dimensional graphite. *Physical Review B* **2002,** *66* (3) 035415/1-5.
12. Cancado, L. G.; Takai, K.; Enoki, T.; Endo, M.; Kim, Y. A.; Mizusaki, H.; Speziali, N. L.; Jorio, A.; Pimenta, M. A., Measuring the degree of stacking order in graphite by Raman spectroscopy. *Carbon* **2008,** *46* (2), 272-275.
13. Reich, S.; Thomsen, C., Raman spectroscopy of graphite. *Philosophical Transactions of the Royal Society a-Mathematical Physical and Engineering Sciences* **2004,** *362* (1824), 2271-2288.
14. Saito, R.; Jorio, A.; Souza, A. G.; Dresselhaus, G.; Dresselhaus, M. S.; Pimenta, M. A., Probing phonon dispersion relations of graphite by double resonance Raman scattering. *Physical Review Letters* **2002,** *88* (2) 027401/1-4.
15. Eckmann, A.; Felten, A.; Mishchenko, A.; Britnell, L.; Krupke, R.; Novoselov, K. S.; Casiraghi, C., Probing the Nature of Defects in Graphene by Raman Spectroscopy. *Nano Letters* **2012,** *12* (8), 3925-3930.
16. Park, S.; Ruoff, R. S., Chemical methods for the production of graphenes. *Nature Nanotechnology* **2009,** *4* (4) 217 - 224.
17. Kudin, K. N.; Ozbas, B.; Schniepp, H. C.; Prud'homme, R. K.; Aksay, I. A.; Car, R., Raman spectra of graphite oxide and functionalized graphene sheets. *Nano Letters* **2008,** *8* (1), 36-41.
18. Kaniyoor, A.; Ramaprabhu, S., A Raman spectroscopic investigation of graphite oxide derived graphene. *AIP Advances* **2012,** *2* (3) 032183/1-13.
19. Krishnamoorthy, K.; Veerapandian, M.; Yun, K.; Kim, S. J., The Chemical and structural analysis of graphene oxide with different degrees of oxidation. *Carbon* **2013,** *53*, 38-49.
20. Coleman, J. N., Liquid Exfoliation of Defect-Free Graphene. *Accounts of Chemical Research* **2013,** *46* (1), 14-22.
21. Chen, G.; Zhai, S.; Zhai, Y.; Zhang, K.; Yue, Q.; Wang, L.; Zhao, J.; Wang, H.; Liu, J.; Jia, J., Preparation of sulfonic-functionalized graphene oxide as ion-exchange material and its application into electrochemiluminescence analysis. *Biosensors & Bioelectronics* **2011,** *26* (7), 3136-3141.
22. Hu, X.-j.; Liu, Y.-g.; Wang, H.; Chen, A.-w.; Zeng, G.-m.; Liu, S.-m.; Guo, Y.-m.; Hu, X.; Li, T.-t.; Wang, Y.-q.; Zhou, L.; Liu, S.-h., Removal of Cu(II) ions from aqueous solution using sulfonated magnetic graphene oxide composite. *Separation and Purification Technology* **2013,** *108*, 189-195.
23. Shen, J.; Hu, Y.; Shi, M.; Lu, X.; Qin, C.; Li, C.; Ye, M., Fast and Facile Preparation of Graphene Oxide and Reduced Graphene Oxide Nanoplatelets. *Chemistry of Materials* **2009,** *21* (15), 3514-3520.
24. Langner, R.; Zundel, G., FTIR investigation of O center dot center dot center dot H center dot center dot center dot O hydrogen bonds with large proton polarizability in

sulfonic acid-N-oxide systems in the middle and far-IR. *Journal of the Chemical Society-Faraday Transactions* **1998,** *94* (13), 1805-1811.
25. Silverstein, R. M.; Clayton Bassler, G.; Morrill, T. C., Spectromeric identification of organic compounds. Fifth ed.; John Wiley and sons, inc.: New York.
26. Sing, K. S. W.; Everett, D. H.; Haul, R. A. W.; Moscou, L.; Pierotti, R. A.; Rouquerol, J.; Siemieniewska, T., Reporting physisorption data for gas solid systems with special reference to the determination of surface-area and porosity (recommendations 1984). *Pure and Applied Chemistry* **1985,** *57* (4), 603-619.
27. *Rouquerol, J.*; R*ouquerol, F.*; Sing, K., General conclusions and recommendations. In *Adsorption by powders and porous solids:Principles, methodology and applications* Academic Press: London, 1999; pp 440-447.

28. Rouquerol, F.; Rouquerol,J.; Imelik, B., Etude de la texture des solides poreux .4. Validite de la loi bet dans le cas de ladsorption dazote dargon et de butane sur des adsorbants poreux. *Bulletin De La Societe Chimique De France* **1964,** (3), 635-648.
29. Ismail, I. M. K., Cross-sectional areas of adsorbed N_2, Ar, Kr, and O_2 on carbons and fumed silicas at liquid-nitrogen temperature. *Langmuir* **1992,** *8* (2), 360-365.
30. Zhu, Y.; Murali, S.; Cai, W.; Li, X.; Suk, J. W.; Potts, J. R.; Ruoff, R. S., Graphene and Graphene Oxide: Synthesis, Properties, and Applications. *Advanced Materials* **2010,** *22* (35), 3906-3924.
31. Jeon, I.-Y.; Choi, H.-J.; Jung, S.-M.; Seo, J.-M.; Kim, M.-J.; Dai, L.; Baek, J.-B., Large-Scale Production of Edge-Selectively Functionalized Graphene Nanoplatelets via Ball Milling and Their Use as Metal-Free Electrocatalysts for Oxygen Reduction Reaction. *Journal of the American Chemical Society* **2013,** *135* (4), 1386-1393.
32. Jeon, I.-Y.; Zhang, S.; Zhang, L.; Choi, H.-J.; Seo, J.-M.; Xia, Z.; Dai, L.; Baek, J.-B., Edge-Selectively Sulfurized Graphene Nanoplatelets as Efficient Metal-Free Electrocatalysts for Oxygen Reduction Reaction: The Electron Spin Effect. *Advanced Materials* **2013,** *25* (42), 6138-6145.
33. Taherian, F.; Marcon, V.; van der Vegt, N. F. A.; Leroy, F., What Is the Contact Angle of Water on Graphene? *Langmuir* **2013,** *29* (5), 1457-1465.
34. Carr, D. H.; Gadian, D. G., Contrast agents in magnetic-resonance imaging. *Clinical Radiology* **1985,** *36* (6), 561-568.
35. Rashid, H. U.; Martines, M. A. U.; Jorge, J.; de Moraes, P. M.; Umar, M. N.; Khan, K.; Rehman, H. U., Cyclen-based Gd3+ complexes as MRI contrast agents: Relaxivity enhancement and ligand design. *Bioorganic & Medicinal Chemistry* **2016,** *24* (22), 5663-5684.
36. Schumann, H.; Kuse, K., Lanthanide Complexes of 1-(2-Propenyl)- and 1-(3-Butenyl)-1,4,7,10-tetraazacyclododecane-4,7,10-tris-Acetic Acid. *Zeitschrift Fur Anorganische und Allgemeine Chemie* **2008,** *634* (15), 2954-2958.
37. Liu, L. Z.; Zhang, J. F.; Zhao, J. J.; Liu, F., Mechanical properties of graphene oxides. *Nanoscale* **2012,** *4* (19), 5910-5916.
38. Suk, J. W.; Piner, R. D.; An, J. H.; Ruoff, R. S., Mechanical Properties of Mono layer Graphene Oxide. *ACS Nano* **2010,** *4* (11), 6557-6564.
39. Thomas, H. R.; Valles, C.; Young, R. J.; Kinloch, I. A.; Wilson, N. R.; Rourke, J. P., Identifying the fluorescence of graphene oxide. *Journal of Materials Chemistry C* **2013,** *1* (2), 338-342.
40. Li, D.; Mueller, M. B.; Gilje, S.; Kaner, R. B.; Wallace, G. G., Processable aqueous dispersions of graphene nanosheets. *Nature Nanotechnology* **2008,** *3* (2), 101-105.
41. Konkena, B.; Vasudevan, S., Understanding Aqueous Dispersibility of Graphene Oxide and Reduced Graphene Oxide through pK(a) Measurements. *Journal of Physical Chemistry Letters* **2012,** *3* (7), 867-872.

42. Gupta, A.; Chen, G.; Joshi, P.; Tadigadapa, S.; Eklund, P. C., Raman scattering from high-frequency phonons in supported n-graphene layer films. *Nano Letters* **2006,** *6* (12), 2667-2673.
43. Xu, C. X.; Cao, Y. C.; Kumar, R.; Wu, X.; Wang, X.; Scott, K., A polybenzimidazole/sulfonated graphite oxide composite membrane for high temperature polymer electrolyte membrane fuel cells. *Journal of Materials Chemistry* **2011,** *21* (30), 11359-11364.
44. Chen, J. Y.; Luo, G. B.; Cao, W. X., The study of layer-by-layer ultrathin films by the dynamic contact angle method. *Journal of Colloid and Interface Science* **2001,** *238* (1), 62-69.
45. Zhao, L. L.; Sun, H. X.; Kim, N.; Lee, J.; Kong, Y.; Li, P., Hydrogen gas barrier property of polyelectrolyte/GO layer-by-layer films. *Journal of Applied Polymer Science* **2015,** *132* (20) 41973/1-9.
46. Kim, S. G.; Park, O. K.; Lee, J. H.; Ku, B. C., Layer-by-layer assembled graphene oxide films and barrier properties of thermally reduced graphene oxide membranes. *Carbon Letters* **2013,** *14* (4), 247-250.

4. THE EFFECT OF FUNCTIONALISED GRAPHENE LAYER-BY-LAYER CONSTRUCTS ON 3T3 SWISS ALBINO FIBROBLAST VIABILITY

In chapter 3, the edge functionalisation of pristine graphene to produce graphene sulfonate (G-SO_3) and graphene thiol (G-SH) was characterised. G-SO_3 was also incorporated into a layer-by-layer (LbL) construct with polyethyleneimine (PEI), in addition to analogous LbL constructs containing graphene oxide (GO) and sulfonated graphene oxide (GO-SO_3). PEI/G-SO_3 LbL constructs were compared to PEI/GO and PEI/GO-SO_3 LbL constructs in terms of roughness, wettability and surface coverage, with the roughness and graphene coverage in PEI/G-SO_3 LbL constructs found to be lower than for PEI/GO and PEI/GO-SO_3 LbL constructs. The differences in loading in these LbL constructs can be rationalised by the higher density of charged functional groups in GO and GO-SO_3. However, the PEI/G-SO_3 LbL construct serves as a unique example of edge-functionalised pristine graphene in a LbL construct. As previously outlined, 3 bilayers (6 layers in total) was selected as the initial target, as this number of layers produced LbL constructs which showed a visual colour change, enabling swift and facile confirmation of LbL formation. In addition, at this point the G-SO_3 LbL construct still has a linear increase in UV-vis absorbance, incidating that the layers are still quite well associated at this stage.

Graphene-family nanomaterials (GFNs) have been reported to show antibacterial properties, leading to increased interest in their use for wound healing applications.[1,2,3,4,5] In addition, the high mechanical strength of GFNs, their flexibility and the water resistant nature of pristine graphene mean that it is favourable for use in dressings.[6,7] Furthermore, the LbL process is a quick, straightforward and cheap process, driven by electrostatics, which has been shown to

effectively incorporate GFNs.[8,9,10,11,12,13] The LbL process also presents the opportunity of achieving 'spray-on' wound dressings. In this work, therefore, PEI/GO, PEI/GO-SO_3 and PEI/G-SO_3 LbL constructs, characterised in Chapter 3, are compared as potential membranes for use in wound healing applications.

The importance of assessing the biocompatibility of GFNs has been outlined in Chapter 1, due to the conflicting research regarding their biocompatibility. In addition, the incorporation of GFNs into composites and their functionalisation may alter their biocompatibility both *in-vitro* and *in-vivo*. In this chapter, the biocompatibility of the PEI/GO, PEI/GO-SO_3 and PEI/G-SO_3 LbL constructs towards 3T3 Swiss Albino (3T3 SA) cells was investigated. As well as indicating any potential toxicity of these GFN composites, the same rank order of cytotoxicity on surfaces has been observed among different cells lines,[14] meaning that 3T3 SA cell adhesion and proliferation studies could also give an indication of potential toxicity towards other cell lines.

Fibroblasts play an important role in wound healing. In damaged tissues, following blood clotting and inflammatory response, fibroblasts migrate to the site of injury and excrete 'granulation tissue', which contains extracellular matrix proteins such as collagen and fibronectin.[15] These fibroblasts differentiate into myofibroblasts, which then contract, in a similar way to muscle, bringing the matrix and the wound together.[15] The resulting collagen-rich scar tissue re-models itself into ordinary tissue over time.[15] 3T3 mouse fibroblast cell lines have been used to study cell shape, adhesion and proliferation, as well as the role of the cytoskeleton in cell adhesion, growth and proliferation.[16]

There is evidence to show that, in LbL constructs, the terminal layer has the greatest influence on cell viability.[17] Therefore the PEI/GO, PEI/GO-SO_3 and PEI/G-SO_3 LbL constructs were terminated with GO, GO-SO_3 and G-SO_3 layers, respectively. To confirm the effect on the terminal layer on cell viability, LbL constructs with alternating polyethyleneimine (PEI) and polystyrene sulfonate (PSS) layers, but with differing terminal layers, were also assessed. The PEI/PSS(+) construct was terminated with a PEI layer and the PEI/PSS(-) with a PSS layer, thus determining any influence of altering the terminal layer on 3T3 SA cell viability. The LbL constructs used for this study are outlined in Table 4-1. Borosilicate glass was used as the control substrate.

Table 4-1. Composition of LbL constructs. PEI - Polyethyleneimine, PSS - polystyrene sulfonate, GO - graphene oxide, GO-SO_3 - sulfonated graphene oxide, G-SO_3 - graphene sulfonate. Glass here refers to 13mm borosilicate glass.

Surface	Components	# layers	Terminal layer
Glass	N/A	N/A	N/A
PEI/PSS(+)	PEI, PSS	7	PEI
PEI/PSS(-)	PEI, PSS	6	PSS
PEI/GO	PEI, GO	6	GO
PEI/GO-SO_3	PEI, GO-SO_3	6	GO-SO_3
PEI/G-SO_3	PEI/ G-SO_3	6	G-SO_3

The aims of the research discussed in this chapter were to:

- Assess and compare the biocompatibility of PEI/G-SO_3, PEI/GO and PEI/GO-SO_3 LbL constructs towards 3T3 SA cells.
- Investigate the effect of different graphene functionalisations on 3T3 SA adhesion and proliferation.
- Highlight interesting conclusions and potential for further research arising from this study.

3T3 SA cells were seeded at a density of 50,000 cells per well (~38,000 cells per cm^2) on the LbL constructs (PEI/PSS(+), PEI/PSS(-), PEI/GO, PEI/GO-SO_3 and PEI/G-SO_3) and were cultured for a period of 6 days, after which they reached confluence. LIVE/DEAD staining, AlamarBlue cell viability assays and PicoGreen DNA quantification assays were performed at 1 day, 3 days and 6 days post-seeding. The adsorption of fibronectin (Fn) and bovine serum albumin (BSA) onto the LbL constructs was assessed using a NanoOrange assay. The actin cytoskeleton, nuclei and focal adhesions of 3T3 SA cells on the LbL constructs were visualised using a ChemiCon triple staining kit (TRITC-conjugated phalloidin, anti-vinculin and DAPI) and analysed using Cell Profiler software. All methods are outlined in Chapter 2. Statistical analysis was performed on GraphPad software using mean, standard deviation and *n* values using a two-way ANOVA test, with confidence set at $p < 0.05$. The term 'GFN-containing LbL constructs', used throughout this chapter, refers to the PEI/GO, PEI/GO-SO_3 and PEI/G-SO_3 LbL constructs.

4.1. LIVE/DEAD assay

LIVE/DEAD assays were used to assess the viability and proliferation of 3T3 SA cells incubated on the LbL constructs over a period of 6 days; live cells were stained with calcein-AM (shown as green), while dead cells were stained with ethidium homodimer (shown as red). Representative composite LIVE/DEAD images are shown in Figure 4-1 and indicate the successful proliferation of 3T3 SA cells on all LbL constructs (PEI/PSS(+), PEI/PSS(-), PEI/GO, PEI/GO-SO_3 and PEI/G-SO_3). However, the coverage of 3T3 SA cells on the PEI/PSS(-) construct, appears to be lower than the other LbL constructs, most noticeably at 3 days.

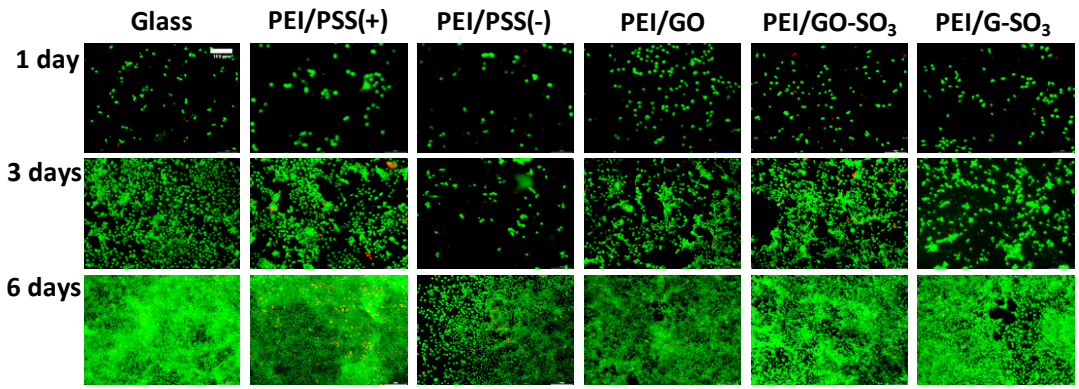

Figure 4-1. Images taken of 3T3 SA cells on LbL constructs, stained with LIVE/DEAD reagent, at 1 day, 3 days and 6 days post-seeding. Scale bar represents 100 μm.

4.1.1. Cell counts

Cell counts were conducted at each time point, on each LbL construct., by analysis of several LIVE/DEAD images ($n \geq 7$). Cell counts are displayed in Figure 4-2, showing an increase in 3T3 SA cell numbers from 1 day to 6 days post-seeding, on all the LbL constructs.

There was a significant increase in 3T3 SA cell counts on all substrates between 1 day and 3 days post-seeding, except for PEI/PSS(-). A significant increase in cell count was observed between 3 days and 6 days post-seeding, for all LbL constructs, indicating that all the LbL constructs support the adhesion and proliferation of 3T3 SA cells.

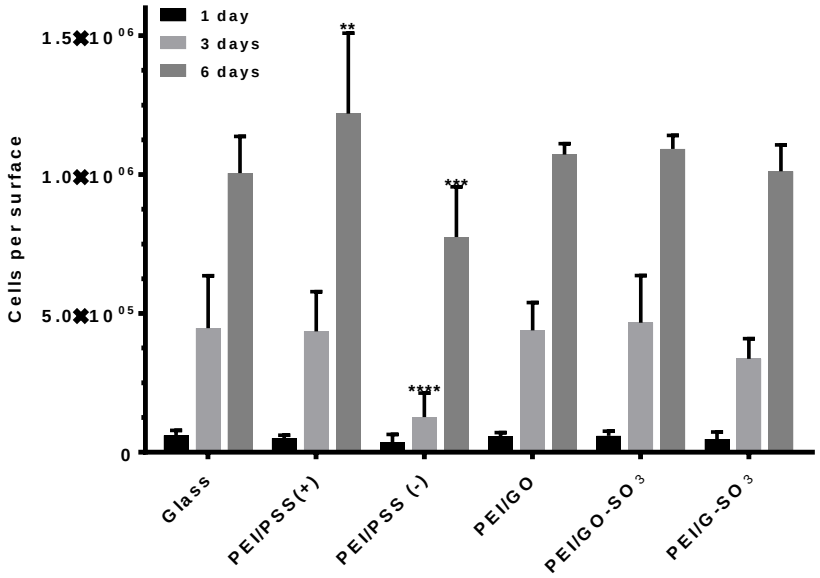

Figure 4-2. Viable cell counts obtained from analysis of images of 3T3 SA cells seeded onto LbL constructs and stained with LIVE/DEAD stains. Cell counts were estimated using the ITCN plug-in on ImageJ. Stars above bars show results with statistical significance compared to the control, glass, at the same time point. Significant differences between GFN-containing LbL constructs are indicated by horizontal lines. Significant differences between the PEI/PSS(+) and PEI/PSS(-) LbL constructs are not displayed here for clarity, but can be found in section 4.4.3. ****$p \leq 0.0001$, *** $p \leq 0.001$, ** $p \leq 0.01$, * $p < 0.05$.

At 1 day, post-seeding, there were no significant differences in 3T3 SA cell counts on any of the LbL constructs (PEI/PSS(+), PEI/PSS(-), PEI/GO, PEI/GO-SO_3 or PEI/G-SO_3) in comparison to the control. At 3 days, post-seeding, there was a significantly lower 3T3 SA cell count on the PEI/PSS(-) LbL construct than on the glass control, but no other significant differences in 3T3 SA cell count on the LbL constructs were observed, in comparison to the control. At 6 days post-seeding, there was a significantly higher 3T3 SA cell count on the PEI/PSS(+) LbL construct than on the control and significantly lower 3T3 SA cell count on PEI/PSS(-) than on the control, with no other significant differences in cell count between the LbL constructs and the control. There were no significant differences in 3T3 SA cell counts on any of the GFN-containing LbL constructs (PEI/GO, PEI/GO-SO_3 and PEI/G-SO_3), at any of the time points.

Relative increases in cell counts between day 1 and day 6 are summarised in Table 4-2. The relative increase in 3T3 SA cell counts is not statistically different for 3T3 SA cells on any of the LbL constructs and indicate that all LbL constructs support the proliferation of 3T3 SA cells.

Table 4-2. Relative increase in cell count for 3T3 SA cells. Errors are from the propagation of the errors at each time point.

Substrate	Relative cell count increase
Glass	16.5 ± 5.3
PEI/PSS(+)	24.1 ± 7.7
PEI/PSS(-)	21.9 ± 18.3
PEI/GO	18.9 ± 4.72
PEI/GO-SO_3	18.4 ± 5.16
PEI/G-SO_3	21.2 ± 11.5

4.1.2. Cell viability quantification

3T3 SA cell viabilities on each LbL construct were calculated from counting the number of live cells (green) and dead cells (red) in all the LIVE/DEAD® images ($n \geq 7$). Cell viability percentages at each timepoint are displayed in Figure 4-3. Cell viability remained above 79 % for all LbL constructs, over all time points.

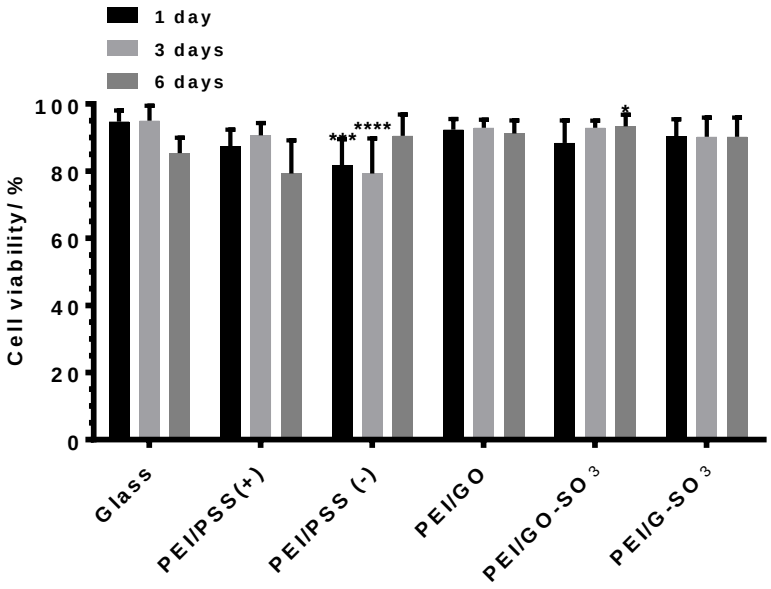

Figure 4-3. Cell viability % calculated from the number of live cells as a percentage of the total number of cells (live + dead cells), from 3T3 SA cells seeded onto LbL constructs, stained with LIVE/DEAD®. Cell counting was performed using ITCN plug in. Stars above bars show results with statistical significance compared to the control, glass, at the same time point. Significant differences between GFN-containing LbL constructs are indicated by horizontal lines. Significant differences between the PEI/PSS(+) and PEI/PSS(-) LbL constructs are not displayed here for clarity, but can be found in section 4.4.3. ****$p \leq 0.0001$, *** $p \leq 0.001$, ** $p \leq 0.01$, * $p < 0.05$.

The cell viability was significantly lower on PEI/PSS(-) in comparison to the control at 1 day post-seeding, but there were no other significant differences in cell viability after 1 day. After 3 days, 3T3 SA cell viability was significantly lower on PEI/PSS(-) in comparison to the control; there were no other significant differences in cell viability between the LbL constructs and the control. After 6 days, cell viability was significantly higher on PEI/GO-SO_3 compared to the control, but there were no other significant differences between the LbL constructs and the control. There were no significant differences in cell viability on the GFN-containing LbL constructs (PEI/GO, PEI/GO-SO_3 and PEI/G-SO_3) at any of the time points. The cell viability remained above 91 % for PEI/GO, 88 % for PEI/GO-SO_3 and 90 % on PEI/G-SO_3 over the test period.

4.2. Cell activity assays

The metabolic activity of 3T3 SA cells on each LbL construct was measured over the 6-day period to further assess the effect of each LbL construct upon 3T3 SA cell behaviour. DNA quantification of 3T3 SA cells cultured on the LbL constructs was assessed using the PicoGreen DNA assay and metabolic activity measured using the AlamarBlue Assay. PicoGreen and AlamarBlue assays were performed at 1, 3 and 6 days post-seeding, with results displayed in Figure 4-4 and Figure 4-5, respectively.

4.2.1. PicoGreen assay

The PicoGreen assay was used to quantify the amount of DNA extracted from 3T3 SA cells seeded on each LbL construct. The worked up PicoGreen data is shown in Figure 4-4, clearly showing an increase in 3T3 SA DNA concentration over the test period, for all LbL constructs (PEI/PSS(+), PEI/PSS(-), PEI/GO, PEI/GO-SO_3 and PEI/G-SO_3).

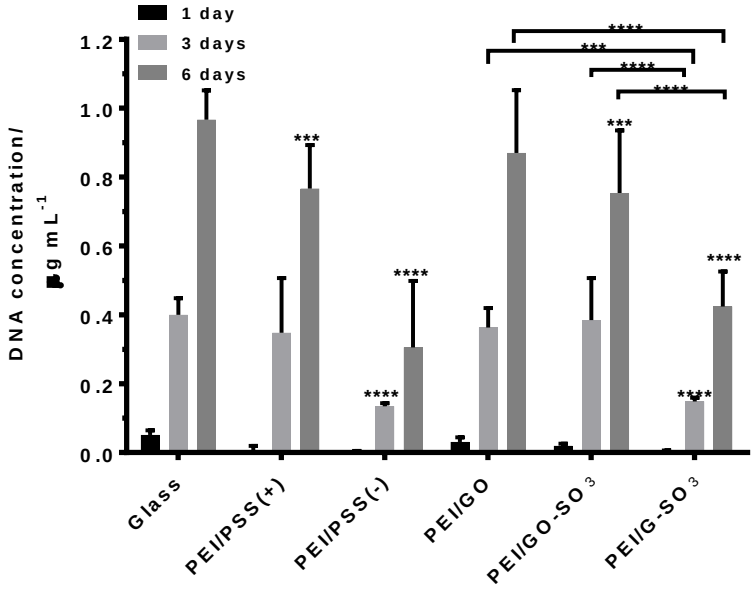

Figure 4-4. Quantification of cell activity on LbL constructs. PicoGreen assay for dsDNA quantification. Stars above bars show results with statistical significance compared to the control, glass, at the same time point. Significant differences between GFN-containing LbL constructs are indicated by horizontal lines. Significant differences between the PEI/PSS(+) and PEI/PSS(-) LbL constructs are not displayed here for clarity, but can be found in section 4.4.3. ****$p \leq 0.0001$, *** $p \leq 0.001$, ** $p \leq 0.01$, * $p < 0.05$.

Lysed 3T3 SA cells on all LbL constructs showed a significant increase in DNA concentration from 1 day to 3 days post-seeding, and from 3 days to 6 days post-seeding. The relative increase in the DNA concentration of lysed cells was calculated between day 3 and day 6, as DNA readings for the PEI/PSS(-) and PEI/G-SO_3 were in the limit of detection after 1 day. The relative increases in DNA concentration are shown in Table 4-3. Though absolute DNA concentrations differ significantly between the LbL constructs, as seen in Figure 4-4, the differences in relative increases in DNA concentration are not statistically significant on any of the LbL constructs, indicating that all the substrates support 3T3 SA proliferation and an increase in cell activity over the test period.

Table 4-3. Relative increase in DNA concentration for 3T3 SA cells grown on LbL constructs. Errors are from the propagation of the errors at each time point.

Substrate	Relative increase in DNA
Glass	2.4 ± 0.4
PEI/PSS(+)	2.2 ± 1.1
PEI/PSS(-)	2.3 ± 1.4
PEI/GO	2.4 ± 0.6
PEI/GO-SO_3	2.0 ± 0.8
PEI/G-SO_3	2.9 ± 0.7

After 1 day, there were no significant differences in 3T3 SA DNA concentration on any of the LbL constructs in comparison to the control. After 3 days, 3T3 SA cells seeded on the PEI/G-SO_3 and the PEI/PSS(-) LbL constructs showed a significantly lower concentration of DNA than those on the control, while 3T3 SA cells seeded on the PEI/GO, PEI/GO-SO_3 and PEI/PSS(+) LbL constructs showed no significant differences in DNA concentration in comparison to the control. After 6 days, 3T3 SA cells seeded on all the LbL constructs showed a lower DNA concentration in comparison to the control, apart from PEI/GO, for which no significant difference was observed.

There were no significant differences in DNA concentration expressed by 3T3 SA cells seeded onto the GFN-containing LbL constructs at 1 day post-seeding but, after 3 days and 6 days, there was a significantly higher DNA concentration for 3T3 SA cells on the PEI/GO and PEI/GO-SO_3 LbL constructs than on PEI/G-SO_3 construct. There were no significant differences in DNA concentration for 3T3 SAs on the PEI/GO and PEI/GO-SO_3, at any of the time points.

4.2.2. AlamarBlue assay

In addition to DNA quantification, cell metabolic activity was measured using an AlamarBlue assay. Metabolically active cells result in the conversion of non-fluorescent resazurin to fluorescent resorufin, meaning that a higher fluorescence intensity at 590 nm ($I_{590\,nm}$) is indicative of higher metabolic activity. The fluorescence intensities for 3T3 SA cells on the LbL constructs are shown in Figure 4-5. All LbL constructs and controls showed an increase in $I_{590\,nm}$ (and hence cell metabolism) over the test period, indicating the proliferation of 3T3 SA cells. From day 1 to day 3, $I_{590\,nm}$ was only found to increase significantly for 3T3 SA cells on the PEI/GO and PEI/GO-SO_3 LbL constructs, while from day 3 to day 6, 3T3 SA cell metabolic activity increased significantly on all LbL constructs.

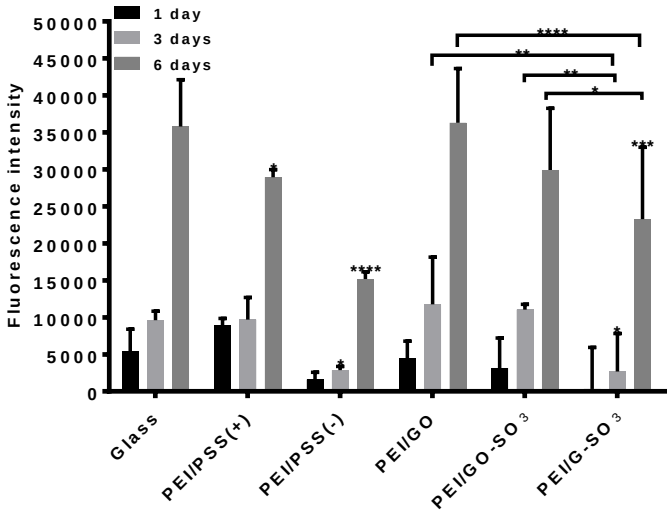

Figure 4-5. Quantification of cell viability on LbL constructs. AlamarBlue Assay for cell viability and proliferation. Stars above bars show results with statistical significance compared to the control, glass, at the same time point. Significant differences between GFN-containing LbL constructs are indicated by horizontal lines. Significant differences between the PEI/PSS(+) and PEI/PSS(-) LbL constructs are not displayed here for clarity, but can be found in section 4.4.3. ****$p \leq 0.0001$, *** $p \leq 0.001$, ** $p \leq 0.01$, * $p < 0.05$. Fluorescence intensity was measured at 590 nm.

The relative increase in cell activity, as measured by $I_{590\,nm}$, was calculated between 3 days and 6 days after seeding, as value of the PEI/G-SO_3 I_{590nm} was in the limit of detection after 1 day. Relative increases in cell activity are shown in Table 4-4.

Though the absolute values of the fluorescence intensity (and hence cell activity) differ between the LbL constructs, the relative increases in cell activity between 3 days and 6 days post-seeding do not differ significantly, indicating that all LbL constructs support 3T3 SA cell proliferation.

Table 4-4. Relative increase in cell activity of 3T3 SA cells on LbL constructs. Errors are from the propagation of the errors at each time point.

Substrate	Relative increase in $I_{590\ nm}$
Glass	3.7 ± 0.8
PEI/PSS(+)	3.0 ± 0.9
PEI/PSS(-)	5.3 ± 1.0
PEI/GO	3.1 ± 1.8
PEI/GO-SO_3	2.7 ± 0.8
PEI/G-SO_3	8.7 ± 17

At 1 day post-seeding, there were no significant differences in 3T3 SA cell metabolic activity on any of the LbL constructs in comparison to the control. After 3 days, 3T3 SA cells on the PEI/PSS(-) and PEI/G-SO_3 LbL constructs displayed significantly lower cell activity than on the control, while cells seeded on all other LbL constructs showed no significant difference in cell activity in comparison to the control. After 6 days, 3T3 SA cells on PEI/PSS(+), PEI/PSS(-) and PEI/G-SO_3 LbL constructs showed significantly lower cell metabolic activity than on the control, with cells on the PEI/GO and PEI/GO-SO_3 LbL constructs showing no significant difference in cell activity to those on the control. 3T3 SA cells on the PEI/GO and PEI/GO-SO_3 LbL constructs showed higher metabolic activity than on the PEI/G-SO_3 LbL construct at 3 days and 6 days after incubation. However, there were no significant differences between the PEI/GO and PEI/GO-SO_3 LbL constructs for any of the time points.

4.3. NanoOrange protein-binding assays

The tissue culture surface, before cell adhesion, interacts with many serum proteins from the media.[18,19] Bovine serum albumin (BSA) is present in serum at a much higher concentration than other proteins and is thought to adhere initially to surfaces. Therefore, albumin binding can be considered an important event in initial cell adhesion. Adhesive proteins, such as fibronectin and vitronectin, must replace the adsorbed albumin to initiate cell attachment.[18]

In this study, the adsorption of fibronectin (Fn) and bovine serum albumin (BSA) onto the LbL constructs was assessed using a NanoOrange assay, to assess whether protein adsorption correlated with cell adhesion. As protein adsorption is thought to occur before cell adhesion, 90-min and 4-hour timepoints were chosen. Surfaces were incubated with 10 $\mu g\,mL^{-1}$ protein solutions, containing the NanoOrange reagent. After the incubation period, the supernatant was removed from the cells and heated to activate the NanoOrange-protein binding. The fluorescence was measured and the concentration of protein remaining in solution was calculated by comparison to a BSA standard curve. The amount of protein adsorbed onto the LbL constructs was then calculated. The adsorption profiles are displayed in Figure 4-6 (BSA) and Figure 4-7 (fibronectin).

4.3.1. BSA adsorption

The BSA adsorption profiles on the LbL constructs can be seen in Figure 4-6. The amount of BSA adsorbed from 90 mins to 4 hours significantly increased for glass and decreased significantly for PEI/PSS(-); all other LbL constructs showed no significant differences in BSA adsorption between 90 mins and 4 hours.

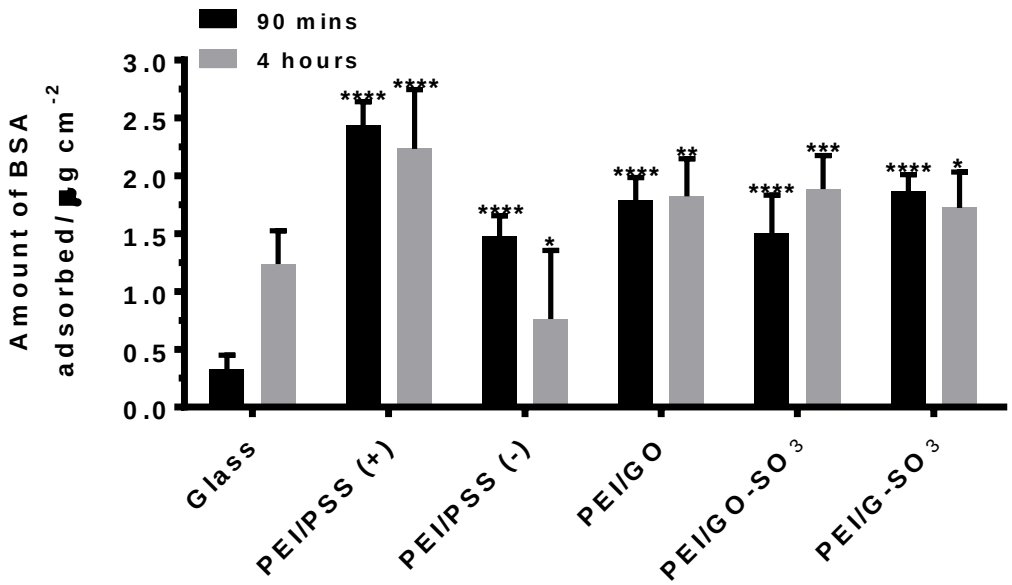

Figure 4-6. Bovine serum albumin binding quantification on LbL constructs measured via the NanoOrange Assay. Stars above bars show results with statistical significance compared to the control, glass, at the same time point. Significant differences between GFN-containing LbL constructs are indicated by horizontal lines. Significant differences between the PEI/PSS(+) and PEI/PSS(-) LbL constructs are not displayed here for clarity, but can be found in section 4.4.3. ****$p \leq 0.0001$, *** $p \leq 0.001$, ** $p \leq 0.01$, * $p < 0.05$.

Following 90 mins' incubation with 10 μg mL^{-1} BSA solution, all LbL constructs adsorbed a greater mass of BSA than the glass control. A greater amount of BSA had adsorbed onto all LbL constructs compared to the control after 4 hours (grey bars), with the exception of PEI/PSS(-). However, there were no significant differences in BSA adsorption between the GFN-containing LbL constructs at either 90 mins or 4 hours after incubation with BSA solution.

4.3.2. Fibronectin adsorption

The Fn adsorption profiles on the LbL constructs can be seen in Figure 4-7. There was an increase in Fn adsorption on all constructs from 90 mins to 4 hours after incubation in protein solution except for PEI/G-SO_3 for which no significant difference was observed.

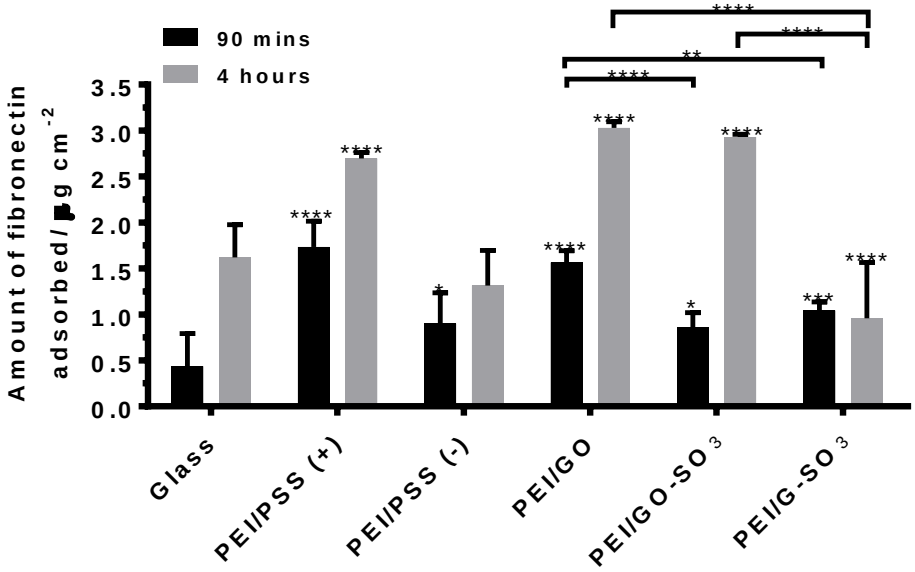

Figure 4-7. Fibronectin binding quantification on LbL constructs measured via the NanoOrange Assay. Stars above bars show results with statistical significance compared to the control, glass, at the same time point. Significant differences between GFN-containing LbL constructs are indicated by horizontal lines. Significant differences between the PEI/PSS(+) and PEI/PSS(-) LbL constructs are not displayed here for clarity, but can be found in section 4.4.3. ****$p \leq 0.0001$, *** $p \leq 0.001$, ** $p \leq 0.01$, * $p < 0.05$.

The adsorption of Fn onto all LbL constructs was significantly higher compared to the control (glass) after 90 mins, as shown in Figure 4-7. After 4 hours, there was a significantly higher amount of Fn adsorption on the PEI/PSS(+), PEI/GO and PEI/GO-SO_3 constructs than the glass control and a significantly lower amount on PEI/G-SO_3. There was no significant difference in Fn adsorption between PEI/PSS(-) and the control.

The difference in Fn adsorption between the graphene containing LbL constructs is marked. After 90 mins' incubation in protein solution, PEI/GO shows a significantly higher protein adsorption than PEI/GO-SO_3 and PEI/G-SO_3. After 4 hours, both PEI/GO and PEI/GO-SO_3 showed significantly higher Fn adsorption than PEI/G-SO_3.

4.4. Actin cytoskeleton and focal adhesion staining of 3T3 SA cells

To assess the morphology and visualize focal adhesions of 3T3 SA cells on each of the LbL constructs, cells were incubated for 1 day and 3 days, respectively, following which they were stained with TRITC-conjugated phalloidin (to reveal the actin cytoskeleton), anti-vinculin antibody (conjugated with a FITC-labelled secondary antibody, to highlight focal adhesions) and 4',6-diamidino-2-phenylindole (DAPI) to stain nuclei. Representative images of the triply-stained 3T3 SA cells on 1 day and 3 days post-seeding can be seen in Figure 4-8 and Figure 4-9, respectively. The actin cytoskeleton staining reveals a similar actin distribution for 3T3 SAs on all LbL constructs. Focal adhesions and cell shape were quantified by use of CellProfiler Software, as described in the Materials and Methods section. Differences in cell shape, nuclear shape and focal adhesions can give indication as to the response of the 3T3 SA cells to the different LbL constructs.

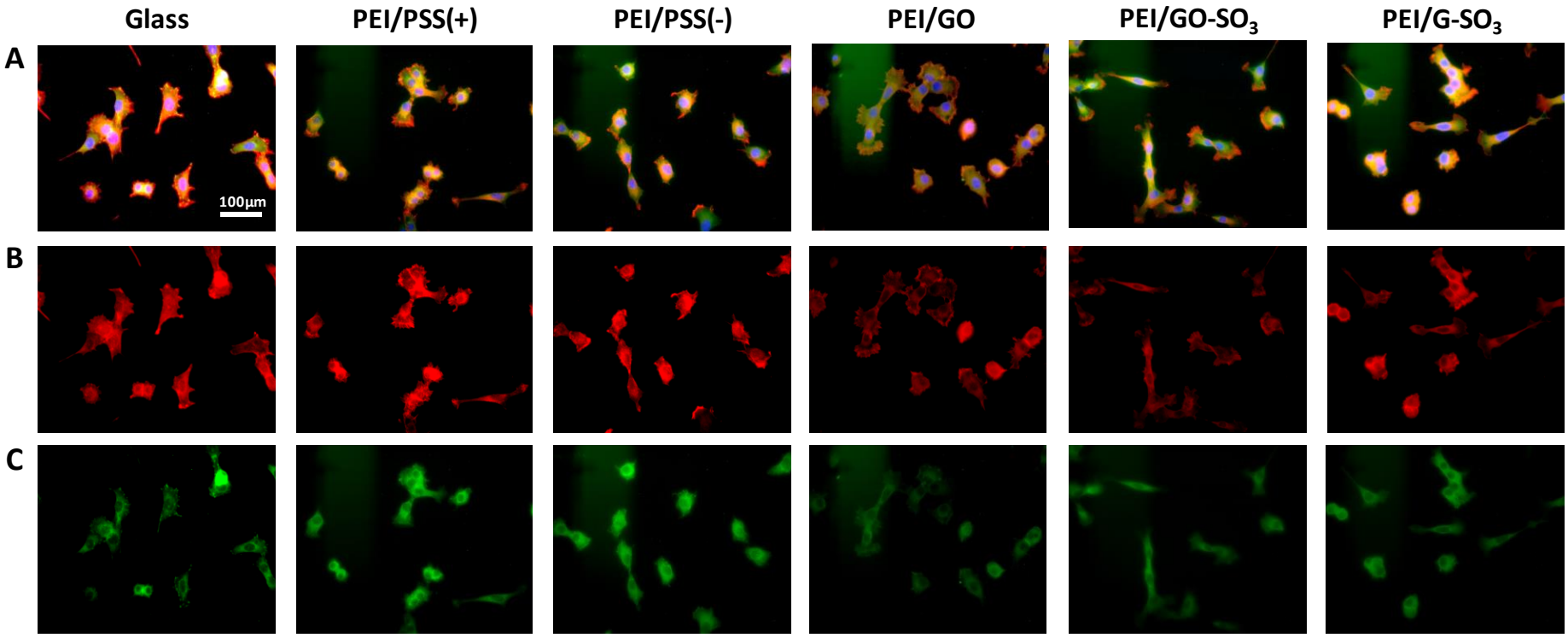

Figure 4-8. Triple staining of 3T3 SA cells seeded onto LbL constructs after 1 day. A) Triple stain image showing DAPI-stained nuclei (blue), phalloidin (red) and vinculin (green) B) Phalloidin antibody staining C) Anti-vinculin stain. Scale is the same for all images.

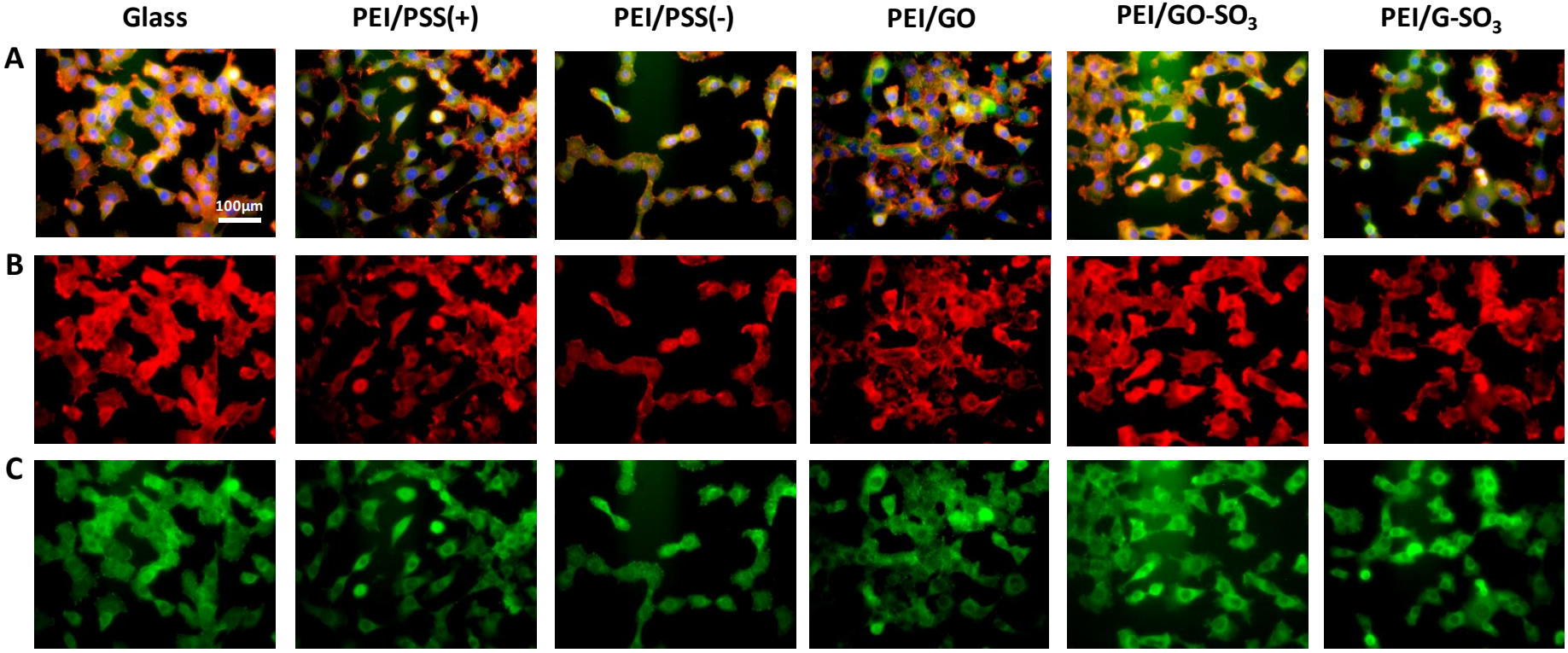

Figure 4-9. Triple staining of 3T3 SA cells on LbL constructs after 3 days' incubation. A) Composite triple stained images. B) Phalloidin staining of actin cytoskeleton C) Vinculin staining of focal adhesions. Scale is the same for all images.

4.4.1. Quantitative analysis of focal adhesions

Using CellProfiler software, the number of focal adhesions was quantified for 3T3 SA cells on each LbL construct by analysis of several images ($n \geq 10$). The number of focal adhesions in each image was divided by the number of cells (as stained by DAPI) in that image to calculate the average number of focal adhesion per cell. This was performed for each LbL construct at both 1 day and 3 days post-seeding. The quantitative focal adhesion analysis is presented in Figure 4-10. Visually, the average number of focal adhesions appears to follow the same trend as the trends in cell activity and DNA expression. All LbL constructs show an increase in focal adhesions between 1 day and 3 days post-seeding apart from PEI/PSS(+), for which no significant difference was observed.

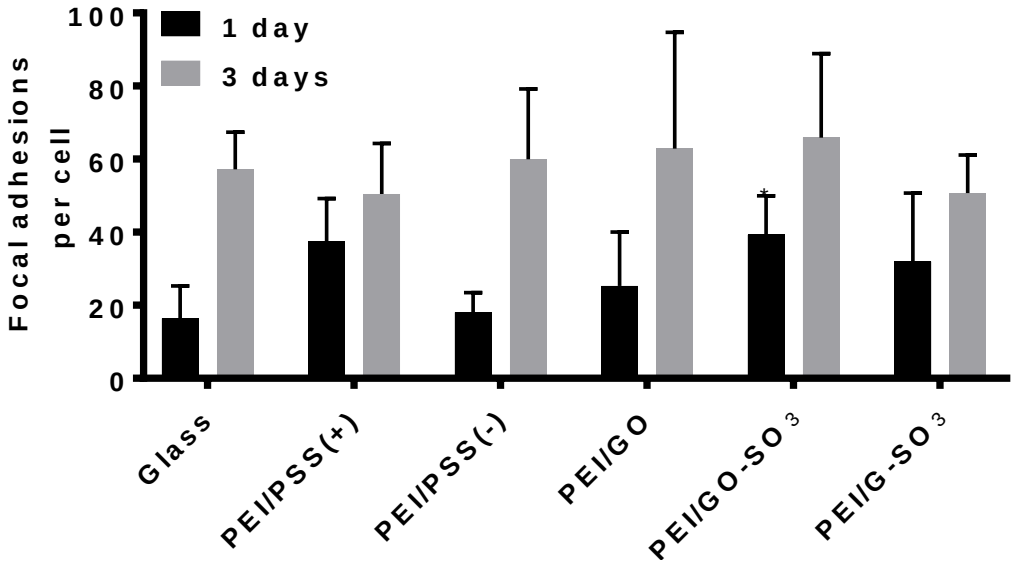

Figure 4-10. Focal adhesion quantification of 3T3 SA cells on LbL constructs as estimated using CellProlifer software. Stars above bars show results with statistical significance compared to the control, glass, at the same time point. ****$p \leq 0.0001$, *** $p \leq 0.001$, ** $p \leq 0.01$, * $p < 0.05$.

After 1 day, 3T3 SA cells on the PEI/GO-SO_3 LbL construct showed a significantly higher number of focal adhesions than on the control. There were no other significant differences in the number of focal adhesions for 3T3 SA cells seeded on

the LbL constructs in comparison to the control. After 3 days, no significant differences in focal adhesions per cell were observed on any of the LbL constructs, in comparison to the control. There was no significant difference in the number of focal adhesions per cell for 3T3 SA cells seeded on the GFN-containing LbL constructs at either 1 day or 3 days post-seeding.

4.4.2. Cell area

CellProfiler software was used to analyse the cell areas of 3T3 SA cells on the LbL constructs. The calculated average cell areas are shown in Figure 4-11. 3T3 SA cells on the PEI/GO and PEI/GO-SO_3 LbL constructs increased in cell area significantly between 1 day and 3 days post-seeding (PEI/GO: 744 μm^2 to 965 μm^2, PEI/GO-SO_3: 813 μm^2 to 1563 μm^2). The other LbL constructs showed no significant difference in cell area between 1 day and 3 days.

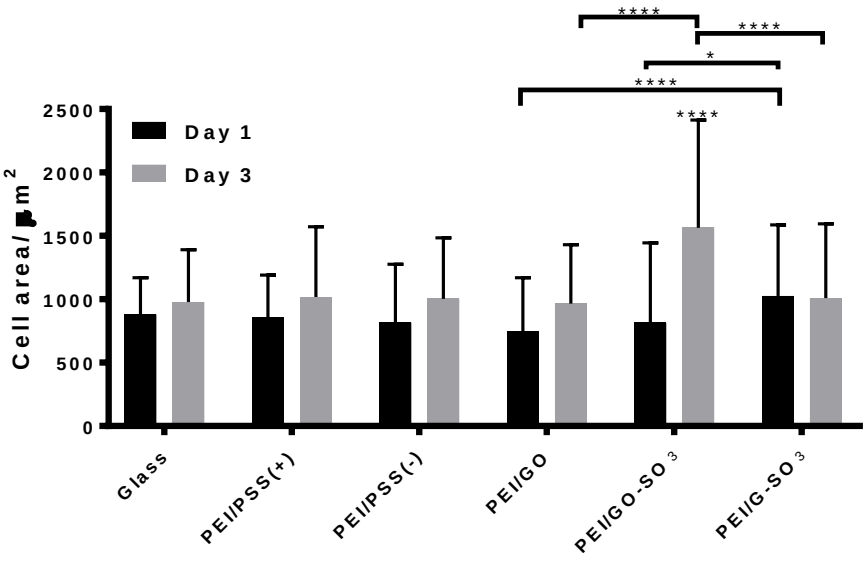

Figure 4-11. Average 3T3 SA cell areas as calculated in CellProfiler software. Stars above bars show results with statistical significance compared to the control, glass, at the same time point. Significant differences between GFN-containing LbL constructs are indicated by horizontal lines. ****$p \leq 0.0001$, *** $p \leq 0.001$, ** $p \leq 0.01$, * $p < 0.05$.

After 1 day, there were no significant differences in 3T3 SA cell area on any of the LbL constructs in comparison to the control. After 3 days, only 3T3 SA cell area on

the PEI/GO-SO_3 LbL construct differed significantly to the control. 3T3 SA cells on the PEI/G-SO_3 construct showed a significantly higher cell area than PEI/GO and PEI/GO-SO_3 while, after 3 days, cells on the PEI/GO-SO_3 LbL construct had a significantly higher area than both PEI/GO and PEI/G-SO_3.

4.4.3. PEI/PSS(+) vs. PEI/PSS(-) LbL constructs for 3T3 SA cell adhesion and proliferation

As previously outlined, to confirm the influence of terminal layer on cell proliferation, two control LbL constructs were made, using alternating layers of PEI and PSS. The PEI/PSS(+) construct was terminated with a PEI layer and the PEI/PSS(-) LbL construct with a PSS layer. The cell count, cell viability, PicoGreen DNA quantification, AlamarBlue assay, BSA adsorption and fibronectin adsorption profiles for 3T3 SA cells on the PEI/PSS(+) and PEI/PSS(-) LbL constructs are shown in Figure 4-12.

Figure 4-12A shows a significantly higher 3T3 SA cell count on the PEI/PSS(+) LbL construct than on the PEI/PSS(-) construct, both at 3 days and 6 days post-seeding. After 3 days post seeding, the 3T3 SA cell viability was significantly higher on PEI/PSS(+) in comparison to PEI/PSS(-), but after 6 days this pattern was reversed with PEI/PSS(-) displaying a significantly higher cell viability than PEI/PSS(+), as seen in Figure 4-12B. Therefore, there was no discernible trend in cell viability between the two PEI/PSS containing LbL constructs.

The cell activity followed the same trend as the cell counts, with a significantly higher DNA concentration for 3T3 SA cells on the PEI/PSS(+) LbL construct compared to the PEI/PSS(-) LbL construct at 3 days and 6 days post-seeding, as seen in Figure 4-12C. Similarly, 3T3 SA cells seeded on the PEI/PSS(+) LbL construct

showed higher metabolic activity than on the PEI/PSS(-) LbL construct at 1 day 3 days and 6 days post incubation, as shown in Figure 4-12D.

In addition, the BSA and fibronectin adsorption profiles followed this trend, as shown in Figure 4-12E and F, with a higher amount adsorbed on to PEI/PSS(+) than on PEI/PSS(-) at both 90 mins and 4 hours incubation.

There was, however, no significant difference in the number of focal adhesions per cell or cell area for 3T3 SA cells seeded onto the PEI/PSS(+) and PEI/ PSS(-) LbL constructs at 1 day or 3 days post-seeding. These findings indicate that there is a strong correlation between the surface chemistry of the terminal layer and cell adhesion and proliferation. There have been several reports which have alluded to the toxicity of PSS, both *in-vitro* and *in-vivo*, which is in agreement with the findings in this work.[20,21]

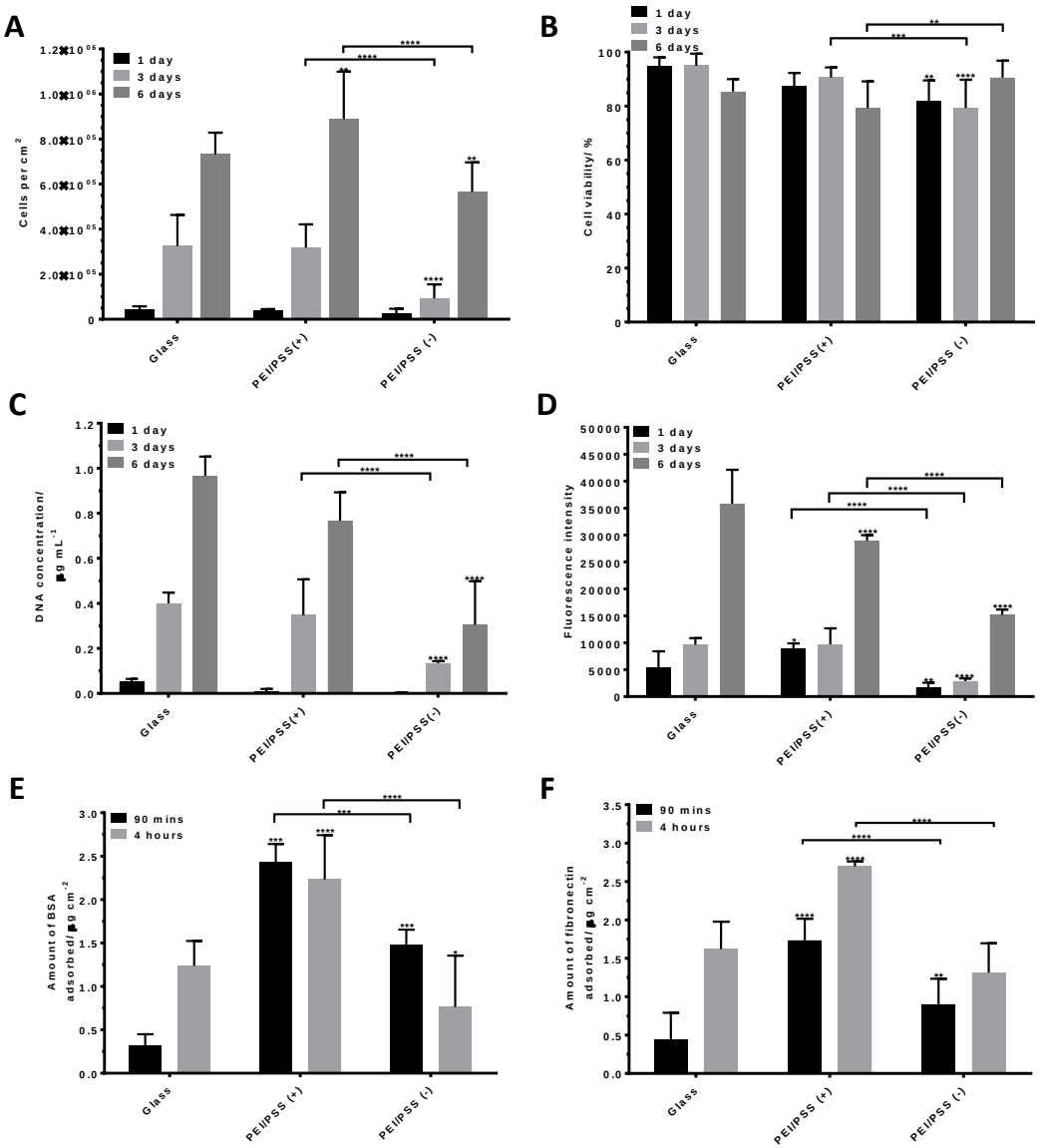

Figure 4-12. Cell proliferation assays for 3T3 SA cells on glass, PEI/PSS(+) and PEI/PSS(-) LbL constructs. A) Cell count B) Cell viability C) PicoGreen DNA quantification D) AlamarBlue metabolic activity assay E) BSA protein adsorption profile F) Fibronectin protein adsorption profile. Stars above bars show results with statistical significance compared to the control, glass, at the same time point. Significant differences between PEI/PSS(+) and PEI/PSS(-) LbL constructs are indicated by horizontal lines. ****$p \leq$ 0.0001, *** $p \leq 0.001$, ** $p \leq 0.01$, * $p < 0.05$.

4.5. Discussion

The cell viability studies demonstrated that the PEI/PSS(+), PEI/PSS(-), PEI/GO, PEI/GO-SO_3 and PEI/G-SO_3 LbL constructs support the attachment and proliferation of 3T3 SA cells, with cell viability above 91 % for PEI/GO, 88 % for PEI/GO-SO_3 and 90 % on PEI/G-SO_3. There were no significant differences in cell count between

the GFN-containing LbL constructs, with PEI/GO, PEI/GO-SO_3 and PEI/G-SO_3 LbL constructs displaying comparable *relative* cell proliferation over the test period. PEI/PSS(+) and PEI/PSS(-) showed significant differences in 3T3 SA cell count, with PEI/PSS(-) showing a significantly lower cell count. This indicates that the terminal functional group has an effect on cell adhesion and proliferation. However, there were no discernible trends in cell viability between the PEI/PSS(+) and PEI/PSS(-) constructs.

Cell counts and viability data are not fully 'blind' assays, since only a small area from selected images were used for analysis compared to the total area occupied by the cells on the surface. In addition, the action of selecting areas to images gives rise to some level of subjectivity. This data therefore cannot be used alone for biocompatibility assessment and must be supplemented by assays which reflect the whole surface. For this reason, PicoGreen and AlamarBlue assays were performed to further investigate the proliferation and activity of 3T3 SA cells on the LbL constructs. All LbL constructs supported the adhesion and proliferation of 3T3 SA cells, as evidenced by the overall increase in cell metabolic activity and DNA concentration over the test period. The trends in both the PicoGreen DNA quantification and AlamarBlue metabolic activity assay corroborate and indicate that 3T3 SA cells on PEI/GO and PEI/GO-SO_3 LbL constructs show greater cell proliferation and display higher cell activity than PEI/G-SO_3. There was a significant difference in the PicoGreen DNA quantification and AlamarBlue metabolic activity assay for 3T3 SAs grown on PEI/PSS(+) vs. PEI/PSS(-), with the former supporting cell adhesion and proliferation to a greater extent. This further supports the notion that the change in the terminal layer has a significant impact on cell behaviour.

The similarity in focal adhesions, cell areas and nuclear shape among all the LbL constructs suggests that 3T3 SA cells display similar characteristics on each of the LbL constructs. This indicates that 3T3 SA cells show no significant changes in morphology on the different LbL constructs. Focal adhesions (FAs), as mentioned previously, are complexes which contain many proteins important for cell signaling.[22] FAs connect the actin filament to integrins, which bind to the extracellular matrix.[22] The assembly of focal adhesions is important for integrating many physical and chemical cues related to cell proliferation.[23] The cell areas reported in this work are similar to those reported by Ryoo *et al.* for NIH-3T3 fibroblast cells on graphene-based susbtrates.[23] The similarity in FAs and cell areas indicate that, once 3T3 SA cells have attached to the LbL constructs, they behave similarly on each construct.

Interestingly, protein adsorption profiles revealed a potential explanation for the observed differences in absolute values of cell activity over the 6-day test period. The GFN-containing LbL constructs showed no significant differences in BSA adsorption, though PEI/PSS(+) exhibited higher BSA adsorption that PEI/PSS(-) at both time points. The pattern in Fn adsorption, however, closely mirrors the trends found in the PicoGreen DNA quantification and AlamarBlue metabolic activity assays, with PEI/GO, PEI/GO-SO_3 and PEI/PSS(+) showing significantly higher Fn adsorption than PEI/G-SO_3 and PEI/PSS(-). This indicates a connection between Fn adsorption and the cell activity. Once bound to the LbL constructs via integrin-fibronectin interactions, 3T3 SA cells appear to show good proliferation and typical morphology on all LbL constructs. The varying amounts of fibronectin adsorbed on the LbL constructs must therefore affect the absolute number of cells which adhere,

but following this event the proliferation of 3T3 SA cells is not hindered on any of the substrates.

The working hypothesis is therefore that the extent of initial fibronectin adsorption, prior to cell attachment, has the dominant influence on the initial numbers of cells able to attach the substrates. All substrates support the adsorption of sufficient amounts of fibronectin to allow for effective 3T3 SA cell adhesion, but the relative amounts of fibronectin adsorption influence the absolute values of the cell activity and metabolism, with higher adsorption leading to enhanced cell activity. The following section outlines the properties of surfaces which are known to affect cell adhesion, and these properties related back to differences between the LbL constructs.

4.5.1. Roughness

On the nanoscale, it has been found that roughness has been widely considered a positive influence for cell adhesion and growth,[24] as this is similar to the extracellular matrix (ECM) that cells would encounter *in-vivo*.[24] Furthermore, Wang *et al.* reported increased 3T3 fibroblast adhesion and proliferation on wrinkled graphene oxide sheets than on planar sheets,[25] indicating that fibroblast adhesion is affected by the topology of the surface. The R_{RMS} roughness values (as measured from AFM) of the PEI/GO and PEI/GO-SO_3 LbL constructs (7.38 nm and 5.38 nm, respectively) were larger than for the PEI/G-SO_3 LbL construct (1.49 nm), which supports the notion that rougher surfaces enhance cell adhesion and growth. The R_{RMS} value of the PEI/PSS(+) construct however, which displayed 3T3 SA activity comparable to PEI/GO and PEI/GO-SO_3, was lower than all other LbL constructs. The differences in roughness of the LbL may have a significant influence on the

attachment and proliferation of 3T3 SA cells seeded onto PEI/GO and PEI/GO-SO_3, as well as the decreased activity on PEI/G-SO_3.

4.5.2. Hydrophilicity and charge

Several studies have found cell attachment and spreading to be more effective on hydrophilic surfaces, than hydrophobic surfaces.[26,27] However the contact angles for the LbL constructs, shown in Table 4-5, are fairly similar,. meaning that the difference in cell activity is not likely to arise from differences in hydrophilicity. In addition, PEI/GO showed higher cell activity than PEI/G-SO_3, despite having a higher contact angle. Generally cells grow most successfully on surface with moderate wettability,[28] meaning that these surfaces all have suitable wettability for effective cell attachment.

Table 4-5. Water contact angle on LbL constructs. Error bars arise from repeats.

Construct	Contact Angle/ °
Glass	42.5° ± 1.8°
PEI/PSS(+)	57.4° ± 2°
PEI/PSS(-)	41.9° ± 7.7°
PEI/GO	58.3° ± 3.5°
PEI/GO-SO_3	44.1° ± 7.4°
PEI/G-SO_3	48.7° ± 3.6°

Webb *et al.* observed that, for hydrophilic surfaces, cell attachment is influenced by the charge and wettability.[26] The charge on surface functional groups is found also to be important for cell adhesion; generally, it has been found that cells adhere more effectively to positively charged surfaces,[29] as cell-adhesion proteins generally carry a negative charge.[24,26] This may explain the origin of the particularly high adhesion on the positively-charged PEI/PSS(+) in comparison to PEI/PSS(-). However, PEI/GO and PEI/GO-SO_3 showed comparable cell proliferation and activity to PEI/PSS(+), despite carrying a net negative charge. The charge, though able to go

some way to explain the difference between PEI/PSS(+) and PEI/PSS(-) LbL constructs, does not fully explain the trends in 3T3 SA cell activity and proliferation.

4.5.3. Surface chemistry

Surface chemistry is important as it affects properties such as the surface energy, polarity and wettability of the surface, in addition to changing the interaction of the surfaces with proteins, all of which have an effect on cell adhesion and spreading.[24] There influence of the terminal layer on cell viability has been previously reported,[17] and was confirmed by the differences in 3T3 SA cell behaviour on the PEI/PSS(+) and PEI/PSS(-) LbL constructs, which were terminated with polyethyleneimine (PEI) and polystyrene sulfonate (PSS), respectively. For this reason, the functional groups of the terminal layers of the LbL-constructs is considered primarily.

Many studies have found cells to attach preferentially to positively charged, amine-containing surfaces.[29,30,31,32] As previously outlined, this is likely due to the positive charge of these functional groups, which promote binding of ECM proteins. Various studies have also reported surfaces with oxygen-containing functional groups to actively promote the adhesion and proliferation of cells.[24,33,34] This is thought to arise from the increase in polarity and wettability of the surface upon functionalisation with oxygen-containing groups,[24] in turn rendering the surface suited for the adsorption of ECM proteins such as fibronectin, collagen and laminin, which mediate cell adhesion.[24,35] This explains the high proliferation and cell activity observed on the PEI/GO LbL construct, which contain high oxygen content, despite possessing a net negative charge. PEI/GO-SO_3 also possesses many oxygen-containing functional groups which may explain why it has comparable activity to PEI/GO.

A similar effect was seen in work by Jeong *et al.*, in which higher cell adhesion and proliferation was seen on a GO coated substrate, in comparison to the same substrate which had undergone annealing, thus lower the amount of oxygen-containing functional groups.[36] In addition, Ku *et al.* found that GO adsorbed a higher amount of serum proteins than reduced GO (rGO), which in turn led to greater myoblast activity and proliferation.[37] Shi *et al*. controlled the reduction states of GO and compared myoblast, osteoblast and fibroblast attachment and proliferation, finding the cell attachment and proliferation to decrease with increasing reduction.[38] Guo *et al.* report higher fibroblast attachment to nitrogen-doped graphene surfaces, than for pristine graphene, which again highlights the effect of functional group on cell binding.[39]

Sulfonate groups, on the other hand, are an example of negatively charged groups which suppress cell adhesion and have been used in anticoagulant blood-contacting surfaces.[40] PEI/GO-SO_3, in addition to oxygen-containing functional groups, also possesses sulfonate groups, but the 3T3 SA studies suggests that the presence of sulfonate groups in this instance poses no significant effect, as there was no significant difference in 3T3 SA cell activity on PEI/GO and PEI/GO-SO_3. This can be rationalised by the fact that the GO starting material contains many oxygen-containing functional groups, which are in more highly abundant than the 0.7 % sulfur. For the PEI/PSS(-) and PEI/G-SO_3, the effect of the sulfonate groups is clearer, with lower cell activity on these constructs. Oxygen-containing defects are much lower in G-SO_3, meaning that the presence of the sulfonate group in this instance is likely to have a greater effect. The positively charged imine group of the PEI/PSS(+) control causes enhanced cell proliferation compared to

negatively-charged sulfonate group of the PEI/PSS(-) control, which differ only in their terminal layer, thus supporting the idea that it is the terminal layer which influences cell binding.

This is not to say, however, that the underlying layers do not play a role in cell proliferation and activity. As evidenced earlier, the incorporation of GO into composites has been found to alter its biocompatibility, meaning that the composite material or polymer may help to enhance cell adhesion and proliferation in comparison to a surface containing only GFN. As the counter layer for the GFN-containing LbL constructs is PEI, which is shown to support 3T3 SA cell adhesion and proliferation successfully, it is logical to reason that the presence of PEI in both the PEI/G-SO_3 and PEI/PSS(-) LbL constructs may enhance the cell adhesion and proliferation in comparison to surfaces containing only PSS or G-SO_3. Similarly, the same effect may be seen for PEI/GO and PEI/GO-SO_3 with the presence of PEI enhancing cell adhesion in comparison to surfaces containing only GO or GO-SO_3.

4.5.4. Importance of fibronectin adsorption on cell activity

The influence of functional groups and roughness on ECM protein adsorption is supported by the fibronectin adsorption profiles of the LbL constructs; the level of Fn adsorption was significantly higher on PEI/PSS(+), PEI/GO and PEI/GO-SO_3 than on PEI/PSS(-) or PEI/G-SO_3. It has been noted elsewhere that there is a correlation between fibronectin adsorption and 3T3 fibroblast cell proliferation.[41]

The adsorption of ECM proteins play a crucial role in mediating cell-material surface interaction because they approach surface, from the serum-containing media, more quickly than cells.[42,43] Cells recognise adsorbed proteins by virtue of surface

receptors, which include integrins;[44] the hydrophilic L-arginyl-glycyl-L-aspartyl (RGD) section of fibronectin forms the initial binding site for integrins.[45,46,47] Integrins in turn, promote cell proliferation, cell signalling and secretion of proteins to replenish the protein layers.[44,48] For example, Schlaepfer *et al.* demonstrated that 3T3 fibroblast binding to fibronectin promotes focal adhesion kinase (FAK) association and the formation of integrin activated signalling complex.[49] The phosphorylation of FAK after fibronectin stimulation links integrin engagement to the RAS/MAPK signal transduction pathway, which leads to processes such as cell division.[49] Other biocompatibility studies of GFN have recognised the importance of fibronectin on cell adhesion. For example, Subbiah *et al.* produced fibronectin/graphene oxide surfaces to enhance binding of preosteoblasts.[50] Shi *et al.* also correlated the fibronectin adsorption onto different reduced GO (rGO) surfaces, which directly correlated to cell adhesion and proliferation.[38]

4.5.5. Additional controls

The cell culture work described in this chapter has highlighted some interesting points regarding 3T3 SA cell adhesion and proliferation. One of the points outlined in this work was that the underlying PEI layer in the graphene-containing LbL constructs could contribute to their biocompatibility towards 3T3 SA cells. Although PEI/PSS LbL constructs were made to explore the effect of the terminal layer upon 3T3 SA cell adhesion and proliferation, any future comparative work using PEI-containing LbL constructs should also incorporate a single PEI layer as a control. Any differences in 3T3 SA activity and adhesion observed between the PEI/GO, PEI/GO-SO_3 and PEI/G-SO_3 and PEI surfaces would therefore be due to the presence of the GFNs and or their coverage. For example, for any work determining the effect of coverage on cell activity would require this surface as a

control, as at the limit of very low coverage the LbL could be expected to behave like a PEI surface toward cells.

4.6. Conclusion

The biocompatibility of GFN-containing LbL constructs has been assessed using a 3T3 SA cell line, with the results finding that PEI/GO, PEI/GO-SO_3 and PEI/G-SO_3 all support the attachment and proliferation of this cell line and display high viability over the test period. There were observed differences in cell activity on the GFN-containing LbL constructs, with PEI/GO and PEI/GO-SO_3 showing enhanced cell activity in comparison to PEI/G-SO_3. There were no clear differences in cell activity between PEI/GO and PEI/GO-SO_3. The difference in cell activity among the GFN-containing LbL constructs was mirrored in the Fn adsorption profiles.

The chemical functionality on the terminal layer of the LbL constructs, in combination with nanoscale roughness, appear to offer the strongest arguments for the differences in cell proliferation and activity on the GFN-containing LbL constructs, which can be directly linked to the extent of initial Fn adsorption from the media, the subsequent anchorage of cells to its RGD binding domains and therefore cell signalling for division and metabolic activity. The oxygen-containing functional groups such as epoxides, carboxyls and alcohols as well as nitrogen-containing groups are reported to be favourable for cell adhesion, which is supported in this work. Sulfonate groups, which have been previously found to cause decreased cell adhesion, were shown to have the same effect in this work. The hypothesised origins of the differences in Fn adsorption on the LbL constructs and the subsequent differences in cell adhesion are summarised below:

- For the PEI/PSS(+) LbL construct, Fn adsorption was enhanced by the positive charge of the surface and the imine functionality of the terminal layer.
- For PEI/GO and PEI/GO-SO_3 Fn adsorption was enhanced through high nanoscale roughness, which mirrors the properties of the extracellular matrix (ECM), and through the presence of oxygen-containing functional groups, which encouraged Fn binding.
- For PEI/GO-SO_3, the presence of the sulfonate functional groups was offset by the roughness and oxygen-containing functionality, meaning that the effect of this functionalisation does not have a large effect on 3T3 SA binding, in comparison to PEI/GO.
- For the PEI/PSS(-) and PEI/G-SO_3 the presence of sulfonate groups in the constructs, along with the relatively lower nanoscale roughness, lead to less favourable conditions for Fn adsorption.

As previously outlined, however, all the LbL constructs adsorbed sufficient amounts of fibronectin to cause significant cell adhesion and proliferation, meaning that these factors explain the magnitude of the cell activity.

4.7. Further work

This study has provided significant insight into the effect of graphene functionalisation on cell activity. The study has shown that surface functional groups, as well as the roughness of the GFN-containing LbL constructs, have a significant effect on the adhesion of 3T3 SA cells. The functionalisation of pristine graphene outlined in this thesis could be used to specifically attach molecules that may enhance cell adhesion, for example RGD peptides or nitrogen-containing functional groups.[51]

A question arising from this study was whether the incorporation of graphene sulfonate (G-SO_3) into the LbL construct would have enhanced cell adhesion and proliferation compared to a surface containing only G-SO_3. The PEI terminal layer was shown to support 3T3 SA adhesion and proliferation well, so an outstanding question is whether cell migration through the LbL construct to the underlying PEI layers could have contributed to the observed cell proliferation and activity of the PEI/G-SO_3 construct. A way to assess this would be to look at cell adhesion and proliferation on CVD graphene and CVD G-SO_3. This was, however, out of the scope of this research as CVD graphene surfaces are expensive, especially given the number of samples required for a full cell study.

Extracellular matrix (ECM) protein adsorption on surfaces was investigated and a link between Fn adsorption onto the GFN-containing LbL constructs and 3T3 SA cell activity and proliferation was identified. However, an extension to this work would be to evaluate whether any similar trends can be seen with other ECM proteins such as vitronectin and laminin to have a more complete adsorption profile. In addition, changes in protein adsorption over time could be monitored and assays performed to assess competitive binding of proteins, to gain a more comprehensive idea of the surface protein environment on each substrate.

Another extension to this research would be to assess any differences in gene expression for adhesion-associated genes using reverse-transcription polymerase chain reaction (RT-PCR). Examples would be integrin, focal adhesion kinase, type I collagen, α-actin, talin and vinculin.[23] Focal adhesion kinase is important in regulating integrin cell signalling for cell survival.[52] Type I collagen is needed to maintain cellular integrity and α-actin is important for cell movement and

modification.[23] This would provide further insight into the response of 3T3 SA cells towards the LbL constructs.

In terms of wound-healing applications, it is important also to assess the adhesion of bacteria to biomaterial surfaces. Graphene has been reported to show antibacterial properties[53,54,55] but, as revealed in this study, the modification of graphene can have a significant effect on cell behaviour. Papers have reported the antibacterial activity of GFN to be dependent on the purity of the GFN,[56] and also on the chemical oxidation level of the GFN.[57] In addition, work by Ostuni *et al.* suggests that the adhesion of bacteria may be facilitated by a layer of adsorbed protein, meaning that biomaterials that resist protein adsorption may be able to prevent bacterial adhesion.[58] This means that, in addition to cell adhesion and biocompatibility studies, bacterial adhesion needs to be assessed on any potential wound healing candidates, prior to their use. Finally, to further assess the suitability of GFN-containing LbL constructs for wound healing applications, the constructs need to be tested on cell types more pertinent to wound healing. For example, it is important to look at whether the effects of the LbL constructs are different for skin fibroblasts and keratinocytes. However, the potential of LbL constructs for wound healing is that, once fully characterised and optimised, 'spray-on' wound dressings would be a possibility.

4.8. References

1. Lu, B. G.; Li, T.; Zhao, H. T.; Li, X. D.; Gao, C. T.; Zhang, S. X.; Xie, E. Q., Graphene-based composite materials beneficial to wound healing. *Nanoscale* **2012,** *4* (9), 2978-2982.
2. Sun, H. J.; Gao, N.; Dong, K.; Ren, J. S.; Qu, X. G., Graphene Quantum Dots-Band-Aids Used for Wound Disinfection. *ACS Nano* **2014,** *8* (6), 6202-6210.
3. Khan, M. S.; Abdelhamid, H. N.; Wu, H. F., Near infrared (NIR) laser mediated surface activation of graphene oxide nanoflakes for efficient antibacterial, antifungal and wound healing treatment. *Colloids and Surfaces B-Biointerfaces* **2015,** *127*, 281-291.

4. Mitra, T.; Manna, P. J.; Raja, S. T. K.; Gnanamani, A.; Kundu, P. P., Curcumin loaded nano graphene oxide reinforced fish scale collagen - a 3D scaffold biomaterial for wound healing applications. *RSC Advances* **2015,** *5* (119), 98653-98665.
5. Li, Z. H.; Wang, H. Q.; Yang, B.; Sun, Y. K.; Huo, R., Three-dimensional graphene foams loaded with bone marrow derived mesenchymal stem cells promote skin wound healing with reduced scarring. *Materials Science & Engineering C-Materials for Biological Applications* **2015,** *57*, 181-188.
6. Lee, C.; Wei, X.; Kysar, J. W.; Hone, J., Measurement of the elastic properties and intrinsic strength of monolayer graphene. *Science* **2008,** *321* (5887), 385-388.
7. Su, Y.; Kravets, V. G.; Wong, S. L.; Waters, J.; Geim, A. K.; Nair, R. R., Impermeable barrier films and protective coatings based on reduced graphene oxide. *Nature Communications* **2014,** *5*, 5843/1-5.
8. Chen, D.; Wang, X. Y.; Liu, T. X.; Wang, X. D.; Li, J., Electrically Conductive Poly(vinyl alcohol) Hybrid Films Containing Graphene and Layered Double Hydroxide Fabricated via Layer-by-Layer Self-Assembly. *ACS Applied Materials & Interfaces* **2010,** *2* (7), 2005-2011.
9. Kwon, S. R.; Jeon, J. W.; Lutkenhaus, J. L., Sprayable, paintable layer-by-layer polyaniline nanofiber/graphene electrodes. *RSC Advances* **2015,** *5* (20), 14994-15001.
10. Kouloumpis, A.; Zygouri, P.; Dimos, K.; Gournis, D., *Layer-by-Layer Assembly of Graphene-Based Hybrid Materials*. 2014; p 359-399.
11. Shen, J.; Hu, Y.; Li, C.; Qin, C.; Shi, M.; Ye, M., Layer-by-Layer Self-Assembly of Graphene Nanoplatelets. *Langmuir* **2009,** *25* (11), 6122-6128.
12. Lee, T.; Min, S. H.; Gu, M.; Jung, Y. K.; Lee, W.; Lee, J. U.; Seong, D. G.; Kim, B. S., Layer-by-Layer Assembly for Graphene-Based Multi layer Nanocomposites: Synthesis and Applications. *Chemistry of Materials* **2015,** *27* (11), 3785-3796.
13. Kim, S. G.; Park, O. K.; Lee, J. H.; Ku, B. C., Layer-by-layer assembled graphene oxide films and barrier properties of thermally reduced graphene oxide membranes. *Carbon Letters* **2013,** *14* (4), 247-250.
14. Thonemann, B.; Schmalz, G.; Hiller, K. A.; Schweikl, H., Responses of L929 mouse fibroblasts, primary and immortalized bovine dental papilla-derived cell lines to dental resin components. *Dental Materials* **2002,** *18* (4), 318-323.
15. Midwood, K. S.; Williams, L. V.; Schwarzbauer, J. E., Tissue repair and the dynamics of the extracellular matrix. *International Journal of Biochemistry & Cell Biology* **2004,** *36* (6), 1031-1037.
16. Fletcher, D. A.; Mullins, D., Cell mechanics and the cytoskeleton. *Nature* **2010,** *463* (7280), 485-492.
17. Tryoen-Toth, P.; Vautier, D.; Haikel, Y.; Voegel, J. C.; Schaaf, P.; Chluba, J.; Ogier, J., Viability, adhesion, and bone phenotype of osteoblast-like cells on polyelectrolyte multilayer films. *Journal of Biomedical Materials Research* **2002,** *60* (4), 657-667.
18. Arima, Y.; Iwata, H., Effect of wettability and surface functional groups on protein adsorption and cell adhesion using well-defined mixed self-assembled monolayers. *Biomaterials* **2007,** *28* (20), 3074-3082.
19. Hirsh, S. L.; McKenzie, D. R.; Nosworthy, N. J.; Denman, J. A.; Sezerman, O. U.; Bilek, M. M. M., The Vroman effect: Competitive protein exchange with dynamic multilayer protein aggregates. *Colloids and Surfaces B-Biointerfaces* **2013,** *103*, 395-404.
20. Harel, Z.; Harel, S.; Shah, P. S.; Wald, R.; Perl, J.; Bell, C. M., Gastrointestinal Adverse Events with Sodium Polystyrene Sulfonate (Kayexalate) Use: A Systematic Review. *American Journal of Medicine* **2013,** *126* (3), 264/1-24.
21. Sergeeva, Y. N.; Huang, T. T.; Felix, O.; Jung, L. R.; Tropel, P.; Viville, S.; Decher, G., What is really driving cell-surface interactions? Layer-by-layer assembled films may help to answer questions concerning cell attachment and response to biomaterials. *Biointerphases* **2016,** *11* (1). 019009/1-14.

22. Horton, E. R.; Humphries, J. D.; James, J.; Jones, M. C.; Askari, J. A.; Humphries, M. J., The integrin adhesome network at a glance. *Journal of Cell Science* **2016,** *129* (22), 4159-4163.
23. Ryoo, S.-R.; Kim, Y.-K.; Kim, M.-H.; Min, D.-H., Behaviors of NIH-3T3 Fibroblasts on Graphene/Carbon Nanotubes: Proliferation, Focal Adhesion, and Gene Transfection Studies. *ACS Nano* **2010,** *4* (11), 6587-6598.
24. Bacakova, L.; Filova, E.; Parizek, M.; Ruml, T.; Svorcik, V., Modulation of cell adhesion, proliferation and differentiation on materials designed for body implants. *Biotechnology Advances* **2011,** *29* (6), 739-767.
25. Wang, Z.; Tonderys, D.; Leggett, S. E.; Williams, E. K.; Kiani, M. T.; Steinberg, R. S.; Qiu, Y.; Wong, I. Y.; Hurt, R. H., Wrinkled, wavelength-tunable graphene-based surface topographies for directing cell alignment and morphology. *Carbon* **2016,** *97*, 14-24.
26. Webb, K.; Hlady, V.; Tresco, P. A., Relative importance of surface wettability and charged functional groups on NIH 3T3 fibroblast attachment, spreading, and cytoskeletal organization. *Journal of Biomedical Materials Research* **1998,** *41* (3), 422-430.
27. Park, K.; Ju, Y. M.; Son, J. S.; Ahn, K.-D.; Han, D. K., Surface modification of biodegradable electrospun nanofiber scaffolds and their interaction with fibroblasts. *Journal of Biomaterials Science-Polymer Edition* **2007,** *18* (4), 369-382.
28. Horbett, T. A.; Schway, M. B.; Ratner, B. D., Hydrophilic-hydrophobic copolymers as cell substrates - Effect on 3T3 cell-growth rates. *Journal of Colloid and Interface Science* **1985,** *104* (1), 28-39.
29. Healy, K. E.; Lom, B.; Hockberger, P. E., Spatial-distribution of mammalian-cells dictated by material surface-chemistry. *Biotechnology and Bioengineering* **1994,** *43* (8), 792-800.
30. Kleinfeld, D.; Kahler, K. H.; Hockberger, P. E., Controlled outgrowth of dissociated neurons on patterned substrates. *Journal of Neuroscience* **1988,** *8* (11), 4098-4120.
31. Georger, J. H.; Stenger, D. A.; Rudolph, A. S.; Hickman, J. J.; Dulcey, C. S.; Fare, T. L., Coplanar patterns of self-assembled monolayers for selective cell-adhesion and outgrowth. *Thin Solid Films* **1992,** *210* (1-2), 716-719.
32. Stenger, D. A.; Georger, J. H.; Dulcey, C. S.; Hickman, J. J.; Rudolph, A. S.; Nielsen, T. B.; McCort, S. M.; Calvert, J. M., Coplanar molecular assemblies of aminoalkylsilane and perfluorinated alkylsilane - characterization and geometric definition of mammalian-cell adhesion and growth. *Journal of the American Chemical Society* **1992,** *114* (22), 8435-8442.
33. Bacakova, L.; Svorcik, V.; Rybka, V.; Micek, I.; Hnatowicz, V.; Lisa, V.; Kocourek, F., Adhesion and proliferation of cultured human aortic smooth muscle cells on polystyrene implanted with N+, F+ and Ar+ ions: Correlation with polymer surface polarity and carbonization. *Biomaterials* **1996,** *17* (11), 1121-1126.
34. Detrait, E.; Lhoest, J. B.; Knoops, B.; Bertrand, P.; de Aguilar, P. V. D., Orientation of cell adhesion and growth on patterned heterogeneous polystyrene surface. *Journal of Neuroscience Methods* **1998,** *84* (1-2), 193-204.
35. Goldstein, I. J.; Hayes, C. E., The lectins: carbohydrate-binding proteins of plants and animals. *Advances in carbohydrate chemistry and biochemistry* **1978,** *35*, 127-340.
36. Jeong, J. T.; Choi, M. K.; Sim, Y.; Lim, J. T.; Kim, G. S.; Seong, M. J.; Hyung, J. H.; Kim, K. S.; Umar, A.; Lee, S. K., Effect of graphene oxide ratio on the cell adhesion and growth behavior on a graphene oxide-coated silicon substrate. *Scientific Reports* **2016,** *6*, 33835/1-10.
37. Ku, S. H.; Park, C. B., Myoblast differentiation on graphene oxide. *Biomaterials* **2013,** *34* (8), 2017-2023.
38. Shi, X. T.; Chang, H. X.; Chen, S.; Lai, C.; Khademhosseini, A.; Wu, H. K., Regulating Cellular Behavior on Few-Layer Reduced Graphene Oxide Films with Well-Controlled Reduction States. *Advanced Functional Materials* **2012,** *22* (4), 751-759.

39. Guo, M. X.; Li, D. J.; Zhao, M. G.; Zhang, Y. T.; Geng, D. S.; Lushington, A.; Sun, X. L., Nitrogen ion implanted graphene as thrombo-protective safer and cytoprotective alternative for biomedical applications. *Carbon* **2013,** *61*, 321-328.
40. Lee, H. J.; Hong, J. K.; Goo, H. C.; Lee, W. K.; Park, K. D.; Kim, S. H.; Yoo, Y. M.; Kim, Y. H., Improved blood compatibility and decreased VSMC proliferation of surface-modified metal grafted with sulfonated PEG or heparin. *Journal of Biomaterials Science-Polymer Edition* **2002,** *13* (8), 939-952.
41. Horbett, T. A.; Schway, M. B., Correlations between mouse 3T3 cell spreading and serum fibronectin adsorption on glass and hydroxyethylmethacrylate-ethylmethacrylate copolymers. *Journal of Biomedical Materials Research* **1988,** *22* (9), 763-793.
42. Ruoslahti, E.; Pierschbacher, M. D., New perspectives in cell-adhesion - RGD and integrins. *Science* **1987,** *238* (4826), 491-497.
43. Wilson, C. J.; Clegg, R. E.; Leavesley, D. I.; Pearcy, M. J., Mediation of biomaterial-cell interactions by adsorbed proteins: A review. *Tissue Engineering* **2005,** *11* (1-2), 1-18.
44. Zelzer, M.; Albutt, D.; Alexander, M. R.; Russell, N. A., The Role of Albumin and Fibronectin in the Adhesion of Fibroblasts to Plasma Polymer Surfaces. *Plasma Processes and Polymers* **2012,** *9* (2), 149-156.
45. Aplin, A. E.; Howe, A.; Alahari, S. K.; Juliani, R. L., Signal transduction and signal modulation by cell adhesion receptors: The role of integrins, cadherins, immunoglobulin-cell adhesion molecules, and selectins. *Pharmacological Reviews* **1998,** *50* (2), 197-263.
46. Hynes, R. O., Integrins - Versatility, modulation, and signaling in cell-adhesion. *Cell* **1992,** *69* (1), 11-25.
47. Rubin, K.; Hook, M.; Obrink, B.; Timpl, R., Substrate adhesion of rat hepatocytes - Mechanism of attachment to collagen substrates. *Cell* **1981,** *24* (2), 463-470.
48. Ostuni, E.; Yan, L.; Whitesides, G. M., The interaction of proteins and cells with self-assembled monolayers of alkanethiolates on gold and silver. *Colloids and Surfaces B-Biointerfaces* **1999,** *15* (1), 3-30.
49. Schlaepfer, D. D.; Hanks, S. K.; Hunter, T.; Vandergeer, P., Integrin-mediated signal-transduction linked to RAS pathway by GRB2 binding to focal adhesion kinase. *Nature* **1994,** *372* (6508), 786-791.
50. Subbiah, R.; Du, P.; Van, S. Y.; Suhaeri, M.; Hwang, M. P.; Lee, K.; Park, K., Fibronectin-tethered graphene oxide as an artificial matrix for osteogenesis. *Biomedical Materials* **2014,** *9* (6), 065003/1-13.
51. Houseman, B. T.; Mrksich, M., Using self-assembled monolayers that present Arg-Gly-Asp peptide ligands to study adhesion of fibroblasts. *Faseb Journal* **1997,** *11* (9), 1095-1095.
52. Mitra, S. K.; Hanson, D. A.; Schlaepfer, D. D., Focal adhesion kinase: In command and control of cell motility. *Nature Reviews Molecular Cell Biology* **2005,** *6* (1), 56-68.
53. Li, J. H.; Wang, G.; Zhu, H. Q.; Zhang, M.; Zheng, X. H.; Di, Z. F.; Liu, X. Y.; Wang, X., Antibacterial activity of large-area monolayer graphene film manipulated by charge transfer. *Scientific Reports* **2014,** *4*, 4359/1-8.
54. Szunerits, S.; Boukherroub, R., Antibacterial activity of graphene-based materials. *Journal of Materials Chemistry B* **2016,** *4* (43), 6892-6912.
55. Zou, X. F.; Zhang, L.; Wang, Z. J.; Luo, Y., Mechanisms of the Antimicrobial Activities of Graphene Materials. *Journal of the American Chemical Society* **2016,** *138* (7), 2064-2077.
56. Barbolina, I.; Woods, C. R.; Lozano, N.; Kostarelos, K.; Novoselov, K. S.; Roberts, I. S., Purity of graphene oxide determines its antibacterial activity. *2D Materials* **2016,** *3* (2), 025025/1-12.
57. Liu, S.; Zeng, T. H.; Hofmann, M.; Burcombe, E.; Wei, J.; Jiang, R.; Kong, J.; Chen, Y., Antibacterial Activity of Graphite, Graphite Oxide, Graphene Oxide, and Reduced Graphene Oxide: Membrane and Oxidative Stress. *ACS Nano* **2011,** *5* (9), 6971-6980.

58. Ostuni, E.; Chapman, R. G.; Liang, M. N.; Meluleni, G.; Pier, G.; Ingber, D. E.; Whitesides, G. M., Self-assembled monolayers that resist the adsorption of proteins and the adhesion of bacterial and mammalian cells. *Langmuir* **2001,** *17* (20), 6336-6343.

5 THE EFFECT OF FUNCTIONALISED GRAPHENE-CONTAINING LAYER-BY-LAYER CONSTRUCTS ON HUMAN MESENCHYMAL STEM CELL FATE

The biocompatibility of PEI/GO, PEI/GO-SO_3 and PEI/G-SO_3 layer-by-layer (LbL) constructs towards 3T3 Swiss Albino (3T3 SA) fibroblasts was compared in Chapter 4, to assess their suitability for wound healing applications. 3T3 SA cells seeded on the PEI/GO and PEI/GO-SO_3 LbL constructs showed higher cell activity than those on PEI/G-SO_3 LbL constructs. The differences in cell activity were attributed to the extent of fibronectin binding on each LbL construct, which dictates the amount of integrin binding to the substrate and therefore cell adhesion and integrin-activated cell signalling. The differences in fibronectin adsorption between the PEI/GO, PEI/GO-SO_3 and PEI/G-SO_3 were thought to arise from a combination of the differences nanoscale roughness and the functional groups present in the terminal layer of the LbL construct.

Human mesenchymal stem cells (hMSCs) are a versatile primary cell type as they are able to differentiate into various cell lineages such as adipocytes, chondrocytes, osteoblasts and neurons, myocytes, fibroblasts, endothelial cells and cardiomyocytes.[1,2] Because of the shortage of donor tissues and organs, there has been increasing interest to develop tissue engineering strategies that can provide a source of cells which are able to differentiate into the desired tissue type.[3] Stem cells can be isolated from many adult tissues,[2,4] meaning that they can provide an alternative option to autologous tissue grafts, for the regeneration of damaged tissues. In addition, the multipotency of stem cells mean that a single source of stem cells can be used to repair a variety of tissues, rather than having to select a healthy tissue to repair the same type of tissue.[2,5] Therefore bioengineered materials which

can support stem cell proliferation or induce stem cells towards specific lineages are useful in tissue engineering applications.

Graphene-family nanomaterials (GFNs) have great potential in tissue engineering applications, as outlined in Chapter 1. For example, the electronic properties of pristine graphene have been explored for use in neurogenesis,[6,7,8,9,10] while the mechanical properties of GFNs have been utilised in many tissue engineering applications,[11,12] including bone regeneration.[13,14] cardiac tissue engineering,[15] cartilage tissue engineering,[16,17] Therefore the interaction of different GFNs and their composites with stem cells is important to evaluate, when considering their use in tissue engineering applications.

Pristine graphene has already been shown to enhance the attachment and differentiation of hMSCs. For example, Kalbacova *et al*. found that CVD derived pristine graphene was able to promote the adhesion and differentiation of hMSCs into osteoblasts.[18] Nayak *et al.* also reported osteogenic differentiation of hMSC in the presence of CVD graphene which was comparable to that observed with the addition of induction media.[19] The osteogenic differentiation of MSCs on pristine graphene is thought to be attributed to its ability to pre-concentrate osteogenic inducers such as β-glycrophosphate.[20] Crowder *et al* also reported the osteogenic differentiation of stem cells in a 3D graphene foam.[21] However, the hydrophobicity of pristine graphene limits its use *in-vivo*, meaning that graphene oxide (GO) has been used widely for osteogenic differentiation.[22,23,24,25] The functionalised graphene sulfonate (G-SO_3) produced in this thesis is more hydrophilic than pristine graphene so has potential for use in composites and implants.

Graphene family nanomaterials (GFNs) have been shown to exhibit different MSC lineages, dependent on functional groups present. For example, GO has been reported to support stem cell growth and adipogenic differentiation lineages, by the interaction of insulin with graphene oxide by electrostatic interactions.[20,26,27] The interaction of pristine graphene and insulin is much weaker, meaning that pristine graphene does not support adipogenesis as strongly.[20] In another example, fluorination of graphene was found to enhance the neuron growth, by enhancing the binding of retinoic acid.[28] It is therefore not known what effect, if any, the edge-functionalisation of graphene will have on stem cell fate. In addition, the incorporation of GO, GO-SO_3 and G-SO_3 into layer-by-layer (LbL) constructs may also alter the fate of stem cells.

The aim of this chapter was to ascertain whether the behaviour of hMSCs are affected by the G-SO_3, GO and GO-SO_3 or by the incorporation of GO, GO-SO_3 and G-SO_3 into the PEI-containing LbL constructs. Bone-marrow derived human mesenchymal stem cells (hMSCs) were cultured on PEI/GO, PEI/GO-SO_3 and PEI/G-SO_3 LbL constructs, with cell viability and activity measured over a 7-day period. In addition, the differentiation lineages of hMSCs on the PEI/GO, PEI/GO-SO_3 and PEI/G-SO_3 LbL constructs were compared, to assess whether the functionalisation of GFNs have an effect on stem cell fate.

The aims of the research discussed in this chapter were to:

- Assess hMSC attachment and proliferation on PEI/GO, PEI/GO-SO_3 and PEI/G-SO_3 LbL constructs.
- Evaluate or determine differences in hMSC attachment, proliferation and activity on PEI/GO, PEI/GO-SO_3 and PEI/G-SO_3 LbL constructs.

- To compare the differentiation of hMSCs cultured onto PEI/GO, PEI/GO-SO_3 and PEI/G-SO_3 LbL constructs.

PEI/GO, PEI/GO-SO_3 and PEI/G-SO_3 LbL constructs were prepared as outlined in materials and methods. LbL constructs were transferred into 24-well plates and were sterilised under UV light for 2 hours, after which hMSCs were seeded at a density of 30,000 cell cm^{-2}. The cells were incubated under standard conditions (37^{O}C, 5% CO_2) and media replenished every 3 days. Initial attachment onto LbL constructs was assessed at 4 hours post-seeding, with additional timepoints at 1 day and 7 days to assess the proliferation and cell activity. LIVE/DEAD staining and AlamarBlue cell viability assays were used to determine patterns in cell attachment and proliferation. Cell morphology and focal adhesions were assessed using antibody staining. The PEI/GO, PEI/GO-SO_3 and PEI/G-SO_3 LbL constructs are referred to collectively as the GFN-containing LbL constructs throughout this chapter.

5.1. Human mesenchymal stem cell attachment and proliferation on LbL constructs

5.1.1. LIVE/DEAD assay

LIVE/DEAD staining was performed on hMSCs seeded onto the LbL constructs at 4 hours, 24 hours and 7 days' post seeding. Representative images are displayed in Figure 5-1, showing clear morphological change between 4 hours and 24 hours of the hMSCs on the control and the PEI/GO and PEI/GO-SO_3 LbL constructs, with cells changing from a rounded to a more elongated shape. There is a clear difference in the shape of hMSCs seeded onto the PEI/G-SO_3 LbL constructs; cells remain rounded after 24 hours. Analysis of hMSC cell shape is outlined in 5.1.3. Furthermore, hMSCs seeded on the control, PEI/GO and PEI/GO-SO_3 LbL

constructs show clear proliferation over the three timepoints, while the hMSCs on the PEI/G-SO_3 LbL construct appear not to proliferate over the time points.

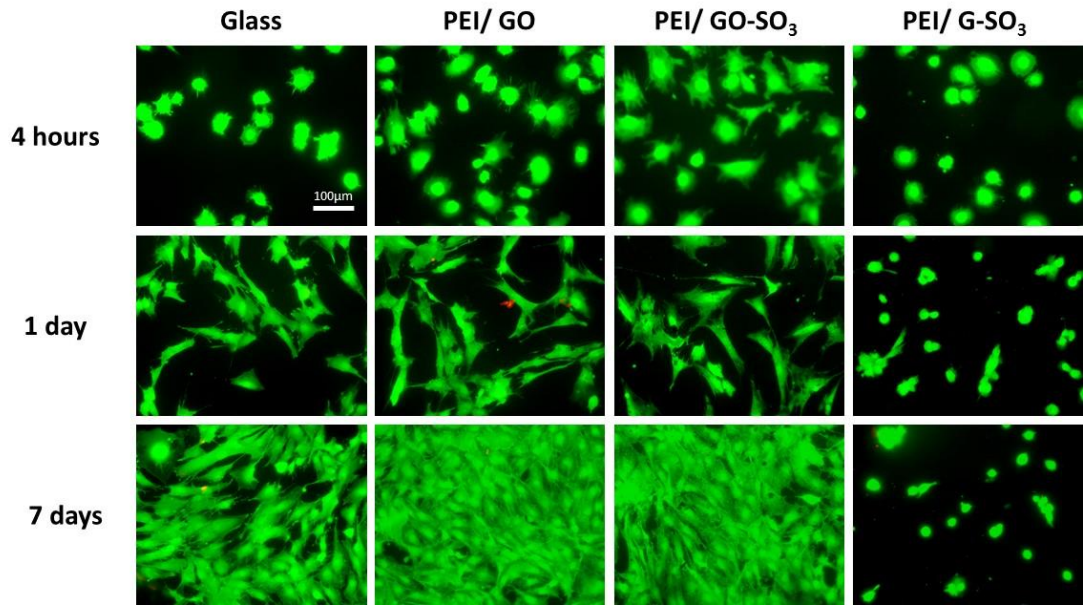

Figure 5-1. LIVE/DEAD Images taken of hMSC cells on LbL constructs, stained with LIVE/DEAD reagent at 4 hours, 1 days and 7 days post-seeding.

5.1.1.1 Cell count

Cell counts were estimated from analysis of several LIVE/DEAD images ($n \geq 14$), with results are displayed in Figure 5-2. There were no significant increases in hMSC cell count on any of the LbL constructs between 4 hours and 1 day post-seeding. There was a significant increase in cell count between 1 day and 7 days post-seeding for hMSCs seeded onto glass, PEI/GO and PEI/GO-SO_3. There was no significant change in cell count for hMSCs on the PEI/G-SO_3 constructs, indicating that the cells did not proliferate over the 7-day test period.

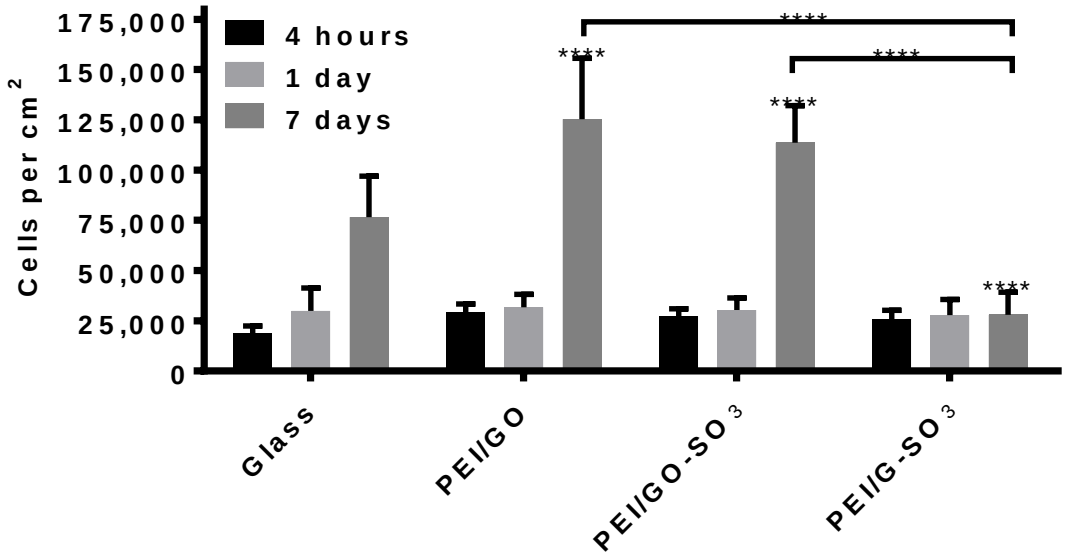

Figure 5-2. Cell count of hMSCs seeded onto LbL constructs. Cell counts were estimated using the ITCN plug in on Image J. Stars above bars show results with statistical significance compared to the control, glass. Significant differences between GFN-containing LbL constructs are indicated by horizontal lines. **** $p \leq 0.0001$, *** $p \leq 0.001$, ** $p \leq 0.01$, * $p < 0.05$.

After 4 hours and 1 day post-seeding there were no significant differences in hMSC cell count on any of the LbL constructs in comparison to the control. After 7 days, hMSCs on the PEI/GO and PEI/GO-SO_3 LbL constructs showed a significantly higher hMSC cell count than on the control, while hMSCs on the PEI/G-SO_3 LbL construct showed a significantly lower cell count than on the control. There were no significant differences in cell count for hMSCs on the GFN-containing LbL constructs at either 4 hours or 1 day post-seeding but, after 7 days, there was a significantly higher hMSC cell count on both PEI/GO and PEI/GO-SO_3 in comparison to PEI/G-SO_3.

The relative increases in cell count between 4 hours and 7 days post-seeding are summarised in Table 5-1.

Table 5-1. Relative increase in cell count for hMSCs

Substrate	Relative cell count increase
Glass	4.1 ± 1.3
PEI/GO	4.3 ± 1.2
PEI/GO-SO_3	4.2 ± 0.9
PEI/G-SO_3	1.1 ± 0.5

The relative increase in cell count did not differ significantly for the hMSCs seeded onto PEI/GO, PEI/GO-SO_3 and glass, but was significantly lower for hMSCs on PEI/G-SO_3. The relative increase in cell count for PEI/G-SO_3 indicates that there is little proliferation of hMSCs on the PEI/G-SO_3 LbL construct over the test period.

5.1.1.2 Cell viability

hMSC cell viability on each LbL construct was calculated from counting the number of live cells (green) and dead cells (red) in all the LIVE/DEAD images. Cell viability percentages at each timepoint are displayed in Figure 5-3. Cell viability remained above 90 % for all time points, on all LbL constructs. The cell viability of hMSCs on glass decreased significantly between 4 hours and 1 day post-seeding, while viability of hMSCs on glass and PEI/GO increased significantly between 1 day and 7 days.

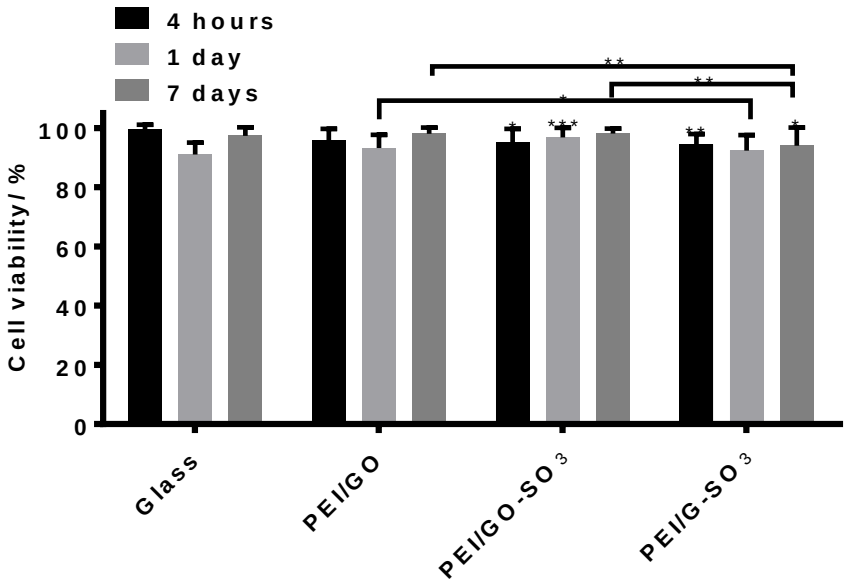

Figure 5-3. Cell viability quantification of hMSCs seeded onto LbL constructs. Stars above bars show results with statistical significance compared to the control, glass. Significant differences between GFN-containing LbL constructs are indicated by horizontal lines. **** $p \leq 0.0001$, *** $p \leq 0.001$, ** $p \leq 0.01$, * $p < 0.05$.

After 4 hours, hMSCs on PEI/GO-SO_3 and PEI/G-SO_3 showed a significantly lower cell viability than on the control, with hMSCs on PEI/GO-SO_3 not differing significantly from the control. After 1 day, only hMSCs on PEI/GO-SO_3 showed a significantly higher cell viability than on the control. After 7 days' post-seeding, hMSCs on PEI/G-SO_3 showed a significantly lower cell viability than on the control. After 4 hours, there were no significant differences in cell viability for hMSCs on the GFN-containing LbL constructs. After 1 day, cells on the PEI/GO-SO_3 construct showed a significantly higher cell viability than those on PEI/G-SO_3 and after 7 days, hMSCs on both PEI/GO and PEI/GO-SO_3 showed a higher cell viability than on PEI/G-SO_3.

5.1.1.3 Cell shape analysis

Cell shape was calculated from analysis of hMSC cells on the LbL constructs ($n \geq 150$ cells), which were stained using the LIVE/DEAD reagent. Cell Profiler software was used, as described in the Materials and Methods section. The average

eccentricity values for hMSCs on the LbL constructs, after 4 hours and 1 day post-seeding, are shown in Figure 5-4. The hMSCs on all LbL constructs showed increased eccentricity, or became more elongated, between 4 hours and 1 day post-seeding.

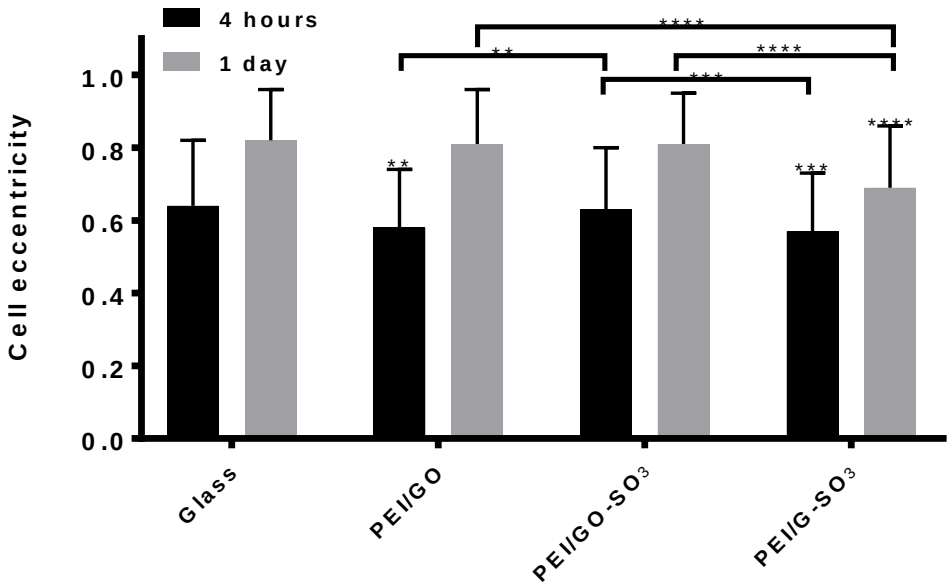

Figure 5-4. Cell shape analysis of hMSC cells, stained with LIVE/DEAD reagent, using CellProfiler software. Stars above bars show results with statistical significance compared to the control, glass. Significant differences between GFN-containing LbL constructs are indicated by horizontal lines. **** $p \leq 0.0001$, *** $p \leq 0.001$, ** $p \leq 0.01$, * $p < 0.05$.

After 4 hours, hMSCs on the PEI/GO LbL and PEI/G-SO_3 construct had a significantly lower cell eccentricity (were more rounded) than the control and, after 1 day, hMSCs on the PEI/G-SO_3 LbL construct had a significantly lower cell eccentricity than the control. There were no other significant differences in cell eccentricity in comparison to the control.

After 4 hours, hMSCs on PEI/GO-SO_3 had a higher cell eccentricity than on PEI/GO and PEI/G-SO_3 while, after 1 day, hMSCs on PEI/GO and PEI/GO-SO_3 showed a significantly higher cell eccentricity than PEI/G-SO_3, therefore indicating more elongated shape of the hMSCs on the PEI/GO and PEI/GO-SO_3 LbL constructs. This is consistent with the images displayed in Figure 5-1, which show the shape of

hMSCs on the PEI/GO and PEI/GO-SO_3 LbL constructs to be elongated after 1 day, in contrast to hMSCs on PEI/G-SO_3, which still appeared rounded.

5.1.1.4 Cell area

The cell area occupied was calculated for hMSCs on each of the LbL constructs after 4 hours and 1 day, to give an average cell area per cell for the hMSCs at early points in cell adhesion and spreading. This can give some indication of cell spreading of the hMSCs on the different LbL constructs. Average cell areas are shown in Figure 5-5. Only hMSCs on the PEI/GO and PEI/GO-SO_3 LbL constructs showed a significant increase in average cell area between 4 hours and 1 day post-seeding. The average hMSC areas on glass and the PEI/G-SO_3 LbL construct did not change significantly between 4 hours and 1 day.

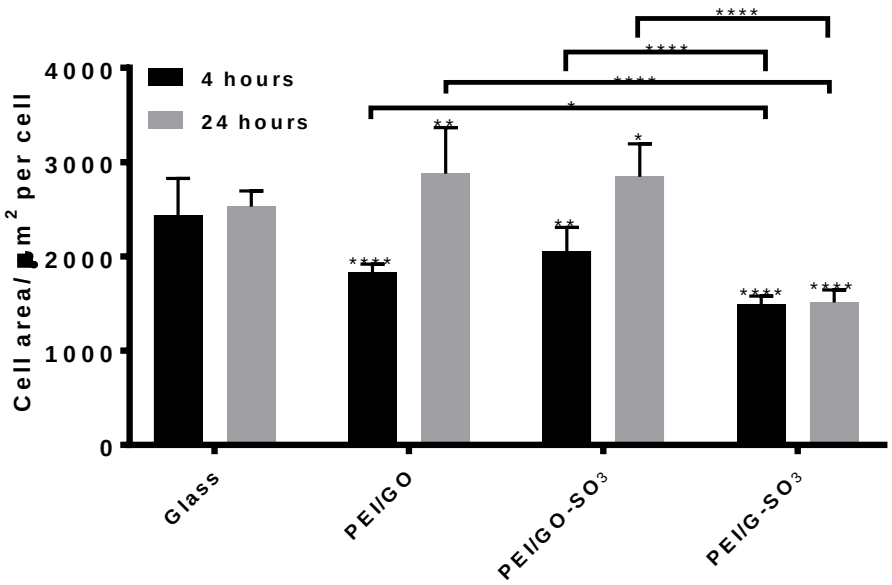

Figure 5-5. Average cell areas per cell for hMSCs seeded onto LbL constructs using CellProfiler software. Stars above bars show results with statistical significance compared to the control, glass. Significant differences between GFN-containing LbL constructs are indicated by horizontal lines. **** $p \leq 0.0001$, *** $p \leq 0.001$, ** $p \leq 0.01$, * $p < 0.05$.

Average cell areas of hMSCs on the PEI/GO, PEI/GO-SO_3 and PEI/G-SO_3 LbL constructs were significantly lower than on the control after 4 hours. After 1 day, however, hMSC cell areas on the PEI/GO, PEI/GO-SO_3 LbL constructs were

significantly higher than on the control, while the average area of hMSCs on the PEI/G-SO_3 LbL construct was significantly lower than on the control.

After 4 hours, the average cell area of hMSCs on the PEI/GO and PEI/GO-SO_3 LbL constructs was significantly higher than for hMSCs on PEI/G-SO_3. After 1 day, the same trend was observed, but with the difference in cell areas more marked. There was, however, no significant difference in hMSCs cell area on PEI/GO and PEI/GO-SO_3 LbL constructs at either 4 hours or 1 day post-seeding.

5.1.2. AlamarBlue assay

In addition to the cell counts, cell viability and cell shape studies, AlamarBlue assays were performed at 4 hours, 1 day and 7 days post-seeding. The AlamarBlue fluorescence intensities (I_{590nm}) are displayed in Figure 5-6. Between 4 hours and 1 day post-seeding, hMSCs on glass and PEI/GO-SO_3 showed a significant increase in cell activity. Between 1 day and 7 days, hMSCs seeded onto all LbL constructs showed a significant increase in cell activity.

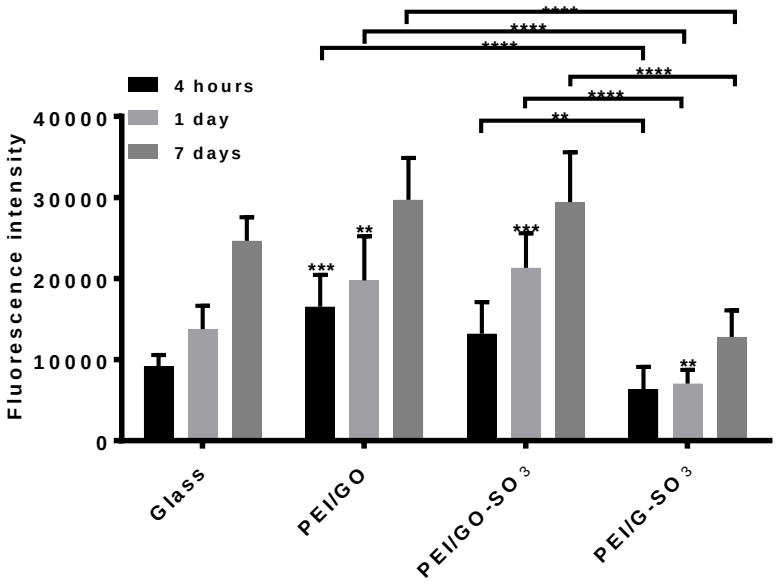

Figure 5-6. AlamarBlue assay for hMSCs seeded onto LbL constructs. Stars above bars show results with statistical significance compared to the control, glass. Significant differences between GFN-containing LbL constructs are indicated by horizontal lines. **** $p \leq 0.0001$, *** $p \leq 0.001$, ** $p \leq 0.01$, * $p < 0.05$.

After 4 hours, PEI/GO had a higher cell activity than the control, but no other significant differences were observed between LbL constructs and the control. After 1 day, hMSCs on the PEI/GO and PEI/GO-SO_3 LbL constructs showed significantly higher cell activity than the control, while hMSCs on PEI/G-SO_3 had a significantly lower cell activity than the control. After 7 days, hMSCs on PEI/GO showed significantly higher cell activity than hMSCs on the control, while PEI/G-SO_3 showed significantly lower cell activity in comparison to the control.

The activities of hMSCs seeded onto the PEI/GO and PEI/GO-SO_3 LbL constructs were higher than hMSCs on the PEI/G-SO_3 LbL constructs at 4 hours, 1 day and 7 days post-seeding, but there was no significant difference between in cell activity between hMSCs on the PEI/GO and PEI/GO-SO_3 constructs at any of the time points.

5.1.3. Focal adhesions, cell morphology and fibronectin staining

The hMSCs were stained with anti-vinculin antibody (conjugated with a FITC-labelled secondary antibody), TRITC-conjugated phalloidin and DAPI, to visualise focal adhesions and the actin cytoskeleton, respectively. Representative staining images are displayed in Figure 5-7. The TRITC-conjugated phalloidin stain, shown in Figure 5-7A, shows the distribution of F-actin in the hMSCs. The hMSCs seeded onto the glass, PEI/GO and PEI/GO-SO_3 show elongated F-actin filaments, while on the PEI/G-SO_3 construct they appear very rounded with much less extension. The anti-vinculin antibody-stained hMSCs, conjugated with a green fluorescent secondary antibody, are shown in Figure 5-7B. The anti-vinculin-stained hMSC images were processed, as described in the Materials and Methods, to highlight the focal adhesions (Fas), and are shown in Figure 5-7C. There appear to be a greater number of FAs for hMSCs on glass, PEI/GO and PEI/GO-SO_3 than for hMSCs on PEI/G-SO_3.

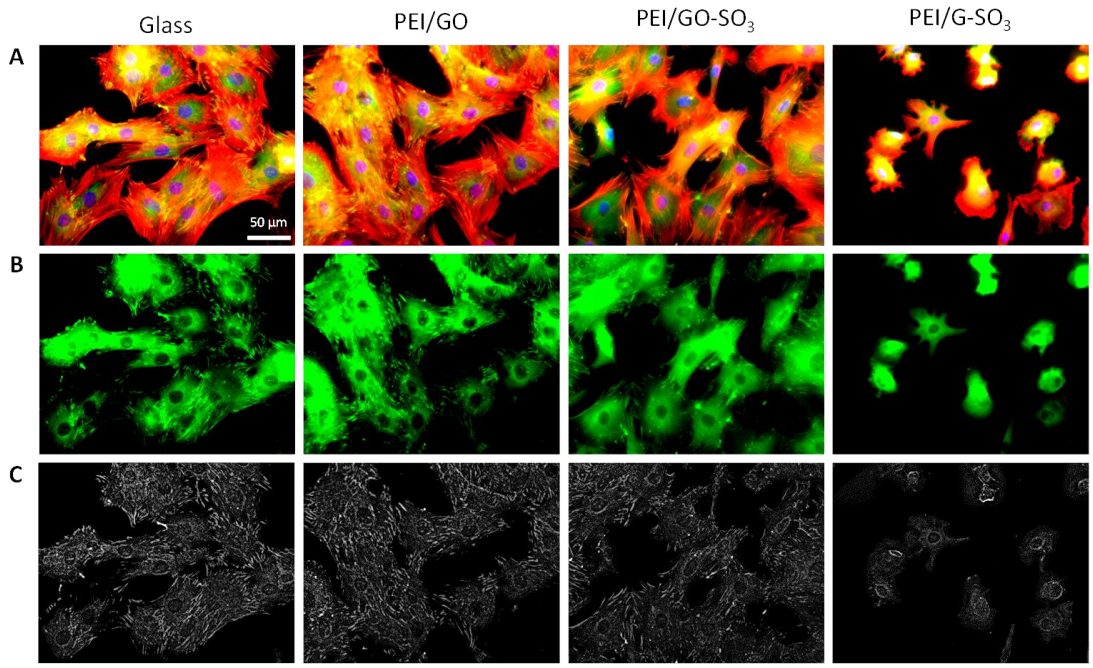

Figure 5-7. A) Composite images of triple stained hMSCs on LbL constructs, at 1 day post-seeding. Vinculin (green), phalloidin (red) and DAPI (blue). B) Green image of vinculin staining. C) Processed green images highlighting focal adhesions. Scale bar represents 50 µm.

The number of FAs was quantified by looking at several processed green images from the vinculin staining (such as those in Figure 5-7C) and calculating the number of FA speckles in the image. This number was normalised to the number of DAPI-stained nuclei in each composite image. The average numbers of FAs per cell are shown in Figure 5-8.

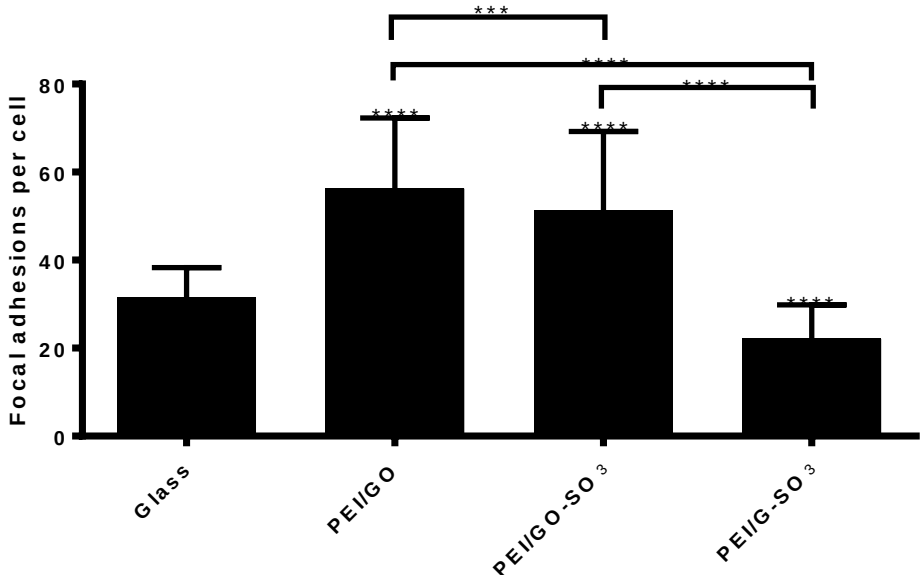

Figure 5-8. The number of focal adhesions per cell of hMSCs on the LbL constructs after 1 day post-seeding. Stars above bars show results with statistical significance compared to the control, glass. Significant differences between GFN-containing LbL constructs are indicated by horizontal lines. **** $p \leq 0.0001$, *** $p \leq 0.001$, ** $p \leq 0.01$, * $p < 0.05$.

The number of FAs per cell for hMSCs, after 1 day post-seeding, were significantly higher on the PEI/GO and PEI/GO-SO_3 LbL constructs than on the control, while for hMSCs on PEI/G-SO_3, the average number of FAs was significantly lower than the control (22 vs. 31 FAs per cell, respectively). There were significantly fewer FAs per cell for hMSCs on the PEI/G-SO_3 LbL construct than on PEI/GO and PEI/GO-SO_3 (22 vs. 56 and 51 FAs per cell, respectively). There were also significantly more FAs per cell for hMSCs on PEI/GO than on PEI/GO-SO_3.

5.2. hMSC growth and proliferation on pre-treated LbL constructs

Pre-treatment of biomaterials surface is often performed before cell seeding to allow cell adhesion proteins additional time to adsorb onto the biomaterial surface and therefore to further encourage cell adhesion. Due to the limited hMSC cell proliferation on the PEI/G-SO_3 LbL construct, pre-treatment of the surfaces with media was performed before cell seeding, to analyse whether this had any effect on hMSC cell activity or proliferation. Surfaces were pre-treated with 200 μL

Dulbecco's modified eagle's medium (4500 g L^{-1} glucose), supplemented with 10 % foetal bovine serum, 1% Antibiotics and antimyotics and 1 % non-essential amino acids.

5.2.1. LIVE/DEAD assay

Representative LIVE/DEAD images of hMSCs on the pre-treated LbL constructs are shown in Figure 5-9. In contrast to the LIVE/DEAD images of the hMSCs on the non-pretreated LbL constructs, there appears to be a denser coverage of cells. In addition, hMSCs on the pre-treated PEI/G-SO_3 LbL construct begin to adopt a more elongated and typical hMSC morphology after 1 day post-seeding, in contrast to non-pretreated samples (Figure 5-1), in which the hMSCs remained very rounded on the PEI/G-SO_3 LbL construct.

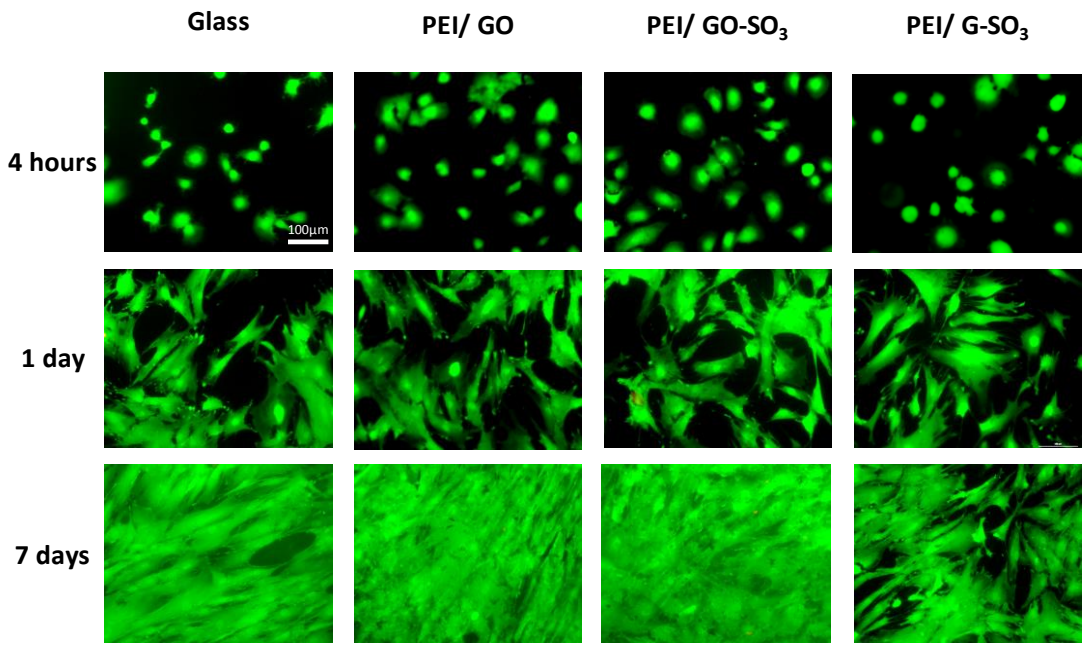

Figure 5-9. LIVE/DEAD images of hMSCs on pre-treated LbL constructs at 4 hours, 1 day and 7 days post-seeding. Pre-treatment conditions: 90 mins' incubation of constructs with 200 µL 'hMSC media' (DMEM +1% antibiotics and antimyotics, 10% FBS, 1% non-essential amino acids)**.**

However, several images of hMSCs on the pre-treated PEI/G-SO_3 LbL construct at 7 days post-seeding are presented in Figure 5-10 revealing that, although many of the

hMSCs are more elongated as a result of pre-treatment with media, there are still several areas on the pre-treated PEI/G-SO_3 LbL construct where hMSCs remain rounded and do not adopt the typical elongated morphology of hMSCs. Therefore, the pre-treatment can somewhat counter the effects of the underlying substrate and help to encourage cell adhesion, the surface is still not homogeneously covered with hMSCs after 7 days.

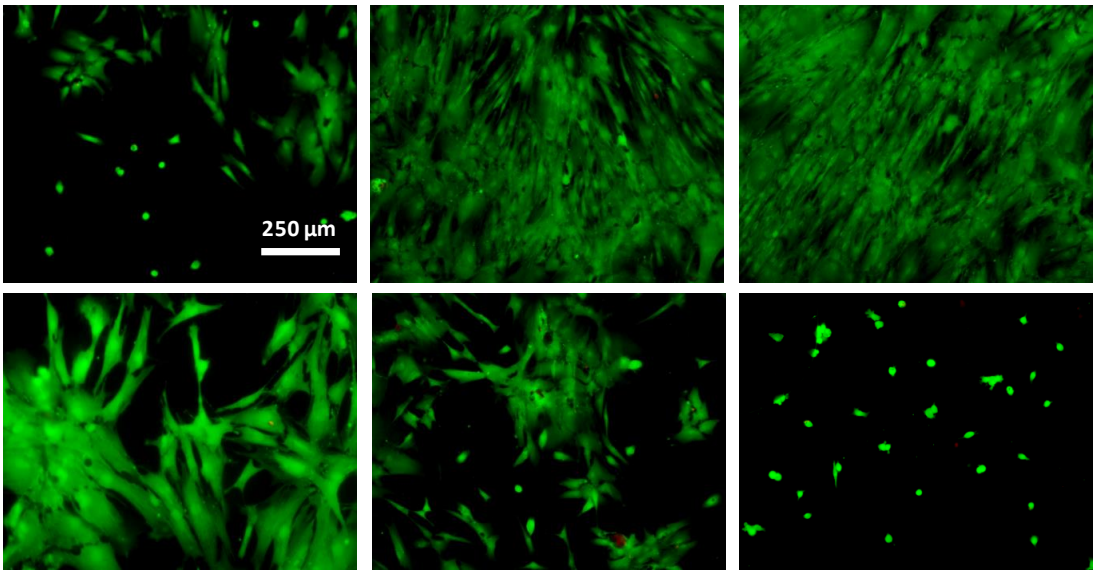

Figure 5-10. Selected LIVE/DEAD images of images of hMSCs on pre-treated PEI/G-SO_3 LbL constructs, at 7 days post-seeding. Pre-treatment conditions: 90 mins' incubation of constructs with 200 µL 'hMSC media' (DMEM +1% antibiotics and antimyotics, 10% FBS, 1% non-essential amino acids).

5.2.1.1 Cell counts

Cell counts for hMSCs seeded onto pre-treated LbL constructs were calculated from LIVE/DEAD images and are displayed in Figure 5-11. There was a significant increase in hMSC cell count on all pre-treated LbL constructs over the 7-day test period. No significant differences in hMSC cell counts were observed on pre-treated LbL constructs after 4 hours and 1 day post-seeding, in comparison to the pre-treated control. However, after 7 days hMSCs on the pre-treated PEI/GO and PEI/GO-SO_3 LbL constructs showed a significantly higher cell counts than the pre-treated control.

The calculated cell count was not found to differ significantly between pre-treated PEI/G-SO_3 and the pre-treated control.

There were no significant differences in cell count for hMSCs on the pre-treated PEI/GO, PEI/GO-SO_3 and PEI/G-SO_3 LbL constructs after 4 hours or 1 day post-seeding. However, after 7 days, the hMSC cell counts were significantly higher on the pre-treated PEI/GO and PEI/GO-SO_3 LbL constructs than on PEI/G-SO_3. The hMSC cell counts on pre-treated PEI/GO and PEI/GO-SO_3 did not differ significantly after 7 days post-seeding.

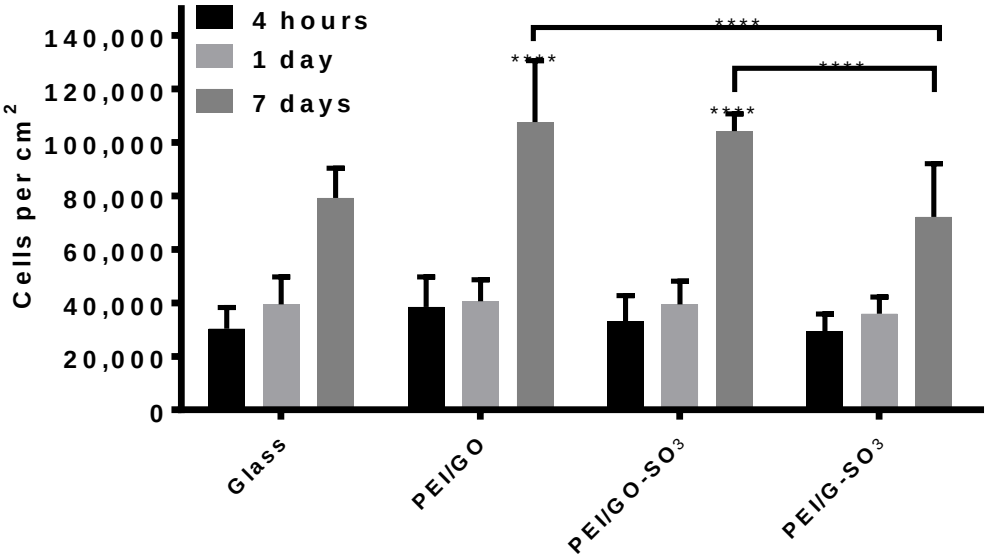

Figure 5-11. Cell count of hMSC seeded onto pre-treated LbL constructs. Stars above bars show results with statistical significance compared to the control, glass. Significant differences between GFN-containing LbL constructs are indicated by horizontal lines. **** $p \leq 0.0001$, *** $p \leq 0.001$, ** $p \leq 0.01$, * $p < 0.05$.

Figure 5-12 displays the comparative cell counts for hMSCs on untreated and pre-treated LbL constructs. After 4 hours, only hMSCs on glass and PEI/GO showed a significant increase in cell count as a result of pre-treatment. After 1 day, hMSCs on all LbL constructs exhibited an increase in cell count as a result of pre-treatment. After 7 days, however, only hMSCs on PEI/G-SO_3 showed a significant increase in cell count as a result of pre-treatment, with PEI/GO showing a lower cell count.

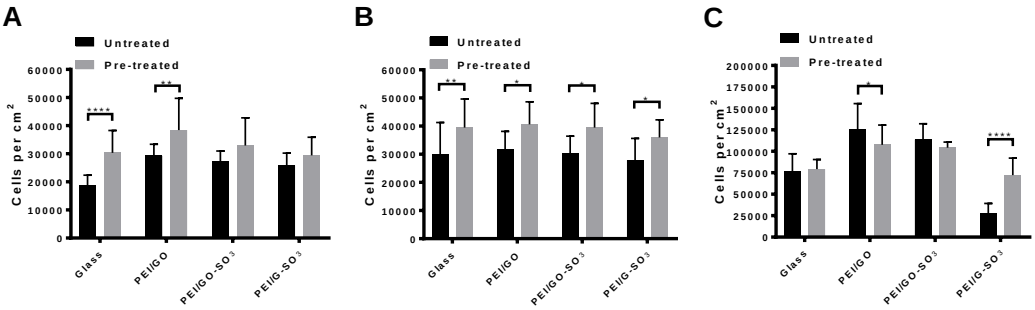

Figure 5-12. Cell counts of hMSCs on untreated and pre-treated LbL constructs at A) 4 hours B) 1 day and C) 7 days, post seeding. Vertical lines indicate significant differences between untreated and pre-treated LbL constructs. **** $p \leq 0.0001$, *** $p \leq 0.001$, ** $p \leq 0.01$, * $p < 0.05$.

5.2.1.2 Cell viability

Average cell viabilities for hMSCs seeded onto pre-treated LbL constructs are displayed in Figure 5-13. The hMSC cell viability remained above 95% on all pre-treated LbL constructs over the 7-day test period. Furthermore, there were no significant changes in hMSC viability on pre-treated LbL constructs over the test period. There were no significant differences in hMSC viability on any of the pre-treated LbL constructs in comparison to the pre-treated control, at any of the time points. The only significant difference in cell viability observed was after 4 hours, at which point hMSCs on the pre-treated PEI/GO LbL constructs showed a higher viability than on pre-treated PEI/G-SO_3.

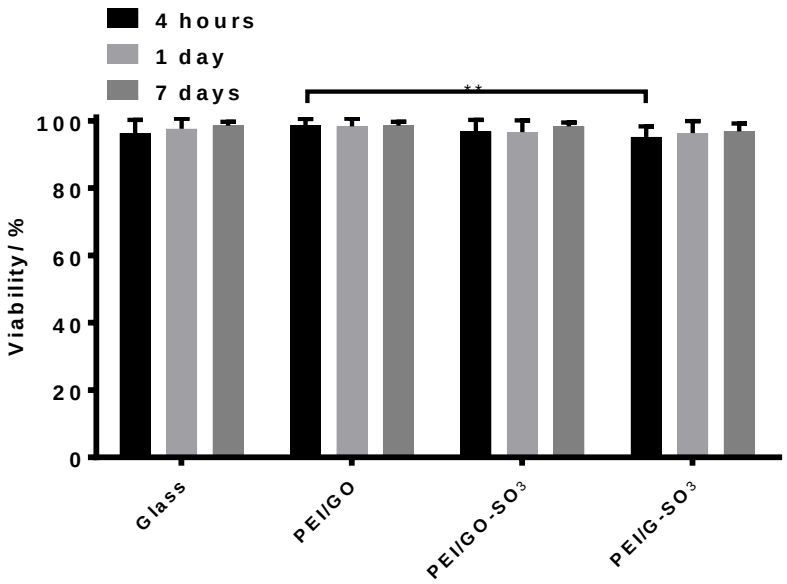

Figure 5-13. Viability of hMSC seeded onto pre-treated LbL constructs. Stars above bars show results with statistical significance compared to the control, glass. Significant differences between GFN-containing LbL constructs are indicated by horizontal lines. **** $p \leq 0.0001$, *** $p \leq 0.001$, ** $p \leq 0.01$, * $p < 0.05$.

Comparative hMSC cell viabilities on untreated and pre-treated LbL constructs are shown in Figure 5-14.

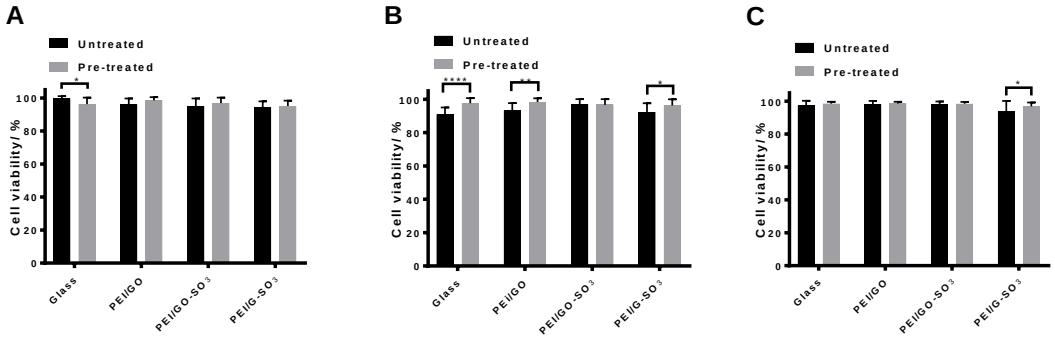

Figure 5-14. Cell viabilities of hMSCs seeded onto untreated and pre-treated LbL constructs after A) 4 hours B) 1 day and C) 7 days post-seeding. Vertical lines indicate significant differences between untreated and pre-treated LbL constructs. **** $p \leq 0.0001$, *** $p \leq 0.001$, ** $p \leq 0.01$, * $p < 0.05$.

After 4 hours, hMSC cell viability was lower on pre-treated glass than untreated glass. After 1 day, the hMSC cell viability was significantly higher on pre-treated glass, PEI/GO and PEI/G-SO_3 than on untreated constructs. After 7 days, hMSCs on pre-treated PEI/G-SO_3 showed higher cell viability than on untreated PEI/G-SO_3.

5.2.1.3 Cell shape analysis

Cell shape analysis was performed on hMSC cells seeded on to pre-treated LbL constructs, to assess changes in cell morphology during the early stages of adhesion. The average cell eccentricities are shown in Figure 5-15. There is a significant increase in cell eccentricity between 4 hours and 1 day for hMSCs on all pre-treated LbL constructs.

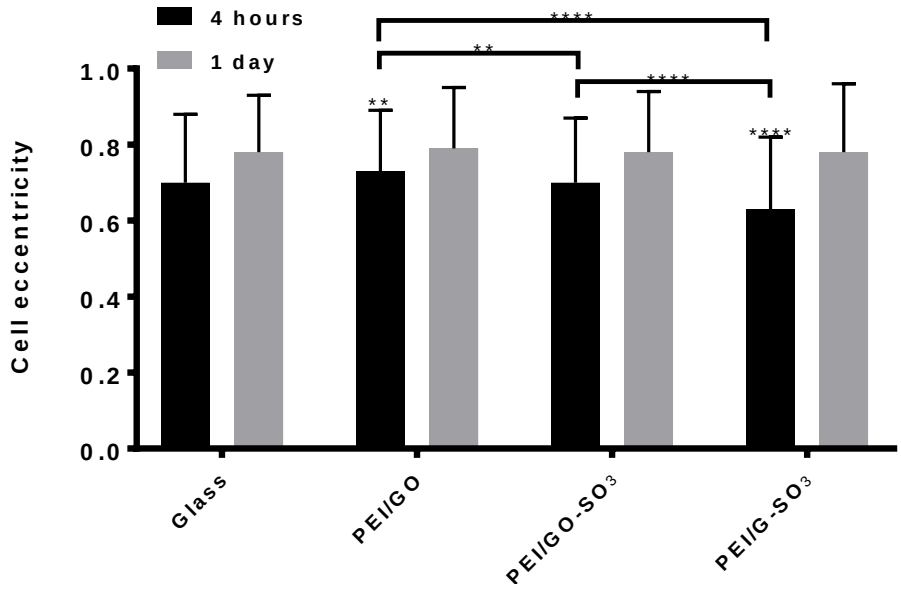

Figure 5-15. Cell shape analysis of hMSC cells seeded onto pre-treated LbL constructs, stained with LIVE/DEAD reagent, and analysed using CellProfiler software. Stars above bars show results with statistical significance compared to the control, glass. Significant differences between GFN-containing LbL constructs are indicated by horizontal lines. **** $p \leq 0.0001$, *** $p \leq 0.001$, ** $p \leq 0.01$, * $p < 0.05$.

There was a significantly higher average cell eccentricity for hMSCs on the pre-treated PEI/GO LbL construct in comparison to the pre-treated control after 4 hours, indicating a more elongated morphology. The average cell eccentricity of hMSCs on the pre-treated PEI/G-SO_3 LbL constructs was significantly lower than on the pre-treated control after 4 hours. However, after 1 day there were no significant differences in hMSC cell eccentricity on any of the pre-treated LbL constructs in comparison to the pre-treated control.

The hMSCs seeded onto the pre-treated PEI/GO and PEI/GO-SO_3 LbL constructs showed significantly higher average cell eccentricities than on pre-treated PEI/G-SO_3 after 4 hours, but after 1 day no significant difference was observed. The average cell eccentricity of hMSCs seeded on the pre-treated PEI/GO LbL construct was significantly higher than on pre-treated PEI/GO-SO_3 after 4 hours, but after 1 day no significant difference was observed.

The relative cell eccentricities on untreated and pre-treated LbL constructs can be seen in Figure 5-16. After 4 hours, the hMSC cell eccentricity was significantly higher on all pre-treated LbL constructs than untreated LbL constructs. However, after 1 day, only the cell eccentricity of hMSCs on PEI/G-SO_3 was significantly higher because of pre-treatment, with the eccentricity of hMSCs on glass and PEI/GO-SO_3 lower because of pre-treatment.

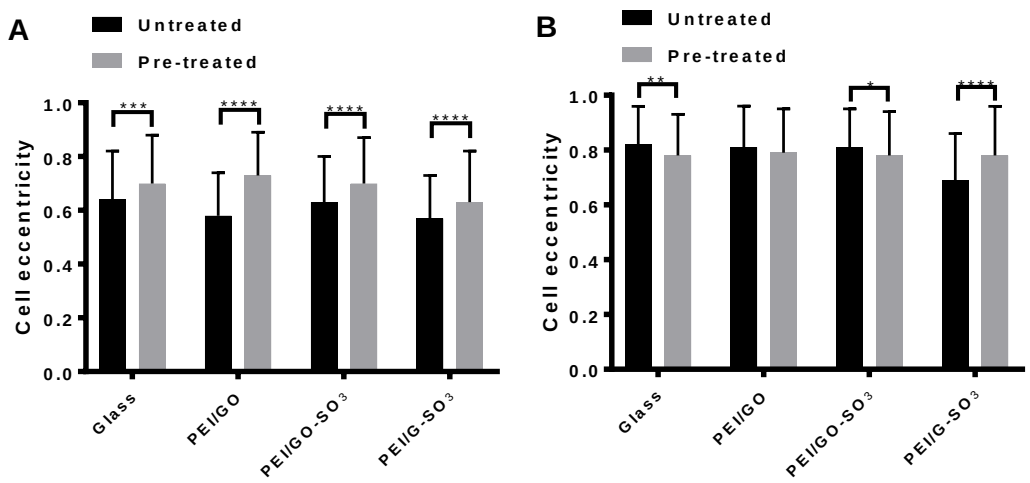

Figure 5-16. Cell shape analysis of hMSC cells seeded onto untreated and pre-treated LbL constructs after A) 4 hours B) 1 day. Vertical lines indicate significant differences between untreated and pre-treated LbL constructs. **** $p \leq 0.0001$, *** $p \leq 0.001$, ** $p \leq 0.01$, * $p < 0.05$.

5.2.1.4 Cell area

The average cell area was analysed for hMSCs seeded onto pre-treated LbL constructs with data shown in Figure 5-17. The hMSCs on all pre-treated LbL

constructs showed a significant increase in cell area between 4 hours and 1 day post-seeding. The hMSCs on the pre-treated PEI/GO and PEI/GO-SO_3 LbL constructs showed a significantly higher average cell area than on the pre-treated control after 4 hours and 1 day post-seeding. There were no significant differences in average cell area between hMSCs on the pre-treated PEI/G-SO_3 construct and the pre-treated control for either time point. The average cell areas for hMSCs on pre-treated PEI/GO and PEI/GO-SO_3 LbL constructs was significantly higher than for those on pre-treated PEI/G-SO_3 after both 4 hours and 1 day post-seeding. There were no significant differences in cell area between hMSCs on pre-treated PEI/GO and PEI/GO-SO_3.

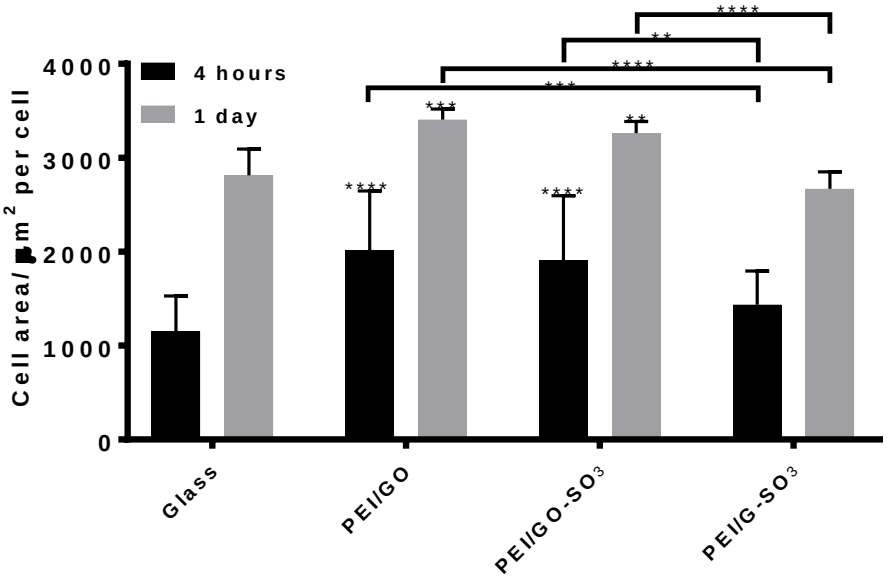

Figure 5-17. Average cell areas for hMSCs seeded onto pre-treated LbL constructs. Stars above bars show results with statistical significance compared to the control, glass. Significant differences between GFN-containing LbL constructs are indicated by horizontal lines. **** $p \leq 0.0001$, *** $p \leq 0.001$, ** $p \leq 0.01$, * $p < 0.05$.

The comparative cell areas of hMSCs on untreated and pre-treated LbL constructs are shown in Figure 5-18. After 4 hours, the cell area of hMSCs on pre-treated glass was significantly lower than on untreated glass, with no other significant differences

observed. After 1 day, the cell area of hMSCs on all pre-treated LbL constructs were higher than on untreated surfaces.

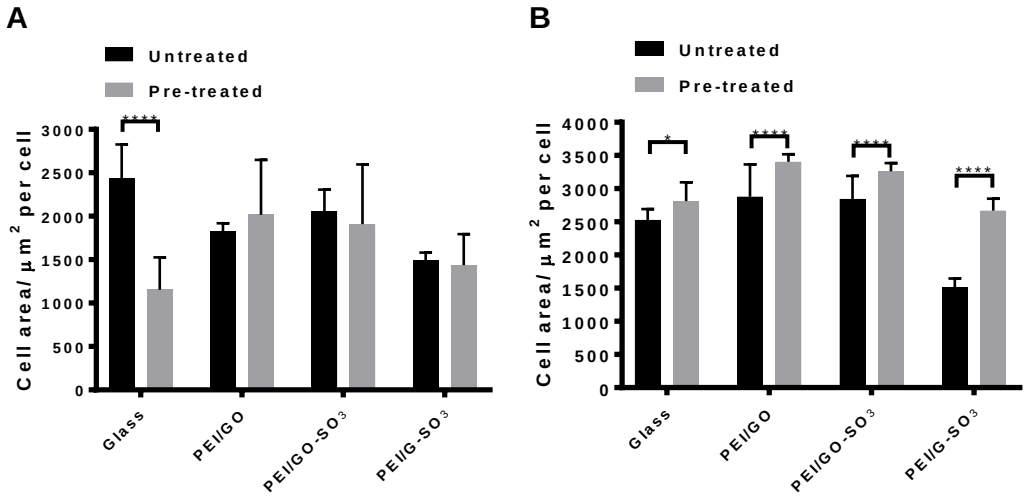

Figure 5-18. Cell area of hMSCs on untreated and pre-treated LbL constructs after A) 4 hours and B) 1 day. Vertical lines indicate significant differences between untreated and pre-treated LbL constructs. **** $p \leq 0.0001$, *** $p \leq 0.001$, ** $p \leq 0.01$, * $p < 0.05$.

After 4 hours, the cell area of hMSCs on pre-treated glass was significantly lower than on untreated glass, with no other significant differences observed. After 1 day, the cell area of hMSCs on all pre-treated LbL constructs were higher than on untreated surfaces.

5.2.2. AlamarBlue assay

The AlamarBlue cell activity assay was performed on hMSCs seeded onto pre-treated LbL constructs, with the fluorescence intensities shown in Figure 5-19. Between 4 hours and 1 day, only hMSCs seeded onto pre-treated PEI/GO LbL constructs showed a significant increase in cell activity, but between 1 day and 7 days, hMSCs on the all pre-treated LbL constructs showed an increase in cell activity.

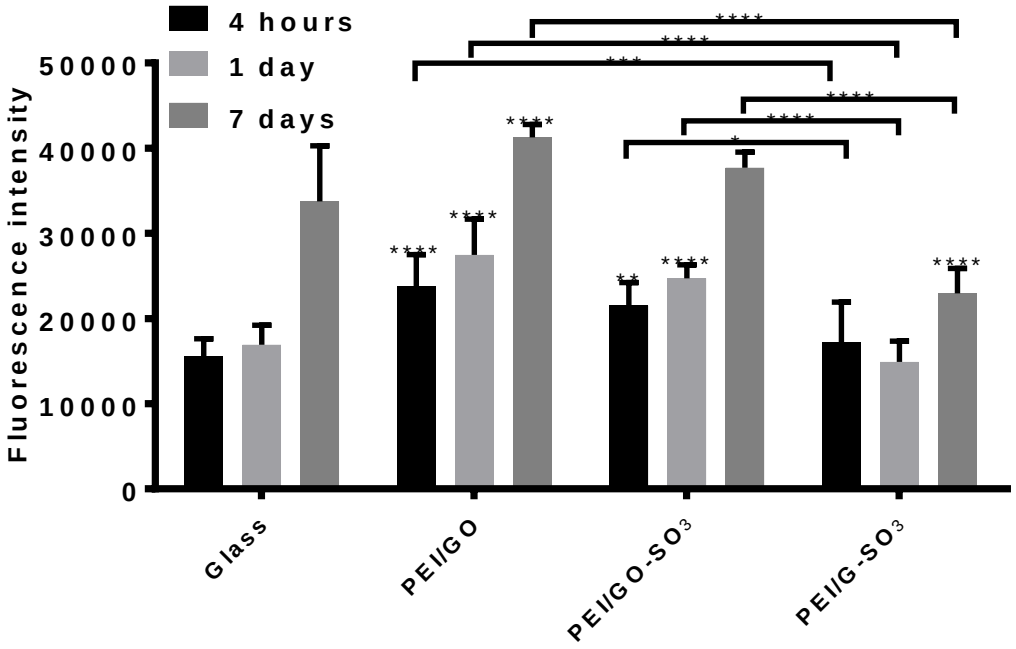

Figure 5-19. AlamarBlue assay for hMSCs seeded onto pre-treated LbL constructs. Stars above bars show results with statistical significance compared to the control, glass. Significant differences between GFN-containing LbL constructs are indicated by horizontal lines. **** $p \leq 0.0001$, *** $p \leq 0.001$, ** $p \leq 0.01$, * $p < 0.05$.

After 4 hours, hMSCs on pre-treated PEI/GO and PEI/GO-SO_3 LbL constructs showed a significantly higher cell activity than on the pre-treated control. After 1 day, hMSCs on pre-treated PEI/GO and PEI/GO-SO_3 LbL constructs showed a significantly higher cell activity than on the pre-treated control. After 7 days, hMSCs on the pre-treated PEI/GO LbL constructs showed a significantly higher cell activity than on the pre-treated control, while hMSCs on PEI/G-SO_3 constructs showed a significantly lower activity.

The hMSCs on pre-treated PEI/GO and PEI/GO-SO_3 LbL constructs showed higher cell activity than those on pre-treated PEI/G-SO_3 LbL constructs after 4 hours, 1 day and 7 days. The comparative cell activity on untreated and pre-treated LbL constructs is shown in Figure 5-20.

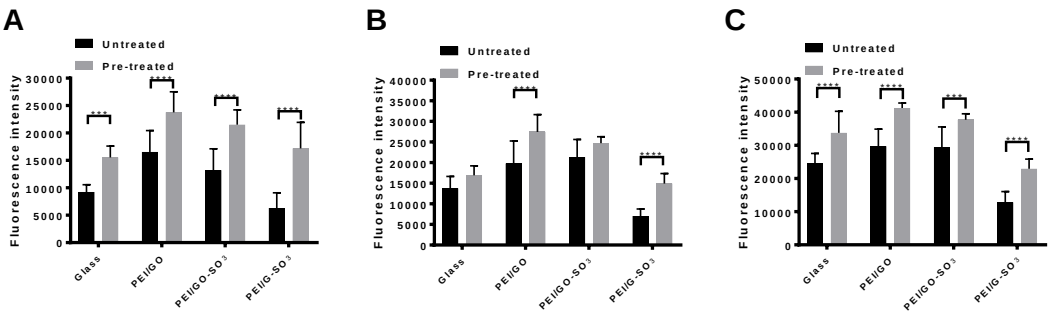

Figure 5-20. AlamarBlue assay for hMSCs on untreated and pre-treated LbL constructs after A) 4 hours B) 1 day and C) 7 days. Vertical lines indicate significant differences between untreated and pre-treated LbL constructs. **** $p \leq 0.0001$, *** $p \leq 0.001$, ** $p \leq 0.01$, * $p < 0.05$.

After 4 hours, all LbL constructs showed higher fluorescence intensity (hence cell activity) on pre-treated vs. untreated substrates. After 1 day, only the cell activity on PEI/GO and PEI/G-SO_3 differed significantly between untreated and pre-treated surfaces. After 7 days, the hMSC cell activity on all LbL constructs was higher on pre-treated vs. untreated substrates.

5.2.3. Focal adhesions, cell morphology and fibronectin staining

The hMSCs seeded on to pre-treated LbL constructs were stained, at 1 day post-seeding, with TRITC-conjugated phalloidin, anti-vinculin antibody (with a green fluorescent secondary antibody) and DAPI, to stain the actin cytoskeleton, focal adhesions and nuclei, respectively. Triply-stained hMSCs are shown in Figure 5-21A, the anti-vinculin stain in Figure 5-21B and processed focal adhesions in Figure 5-21C.

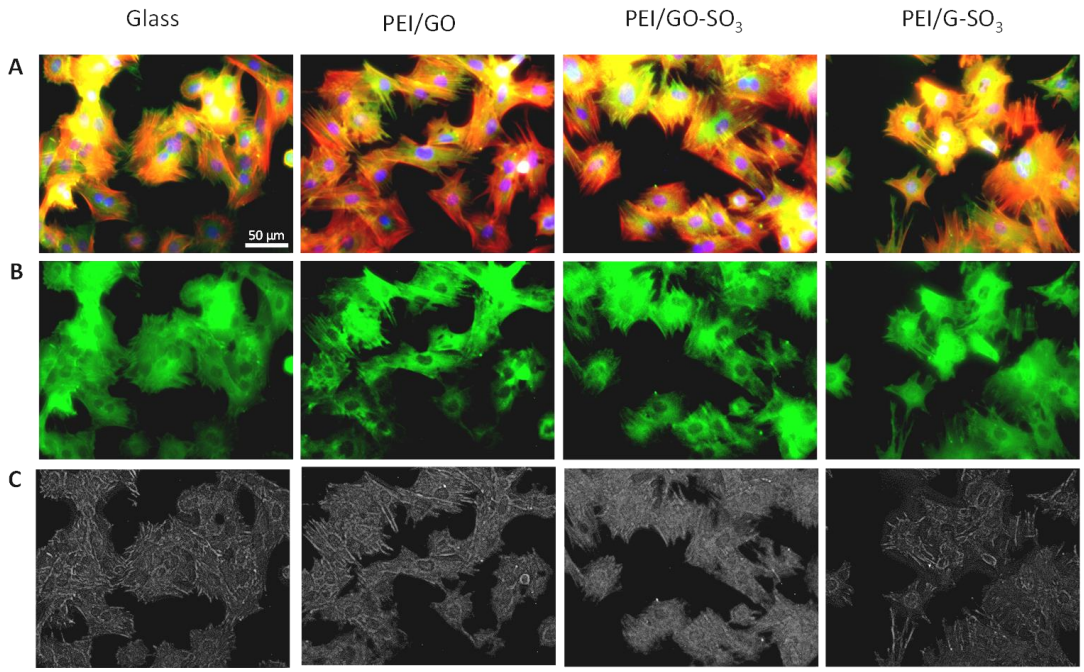

Figure 5-21. A) Composite images of triple stained hMSCs on pre-treated LbL constructs, at 1 day post-seeding. Vinculin (green), phalloidin (red) and DAPI (blue). B) Green image of vinculin staining. C) Processed green images highlighting focal adhesions. Scale bar represents 50 µm.

Focal adhesions (FAs) were quantified by analysing a series of processed anti-vinculin stains of hMSCs on the pre-treated LbL constructs. The number of FAs was normalised to the number of DAPI stained nuclei in the composite image. Average FAs per cell on the pre-treated LbL constructs are summarised in Figure 5-22. The average number of FAs per cell was higher for hMSCs on pre-treated PEI/GO and PEI/GO-SO_3 LbL constructs than on the pre-treated control. The average number of FAs for hMSCs on the pre-treated PEI/G-SO_3 LbL construct was significantly lower than on the pre-treated control.

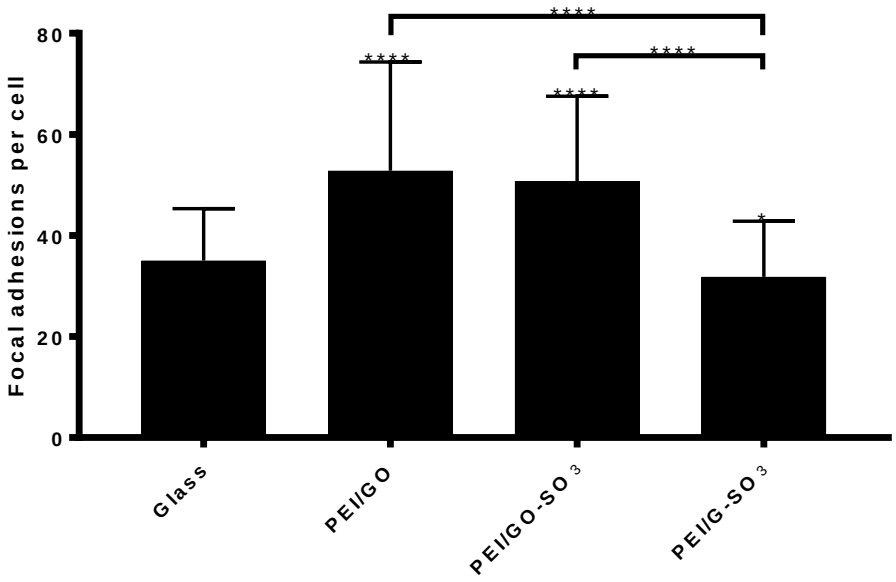

Figure 5-22. Focal adhesion quantification for hMSCs seeded onto pre-treated LbL constructs, at 1 day post-seeding. Stars above bars show results with statistical significance compared to the control, glass. Significant differences between GFN-containing LbL constructs are indicated by horizontal lines. **** $p \leq 0.0001$, *** $p \leq 0.001$, ** $p \leq 0.01$, * $p < 0.05$.

There was a significantly higher number of FAs for hMSCs on pre-treated PEI/GO and PEI/GO-SO_3 than on pre-treated PEI/G-SO_3. There was so significant difference in the number of FAs per cell for hMSCs on pre-treated PEI/GO and pre-treated PEI/GO-SO_3. The comparative FAs per cell on untreated and pre-treated LbL constructs can be seen in Figure 5-23. The number of FAs per cell was significantly higher for hMSCs on pre-treated glass, and PEI/G-SO_3 than on the untreated surfaces, whereas the number of FAs per cell for hMSCs on pre-treated PEI/GO was lower than that on untreated PEI/GO.

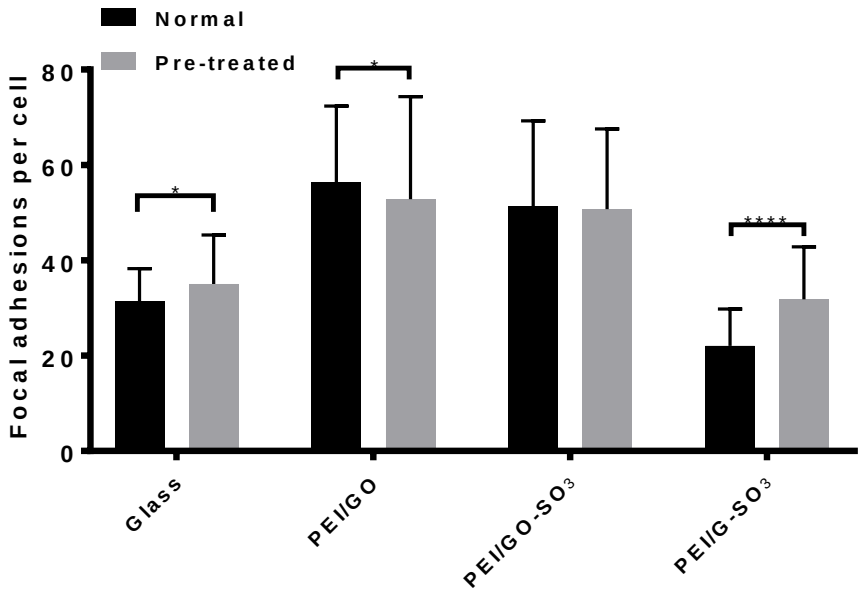

Figure 5-23. Focal adhesion quantification of the untreated and pre-treated LbL constructs after 1 day. Vertical lines indicate significant differences between untreated and pre-treated LbL constructs. **** $p \leq 0.0001$, *** $p \leq 0.001$, ** $p \leq 0.01$, * $p < 0.05$.

5.3 Differentiation of hMSCs on GFN-containing LbL constructs

Motivated by the observed differences in hMSC cell adhesion and proliferation on the GFN-containing LbL constructs, the adipogenic and osteogenic differentiation of hMSCs on the LbL constructs was compared.

5.3.1. Adipogenic differentiation

The adipogenic differentiation of hMSCs on the PEI/GO, PEI/GO-SO_3 and PEI/G-SO_3 was assessed using the Oil Red O lipid stain, to test for the presence of lipids. Oil Red O staining was performed at 7 days, 14 days and 21 days after the addition of adipogenic media, with simultaneous staining of hMSCs grown in cultured in normal media in the place of adipogenic media. Representative images of the Oil Red O stains for hMSCs on PEI/GO, PEI/GO-SO_3 and PEI/G-SO_3 in the presence and absence of adipogenic media are displayed in Figure 5-24 and Figure 5-25, respectively.

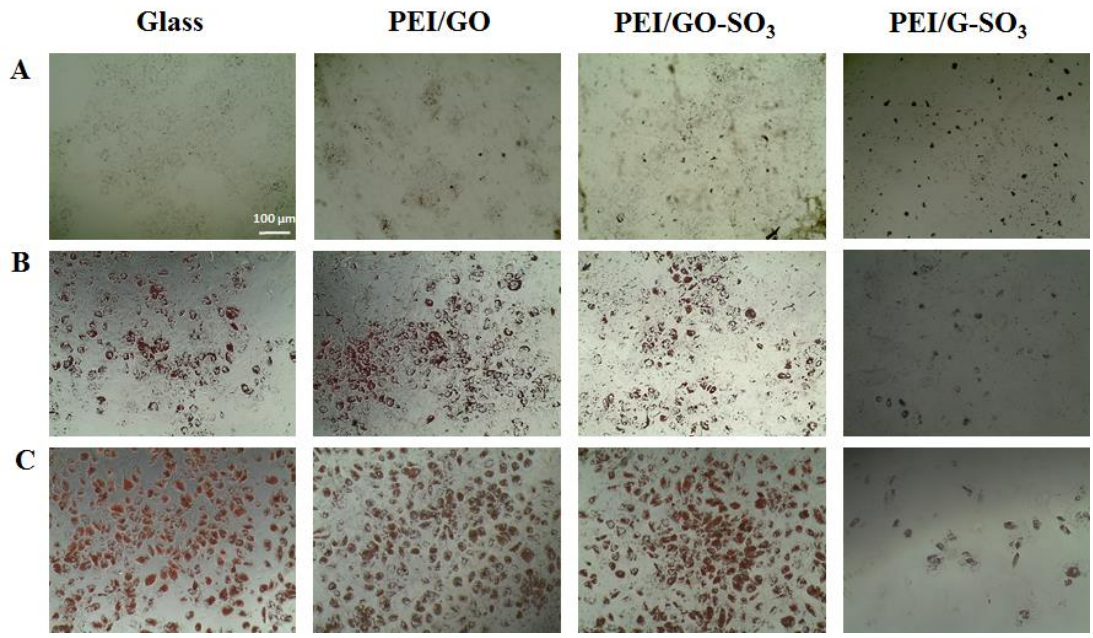

Figure 5-24. Oil Red O lipid staining of hMSCs on GFN-containing LbL constructs, after incubation with adipogenic induction media for A) 7 days B) 14 days and C) 21 days. Scale is the same for all images.

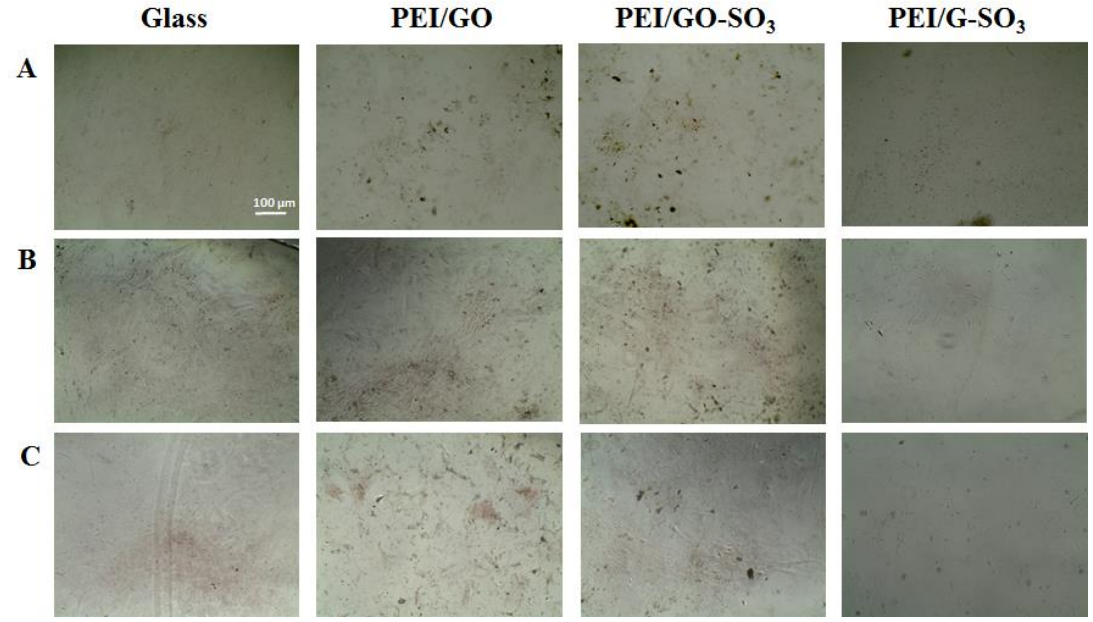

Figure 5-25. Oil Red O lipid staining of hMSCs on GFN-containing LbL constructs, after incubation with standard (non-induction) media for A) 7 days B) 14 days and C) 21 days. Scale is the same for all images.

In the presence of adipogenesis media, hMSCs on PEI/GO, PEI/GO-SO_3 and PEI/G-SO_3 showed positive staining for lipids after 14 days, as seen in Figure 5-24. The number of cells positively stained for lipids was higher for hMSCs on the PEI/GO and PEI/GO-SO_3 LbL constructs than on PEI/G-SO_3. In the absence of

adipogenesis media, there was no significant positive staining for lipids after 21 days, as seen in Figure 5-25. Therefore, the PEI/GO and PEI/GO-SO_3 support the adipogenesis of hMSCs in the presence of induction media, but the surfaces alone are not sufficiently inductive to drive differentiation spontaneously without chemical cues.

Many of the cells on the PEI/G-SO_3 substrate delaminated over the test period, with most of the remaining cells distributed close to the edges of the LbL construct. The peeling of the PEI/G-SO_3 LbL construct became apparent during the extended differentiation study. This is most likely due to the weaker interactions between the layers for this LbL construct. In addition, when doing performing the imaging of Oil Red O stained cells, the only cells were positively stained on the PEI/G-SO_3 construct were found predominantly near to the edges of the coverslips. This may be due to the stronger adhesion nearer to the contact point to the surrounding tissue culture plastic of the wells. the positive staining on this LbL construct is not representative of the whole surface.

The calculated area of positively-stained cells on the LbL constructs was calculated as a percentage of the image. This was calculated at 14 days and 21 days, post-induction, as no cells showed positive staining after 7 days. The percentage areas stained by cells is shown in Figure 5-26 and was calculated by comparing the area positively stained with Oil Red O as a percentage of the total area of the images. The PEI/G-SO_3 area was not calculated because, as previously mentioned, the positively stained areas only occurred on the periphery of the LbL construct, meaning that they were not representative of the substrate as a whole.

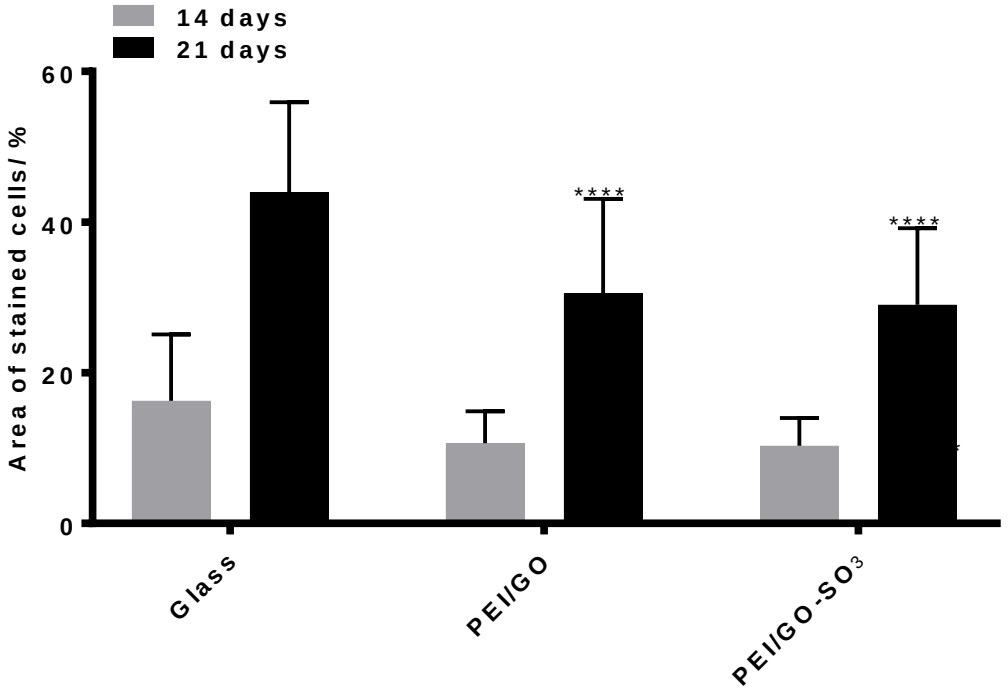

Figure 5-26. Analysis of the percentage area of images positively stained with OilRed O stain. hMSCs grown on LbL constructs. Stars above bars show results with statistical significance compared to the control, glass. **** $p \leq 0.0001$, *** $p \leq 0.001$, ** $p \leq 0.01$, * $p < 0.05$.

After 14 days, the percentage area positively stained for lipids did not differ significantly for hMSCs on the PEI/GO, PEI/GO-SO_3 and control. After 21 days, the area of cells positively stained for lipids was significantly higher on the control than on PEI/GO and PEI/GO-SO_3.

5.3.2. Osteogenic differentiation

The osteogenic differentiation of hMSCs on PEI/GO, PEI/GO-SO_3 and PEI/G-SO_3 was measured using the Alizarin Red stain, which detects calcium deposits in the mineralised matrix. Alizarin red staining was performed on hMSCs at 7 days, 14 days and 21 days after the addition of osteogenic media, with simultaneous staining of hMSCs cultured in normal media. The Alizarin red staining images for hMSCs on PEI/GO, PEI/GO-SO_3 and PEI/G-SO_3 in the presence and absence of osteogenic media are shown in Figure 5-27 and Figure 5-28, respectively.

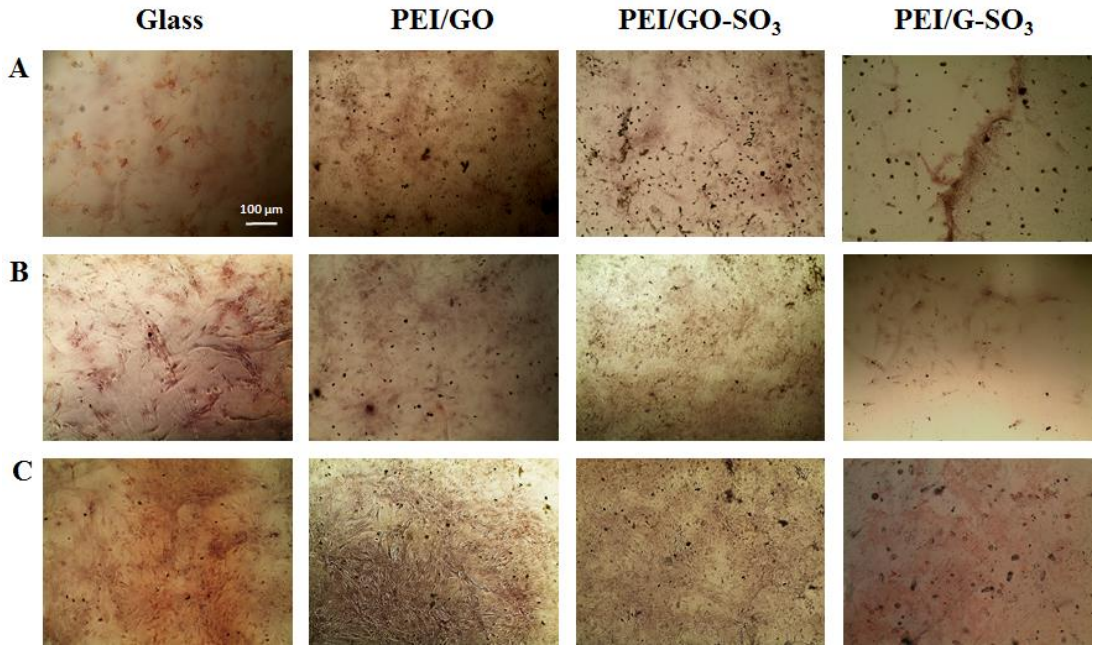

Figure 5-27. Alizarin Red staining of hMSCs on GFN-containing LbL constructs, after incubation with osteogenic induction media for A) 7 days B) 14 days and C) 21 days. Scale bar represents 100 µm.

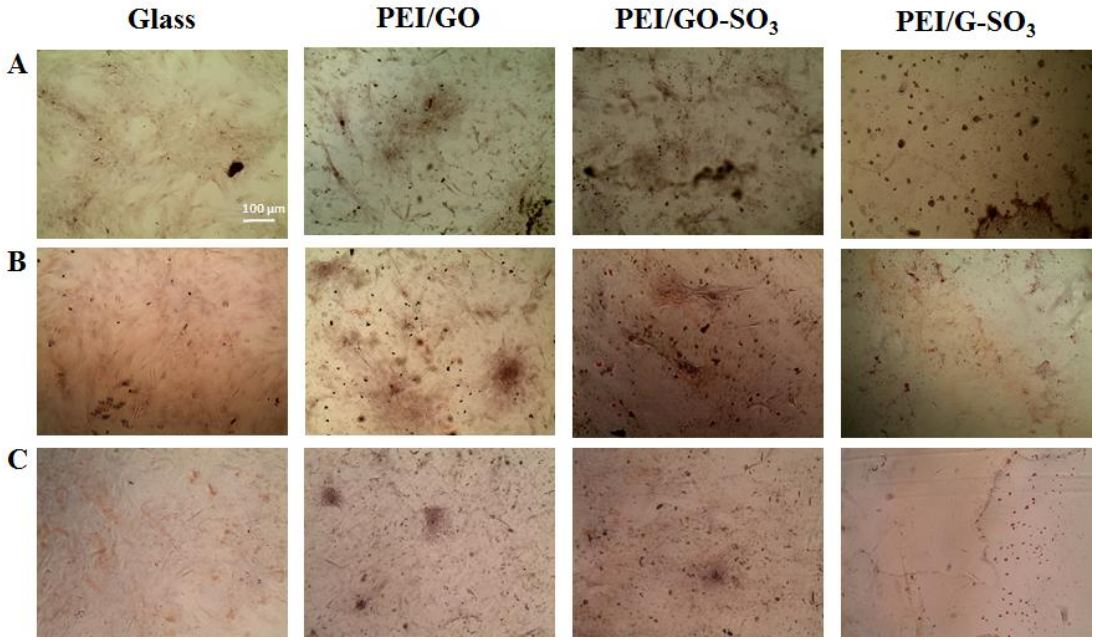

Figure 5-28. Alizarin Red staining of hMSCs on GFN-containing LbL constructs, after incubation with standard (non-induction) media for A) 7 days B) 14 days and C) 21 days. Scale bar represents 100 µm.

The hMSCs on the control substrate showed positive alizarin red staining after 14 days, in the presence of osteogenic media. No positive staining was observed on any of the GFN-containing LbL constructs after 21 days, in the presence of osteogenic

media. In the absence of osteogenic media, neither the GFN-containing LbL constructs nor the control displayed any positive alizarin red staining after 21 days. This indicates that none of the GFN-containing LbL constructs support osteogenic differentiation of hMSCs.

5.4. Summary

The hMSCs seeded on the PEI/GO and PEI/GO-SO_3 LbL constructs showed significant increases in cell count over the test period, which were comparable to the control, while hMSCs on the PEI/G-SO_3 only showed an 8.8 % increase in cell count over the 7-day test period. The morphology of the hMSCs seeded on PEI/GO, PEI/GO-SO_3 and PEI/G-SO_3 were similar after 4 hours post-seeding. After 1 day, however, hMSCs on glass, PEI/GO and PEI/GO-SO_3 showed a significantly higher eccentricity (more elongated shape) than on PEI/G-SO_3, with hMSCs on PEI/G-SO_3 not adopting a typical elongated morphology. The average cell area increased significantly for hMSCs seeded on the PEI/GO, PEI/GO-SO_3 LbL constructs between 4 hours and 1 day post-seeding, indicating cell spreading. However, the average area of hMSCs on the PEI/G-SO_3 did not increase significantly and was significantly lower than the hMSC areas on the PEI/GO and PEI/GO-SO_3 LbL constructs, indicating little cell spreading.

The cell activity of hMSCs on PEI/GO, PEI/GO-SO_3 and PEI/G-SO_3 increased over the 7-day test period. The cell activities of hMSCs PEI/GO and PEI/GO-SO_3 were higher than on PEI/G-SO_3 and were comparable to the control. The hMSCs on the PEI/G-SO_3 had a significantly lower activity than on the control. Furthermore, the hMSCs on glass, PEI/GO and PEI/GO-SO_3 showed elongated actin filaments, where those on PEI/G-SO_3 were less extended. The number of focal adhesions per cell for

hMSCs on PEI/GO and PEI/GO-SO_3 was also significantly higher than for hMSCs on the control and PEI/G-SO_3, indicating that cells do not attach as readily to the PEI/G-SO_3 substrate.

The same rank order of hMSC activity and cell count was seen with pre-treated GFN-containing LbL constructs as the untreated constructs, with pre-treated PEI/GO and PEI/GO-SO_3 showing higher hMSC cell count, cell area and activity than pre-treated PEI/G-SO_3 and the pre-treated control. However, the values of hMSC cell area, cell eccentricity and cell count between the pre-treated PEI/G-SO_3 and the pre-treated control were comparable because of pre-treatment, although the cell activity was still lower on pre-treated PEI/G-SO_3 than on the control.

The pre-treatment of the LbL constructs had the most significant impact on hMSC growth on the PEI/G-SO_3 LbL construct. The number of focal adhesions per cell increased, as did the cell activity, cell area, cell eccentricity and cell counts. The difference in these values on the other pre-treated LbL constructs was much less marked and varied more widely, with the parameters on some of the LbL constructs not affected by pre-treatment. This study indicates that, like the 3T3 SA study, the activity of cells on the different GFN-containing LbL constructs is affected significantly by media adsorption, as the increase in cell adhesion, proliferation and activity of hMSC on PEI/G-SO_3 following pre-treatment indicated that additional time for the adsorption of proteins from the media was required to enable effective hMSC attachment on the PEI/G-SO_3 LbL construct. The effect of the substrates on hMSC adhesion and proliferation is much more marked, as hMSCs do not secrete as much ECM and are therefore more sensitive to surface topology and chemistry.

The PEI/GO and PEI/GO-SO_3 LbL constructs show positive staining for lipids, indicating significant adipogenesis, in the presence of adipogenic induction media. However, hMSCs on these substrates did not show significant adipogenesis in the absence of adipogenic media. The hMSCs on the PEI/G-SO_3 LbL construct showed some positive staining for lipids, when cultured in the presence of adipogenic media, but the number of positively stained cells was less than for hMSCs on PEI/GO and PEI/GO-SO_3, which can be attributed to the lower cell count on the PEI/G-SO_3 LbL construct. The delamination of cells and peeling of the PEI/G-SO_3 LbL construct was also observed, which presents difficulty in measuring differentiation of hMSCs on this substrate.

Only hMSCs on the control substrate showed significant positive alizarin red staining after 21 days, in the presence of osteogenic media. There were small areas on the on the GFN-containing LbL constructs around which hMSCs showed positive staining, but no significant was observed. In the absence of osteogenic media, there was no positive Alizarin Red staining after 21 days on any of the substrates.

5.5. Discussion

5.5.1. Attachment and proliferation

The effective proliferation of stem cells on the PEI/GO and PEI/GO-SO_3 supports work in literature which demonstrates good attachment and proliferation of various stem cell types to GO-based substrates.[20,27,29,30,31] However, the lack of proliferation on the untreated PEI/G-SO_3 LbL construct is at odds with work found in literature regarding pristine graphene substrates. Good proliferation of a variety of stem cells on pristine graphene has been reported, including hMSCs,[19,20,32] human pluripotent stem cells,[33] neural stem cells,[8] dental pulp stem cells[34] and embryonic stem cells.[35]

The difference between the pristine graphene used in these studies and the composite used in this study arise both from the edge-functionalisation of the pristine graphene, the nature of the graphene starting material (powdered graphene rather than single CVD sheets), which could affect the roughness of the substrate, as well as the incorporation of the functionalised graphene into a PEI-containing LbL construct.

The PEI/GO, PEI/GO-SO_3 and PEI/G-SO_3 LbL constructs all contain PEI, which means that it is unlikely that the difference in hMSC behaviour on the PEI/G-SO_3 LbL construct is a result of the presence of PEI. In addition, many papers have used PEI as a gene-delivery vector in various stem cell types, indicating that it causes no adverse effects upon stem cells.[36,37,38,39] Therefore, the lack of hMSC proliferation on the PEI/G-SO_3 LbL construct may be a result of the sulfonate functionalisation of the pristine graphene, in addition to the decreased roughness of the PEI/G-SO_3 LbL construct in comparison to PEI/GO and PEI/GO-SO_3 and the nature of the pristine graphene material.

As shown in Chapter 4, the attachment and proliferation of 3T3 SA cells on GFN-containing LbL constructs was found to mirror the order of fibronectin (Fn) adsorption to the constructs, with PEI/GO and PEI/GO-SO_3 showing higher Fn adsorption and 3T3 SA cell activity than PEI/G-SO_3. Similarly, the attachment and proliferation of hMSCs on the GFN-containing LbL constructs follows the same order as the Fn adsorption, but in this case the differences are more marked, with hMSCs proliferating well on PEI/GO and PEI/GO-SO_3, but not proliferating on PEI/G-SO_3, unless pre-treatment of the surface with media is undertaken. The hypothesis is that the difference in hMSC cell activity is still dependent on the differences in Fn adsorption onto the LbL constructs, but that additional factors must

contribute to the lack of cell attachment to the PEI/G-SO_3 construct. The lack of cell adhesion and proliferation on PEI/G-SO_3 is somewhat improved by the pre-adsorption of media indicating that additional protein adsorption can alleviate the poor binding to PEI/G-SO_3. Lower serum protein binding on pristine graphene vs. GO was reported by Lee et al. but was still higher on GFN surfaces than on typical stem cell substrate, polydimethylsiloxane (PDMS).[20]

5.5.1.1.Functional group

Phillips *et al.* compared the growth and differentiation of hMSCs on surfaces with differing terminal chemistry, finding that -OH, -CO_2H and -NH_2 terminated surfaces were favourable for stem cell adhesion and proliferation, whereas the relatively more hydrophobic -CH_3 terminated surface showed little cell adhesion.[40] However, upon incubation with fibronectin prior to cell seeding largely compensated for the poor cell attachment to -CH_3 terminated surfaces and allowed for significant stem cell adhesion.[40] Similarly, in this study, good stem cell attachment and proliferation was observed on the PEI/GO and PEI/GO-SO_3 LbL constructs, which contain -OH and -COOH functional groups, supporting this finding. In addition, the pre-treatment of the PEI/G-SO_3 LbL construct prior to cell adhesion has a similar effect to that seen for the pre-treatment of the -CH_3 terminated surface because of pre-treatment, suggesting that the pre-treatment enhances the adsorption of adhesion-related proteins, thus improving cell attachment. Keselowsky *et al.* showed that the conformation of fibronectin was altered by different functional groups, which in turn affected $\alpha_5\beta_1$ integrin binding.[41]

Work by Kwon *et al.*, found that coating hydrogels with sulfonate-terminated functional groups increased the adhesion rate of MSCs on the gels, in comparison to

the hydrogels alone, though the presence of these functional groups also modulated the stiffness of the hydrogels, which also has an effect on cell adhesion.[42] The effect of functional group on hMSC growth could be further elucidated by introducing an alternative, negatively charged functional group the edges of the graphene sheet, and incorporating it into an analogous LbL construct. Presuming then that the approximate graphene distribution and roughness would be comparable, any differences between these substrates would therefore be a result of the surface functional group. If the hMSCs behaved in a similar way, this could indicate that the effect was due to surface topography.

5.5.1.2.Topography

In graphene-related stem cell studies, however, stem cells have been reported to show similar adhesion and proliferation has been observed on pristine graphene and GO.[20] The attachment of stem cells to CVD graphene has been attributed to wrinkles in the graphene sheet,[19] which has been related to other studies in which nanoscale topography has an influence in the proliferation of stem cells,[43] with several papers reporting enhanced stem cell attachment and proliferation with increased surface roughness.[44,45,46] In this study, the GFNs were incorporated into LbL constructs, meaning that the coverage of graphene is not as high as when, for example, a full CVD graphene sheet is used. This may have important consequences in terms of the roughness of the surfaces. The PEI/GO and PEI/GO-SO_3 were found to be rougher than the PEI/G-SO_3, which may contribute to the differences in stem cell adhesion and proliferation. Therefore, the reported cell proliferation and activity on pristine graphene-based substrates may be largely attributed to the wrinkling of CVD graphene sheets.

5.5.1.3.Cellular senescence

The differences in hMSC adhesion and proliferation on the PEI/GO, PEI/GO-SO_3 and PEI/G-SO_3 LbL constructs was more marked than with 3T3 SA cells, with hMSCs on the PEI/G-SO_3 LbL construct showing little proliferation over the 7-day test period, unless the substrate was pre-treated with media prior to cell seeding. The fact that hMSCs did not proliferate on the PEI.G-SO_3 LbL construct, but remained metabolically active, could indicate that the PEI/G-SO_3 LbL construct induced hMSC senescence. When cells enter senescence, they undergo irreversible growth inhibition.[47] Senescence can be caused by DNA damage and oxidative stress, and can be characterised by irregular cell shapes.[48] In addition there are several senescence-associated genes which are upregulated in senescent cells, for example p16, p21 and p53.[49]

Geissler and co-workers assessed the morphological changes associated with the increase in senescence of hMSCs as a function of passage number.[50] The increase in passage number was correlated with increased expression of senescence associated genes and were accompanied by clear morphological changes in the actin cytoskeleton. Figure 5-29 shows the phalloidin-stained hMSCs as a function of increased passage number, with hMSCs at higher passage showing fewer filopodia, lamellipodia or cell spreading.[50] The morphology of the cells at P30 and P100 in Figure 5-29 are similar to the morphology of phalloidin-stained hMSCs on PEI/G-SO_3, shown in Figure 5-7, suggesting that a number of the hMSCs on PEI/G-SO_3 may have entered senescence. However, in the case of the PEI/G-SO_3, this would not be caused by the ageing of the hMSCs, but instead by the surface onto

which they are seeded. However, this would have to be confirmed by evaluating the expression of senescence related genes in hMSCs on the PEI/G-SO_3 LbL construct.

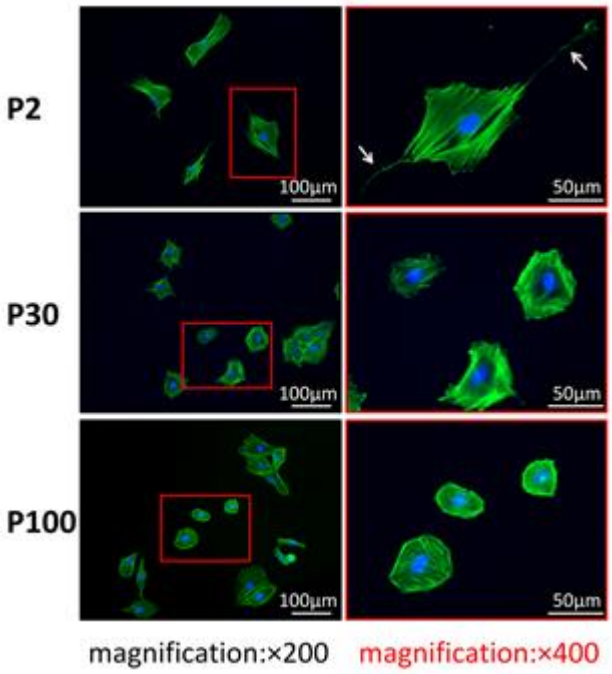

Figure 5-29. Phalloidin/DAPI stained images of hMSCs at top-bottom: Passage 2 (P2), passage 30 (P30) and passage 100 (P100). Geissler *et al.*[50]

5.5.2. Stem cell differentiation on graphene-containing LbL constructs

5.5.2.1 Adipogenesis

The adipogenic differentiation of hMSCs on the PEI/GO and PEI/GO-SO_3 in the presence of adipogenic media follows other work which reports the tendency of GO-based substrates to direct towards adipogenic lineages,[20,26,27] with Patel and Lee separately attributing this to the ability of GO to bind strongly to insulin, an important adipogenic inductor, by electrostatic interactions.[20,26] The incorporation of GO into an LbL construct still allows for this tendency towards adipogenesis but, in the absence of adipogenic media, no adipogenesis was observed after 21 days. This is consistent with the work by Lee *et al.*, which observed no significant adipogenesis on GO substrates in the absence of inductive media.[20] It is clear that the PEI/GO and

PEI/GO-SO_3 respond in a similar way to other GO-based substrates reported in literature. The lower amount of positive staining for adipogenesis on the PEI/G-SO_3 is expected, as literature has reported that pristine graphene does not support adipogenesis as successfully as GO.[20] However, this effect is compounded by the poor attachment of the hMSCs on the PEI/G-SO_3 LbL construct.

5.5.2.2 Osteogenic differentiation

The osteogenic differentiation of hMSCs on the GFN-containing LbL constructs was not as would have been expected by comparison to literature. Work in literature has widely reported osteogenic differentiation of stem cells on both graphene and GO-containing substrates.[20,21,22,51] Therefore, the expected outcome would have been that these substrates would show positive staining for osteogenesis, especially in the presence of osteogenic media. However, none of the GFN-containing LbL constructs supported osteogenic differentiation of the hMSCs. Nayak and Lee both showed positive alizarin red staining after 15 days and 12 days, respectively,[19,20] which indicates that positive staining should be expected by the 21 day timepoint. However, work is currently being undertaken both to assess osteogenic differentiation after 28 days, to assess whether osteogenesis is simply slower on these substrates than other GFNs. In addition, tests for osteogenic gene expression on each of the GFN-containing LbL constructs could point to earlier signs of osteogenesis.

The argument presented previously for hMSC senescence on the PEI/G-SO_3 LbL constructs may explain the absence of osteogenic differentiation and low level of adipogenic differentiation of hMSCs on the PEI/G-SO_3 construct. For example, a paper by Geissler *et al*. compared the differentiation potential of hMSCs with

increasing passage number, revealing that they completely lose osteogenic differentiation potential and have a lowered adipogenic potential after 100 passages, which was accompanied by increased expression of senescence-associated genes.[50] Osteogenic differentiation should be expected on the PEI/G-SO_3 LbL construct, as pristine graphene is able to pre-concentrate dexamethasone and β-glycerophosphate, which are both important osteogenic factors.[20] The lack of osteogenesis could therefore be explained by the senescence of the hMSCs on this substrate. To confirm this hypothesis, the expression of senescence related genes should be measured on this substrate.

However, other justifications for the lack of osteogenesis on PEI/G-SO_3 LbL constructs may arise from the connection between roughness and osteogenesis. Many papers have reported increased osteogenesis on surfaces as roughness increases, which is thought to be due to the aggregation of hMSCs in the troughs of rough surfaces.[52,53,54] Therefore the PEI/G-SO_3 LbL construct, which only has a RMS roughness value of 1.5 nm, may not be sufficiently rough to drive osteogenesis. However, the lack of osteogenesis seen for hMSCs on the PEI/GO and PEI/GO-SO_3 LbL constructs, which had RMS roughness values of 7.4 and 5.4 nm, respectively, is more unusual.

The cell number for the osteogenic differentiation was justified by referring to similar works on GFNs which uses a low seeding density and begins osteogenic induction after 24 hours growth period. However, ossification is usually triggered by the aggregation of cells, which then secrete bone matrix and mineralise.[55,56] Therefore, it would be important to determine whether the extent of osteogenic

differentiation would increase if the initial cell seeding density was higher and if the incubation period prior to differentiation was increased.

5.5.3. Additional controls

As discussed in Chapter 4, the positive charge of PEI is likely to have a significant effect upon hMSC adhesion and proliferation, where the coverage of GFN in the LbL construct is not high. Therefore, for future investigation PEI should be used as a control rather than glass, as it is more meaningful in understanding the origin of the cell behaviour on the different LbL constructs and its probable contribution to the behaviour of cells cannot be neglected.

5.6. Further work

The PEI/GO and PEI/GO-SO_3 LbL constructs are useful in stimulating differentiation of hMSCs to adipogenic lineages. In addition, the simplicity of the LbL process, as well as its higher cost effectiveness make it a viable alternative to using expensive GFN substrates such as CVD graphene, or fashioning substrates by Langmuir Blodgett techniques, thus being more scalable. This study demonstrates the potential of this technology to incorporating further functional groups and moieties which can enhance stem cell growth and/or differentiation.

The research conducted in has indicated that, although GFN-containing LbL constructs promote the attachment and proliferation of hMSCs, the differences in roughness and surface chemistry of the GFNs can have a profound effect upon cell response. This study also indicated that the type of graphene used may have an influence on the cell attachment. The wrinkles which are found in CVD graphene materials are favourable for both cell adhesion and for osteogenic differentiation.

An interesting observation in this work was the lack of hMSC proliferation on the PEI/G-SO_3 LbL construct, which indicates the possible senescence of hMSCs as a result of their interaction with this construct. Testing for senescence in the hMSCs could be monitored by looking at gene expression, as work by Sepulveda *et al.* identified over 20 proteins which were secreted in higher amounts in senescent cells.[57] Genes which have been commonly found to be upregulated in senescent cells are p16, p21 and p53,[49] which could therefore be used to assess the hMSCs on this construct. In addition, hMSCs can also be stained for senescence associated β-galactosidase (SA-β-gal), which is a common method of identifying senescent cells.[47] If the hMSCs on this LbL construct were found to be senescent, then further work would be required to identify the origin of this senescence.

There has been significant interest in the synergistic enhancement of osteogenesis by incorporation of GFNs and phosphates. For example, Tatavarty *et al.* reported the increase in osteogenesis by the effect of both GO and calcium phosphate, in a composite,[58] with similar effects reported by Wu *et al.*[24] A further research aim would be to produce a phosphate functionalisation of graphene and assess its effect on osteogenesis. This work will be outlined in the future work section.

As hMSC multipotency can be affected by donor, due to factors such as age, genetics,[59] it is important to assess the effect of these LbL constructs on cells from a variety of donors. For example, the hMSCs used in this study were purchased from commercial source, but it would be interesting to compare the effect of these LbL constructs on samples from different donors and on other types of hMSC such as embryonic stem cells, to compare the response.

5.7. References

1. Meirelles, L. D. S.; Chagastelles, P. C.; Nardi, N. B., Mesenchymal stem cells reside in virtually all post-natal organs and tissues. *Journal of Cell Science* **2006,** *119* (11), 2204-2213.
2. Marion, N. W.; Mao, J. J., Mesenchymal stem cells and tissue engineering. *Stem Cell Tools and Other Experimental Protocols* **2006,** *420*, 339-361.
3. Eberli, D.; Atala, A., Tissue engineering using adult stem cells. *Stem Cell Tools and Other Experimental Protocols* **2006,** *420*, 287-302.
4. Crisan, M.; Yap, S.; Casteilla, L.; Chen, C. W.; Corselli, M.; Park, T. S.; Andriolo, G.; Sun, B.; Zheng, B.; Zhang, L.; Norotte, C.; Teng, P. N.; Traas, J.; Schugar, R.; Deasy, B. M.; Badylak, S.; Buhring, H. J.; Giacobino, J. P.; Lazzari, L.; Huard, J.; Peault, B., A perivascular origin for mesenchymal stem cells in multiple human organs. *Cell Stem Cell* **2008,** *3* (3), 301-313.
5. Mao, J. J., Stem-cell-driven regeneration of synovial joints. *Biology of the Cell* **2005,** *97* (5), 289-301.
6. Kim, J.; Park, S.; Kim, Y. J.; Jeon, C. S.; Lim, K. T.; Seonwoo, H.; Cho, S. P.; Chung, T. D.; Choung, P. H.; Choung, Y. H.; Hong, B. H.; Chung, J. H., Monolayer Graphene-Directed Growth and Neuronal Differentiation of Mesenchymal Stem Cells. *Journal of Biomedical Nanotechnology* **2015,** *11* (11), 2024-2033.
7. Fabbro, A.; Scaini, D.; Leon, V.; Vazquez, E.; Cellot, G.; Privitera, G.; Lombardi, L.; Torrisi, F.; Tomarchio, F.; Bonaccorso, F.; Bosi, S.; Ferrari, A. C.; Ballerini, L.; Prato, M., Graphene-Based Interfaces Do Not Alter Target Nerve Cells. *ACS Nano* **2016,** *10* (1), 615-623.
8. Park, S. Y.; Park, J.; Sim, S. H.; Sung, M. G.; Kim, K. S.; Hong, B. H.; Hong, S., Enhanced Differentiation of Human Neural Stem Cells into Neurons on Graphene. *Advanced Materials* **2011,** *23* (36), 263–267.
9. Bouzid, T.; Sinitskii, A.; Lim, J. Y., Graphene platform for neural regenerative medicine. *Neural Regeneration Research* **2016,** *11* (6), 894-895.
10. Ryu, S.; Kim, B. S., Culture of Neural Cells and Stem Cells on Graphene. *Tissue Engineering and Regenerative Medicine* **2013,** *10* (2), 39-46.
11. Fan, H.; Wang, L.; Zhao, K.; Li, N.; Shi, Z.; Ge, Z.; Jin, Z., Fabrication, Mechanical Properties, and Biocompatibility of Graphene-Reinforced Chitosan Composites. *Biomacromolecules* **2010,** *11* (9), 2345-2351.
12. Sayyar, S.; Murray, E.; Thompson, B. C.; Gambhir, S.; Officer, D. L.; Wallace, G. G., Covalently linked biocompatible graphene/polycaprolactone composites for tissue engineering. *Carbon* **2013,** *52*, 296-304.
13. Fan, Z. J.; Wang, J. Q.; Wang, Z. F.; Ran, H. Q.; Li, Y.; Niu, L. Y.; Gong, P. W.; Liu, B.; Yang, S. R., One-pot synthesis of graphene/hydroxyapatite nanorod composite for tissue engineering. *Carbon* **2014,** *66*, 407-416.
14. Wan, C. Y.; Frydrych, M.; Chen, B. Q., Strong and bioactive gelatin-graphene oxide nanocomposites. *Soft Matter* **2011,** *7* (13), 6159-6166.
15. Shin, S. R.; Zihlmann, C.; Akbari, M.; Assawes, P.; Cheung, L.; Zhang, K. Z.; Manoharan, V.; Zhang, Y. S.; Yuksekkaya, M.; Wan, K. T.; Nikkhah, M.; Dokmeci, M. R.; Tang, X. W.; Khademhosseini, A., Reduced Graphene Oxide-GelMA Hybrid Hydrogels as Scaffolds for Cardiac Tissue Engineering. *Small* **2016,** *12* (27), 3677-3689.

16. Liao, J. F.; Qu, Y.; Chu, B. Y.; Zhang, X. N.; Qian, Z. Y., Biodegradable CSMA/PECA/Graphene Porous Hybrid Scaffold for Cartilage Tissue Engineering. *Scientific Reports* **2015,** *5*, 9879/1-16.
17. Marrella, A.; Lagazzo, A.; Barberis, F.; Catelani, T.; Quarto, R.; Scaglione, S., Enhanced mechanical performances and bioactivity of cell laden-graphene oxide/alginate hydrogels open new scenario for articular tissue engineering applications. *Carbon* **2017,** *115*, 608-616.
18. Kalbacova, M.; Broz, A.; Kong, J.; Kalbac, M., Graphene substrates promote adherence of human osteoblasts and mesenchymal stromal cells. *Carbon* **2010,** *48* (15), 4323-4329.
19. Nayak, T. R.; Andersen, H.; Makam, V. S.; Khaw, C.; Bae, S.; Xu, X.; Ee, P.-L. R.; Ahn, J.-H.; Hong, B. H.; Pastorin, G.; Oezyilmaz, B., Graphene for Controlled and Accelerated Osteogenic Differentiation of Human Mesenchymal Stem Cells. *ACS Nano* **2011,** *5* (6), 4670-4678.
20. Lee, W. C.; Lim, C.; Shi, H.; Tang, L. A. L.; Wang, Y.; Lim, C. T.; Loh, K. P., Origin of Enhanced Stem Cell Growth and Differentiation on Graphene and Graphene Oxide. *ACS Nano* **2011,** *5* (9), 7334-7341.
21. Crowder, S. W.; Prasai, D.; Rath, R.; Balikov, D. A.; Bae, H.; Bolotin, K. I.; Sung, H.-J., Three-dimensional graphene foams promote osteogenic differentiation of human mesenchymal stem cells. *Nanoscale* **2013,** *5* (10), 4171-4176.
22. Luo, Y.; Shen, H.; Fang, Y. X.; Cao, Y. H.; Huang, J.; Zhang, M. X.; Dai, J. W.; Shi, X. Y.; Zhang, Z. J., Enhanced Proliferation and Osteogenic Differentiation of Mesenchymal Stem Cells on Graphene Oxide-Incorporated Electrospun Poly(lactic-co-glycolic acid) Nanofibrous Mats. *ACS Applied Materials & Interfaces* **2015,** *7* (11), 6331-6339.
23. Kang, S.; Park, J. B.; Lee, T. J.; Ryu, S.; Bhang, S. H.; La, W. G.; Noh, M. K.; Hong, B. H.; Kim, B. S., Covalent conjugation of mechanically stiff graphene oxide flakes to three-dimensional collagen scaffolds for osteogenic differentiation of human mesenchymal stem cells. *Carbon* **2015,** *83*, 162-172.
24. Wu, C. T.; Xia, L. G.; Han, P. P.; Xu, M. C.; Fang, B.; Wang, J. C.; Chang, J.; Xiao, Y., Graphene-oxide-modified beta-tricalcium phosphate bioceramics stimulate in vitro and in vivo osteogenesis. *Carbon* **2015,** *93*, 116-129.
25. La, W. G.; Park, S.; Yoon, H. H.; Jeong, G. J.; Lee, T. J.; Bhang, S. H.; Han, J. Y.; Char, K.; Kim, B. S., Delivery of a Therapeutic Protein for Bone Regeneration from a Substrate Coated with Graphene Oxide. *Small* **2013,** *9* (23), 4051-4060.
26. Patel, M.; Moon, H. J.; Ko, D. Y.; Jeong, B., Composite System of Graphene Oxide and Polypeptide Thermogel As an Injectable 3D Scaffold for Adipogenic Differentiation of Tonsil-Derived Mesenchymal Stem Cells. *ACS Applied Materials & Interfaces* **2016,** *8* (8), 5160-5169.
27. Kim, J.; Choi, K. S.; Kim, Y.; Lim, K. T.; Seonwoo, H.; Park, Y.; Kim, D. H.; Choung, P. H.; Cho, C. S.; Kim, S. Y.; Choung, Y. H.; Chung, J. H., Bioactive effects of graphene oxide cell culture substratum on structure and function of human adipose-derived stem cells. *Journal of Biomedical Materials Research Part A* **2013,** *101* (12), 3520-3530.
28. Wang, Y.; Lee, W. C.; Manga, K. K.; Ang, P. K.; Lu, J.; Liu, Y. P.; Lim, C. T.; Loh, K. P., Fluorinated Graphene for Promoting Neuro-Induction of Stem Cells. *Advanced Materials* **2012,** *24* (31), 4285-4290.
29. Garcia-Alegria, E.; Iluit, M.; Stefanska, M.; Silva, C.; Heeg, S.; Kimber, S. J.; Kouskoff, V.; Lacaud, G.; Vijayaraghavan, A.; Batta, K., Graphene Oxide

promotes embryonic stem cell differentiation to haematopoietic lineage. *Scientific Reports* **2016,** *6*, 25917/1-13.
30. Kumar, S.; Raj, S.; Kolanthai, E.; Sood, A. K.; Sampath, S.; Chatterjee, K., Chemical Functionalization of Graphene To Augment Stem Cell Osteogenesis and Inhibit Biofilm Formation on Polymer Composites for Orthopedic Applications. *ACS Applied Materials & Interfaces* **2015,** *7* (5), 3237-3252.
31. Mazaheri, M.; Akhavan, O.; Simchi, A., Flexible bactericidal graphene oxide-chitosan layers for stem cell proliferation. *Applied Surface Science* **2014,** *301*, 456-462.
32. Li, J. H.; Wang, G.; Geng, H.; Zhu, H. Q.; Zhang, M.; Di, Z. F.; Liu, X. Y.; Chu, P. K.; Wang, X., CVD Growth of Graphene on NiTi Alloy for Enhanced Biological Activity. *ACS Applied Materials & Interfaces* **2015,** *7* (36), 19876-19881.
33. Lee, H.; Nam, D.; Choi, J. K.; Arauzo-Bravo, M. J.; Kwon, S. Y.; Zaehres, H.; Lee, T.; Park, C. Y.; Kang, H. W.; Scholer, H. R.; Kim, J. B., Establishment of feeder-free culture system for human induced pluripotent stem cell on DAS nanocrystalline graphene. *Scientific Reports* **2016,** *6*, 20708/1-11.
34. Rodriguez, C. L. C.; Kessler, F.; Dubey, N.; Rosa, V.; Guilhermino, J. M., CVD graphene transfer procedure to the surface of stainless steel for stem cell proliferation. *Surface and coatings technology* **2017,** *311*, 10-18.
35. Sebaa, M.; Nguyen, T. Y.; Paul, R. K.; Mulchandani, A.; Liu, H. N., Graphene and carbon nanotube-graphene hybrid nanomaterials for human embryonic stem cell culture. *Materials Letters* **2013,** *92*, 122-125.
36. Wang, W. W.; Li, W. Z.; Ou, L. L.; Flick, E.; Mark, P.; Nesselmann, C.; Lux, C. A.; Gatzen, H. H.; Kaminski, A.; Liebold, A.; Luetzow, K.; Lendlein, A.; Li, R. K.; Steinhoff, G.; Ma, N., Polyethylenimine-mediated gene delivery into human bone marrow mesenchymal stem cells from patients. *Journal of Cellular and Molecular Medicine* **2011,** *15* (9), 1989-1998.
37. Chen, X. A.; Zhang, L. J.; He, Z. J.; Wang, W. W.; Xu, B.; Zhong, Q.; Shuai, X. T.; Yang, L. Q.; Deng, Y. B., Plasmid-encapsulated polyethylene glycol-grafted polyethylenimine nanoparticles for gene delivery into rat mesenchymal stem cells. *International Journal of Nanomedicine* **2011,** *6*, 843-853.
38. Ahn, H. H.; Lee, J. H.; Kim, K. S.; Lee, J. Y.; Kim, M. S.; Khang, G.; Lee, I. W.; Lee, H. B., Polyethyleneimine-mediated gene delivery into human adipose derived stem cells. *Biomaterials* **2008,** *29* (15), 2415-2422.
39. Bartman, C. M.; Egelston, J.; Ren, X. J.; Das, R.; Phiel, C. J., A simple and efficient method for transfecting mouse embryonic stem cells using polyethylenimine. *Experimental Cell Research* **2015,** *330* (1), 178-185.
40. Phillips, J. E.; Petrie, T. A.; Creighton, F. P.; Garcia, A. J., Human mesenchymal stem cell differentiation on self-assembled monolayers presenting different surface chemistries. *Acta Biomaterialia* **2010,** *6* (1), 12-20.
41. Keselowsky, B. G.; Collard, D. M.; Garcia, A. J., Surface chemistry modulates fibronectin conformation and directs integrin binding and specificity to control cell adhesion. *Journal of Biomedical Materials Research Part A* **2003,** *66A* (2), 247-259.
42. Kwon, H. J., Chondrogenesis on sulfonate-coated hydrogels is regulated by their mechanical properties. *Journal of the Mechanical Behavior of Biomedical Materials* **2013,** *17*, 337-346.
43. Dulgar-Tulloch, A. J.; Bizios, R.; Siegel, R. W., Human mesenchymal stem cell adhesion and proliferation in response to ceramic chemistry and nanoscale

topography. *Journal of Biomedical Materials Research Part A* **2009,** *90A* (2), 586-594.
44. Deligianni, D. D.; Katsala, N. D.; Koutsoukos, P. G.; Missirlis, Y. F., Effect of surface roughness of hydroxyapatite on human bone marrow cell adhesion, proliferation, differentiation and detachment strength. *Biomaterials* **2001,** *22* (1), 87-96.
45. Logan, N.; Bozec, L.; Traynor, A.; Brett, P., Mesenchymal stem cell response to topographically modified CoCrMo. *Journal of Biomedical Materials Research Part A* **2015,** *103* (12), 3747-3756.
46. Mazon, P.; Garcia-Bernal, D.; Meseguer-Olmo, L.; Cragnolini, F.; De Aza, P. N., Human mesenchymal stem cell viability, proliferation and differentiation potential in response to ceramic chemistry and surface roughness. *Ceramics International* **2015,** *41* (5), 6631-6644.
47. Turinetto, V.; Vitale, E.; Giachino, C., Senescence in Human Mesenchymal Stem Cells: Functional Changes and Implications in Stem Cell-Based Therapy. *International Journal of Molecular Sciences* **2016,** *17* (7), 1164/1-18.
48. Wagner, W.; Horn, P.; Castoldi, M.; Diehlmann, A.; Bork, S.; Saffrich, R.; Benes, V.; Blake, J.; Pfister, S.; Eckstein, V.; Ho, A. D., Replicative Senescence of Mesenchymal Stem Cells: A Continuous and Organized Process. *Plos One* **2008,** *3* (5), 2213/1-12.
49. Cheng, H. C.; Qiu, L.; Ma, J.; Zhang, H.; Cheng, M.; Li, W.; Zhao, X. F.; Liu, K. Y., Replicative senescence of human bone marrow and umbilical cord derived mesenchymal stem cells and their differentiation to adipocytes and osteoblasts. *Molecular Biology Reports* **2011,** *38* (8), 5161-5168.
50. Geissler, S.; Textor, M.; Kuhnisch, J.; Konnig, D.; Klein, O.; Ode, A.; Pfitzner, T.; Adjaye, J.; Kasper, G.; Duda, G. N., Functional Comparison of Chronological and In Vitro Aging: Differential Role of the Cytoskeleton and Mitochondria in Mesenchymal Stromal Cells. *Plos One* **2012,** *7* (12), 52700/1-13.
51. Liu, Y. S.; Chen, T.; Du, F.; Gu, M.; Zhang, P.; Zhang, X.; Liu, J. Z.; Lv, L. W.; Xiong, C. Y.; Zhou, Y. S., Single-Layer Graphene Enhances the Osteogenic Differentiation of Human Mesenchymal Stem Cells In Vitro and In Vivo. *Journal of Biomedical Nanotechnology* **2016,** *12* (6), 1270-1284.
52. Deng, Y.; Liu, X. C.; Xu, A. X.; Wang, L. X.; Luo, Z. Y.; Zheng, Y. F.; Deng, F.; Wei, J.; Tang, Z. H.; Wei, S. C., Effect of surface roughness on osteogenesis in vitro and osseointegration in vivo of carbon fiber-reinforced polyetheretherketone-nanohydroxyapatite composite. *International Journal of Nanomedicine* **2015,** *10*, 1425-1447.
53. Faia-Torres, A. B.; Guimond-Lischer, S.; Rottmar, M.; Charnley, M.; Goren, T.; Maniura-Weber, K.; Spencer, N. D.; Reis, R. L.; Textor, M.; Neves, N. M., Differential regulation of osteogenic differentiation of stem cells on surface roughness gradients. *Biomaterials* **2014,** *35* (33), 9023-9032.
54. Zan, X. J.; Sitasuwan, P.; Feng, S.; Wang, Q., Effect of Roughness on in Situ Biomineralized CaP-Collagen Coating on the Osteogenesis of Mesenchymal Stem Cells. *Langmuir* **2016,** *32* (7), 1808-1817.
55. Safadi, F.; Barbe, M.; Abdelmagid, S. M.; Rico, M. C.; Aswad, R. A.; Litvin, J.; Popoff, S. N., *Bone Pathology*. Springer Science and Business media: New York, USA., 2009.
56. Gilbert, S. F., Developmental Biology. 6th ed.; Palgrave MacMillan: Sunderland, MA., 2000.

57. Sepulveda, J. C.; Tome, M.; Fernandez, M. E.; Delgado, M.; Campisi, J.; Bernad, A.; Gonzalez, M. A., Cell Senescence Abrogates the Therapeutic Potential of Human Mesenchymal Stem Cells in the Lethal Endotoxemia Model. *Stem Cells* **2014,** *32* (7), 1865-1877.
58. Tatavarty, R.; Ding, H.; Lu, G. J.; Taylor, R. J.; Bi, X. H., Synergistic acceleration in the osteogenesis of human mesenchymal stem cells by graphene oxide-calcium phosphate nanocomposites. *Chemical Communications* **2014,** *50* (62), 8484-8487.
59. Duggal, S.; Brinchmann, J. E., Importance of Serum Source for the In Vitro Replicative Senescence of Human Bone Marrow Derived Mesenchymal Stem Cells. *Journal of Cellular Physiology* **2011,** *226* (11), 2908-2915.

6. SUMMARY AND FUTURE WORK

6.1 Aims, objectives and key research findings

The main aims of this thesis were to develop edge functionalisations of pristine graphene that would increase the aqueous dispersibility of graphene and provide functional groups by which to tether biologically-relevant molecules, whilst leaving the majority of the graphene sheet intact. A further aim was to demonstrate the attachment of biologically relevant molecules to functionalised graphene. The incorporation of edge-functionalised graphene sulfonate (G-SO_3), GO and GO-SO_3 into a layer-by-layer (LbL) constructs was a further research goal, for use in tissue engineering applications. Finally, the biocompatibility of PEI/GO, PEI/GO-SO_3 and PEI/G-SO_3 LbL constructs towards 3T3 Swiss Albino (3T3 SA) fibroblasts and human mesenchymal stem cells (hMSCs) was assessed and compared and the effect of these LbL constructs on the differentiation lineages of hMSCs was analysed.

The sulfonation and thiol functionalisation of pristine graphene, to make graphene sulfonate (G-SO_3) and graphene thiol (G-SH), respectively, were outlined in Chapter 3. The evidence provided in this chapter indicated the presence of the sulfur-containing functional groups, changes in aqueous dispersibility and wettability and the preservation of the lateral dimension and little change in the defect density of the graphene sheets. Chapter 3 also included the characterisation of PEI/GO, PEI/GO-SO_3 and PEI/G-SO_3 LbL constructs. The presence of GO, GO-SO_3 and G-SO_3, respectively, was confirmed by Raman mapping and imaging of the LbL constructs, although the coverage in the PEI/G-SO_3 LbL construct was lower than for analogous PEI/GO or PEI/GO-SO_3 LbL constructs, likely due to the lower charge density on G-SO_3, as a result of the edge-specific functionalisation. The attachment

of a cyclen-based compound (AllylDO3A) and a fluorescently labelled lectin to G-SH were also outlined in Chapter 3, to demonstrate the tethering of biologically relevant molecules to edge-functionalised graphene.

The biocompatibility of the PEI/GO, PEI/GO-SO_3 and PEI/G-SO_3 LbL constructs towards 3T3 SA fibroblast cells was assessed, with results outlined in Chapter 4. The PEI/GO, PEI/GO-SO_3 and PEI/G-SO_3 LbL constructs all supported 3T3 SA cell adhesion and proliferation over the 6-day test period, with no significant toxicity and a high cell viability. 3T3 SA cells on the PEI/GO and PEI/GO-SO_3 LbL constructs, however, showed a higher cell activity than on PEI/G-SO_3. This difference in cell activity was linked to the extent of fibronectin (Fn) adsorption on the LbL constructs, which was higher on the PEI/GO and PEI/GO-SO_3 LbL constructs in comparison to PEI/G-SO_3. These differences in Fn adsorption were related to the surface chemistry and roughness of the LbL constructs. The PEI/GO and PEI/GO-SO_3 LbL constructs were rougher than the PEI/G-SO_3 LbL construct and contained functional groups such as carboxylates, epoxides and hydroxyl groups, which were more favourable for fibronectin adsorption. This study provided a basis for design of other functional groups which could increase cell activity, and performs a basis for further cell viability studies.

The effect of the PEI/GO, PEI/GO-SO_3 and PEI/G-SO_3 LbL constructs on human mesenchymal stem cell (hMSC) fate was explored in Chapter 5. The hMSCs seeded onto the PEI/G-SO_3 LbL construct, though showing high viability, did not appear to proliferate significantly over the test period, in contrast to hMSCs on the PEI/GO and PEI/GO-SO_3 LbL constructs, which showed good proliferation and a large increase in cell activity over the test period. In addition, the morphology of hMSCs

on the PEI/G-SO_3 LbL constructs remained quite rounded, while those on the PEI/GO and PEI/GO-SO_3 LbL constructs had an elongated morphology even after 24 hours and displayed a significantly higher number of focal adhesions.

The differentiation of hMSCs on the PEI/GO, PEI/GO-SO_3 and PEI/G-SO_3 LbL constructs was also investigated. The PEI/GO and PEI/GO-SO_3 LbL constructs showed significant adipogenic differentiation after 21 days, which is consistent with other differentiation studies on graphene oxide.[1] The PEI/G-SO_3 LbL construct however, showed no significant osteogenic differentiation, while pristine graphene is known to support osteogenic differentiation. However, the lack of osteogenic differentiation observed may have been due to the low cell count of hMSCs on this substrate.

6.2 Future work

The following section outlines the future scope of the research presented in this thesis, including the remaining or resulting research questions. This section includes work currently being completed, as well as experimental work which would complement and strengthen the work outlined in this thesis. New research avenues have been identified as a result of work conducted in this thesis, which are summarized in the following sections.

6.2.1 Graphene functionalisations

The functionalisation of graphene to G-SO_3 and G-SH, was characterised in Chapter 1, as were the attachment of several biologically relevant molecules to graphene. Several extensions to this work are outlined, which include additional characterisation of functionalised graphene materials, as well as different functionalisations and a future application of edge-functionalised graphene.

6.2.1.1 Energy-dispersive X-ray spectroscopy mapping

A characterisation method which can provide valuable information about the distribution of atoms in material is energy-dispersive X-ray spectroscopy (EDX). EDX works by an incident beam of electrons, protons or X-rays, exciting an inner shell electron of an atom within a sample from its ground state, causing the creation of an electron hole. Electron from a higher energy shell fills this hole and the difference in energy released as an X-ray. The emitted X-rays are then measured by an energy dispersive spectrometer.[2] This can be performed on a scanning transmission electron microscopy (STEM) and enables the mapping of different elements in a sample, as the energies of X-rays are characteristic for different elements. An example of a STEM EDX map of the Eu^{3+}/DO3A-$(CH_2)_3$-(G-SH) is shown in Figure 6-1 and shows the distribution of carbon (green), oxygen (yellow) and sulfur (pink) in the flake. In this sample, Eu^{3+} was difficult to locate and, due to limitations in time and equipment availability, further samples were not able to be assessed. The flake which was imaged is agglomerated and so the edges are not clearly defined. Future work would involve looking at a large number of flakes, first identifying suitable flakes on a TEM using a finder grid. The finder grids have coordinates marked, which enables flakes to be located under STEM for EDX mapping, making the process more efficient.

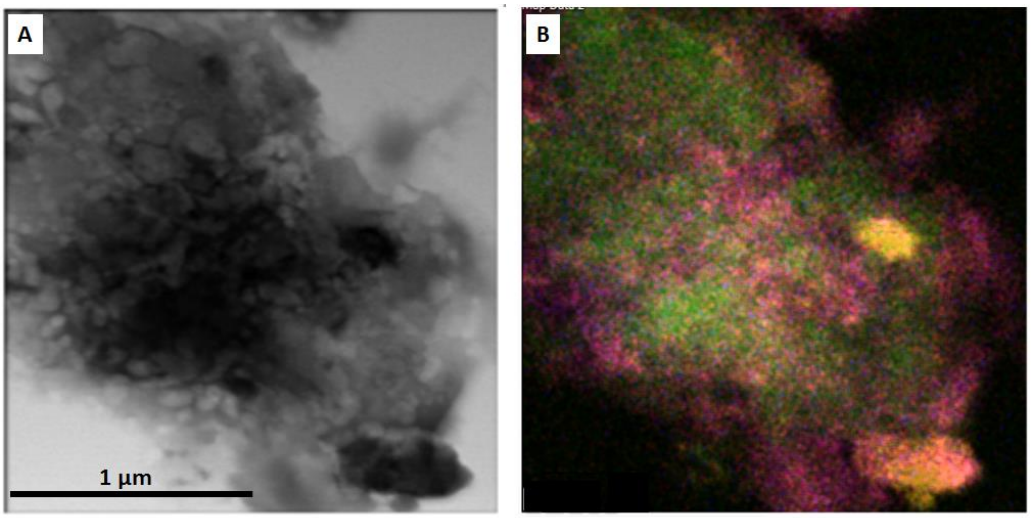

Figure 6-1 STEM-EDX map of a Eu^{3+}/DO3A-$(CH_2)_3$-(G-SH) graphene sheet, re-dispersed in ethanol and pipetted onto a holey carbon grid. A) Bright field image B) Elemental map of the flake. Green: carbon Pink: Sulfur Yellow: oxygen.

6.2.1.2 Four-point probe measurement

The high electron mobility of graphene, is something that the edge functionalisation outlined in this thesis aims to preserve. The conductivity of the functionalised graphene can be measured on CVD functionalised graphene, which consists of one extended sheet. The method currently being developed for conductivity testing of functionalised graphene is based on the Van der Pauw method, in which contacts are placed around the perimeter of a sample and the average conductivity of the material measured.[3] A diagram of the set up can be seen in Figure 6-2.

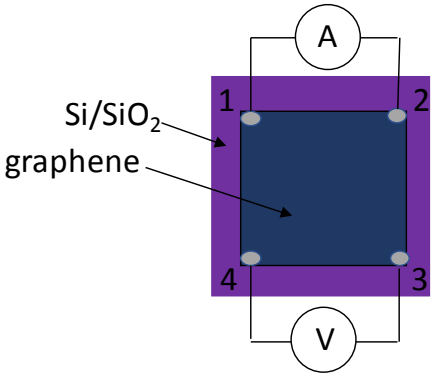

Figure 6-2. Set up for Van der Pauw conductivity measurement on CVD graphene, showing electrical contacts made at the corners of the CVD graphene sheet. Current flows through one side of the sheet and the potential differences across the other side is measured. Several combinations are used to find the average conductivity.

6.2.1.3 Investigating the effect of flake size.

As the lateral dimensions of graphene flakes becomes smaller, the number of edges will increase, meaning that an increase in the degree of functionalisation of graphene can be expected with decreasing lateral dimensions. An understanding of how the lateral dimensions of graphene flakes affects the degree of functionalisation is important to determine for future applications, as specific lateral sizes and/or degree of functionalisation may be required for specific applications.

6.2.1.4 Optimisation of functionalisation parameters

It is important to find the optimum conditions for the edge functionalisations of graphene, to avoid wasting of reagents and to decrease production costs. Initial work has shown that the wt. % S in G-SH is at a maximum using a 1-5 % volume chlorosulphonic acid, but this needs to be further optimised, as does the reaction temperature.

6.2.1.5 Amine functionalisation

An amine edge functionalisation of graphene was also attempted, using the synthetic path outlined in Figure 6-3. Sonochemically exfoliated graphene was reacted with a mixture of nitric acid and sulphuric acid to form nitrographene (G-NO_2). Reduction

was then performed using a Raney Ni catalyst and formic acid to form aminographene (G-NH_2).

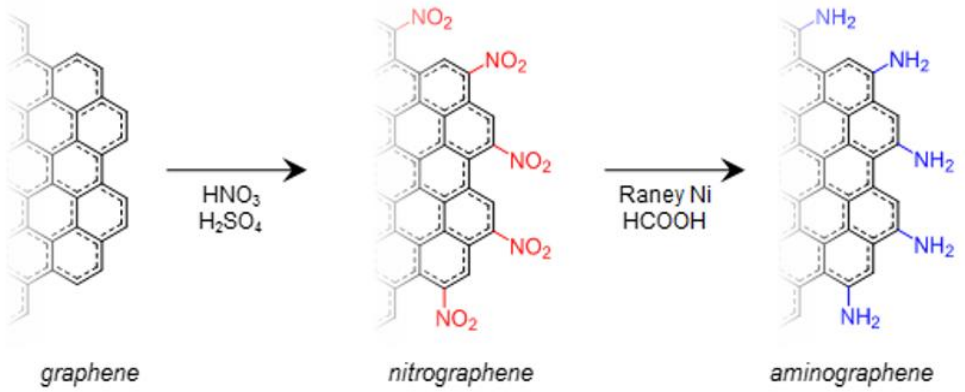

Figure 6-3. Reaction scheme depicting the edge-specific amine functionalisation of graphene.

Due to the dispersibility issues of graphene, this reaction was performed in NMP or DMF. Therefore, nitrogen was already present in the solvent, and it was difficult to determine differences in nitrogen content as a result of the functionalisation, as the amount of nitrogen remaining from the solvent and that from the functionalisation could not be differentiated. The initial reaction should be performed in an alternative solvent, which would need to disperse graphene well, but also be suitable under the reaction conditions.

There was, however, a significant change in the contact angles between graphene, G-NO_2 and G-NH_2, as shown in Figure 6-4. The dispersibility of the materials also differs, as shown in Figure 6-5, indicating that there is some change upon functionalisation. The XPS and Raman for amine functionalisations can be found in the appendix.

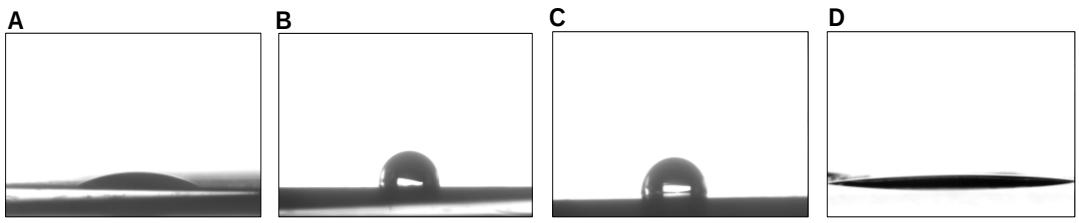

Figure 6-4. Water contact angles for A) Anodisc control (26 ^{O}) B) Graphene (105.1^{O} ± 7.7^{O}) C) Nitrographene (75.2 ^{O} ± 4.8 ^{O}) D) Aminographene (angle not measurable)

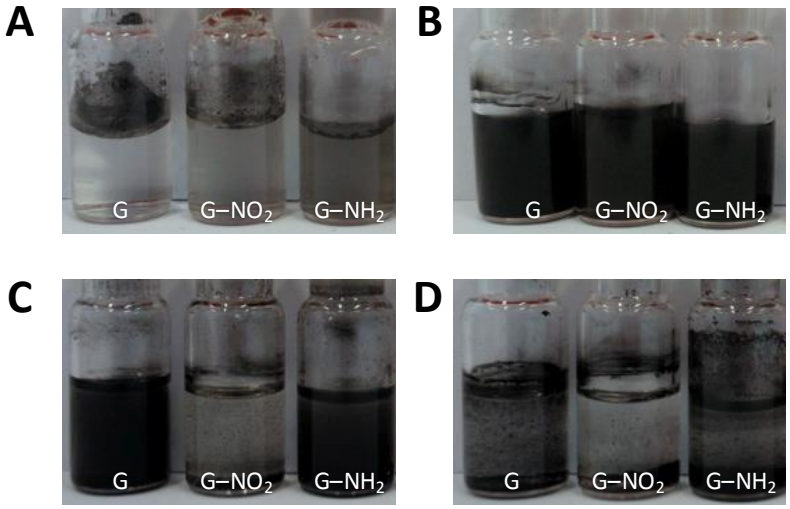

Figure 6-5. Dispersibility measurements of graphene, G-NO_2 and G-NH_2.

Another problem with the amine functionalisation was that the reduction step includes the use of Raney Ni, which is difficult to remove afterwards. The common reduction methods for nitro compounds involve metal catalysts, so alternative methods need to be developed which do not involve metal. A potential alternative route to G-NH_2, which eliminates the use of metal catalyst, could be via a brominated graphene, by reaction with potassium amide (KNH_2) in liquid ammonia, or by electrochemical reduction of G-NO_2.

6.2.1.6 Orthogonal functionalisation

In addition to developing of a catalogue of edge functionalisations of graphene, a further research aim is to add different functional groups on either side of the graphene sheet. The 'bio-orthogonal functionalisation' could be achieved by only exposing one side of a CVD sheet to functionalisation reagents, by masking one side

of the flake. The orthogonal functionalisation of graphene would present the possibility of tethering different species to either side of the sheet, to produce a 'lab-on-a-flake'. An example of a 'lab-on-a-flake' can be seen in Figure 6-6.

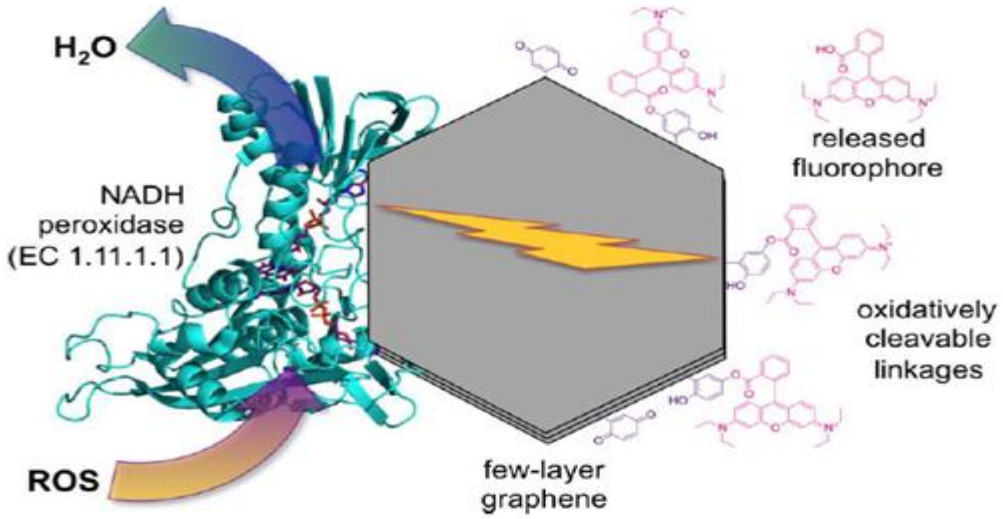

Figure 6-6. Schematic diagram of a graphene 'lab-on-a-flake, for detection of reactive oxygen species. Figure produced by Christopher Blanford.

In this example, an NADH peroxidase enzyme is covalently linked to one side of the graphene sheet and a fluorophore to the opposite side. In the presence of reactive oxygen species (ROS), the enzyme can catalyse their reduction to water. The electrons required for this reduction are provided by quinol linkers attached to the opposite side of the graphene sheet, which are consequently oxidised to quinones. The quinol linkers are attached to the fluorophores, which are released following the quinol/quinone conversion. This 'lab-on-a-flake' would therefore be able to detect ROS, release a fluorophore in response to their presence, and reduce the ROS to water. The 'lab-on-a-flake' idea could be extended to many different systems, in which detection and therapeutics could be combined on one flake.

A first step towards the 'lab-on-a-flake' idea is to demonstrate redox-cleavable linkages to functionalised CVD graphene. For example, graphene thiol (G-SH) presents the possibility of forming disulphide bonds with thiol terminated species such as fluorophores. Disulphide bonds can be reduced back to thiols, releasing the fluorophore. The attachment of G-SH to thiol terminated fluorophores and their electrochemical cleavage is currently being explored.

6.2.2 Graphene-containing layer-by-layer constructs

The incorporation of functionalised graphene sulfonate (G-SO_3), graphene oxide (GO) and sulfonated graphene oxide (GO-SO_3) into LbL constructs was evidenced in Chapter 3. Extensions of this work are outlined in the following section.

6.2.2.1 Thickness measurements from ellipsometry

One parameter which was not determined in this work was the thickness of the LbL constructs. An effective method for determining the thickness of LbL constructs is ellipsometry. Ellipsometry detects the changes in the polarization of light upon reflection from, in general, multilayer systems.[4] Light is passed through a polariser and, after reflection off the surface, the polarisation is changed and is measured by a polariser and a detector. The polarisation of the reflected light depends on the angle of incidence, thickness of layers and complex refractive indices of the layers, meaning that this information can be determined from the change in polarisation.[4]

6.2.2.2 Lateral dimensions and graphene coverage

Once G-SO_3 has been made using flakes with differing lateral dimensions and is fully characterised, the G-SO_3 materials could be incorporated into PEI/G-SO_3 LbL constructs and characterised using AFM, Raman mapping and ellipsometry, to

determine changes in G-SO_3 coverage in the LbL constructs as a function of the lateral dimensions of graphene flakes.

6.2.3 3T3 SA cell viability studies

Initial 3T3 SA cell viability studies on the graphene-containing LbL constructs showed that they all supported their attachment and proliferation, but revealed that relative cell activities were determined by the extent of fibronectin binding, which in turn was related to the surface functional groups and roughness of the LbL constructs. The following sections outline further experimental work which would complement the work presented in this thesis.

6.2.3.1. Effect of graphene coverage on cell viability.

As mentioned in 6.2.2.2, the loading of G-SO_3 into LbL constructs would be expected to vary as the lateral dimensions of the sheet decrease. It would be important to assess the effect of the lateral dimensions/loading of the G-SO_3 in PEI/G-SO_3 LbL constructs upon 3T3 SA cell viability. If the loading becomes greater as the starting graphene flake sizes become smaller, this could both increase the roughness of the LbL construct while also increasing the number sulfonate groups present in the LbL construct. It will be interesting to explore how these two characteristics affect 3T3 SA cell activity.

6.2.3.2 Primary skin cells

To further assess the suitability of PEI/GO, PEI/GO-SO_3 and PEI/G-SO_3 LbL constructs for wound healing applications, they should also be tested on cell lines pertinent to wound healing. A suggested cell lines would be Normal Human Dermal Fibroblasts from Adult and Neonatal Tissue (Lonza).

6.2.3.3 RGD functionalised graphene

The investigation of 3T3 SA viability and cell activity on the PEI/GO, PEI/GO-SO_3 and PEI/G-SO_3 LbL constructs highlighted patterns between functional group and cell activity. Positively-charged nitrogen-containing groups were found to increase cell activity, as were carboxyl, hydroxyl and epoxide functional groups. The increase in cell activity was linked to amount of fibronectin adsorption onto surface. Because the Arg-Gly-Asp (RGD) peptides sequence of fibronectin constitutes the binding sites for integrins, the production of RGD functionalised graphene could enhance cell adhesion. For example, Cai *et al.* and Yoon *et al* report the production thiol terminated RGD peptides,[5,6] which could be coupled to graphene thiol (G-SH).

6.2.4 Human mesenchymal stem cells

The behaviour of human mesenchymal stem cells (hMSCs) seeded onto PEI/GO, PEI/GO-SO_3 and PEI/G-SO_3 LbL constructs, though showing the same rank order of activity, differed much more greatly than the 3T3 SA cells, with hMSCs on the PEI/G-SO_3 LbL not showing significant increases in cell activity and displaying non-typical morphology. The differentiation of hMSCs seeded on the PEI/GO, PEI/GO-SO_3 and PEI/G-SO_3 to osteogenic and adipogenic lineages was also assessed and showed significant adipogenic differentiation of hMSCs on PEI/GO and PEI/GO-SO_3. The following section outlines further research arising from this work.

6.2.4.1 Neurogenesis

Initial studies on the effect of the GFN-containing LbL constructs on hMSC neurogenesis have been conducted. It has been documented that graphene has the ability to support neurogenesis and so it was interesting to see whether the PEI/GO,

PEI/GO-SO_3 and PEI/G-SO_3 LbL constructs were able to induce neurogenesis.[7] MSCs were grown up for four days, after which media was switched to neurogenesis media (C28015, Promocell). After 2 days' incubation in neurogenic media, hMSCs were stained with the neurogenesis markers anti-beta III tubulin antibody (ab7751, Abcam with ab194987, Alexa Fluor 488 secondary antibody) and anti-microtubule associated protein 2 (MAP-2) antibody (ab 11267 with ab1150116 Alexa Fluor 594, Abcam). Images of the beta III tubulin/MAP2/DAPI stained hMSCs are shown in Figure 6-7.

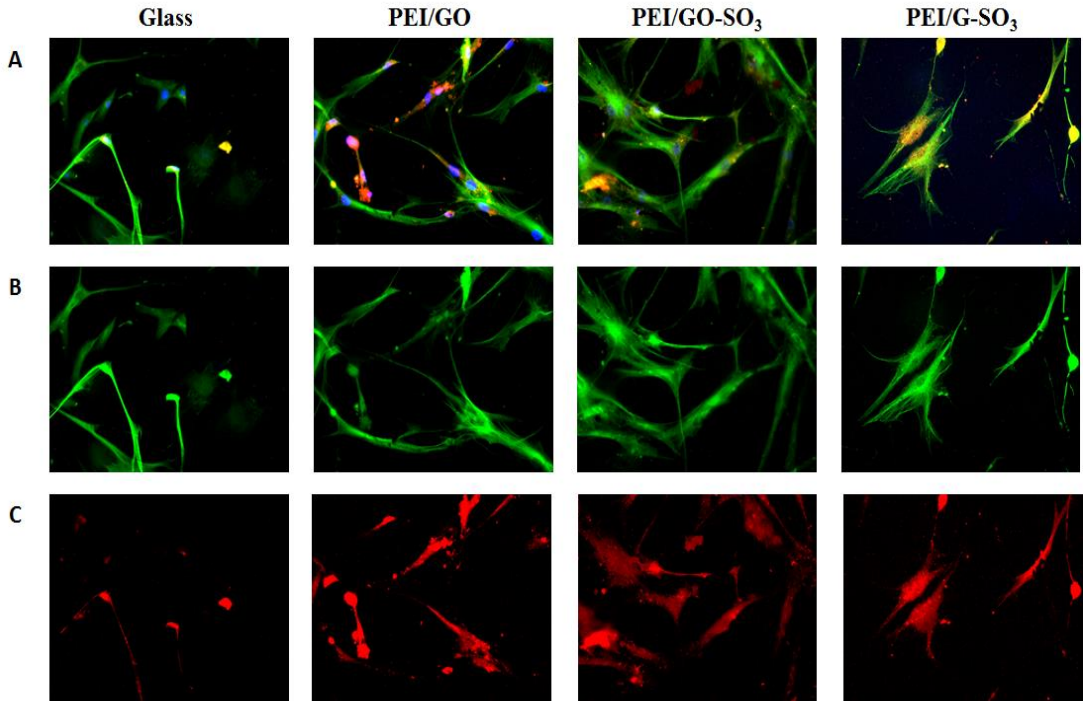

Figure 6-7. Antibody staining for neurogenically induced hMSCs on LbL constructs. A) Composite image (Blue: DAPI Green: Beta III tubulin Red: MAP-2) B) Beta III Tubulin C) MAP-2

All substrates showed positive staining for Beta III tubulin and MAP2, indicating the neurogenesis of hMSCs on all LbL constructs. Again, there were far fewer cells on the PEI/G-SO_3 LbL construct, but those that were present showed positive staining for neuron markers. Further stains such as glial fibrillary acid protein (GFAP), could

be used to further support that the cells on these substrates are neurons and not glial cells.

In addition to the antibody staining, the morphology of hMSCs before and after neurogenic induction was assessed by LIVE/DEAD staining, with representative images shown in Figure 6-8. The morphology of the hMSCs shows a clear change towards a much more elongated shape after neurogenic induction, on all substrates.

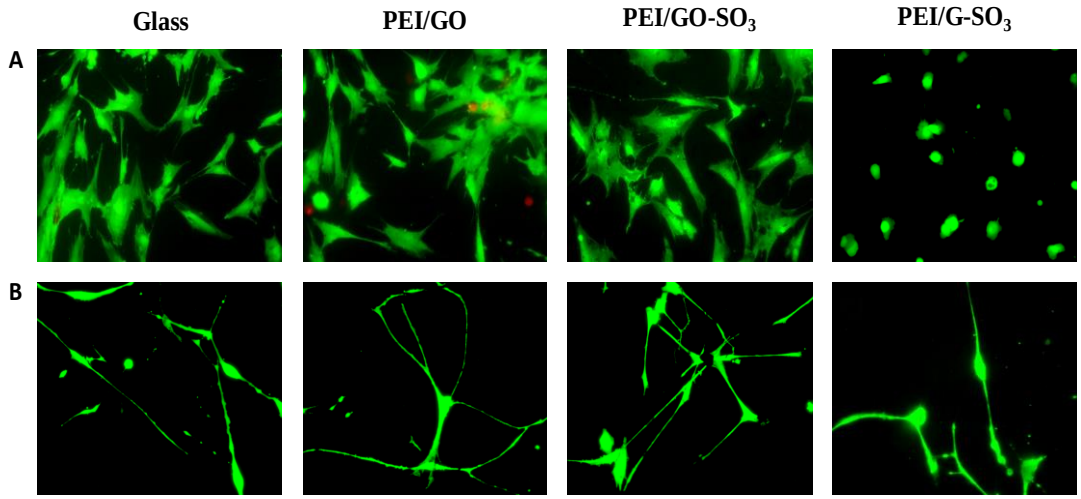

Figure 6-8. LIVE/DEAD images of hMSCs on LbL constructs A) Before induction B) 7 days post-induction.

6.2.4.2 Stem cell and differentiation markers

In this thesis, hMSC differentiation was assessed using stains and antibodies, therefore showing the translational protein expression. These included stains of the mineralised matrix such as fat and calcium deposits. These are late stage signals in differentiation and so early differentiation could be detected by looking at differentiation-related genes and their expression over the test period. This also would give quantitative information regarding the extent of differentiation between the different substrates to complement the semi-quantitative analysis performed.

In order to achieve this, reverse-transcriptase polymerase chain reaction (RT-PCR) can be used to look at the transcription level of key genes. For example, the

expression of resistin, an adipose specific secretory factor.[8] and adiponectin, an adipocyte specific protein,[9] could be measured to quantify the extent of adipogenesis. Similarly, expression of runt related transcription factor 2 (*RunX2*), which regulates the transcription of numerous genes involved in osteoblast development,[10] as well as bone specific alkaline phosphatase (BALP), which is synthesised by osteoblasts,[11] can be used to assess osteogenesis. The expression of osteopontin, osteocalcin, bone sialo protein could also be measured.

RT-PCR works by cloning the expressed genes by targeting the RNA of interest using reverse transcriptase and a primer (short strand of RNA/DNA that serves as a starting point for DNA synthesis). The primer is needed as DNA polymerase can only add new nucleotides to existing strands. Then the as-prepared complementary DNA is amplified using traditional PCR.[12]

6.2.4.3 Phosphonate-functionalised graphene

An interesting finding from the hMSC and 3T3 SA studies with PEI/G-SO_3 was that the sulfonate functional group of G-SO_3 may have contributed to decreased cell activity and proliferation, more notably for the case of hMSCs. Oxygen-containing groups in PEI/GO and PEI/GO-SO_3 may also have had a significant effect on cell adhesion and activity. This highlighted the significant effect of functional groups on graphene on the fate of different cell lines. A new project, developed as a result of this research, is to produce phosphonate-functionalised graphene for use in bone repair. This work is motivated by work by Bassi *et al*. who found that the incorporation of polyvinylphosphonic acid co-acrylic acid (PVPA) into poly (ε-caprolactone) caused an increase in bone filling in bone defects.[13] Therefore the combination of pristine graphene, which has been reported to support osteogenesis,

with phosphonate functional groups may enhance bone regeneration. The proposed route to phosphonated graphene is via the radical addition of vinylphosphonic acid to G-SH, after which phosphonated graphene would be incorporated into 3D gel-based scaffolds. The high mechanical strength of pristine graphene can be used to modulate the properties of the gel, to match more closely with bone tissues.

6.3 References

1. Lee, W. C.; Lim, C.; Shi, H.; Tang, L. A. L.; Wang, Y.; Lim, C. T.; Loh, K. P., Origin of Enhanced Stem Cell Growth and Differentiation on Graphene and Graphene Oxide. *ACS Nano* **2011,** *5* (9), 7334-7341.
2. Goldstein, J. I.; Newbury, D. E.; Echlin, P.; Joy, D. C.; Romig, A. D.; Lyman, C. E.; Fiori, C.; Lifshin, E., Scanning Electron Microscopy and X-ray Microanalysis. Plenum Press: New York, 1992.
3. van der Pauw, L. J., A method of measuring specific resistivity and Hall effect of discs of arbitrary shape. *Philips Research Reports* **1958,** *13* (1), 1-9.
4. Ogieglo, W.; Wormeester, H.; Eichhorn, K. J.; Wessling, M.; Benes, N. E., In situ ellipsometry studies on swelling of thin polymer films: A review. *Progress in Polymer Science* **2015,** *42*, 42-78.
5. Cai, W. B.; Chen, X. Y., Preparation of peptide-conjugated quantum dots for tumor vasculature-targeted imaging. *Nature Protocols* **2008,** *3* (1), 89-96.
6. Yoon, S. H.; Mofrad, M. R. K., Cell adhesion and detachment on gold surfaces modified with a thiol-functionalized RGD peptide. *Biomaterials* **2011,** *32* (30), 7286-7296.
7. Park, S. Y.; Park, J.; Sim, S. H.; Sung, M. G.; Kim, K. S.; Hong, B. H.; Hong, S., Enhanced Differentiation of Human Neural Stem Cells into Neurons on Graphene. *Advanced Materials* **2011,** *23* (36), H263–H267.
8. Jamaluddin, M. S.; Weakley, S. M.; Yao, Q. Z.; Chen, C. Y., Resistin: functional roles and therapeutic considerations for cardiovascular disease. *British Journal of Pharmacology* **2012,** *165* (3), 622-632.
9. Lihn, A. S.; Pedersen, S. B.; Richelsen, B., Adiponectin: action, regulation and association to insulin sensitivity. *Obesity Reviews* **2005,** *6* (1), 13-21.
10. Schroeder, T. M.; Jensen, E. D.; Westendorf, J. J., Runx2: a master organizer of gene transcription in developing and maturing osteoblasts. *Birth Defects Res C Embryo Today* **2005,** *75* (3), 213-225.
11. Leung, K. S.; Fung, K. P.; Sher, A. H. L.; Li, C. K.; Lee, K. M., Plasma bone-specific alkaline-phosphatase as an indicator of osteoblastic activity. *Journal of Bone and Joint Surgery-British Volume* **1993,** *75* (2), 288-292.
12. Rapley, R., *Molecular biology and biotechnology*. 4th Edition ed.; Royal Society of Chemistry: Cambridge, UK, 2000.
13. Bassi, A. K.; Gough, J. E.; Downes, S., A novel phosphonate for the repair of critical size bone defects. *Journal of Tissue Engineering and Regenerative Medicine* **2012,** *6* (10), 833-840.

APPENDIX

A.1 Isotherm classifications

Nitrogen adsorption isotherms provide information about pore filling and surface coverage of gas onto surface, with six distinct isotherms classified by the International Union of Pure and Applied Chemistry (IUPAC).[1] Type I isotherms contain a long plateau, are concave to the axis and are characteristic of small surfaces on which uptake is limited by micropore volume.[1] Type II isotherms have smooth, non-stepwise character, with an inflexion point, at which multilayers begin to form and arise from non-porous or macroporous adsorbents.[1] Type IIb isotherms are achieved with aggregates of plate-like particles which possess non-rigid slit-shaped pores.[1] Type III isotherms are convex to P/P_0, with no inflexion point and occur when the monolayer is unevenly distributed on the surface.[1] Type IV isotherms possess an initial part of the isotherm which is attributed to monolayer-multilayer adsorption (similar to Type II). They also possess a characteristic hysteresis loop, from capillary condensation which occurs in the mesopores.[1] There are two types of hysteresis loops observed for Type IV isotherms; H1, which has a narrow loop and parallel adsorption and desorption branches (Type Iva isotherm),[1] or a broad H2 loop, which has a steeper desorption branch (Type IVb isotherm).[1] This isotherm corresponds to pore-filling and emptying in narrow range of near-cylindrical pores.[1] A depiction of type I-IV isotherms can be seen in Figure A-1.

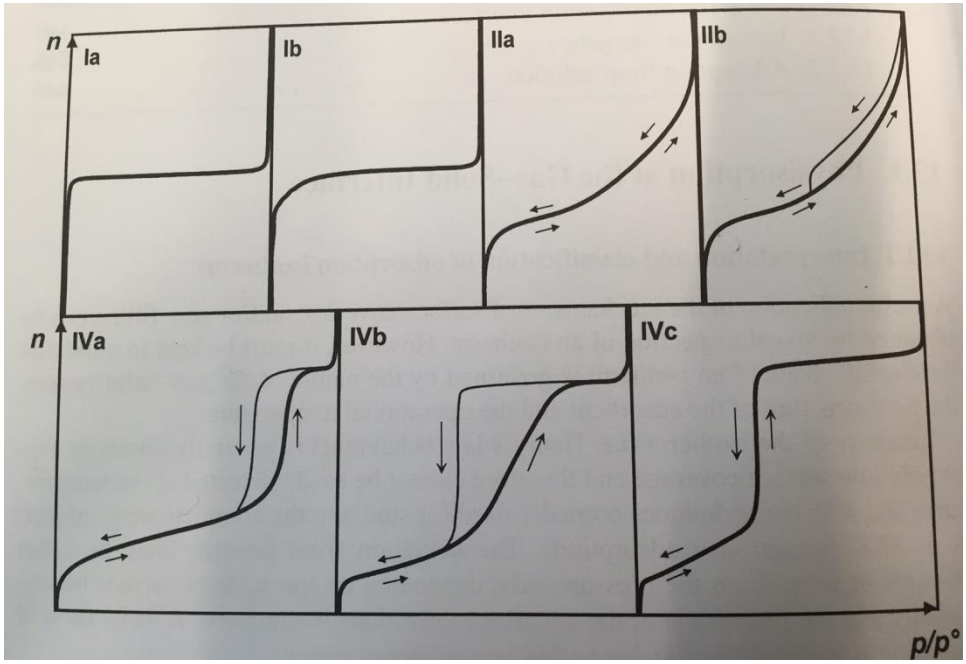

Figure A-1. Isotherm classifications. Taken from 'Adsorption by powders and porous solids, by Rouquerol *et al.*[1]

Type V isotherms are similar to Type III isotherms, but show a sharp increase in adsorption at high P/P_0 and are indicative of weak adsorbent-adsorbate interactions.[1] The shape of type VI arise from a stepwise layer-by-layer adsorption process, with vertical rises representing the monolayer capacity of each layer,[1] which are from the adsorption of non-polar molecules onto uniform surfaces. Type V and VI isotherm shapes are shown in Figure A-2.

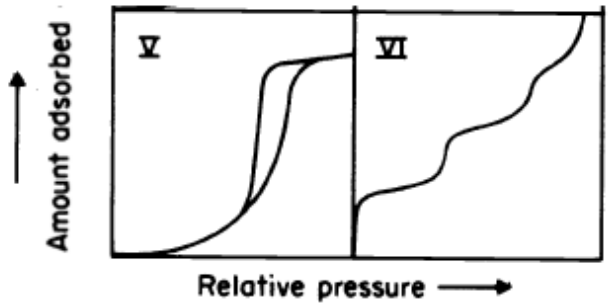

Figure A-2. Type V and VI isotherms. Taken from IUPAC recommendations.[1]

A.2 Hysteresis classifications

Hystereses are associated with capillary condensation in mesoporous structures, with the shapes of hysteresis loops have often been identified with specific pore structures. H1 hysteresis occurs when adsorbents have a narrow pore size distribution, or are agglomerated,[1] while porous adsorbents give H2 hysteresis loops[1] and tend to be formed from networks of pores with differing sizes and shapes.[1] H3 loops have limiting adsorption at high P/P_0 and arise for aggregated plate-like particles, which form slit-shaped pores. The H4 loop is indicative of slit-like micropores.[1] The types of hysteresis are shown in Figure A-3

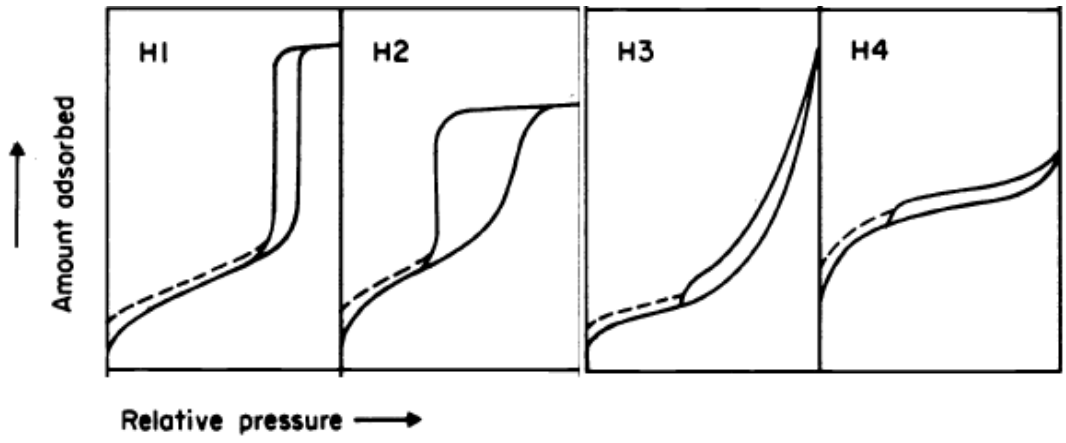

Figure A-3. Types of hysteresis observed in BET measurements.[1]

A.3 Cell shape parameters

Area- number of pixels in the region.

Perimeter- total number of pixels around the boundary of each region in the image.

Center_X, Center_Y- The x- and y-coordinates of the point farthest away from any object edge.

Form factor- $4*\pi*\text{Area}/\text{Perimeter}^2$. The form factor is 1 for a circular object.

Ferret diameter- distance between two parallel lines tangent on either side of the object. The minimum and maximum Feret diameters are the smallest and largest possible diameters.

Median radius- median distance of any pixel in the object to the closest pixel outside of the object.

Maximum radius- maximum distance of any pixel in the object to the closest pixel outside of the object.

Compactness- mean squared distance of the object's pixels from the centroid divided by the area.

Orientation- angle (in degrees ranging from -90 to 90 degrees) between the x-axis and the major axis of the ellipse that has the same second-moments as the region.

Minor axis length- length (in pixels) of the minor axis of the ellipse that has the same normalized second central moments as the region

Major axis length- length (in pixels) of the major axis of the ellipse that has the same normalized second central moments as the region.

Eccentricity- the ratio of the distance between the foci of the ellipse and its major axis length. The value is between 0 and 1.

Extent- proportion of the pixels in the bounding box that are also in the region. Computed as the Area divided by the area of the bounding box

Euler number- number of objects in the region minus the number of holes in those objects, assuming 8-connectivity.

Solidity- Equals 1 for a solid object (i.e., one with no holes or has a concave boundary), or <1 for an object with holes or possessing a convex/irregular boundary.

A.4 Raman, amine functionalisation

Figure A-4 shows the Raman spectra of graphene, nitrographene (G-NO_2) and aminographene (G-NH_2), while Figure A-5 shows the XPS N 1s spectra of G-NO_2 and G-NH_2.

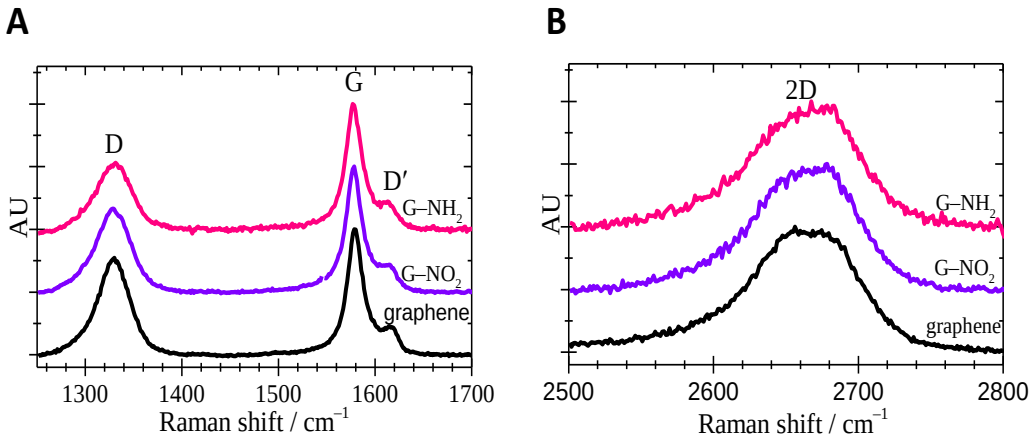

Figure A-4. Raman spectra of graphene (black), nitrographene (purple) and aminographene (pink). A) D and G region B) 2D region.

A.5 XPS, amine functionalisation

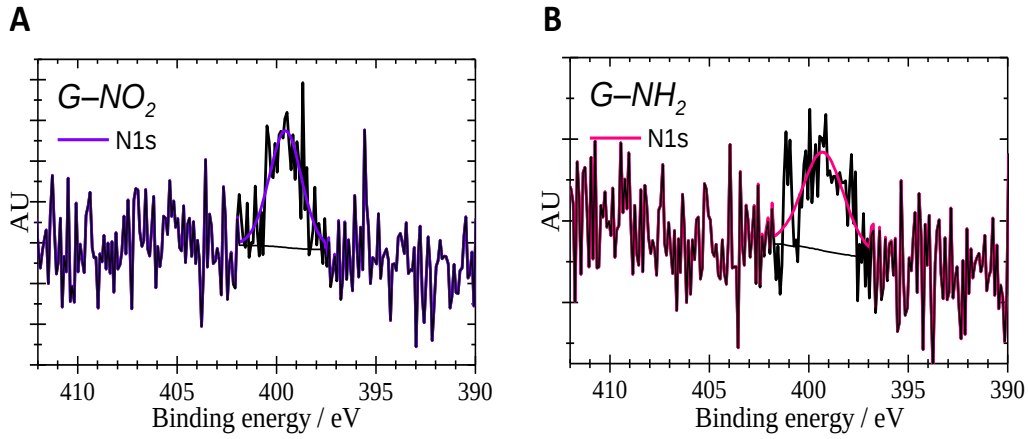

Figure A-5. XPS N 1s spectra for A) nitrographene B) aminographene.

A.6 References

1. Sing, K. S. W.; Everett, D. H.; Haul, R. A. W.; Moscou, L.; Pierotti, R. A.; Rouquerol, J.; Siemieniewska, T., Reporting physisorption data for gas solid systems

with special reference to the determination of surface-area and porosity (recommendations 1984). *Pure and Applied Chemistry* **1985,** *57* (4), 603-619.